

UNIVERSITÀ DELLA CALABRIA



UNIVERSITÀ DELLA CALABRIA

Dipartimento di Fisica

Dottorato di Ricerca in

Scienze e Tecnologie Fisiche, Chimiche e dei Materiali

CICLO

XXIX

High-energy resummation in semi-hard processes at the LHC

Settore Scientifico Disciplinare

FIS/02 - Fisica Teorica, Modelli e Metodi Matematici

Coordinatore: Ch.mo Prof. **Vincenzo Carbone**

Firma Vincenzo Carbone

Supervisore: Ch.mo Prof. **Alessandro Papa**

Firma Alessandro Papa

Dottorando: Dott. **Francesco Giovanni Celiberto**

Firma Francesco Giovanni Celiberto

*Alla mia famiglia
A zio Pinuccio*

Contents

Abstract	1
Sintesi in lingua italiana	3
1 Introduction	6
2 The BFKL resummation	12
2.1 The Regge theory	12
2.1.1 The Pomeron	13
2.2 Towards the BFKL equation	14
2.2.1 Gluon Reggeisation	15
2.3 The amplitude in multi-Regge kinematics	18
2.3.1 The BFKL equation	23
2.3.2 The BFKL equation in the NLA	26
2.3.3 The BFKL cross section	28
2.3.3.1 Representation equivalence	36
2.4 The BLM optimisation procedure	37
A The Mellin transform	45
A.1 Properties of the Mellin transform	46
3 Mueller–Navelet jets	49
3.1 Theoretical framework	49
3.1.1 Inclusive dijet production in proton-proton collisions	49
3.1.2 Dijet cross section and azimuthal correlations	53
3.1.3 BLM scale setting	54
3.1.4 Integration over the final-state phase space	57
3.2 Theory versus experiment	58
3.3 BFKL versus high-energy DGLAP	62
3.3.1 Motivation	62

3.3.2	Results and discussion	63
3.4	Central rapidity range exclusion	70
3.4.1	Motivation	70
3.4.2	Phase-space constraints	71
3.4.3	Results and discussion	73
3.5	Numerical specifics	89
3.5.1	Used tools	89
3.5.2	Uncertainty estimation	89
3.6	Summary	91
B	NLO impact factor for the small-cone forward jet	95
4	Dihadron production	98
4.1	Theoretical framework	100
4.1.1	Inclusive dihadron production	100
4.1.2	Dihadron cross section and azimuthal correlations	102
4.1.3	Integration over the final-state phase space	105
4.1.4	BLM scale setting	105
4.2	A first phenomenological analysis	108
4.3	Full NLA BFKL calculation	112
4.4	Numerical specifics	125
4.4.1	Used tools	125
4.4.2	Uncertainty estimation	126
4.5	Summary	127
C	NLO impact factor for the identified hadron	130
5	Three-jet production	132
5.1	A new way to probe BFKL	134
5.1.1	The three-jet cross section	134
5.1.2	One-cosine projection: <i>À la</i> Mueller–Navelet	138
5.1.2.1	One-cosine azimuthal correlations	138
5.1.2.2	Numerical analysis	139
5.1.3	Two-cosine projection: generalised correlations	140
5.1.3.1	Two-cosine azimuthal correlations	140
5.1.3.2	Numerical analysis	142
5.2	Hadronic level predictions	144
5.2.1	A more phenomenological analysis: inclusion of NLA	144
5.2.2	BLM scale setting	147

5.2.3	Fixed rapidity kinematics for the central jet	148
5.2.4	Dependence on the central-jet rapidity bin	152
5.2.5	Dependence on bins for all three jets	154
5.2.6	Numerical tools	156
5.3	Summary	156
D	y_J-independent integrated distributions	165
6	Four-jet production	167
6.1	Theoretical framework	169
6.1.1	The four-jet cross section	169
6.1.2	The four-jet azimuthal correlations: partonic level	173
6.2	Partonic level analysis	175
6.3	Hadronic level predictions	181
6.3.1	The four-jet azimuthal correlations: hadronic level	181
6.3.2	Integration over the final-state phase space	182
6.3.3	Numerical analysis	183
6.3.3.1	Results and discussion	184
6.3.3.2	Used tools	193
6.4	Summary	193
7	Conclusions and Outlook	195
7.1	Conclusions	195
7.2	Outlook	198
	Bibliography	200

List of Tables

3.1	Dijet BFKL predictions at 7 TeV	60
3.2	Dijet BFKL vs high-energy DGLAP predictions at 7 TeV and for $k_{J_2}^{\min} = 45$ GeV	66
3.3	Dijet BFKL vs high-energy DGLAP predictions at 7 TeV and for $k_{J_2}^{\min} = 50$ GeV	67
3.4	Rapidity veto effect for different BLM scale settings in dijet production	75
3.5	Rapidity veto effect on C_0 in dijet production	76
3.6	Rapidity veto effect on R_{10} in dijet production	77
3.7	Rapidity veto effect on R_{20} in dijet production	78
3.8	Rapidity veto effect on R_{30} in dijet production	79
3.9	Rapidity veto effect on R_{21} in dijet production	80
3.10	Rapidity veto effect on R_{32} in dijet production	81

List of Figures

2.1	Reggeised gluon exchange	16
2.2	Diagrammatic representation of the s-channel unitarity relation	19
2.3	Diagrammatic representation of the amplitude $\mathcal{A}_{AB}^{\tilde{A}\tilde{B}n}$	22
2.4	Diagrammatic representation of the BFKL amplitude	24
2.5	Generalised BFKL integral equation	25
2.6	real part of the BFKL kernel at the Born level	26
2.7	NLA vertex replacements (1)	26
2.8	NLA vertex replacements (2)	27
3.1	Mueller–Navelet jet production process in multi-Regge kinematics	50
3.2	Forward parton impact factor	51
3.3	Forward jet impact factor	52
3.4	Comparison of dijet BFKL predictions with CMS data at 7 TeV	61
3.5	Mueller–Navelet jets at LLA: a back-to-back dijet reaction	63
3.6	Dijet BFKL and high-energy DGLAP predictions at 7 TeV and for $k_{J_2}^{\min} = 45$ GeV	68
3.7	Dijet BFKL and high-energy DGLAP predictions at 7 TeV and for $k_{J_2}^{\min} = 50$ GeV	69
3.8	Central rapidity range exclusion in dijet production	73
3.9	Rapidity veto effect for different BLM scale settings in dijet pro- duction	82
3.10	Rapidity veto effect on C_0 in dijet production	83
3.11	Rapidity veto effect on R_{10} in dijet production	84
3.12	Rapidity veto effect on R_{20} in dijet production	85
3.13	Rapidity veto effect on R_{30} in dijet production	86
3.14	Rapidity veto effect on R_{21} in dijet production	87
3.15	Rapidity veto effect on R_{32} in dijet production	88
4.1	Inclusive dihadron production process in multi-Regge kinematics.	100
4.2	Identified-hadron impact factor	101

4.3	BLM scales for dihadron production	108
4.4	NLA kernel predictions for dihadron production at 13 TeV	110
4.5	NLA kernel predictions for dihadron production at 7 TeV	111
4.6	Full NLA predictions of C_0 for dihadron production in the \overline{MS} scheme	116
4.7	Full NLA predictions for dihadron production for $\mu_F = \mu_R^{\text{BLM}}$, $\sqrt{s} = 13$ TeV, and $Y \leq 4.8$	117
4.8	Full NLA predictions for dihadron production for $\mu_F = \mu_R^{\text{BLM}}$, $\sqrt{s} = 7$ TeV, and $Y \leq 4.8$	118
4.9	Full NLA predictions for dihadron production for $(\mu_F)_{1,2} = \vec{k}_{1,2} $, $\sqrt{s} = 13$ TeV, and $Y \leq 4.8$	119
4.10	Full NLA predictions for dihadron production for $(\mu_F)_{1,2} = \vec{k}_{1,2} $, $\sqrt{s} = 7$ TeV, and $Y \leq 4.8$	120
4.11	Full NLA predictions for dihadron production for $\mu_F = \mu_R^{\text{BLM}}$, $\sqrt{s} = 13$ TeV, and $Y \leq 9.4$	121
4.12	Full NLA predictions for dihadron production for $\mu_F = \mu_R^{\text{BLM}}$, $\sqrt{s} = 7$ TeV, and $Y \leq 9.4$	122
4.13	Full NLA predictions for dihadron production for $(\mu_F)_{1,2} = \vec{k}_{1,2} $, $\sqrt{s} = 13$ TeV, and $Y \leq 9.4$	123
4.14	Full NLA predictions for dihadron production for $(\mu_F)_{1,2} = \vec{k}_{1,2} $, $\sqrt{s} = 7$ TeV, and $Y \leq 9.4$	124
4.15	Full NLA predictions for dihadron production for $\mu = r\sqrt{ \vec{k}_1 \vec{k}_2 }$, with $r = 1/2, 1, 2, 4$, and $Y \leq 4.8$	125
5.1	A three-jet event in a generic detector	135
5.2	Inclusive three-jet production process in multi-Regge kinematics	136
5.3	<i>À la</i> Mueller–Navelet observables in three-jet production	140
5.4	Partonic three-jets: BFKL azimuthal ratios	143
5.5	Lego plot for a three-jet event with fixed kinematics for the central jet rapidity	146
5.6	Lego plot for a three-jet event with integration over a central-jet rapidity bin	152
5.7	Lego plot for a three-jet event with integration over bin on all jet rapidities	154
5.8	LLA and NLA R_{22}^{12} , R_{33}^{12} , and R_{33}^{22} at $\sqrt{s} = 7$ TeV	157
5.9	LLA and NLA R_{22}^{12} , R_{33}^{12} , and R_{33}^{22} at $\sqrt{s} = 13$ TeV	158
5.10	LLA and NLA $^{(i)}R_{22}^{12}$, $^{(i)}R_{33}^{12}$, and $^{(i)}R_{33}^{22}$ at $\sqrt{s} = 7$ TeV	159
5.11	LLA and NLA $^{(i)}R_{22}^{12}$, $^{(i)}R_{33}^{12}$, and $^{(i)}R_{33}^{22}$ at $\sqrt{s} = 13$ TeV	160
5.12	LLA and NLA $^{(i)}R_{22}^{12}(y_i)$, $^{(i)}R_{33}^{12}(y_i)$, and $^{(i)}R_{33}^{22}(y_i)$ at $\sqrt{s} = 7$ TeV	161

5.13	LLA and NLA ${}^{(i)}R_{22}^{12}$, ${}^{(i)}R_{33}^{12}$, and ${}^{(i)}R_{33}^{22}$ at $\sqrt{s} = 13$ TeV	162
6.1	Inclusive four-jet production process in multi-Regge kinematics .	169
6.2	A primitive lego plot depicting a four-jet event	170
6.3	Partonic four-jets: BFKL azimuthal coefficients (1)	177
6.4	Partonic four-jets: BFKL azimuthal coefficients (2)	178
6.5	Partonic four-jets: BFKL azimuthal ratios (1)	179
6.6	Partonic four-jets: BFKL azimuthal ratios (2)	180
6.7	Y-dependence of the R_{221}^{111} four-jet ratios	187
6.8	Y-dependence of the R_{111}^{112} four-jet ratios	188
6.9	Y-dependence of the R_{211}^{112} four-jet ratios	189
6.10	Y-dependence of the R_{111}^{212} four-jet ratios	190
6.11	Y-dependence of the R_{221}^{122} four-jet ratios	191
6.12	Y-dependence of the R_{112}^{221} four-jet ratios	192

Abstract

Semi-hard processes in the large center-of-mass energy limit offer us an exclusive chance to test the dynamics behind strong interactions in kinematical sectors so far unexplored, the high luminosity and the record energies of the LHC providing us with a richness of useful data. In the Regge limit, $s \gg |t|$, fixed-order calculations in perturbative QCD based on *collinear factorisation* miss the effect of large energy logarithms, which are so large to compensate the small QCD coupling α_s and must therefore be accounted for to all perturbative orders. The BFKL approach represents the most powerful tool to perform the resummation to all orders of these large logarithms both in the LLA, which means inclusion of all terms proportional to $(\alpha_s \ln(s))^n$, and NLA, which means inclusion of all terms proportional to $\alpha_s(\alpha_s \ln(s))^n$. The inclusive hadroproduction of forward jets with high transverse momenta separated by a large rapidity gap at the LHC, the so-called Mueller–Navelet jets, has been one of the most studied reactions so far. Interesting observables associated to this process are the azimuthal correlation momenta, showing a very good agreement with experimental data at the LHC. However, new BFKL-sensitive observables should be considered in the context of the LHC physics program. With the aim to further and deeply probe the dynamics of QCD in the Regge limit, we give phenomenological predictions for four distinct semi-hard processes. On one hand, we continue the analysis of reactions with two objects

identified in the final state (i) by addressing open problems in the Mueller–Navelet sector and (ii) by studying the inclusive dihadron production in the full NLA BFKL accuracy. Hadrons can be detected at the LHC at much smaller values of the transverse momentum than jets, allowing us to explore an additional kinematical range, complementary to the one studied typical of Mueller–Navelet jets. Furthermore, this process permits to constrain not only the parton distribution functions for the initial proton, but also the parton fragmentation functions describing the detected hadron in the final state. On the other hand, we show how inclusive multi-jet production processes allow us to define new, generalised and suitable BFKL observables, where transverse momenta and rapidities of the tagged jets, well separated in rapidity from each other, appear in new combinations. We give the first phenomenological predictions for the inclusive three-jet production, encoding the effects of higher-order BFKL corrections. Then, making use of the same formalism, we present the first complete BFKL analysis for the four-jet production.

Sintesi in lingua italiana

Per quanto una teoria fisica possa apparire complessa e formalmente ardua l'origine della sua eleganza risiede quasi sempre in un'idea semplice e concreta. Il Modello Standard (MS) delle particelle elementari, solidamente edificato sull'esistenza di costituenti fondamentali di natura fermionica che interagiscono tra loro attraverso lo scambio di bosoni vettori intermedi, è tra gli esempi più significativi. All'interno del MS, la Cromodinamica Quantistica (QCD) è la teoria che descrive le *interazioni forti* tra i quark, particelle costituenti di natura fermionica, e i gluoni, bosoni mediatori dell'interazione stessa.

Nel limite di alte energie nel centro di massa \sqrt{s} , lo studio dei processi *semi-duri* (ovvero quei processi caratterizzati da scale dure molto maggiori della scala della QCD Λ_{QCD} ma, al contempo, notevolmente inferiori rispetto a \sqrt{s}) permette senza dubbio di effettuare prove stringenti della dinamica delle interazioni forti in regimi cinematici ad ora inesplorati. Nel limite di Regge ($s \gg |t|$, con t la variabile di Mandelstam rappresentante il quadrato della quantità di momento trasferito), le predizioni teoriche di QCD perturbativa ad ordine fisso, basate sulla fattorizzazione collineare, non possono tener conto dell'effetto non trascurabile dei logaritmi in energia, il cui contributo è tale da compensare quello della costante d'accoppiamento della QCD α_s e, per tale ragione, deve essere tenuto in conto a tutti gli ordini dello sviluppo perturbativo. L'approccio Balitsky–Fadin–Kuraev–Lipatov (BFKL) rappresenta di certo lo strumento più

potente in grado di risommare a tutti gli ordini il contributo di tali logaritmi, sia in approssimazione logaritmica dominante (LLA), ossia risommazione di tutti i termini proporzionali a $(\alpha_s \ln(s))^n$, sia in quella sottodominante (NLA), ossia risommazione dei fattori del tipo $\alpha_s(\alpha_s \ln(s))^n$.

Il processo di produzione inclusiva “in avanti” di jet con alto momento trasverso e separati da un grande intervallo di rapidità, meglio noto come produzione di jet di *Mueller–Navelet*, è, ad oggi, tra le reazioni più studiate. La ragione della sua popolarità in ambito scientifico risiede soprattutto nell’aver fornito la possibilità di definire i *momenti di correlazione azimutale*, osservabili *infrared-safe* le cui predizioni teoriche sono in buon accordo con i dati sperimentali ottenuti al Large Hadron Collider (LHC). È tuttavia necessario che nuove osservabili, sensibili alla dinamica BFKL, vengano considerate nell’ambito della fenomenologia di LHC.

Perseguendo lo scopo di approfondire ed estendere la conoscenza della dinamica delle interazioni forti nel limite di Regge, si propone lo studio di quattro distinti processi semiduri.

Nella prima parte dell’analisi fenomenologica presentata, ci si propone di continuare l’indagine di processi caratterizzati da due oggetti identificati nello stato finale, proseguendo lo studio dei problemi aperti nel processo di produzione di jet di *Mueller–Navelet* e, nello stesso tempo, affiancando ad esso quello della produzione inclusiva di una coppia adrone-antiadrone (*dihadron system*) carico leggero del tipo $\pi^\pm, K^\pm, p, \bar{p}$, entrambi caratterizzati da alto momento trasverso e fortemente separati in rapidità. La possibilità di rivelare gli adroni ad LHC a valori del momento trasverso di gran lunga inferiori rispetto ai jet consente di esplorare un settore cinematico complementare a quello studiato attraverso il canale di *Mueller–Navelet*. La produzione di adroni offre, inoltre, la possibilità di investigare simultaneamente il comportamento di

oggetti non perturbativi, quali le funzioni di distribuzione partonica (PDF) del protone nello stato iniziale e le funzioni di frammentazione (FF) caratterizzanti l'adrone rivelato nello stato finale.

Nella seconda parte della tesi, si pone e si evidenzia come lo studio della produzione di più jet nello stato finale (*multi-jet production*) fornisca la possibilità di generalizzare le osservabili definite nel caso di processi con due oggetti nello stato finale, costruendone delle nuove, maggiormente sensibili alla dinamica BFKL a causa della loro dipendenza da momenti trasversi e rapidità dei jet rivelati nelle regioni centrali dei rivelatori. È presentata la prima analisi fenomenologica sulla produzione di tre jet, tenendo conto degli effetti dovuti all'inclusione delle correzioni d'ordine superiore in risommazione BFKL. Infine, facendo uso dello stesso formalismo, viene presentato il primo studio completo sulla produzione di quattro jet.

Chapter 1

Introduction

Insofar as a physical theory may appear complex and formally arduous, the origin of its elegance lies almost always on a simple and concrete idea. The Standard Model (SM) of elementary particles, solidly built up on the existence of fermionic fundamental constituents, their mutual interaction being mediated via the exchange of intermediate vector bosons, represents one of the most significant examples. Inside the SM, Quantum Chromodynamics (QCD) is the theory of strong interactions, describing how fermionic quarks and bosonic gluons, the elementary constituents of hadrons¹, such as the proton and the neutron, interact with each other. What makes QCD a challenging sector surrounded by a broad and constant interest in its phenomenology, is the duality between non-perturbative and perturbative aspects which comes from the coexistence of two peculiar and concurrent properties, as *confinement* and *asymptotic freedom*. The striking feature of confinement is the increasing of the strong coupling α_s with distance. This means that hadrons are described by bound states of quarks and gluons, which cannot be described at the hand of any perturbative calculation. Conversely, the short-distance regime is ruled by asymptotic freedom, so that quarks and gluons behave as quasi-free particles,

¹From the ancient-greek word ἀδρός, which means 'strong'.

making it possible to use perturbative approaches.

The high luminosity and the record energies of the Large Hadron Collider (LHC) provide us with a wealth of useful data. A peerless opportunity to test strong interactions in this so far unexplored kinematical configuration of large center-of-mass energy is given by the study of *semi-hard* processes, *i.e.* hard processes in the kinematical region where the center-of-mass energy squared s is substantially larger than one or more hard scales Q_i^2 (large squared transverse momenta, large squared quark masses and/or t), $s \gg Q_i^2$, which satisfy in turn $Q_i^2 \gg \Lambda_{\text{QCD}}^2$, with Λ_{QCD} the QCD scale. In the kinematical regime ², known as *Regge limit* (see also Section 2.1), $s \gg |t|$, fixed-order calculations in perturbative QCD based on *collinear factorisation* ³ miss the effect of large energy logarithms, entering the perturbative series with a power increasing with the order and thus compensating the smallness of the coupling α_s . The Balitsky–Fadin–Kuraev–Lipatov (BFKL) approach [7–10] serves as the most powerful tool to perform the all-order resummation of these large energy logarithms both in the leading approximation (LLA), which means inclusion of all terms proportional to $(\alpha_s \ln(s))^n$, and the next-to-leading approximation (NLA), which means inclusion of all terms proportional to $\alpha_s(\alpha_s \ln(s))^n$. In the BFKL formalism, it is possible to express the cross section of an LHC process falling in the domain of perturbative QCD as the convolution between two impact factors, which describe the transition from each colliding proton to the respective final-state object, and a process-independent Green’s function. The BFKL Green’s function obeys an integral equation, whose kernel is known at the next-to-leading order (NLO) both for forward scattering (*i.e.* for $t = 0$ and

²Here t represents the t -channel Mandelstam variable [1].

³It is worth to remember that the factorisation theorem allows to write QCD cross sections as the convolution of a hard process-dependent cross section with universal parton distribution functions (PDFs) which are described by the Dokshitzer–Gribov–Lipatov–Altarelli–Parisi (DGLAP) evolution equation [2–6].

colour singlet in the t-channel) [11, 12] and for any fixed (not growing with energy) momentum transfer t and any possible two-gluon colour state in the t-channel [13–16].

The too low \sqrt{s} , bringing to small rapidity intervals among the tagged objects in the final state, had been so far the weakness point of the search for BFKL effects. Furthermore, too inclusive observables were considered. A striking example is the growth of the hadron structure functions at small Bjorken- x values in Deep Inelastic Scattering (DIS). Although NLA BFKL predictions for the structure function $F_{2,L}$ have shown a good agreement with the HERA data [17, 18], also other approaches can fit these data. The LHC record energy, together with the good resolution in azimuthal angles of the particle detectors, can address these issues: on one side larger rapidity intervals in the final state are reachable, allowing us to study a kinematical regime where it is possible to disentangle the BFKL dynamics from other resummations; on the other side, there is enough statistics to define and investigate more exclusive observables, which can, in principle, be only described by the BFKL framework.

With this aim, the production of two jets featuring transverse momenta much larger than Λ_{QCD}^2 and well separated in rapidity, known as *Mueller–Navelet jets*, was proposed [19] as a tool to investigate semi-hard parton scatterings at a hadron collider. This reaction represents a unique venue where two main resummations, collinear and BFKL ones, play their role at the same time in the context of perturbative QCD. On one hand, the rapidity ranges in the final state are large enough to let the NLA BFKL resummation of the energy logarithms come into play. The process-dependent part of the information needed to build up the cross section is encoded in the impact factors (the so-called “jet vertices”), which are known up to NLO [20–28]. On the other hand, the jet vertex can be expressed, within collinear factorisation at the

leading twist, as the convolution of the PDF of the colliding proton, obeying the standard DGLAP evolution, with the hard process describing the transition from the parton emitted by the proton to the forward jet in the final state.

A large number of numerical analyses [29–39] has appeared so far, devoted to NLA BFKL predictions for the Mueller–Navelet jet production process. All these studies are involved in calculating cross sections and azimuthal angle correlations [40,41] between the two measured jets, *i.e.* average values of $\cos(n\phi)$, where n is an integer and ϕ is the angle in the azimuthal plane between the direction of one jet and the direction opposite to the other jet, and ratios of two such cosines [42,43]. Recently [44], the CMS Collaboration presented the first measurements of the azimuthal correlation of the Mueller–Navelet jets at $\sqrt{s} = 7$ TeV at the LHC. Further experimental studies of the Mueller–Navelet jets at higher LHC energies and larger rapidity intervals, including also the effects of using *asymmetric* cuts for the jet transverse momenta, are expected.

In order to reveal the dynamical mechanisms behind partonic interactions in the Regge limit, new observables, sensitive to the BFKL dynamics and more exclusive than the Mueller–Navelet ones, need to be proposed and considered in the next LHC analyses.

A first step in this direction is the study of another reaction, less inclusive than Mueller–Navelet jets although sharing with it the theoretical framework, *i.e.* the inclusive detection of two charged light hadrons (a *dihadron* system) $\pi^\pm, K^\pm, p, \bar{p}$ having high transverse momenta and well separated in rapidity. Since the key ingredient beyond the NLA BFKL Green’s function, *i.e.* the process-dependent vertex describing the production of an identified hadron, was obtained with NLA in [45], it is possible to study this process in the NLA BFKL approach. After the renormalisation of the QCD coupling and the ensuing removal of the ultraviolet divergences, soft and virtual infrared divergences

cancel each other, whereas the surviving infrared collinear ones are compensated by the collinear counterterms related to the renormalisation of PDFs for the initial proton and parton fragmentation functions (FFs) describing the detected hadron in the final state within collinear factorisation. All the theoretical criteria are thus met to give infrared-safe NLA predictions, thus making of this process an additional clear channel to test the BFKL dynamics at the LHC. The fact that hadrons can be detected at the LHC at much smaller values of the transverse momentum than jets, allows to explore a kinematical range outside the reach of the Mueller–Navelet channel, so that the reaction can be considered complementary to Mueller–Navelet jet production. Furthermore, it represents the best context to simultaneously constrain both PDFs and FFs.

The second advance towards further and deeply probing BFKL dynamics is the study of inclusive *multi-jet* production processes where, besides two external jets typical of Mueller–Navelet reactions, the tagging of further jets in more central regions of the detectors and with a relative separation in rapidity from each other is demanded. This allows for the study of even more differential distributions in the transverse momenta, azimuthal angles and rapidities of the central jets, by generalising the two-jet azimuthal correlations $R_{nm} \equiv \cos(n\phi)/\cos(m\phi)$ to new, suitable BFKL observables sensitive to the azimuthal configurations of the tagged extra particles.

Aware of the importance to pursue the phenomenological paths traced above, we work toward the goal of giving testable predictions on the QCD semi-hard sector by proposing the study of four distinct processes. First, we continue the study of Mueller–Navelet jets by addressing issues that still wait to be answered, as the comparison of BFKL with NLO fixed-order perturbative approaches [46] and a 13 TeV analysis, together with the study of the effect of imposing dynamic constraints in the central rapidity region [47]. Second, we

will give the first phenomenological results for cross sections and azimuthal correlations in the inclusive dihadron production. Third, we will show how the inclusive three-jet production process allows to define in a very natural and elegant way new, generalised and suitable BFKL observables. Finally, we will investigate the inclusive four-jet production, extending the BFKL formalism defined and used in the three-jet case.

This thesis is organised as follows. In Chapter 2 a brief overview of the BFKL approach is given, while phenomenological predictions at LHC energies for the considered semi-hard processes are shown in the next four Chapters. In particular, Mueller–Navelet jets and the inclusive dihadron production are discussed in Chapters 3 and 4, respectively, showing the latest results at full NLA accuracy, together with a study on the effect of using different values for the renormalisation and factorisation scales. In Chapter 5 the first complete analysis of the inclusive three-jet production process is presented, including the effects of higher-order BFKL corrections. The four-jet production process is investigated in Chapter 6, giving the first results at LLA accuracy. In each Chapter devoted to phenomenology a related summary Section is provided, while the general Conclusions, together with Outlook, are drawn in Chapter 7.

Chapter 2

The BFKL resummation

2.1 The Regge theory

In 1959 the Italian physicist T. Regge [50] found that, when considering solutions of the Schrödinger equation for non-relativistic potential scattering, it can be advantageous to regard the angular momentum, l , as a complex variable. He showed that, for a wide class of potentials, the only singularities of the scattering amplitude in the complex l -plane are poles, called *Regge poles* [51, 52] after him. If these poles appear in coincidence with integer values of l , they correspond to bound states or resonances and turn out to be important for the analytic properties of the amplitudes. They occur at the values given by the relation

$$l = \alpha(k) , \tag{2.1}$$

where $\alpha(k)$ is a function of the energy, known as *Regge trajectory* or *Reggeon*. Each class of bound states or resonances is related to a single trajectory like (2.1). The energies of these states are obtained from Eq. (2.1), giving physical (integer) values to the angular momentum l . The extension of the Regge's approach to high-energy particle physics was formerly due to Chew and Frautschi [53] and Gribov [54], but many other physicists gave their contribution to the theory

and its applications. Using the general properties of the S-matrix, the relativistic partial wave amplitude $\mathcal{A}_l(t)$ can be analytically continued to complex l values in a unique way. The resulting function, $A(l, t)$, shows simple poles at

$$l = \alpha(t) . \quad (2.2)$$

Each pole contributes to the scattering amplitude with a term which asymptotically behaves (*i.e.* for $s \rightarrow +\infty$ and for fixed t) as

$$A(s, t) \sim s^{\alpha(t)} , \quad (2.3)$$

where s and $-t$ are the square of the center-of-mass energy and of the momentum transfer, respectively. The leading singularity in the t -channel is the one with the largest real part, and rules the asymptotic behaviour of the scattering amplitude in the s -channel. The triumph of Regge theory in its simplest form, *i.e.* the fact that a large class of processes is accurately described by such simple predictions as Eq. (2.3), was simply surprising.

2.1.1 The Pomeron

Regge theory belongs to the class of the so-called t -channel models. They describe hadronic processes in terms of the exchange of “some objects” in the t -channel. In the Regge theory a Reggeon plays the same role as an exchanged virtual particle in a tree-level perturbative process, with the important difference that the Reggeon represents a whole class of resonances, instead of a single particle. In the limit of large s , a hadronic process is governed by the exchange of one or more Reggeons in the t -channel. The exchange of Reggeons instead of particles gives rise to scattering amplitudes of the type of Eq. (2.3). Using the *optical theorem* [55] together with Eq. (2.3), we can write the Regge total cross section:

$$\sigma_{\text{TOT}} \simeq \frac{\text{Im} A(s, t = 0)}{s} \simeq s^{\alpha(0)-1} . \quad (2.4)$$

We know from experiments that hadronic total cross sections, as a function of s , are rather flat around $\sqrt{s} \simeq (10 \div 20)$ GeV and rise slowly as \sqrt{s} increases. If the considered process is described by the exchange of a single Regge pole, then it follows that the intercept $\alpha(0)$ of the exchanged Reggeon is greater than 1, leading to the power growth with energy of the cross section in Eq. (2.4). This Reggeon is called *Pomeron*, in honour of I.Ya. Pomeranchuk. Particles which would provide the resonances for integer values of $\alpha(t)$ for $t > 0$ have not been conclusively identified. Natural candidates in QCD are the so-called *glueballs*. The Pomeron trajectory represents the dominant trajectory in elastic and diffractive processes, namely reactions featuring the exchange of vacuum quantum numbers in the t -channel. The power growth of the cross section violates the Froissart bound [56] and hence the unitarity, which has to be restored through unitarisation techniques (see for instance Ref. [57] and references therein).

2.2 Towards the BFKL equation

The BFKL equation [7–10] made the grade when the growth of the γ^*p cross section at increasing energy, predicted by Balitsky, Fadin, Kuraev, and Lipatov, was experimentally confirmed at HERA. Therefore this equation is usually associated with the evolution of the unintegrated gluon distribution.

The PDF evolution with $\tau = \ln(Q^2/\Lambda_{\text{QCD}})$ is determined by the DGLAP equations [2–6], which allow to resum to all orders collinear logarithms $\ln Q^2$ picked up from the region of small angles between parton momenta. There is another class of logarithms to be taken into account: soft logarithms which originate from ratios of parton energies and are present both in PDFs and in partonic cross sections. At small values of the ratio $x = \ln Q^2/s$ soft logarithms

are even larger than collinear ones.

The BFKL approach describes QCD scattering amplitudes in the limit of small κ , $s \gg |t|$, and t not growing with s (Regge limit). The evolution equation for the unintegrated gluon distribution appears in this approach as a particular result for the imaginary part of the forward scattering amplitude ($t = 0$ and vacuum quantum numbers in the t -channel). This approach was developed (and is more suitable) for the description of processes with just one hard scale, such as $\gamma^* \gamma^*$ scattering with both photon virtualities of the same order, where the DGLAP evolution is not appropriate. The BFKL approach relies on *gluon Reggeisation*, which can be described as the appearance of a modified propagator in the Feynman gauge, of the form [52]

$$D_{\mu\nu}(s, q^2) = -i \frac{g_{\mu\nu}}{q^2} \left(\frac{s}{s_0} \right)^{\alpha_g(q^2)-1}, \quad (2.5)$$

where $\alpha_g(q^2) = 1 + \epsilon(q^2)$ is the gluon Regge trajectory.

2.2.1 Gluon Reggeisation

The Reggeisation of an elementary particle featuring spin j_0 and mass m was introduced in Ref. [58] and it means [59] that, in the Regge limit, a factor $s^{j(t)-j_0}$, with $j_0 \equiv j(m^2)$ appears in Born amplitudes with exchange of this particle in the t -channel. This phenomenon was discovered originally in QED via the backward Compton scattering [58]. It was called Reggeisation because just such form of amplitudes is given by the Regge poles (moving poles in the complex l -plane [50]). In contrast to QED, where the electron reggeises in perturbation theory [58], but the photon remains elementary [60], in QCD the gluon reggeises [7, 8, 61–63] as well as the quark [64–67]. Therefore QCD is the unique theory where all elementary particles reggeise.

Reggeisation represents a key-ingredient for the theoretical description of

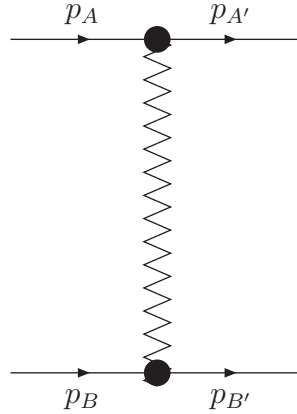


Figure 2.1: Diagrammatical representation of the process $A + B \rightarrow A' + B'$ with colour octet in the t -channel. The waggie line represents the Reggeised gluon exchange.

high-energy processes with fixed momentum transfer. Gluon Reggeisation is particularly important, because cross sections non-decreasing with energy are provided by gluon exchanges, and it determines the form of QCD amplitudes in the Regge limit. The simplest realisation of the gluon Reggeisation happens in the elastic process $A + B \rightarrow A' + B'$, where amplitudes with a colour-octet exchange in the t -channel and negative signature (see Fig. 2.1 for a diagrammatical representation) assume the form

$$(\mathcal{A}_8)_{AB}^{A'B'} = \Gamma_{A'A}^c \frac{s}{t} \left[\left(\frac{s}{-t} \right)^{\omega(t)} + \left(\frac{-s}{-t} \right)^{\omega(t)} \right] \Gamma_{B'B}^c, \quad (2.6)$$

where

$$s = (p_A + p_B)^2, \quad (2.7)$$

$$t = q^2,$$

$$q = p_A - p_{A'},$$

$\omega(t)$ is the gluon trajectory, c is the colour index, and $\Gamma_{B'B}^c$ are the particle-particle-Reggeon (PPR) vertices which are independent of s . The factorisation given in Eq. (2.6) represents the analytical structure of the scattering amplitude,

which is quite simple in the elastic case. It is valid both in the LLA and in the NLA. In particular, it holds when one of the particles A' and B' is replaced by a jet. In general the PPR vertex can be written in the form $\Gamma_{p'p}^C = g_s \langle P'|T^c|P \rangle \Gamma_{p'p}$, where g_s is the QCD coupling and $\langle P'|T^c|P \rangle$ is the matrix element of the colour-group generator in the fundamental (adjoint) representation for quarks (gluons). In the LLA this form of amplitude was proved in Refs. [7–10]. In this approximation, the helicity λ_p of the scattered particle P is a conserved quantity, so $\Gamma_{p'p}^{(0)}$ is given by $\delta_{\lambda_{p'}\lambda_p}$ and the Reggeised gluon trajectory is calculated with 1-loop accuracy [68], having so

$$\begin{aligned} \omega(t) &\simeq \omega^{(1)}(t) = \frac{g_s^2 t}{(2\pi)^{(D-1)}} \frac{N_c}{2} \int \frac{d^{D-2}k_\perp}{k_\perp^2 (q - k_\perp)_\perp^2} \\ &= -\frac{g_s^2 N_c \Gamma(1-\epsilon)}{(4\pi)^{\frac{D}{2}}} \frac{\Gamma^2(\epsilon)}{\Gamma(2\epsilon)} (\bar{q}^2)^\epsilon \end{aligned} \quad (2.8)$$

where $t = q^2 \approx q_\perp^2$, $D = 4 + 2$ is the space-time dimension and N_c is the number of QCD colours. The ϵ parameter has been introduced in order to regularise the infrared divergences, while the integration is done in a $(D - 2)$ -dimensional space, orthogonal to the momenta of the initial colliding particles p_A and p_B . The gluon Reggeisation determines also the form of inelastic amplitudes in the multi-Regge kinematics (MRK), namely where all particles are strongly ordered in the rapidity space with limited transverse momenta and the squared invariant masses $s_{ij} = (k_i + k_j)^2$ of any pair of produced particles i and j are large and increasing with s . This kinematics gives the leading contribution to QCD cross sections. In the LLA, there are exchanges of vector particles (QCD gluons) in all channels. In the NLA, as opposed to LLA, MRK is not the solely contributing kinematic configuration. It can happen then one (and just one) of the produced particles can have a fixed (not increasing with s) invariant mass, *i.e.* components of this pair can have rapidities of the same

order. This is known as quasi-multi-Regge-kinematics (QMRK) [69]. In the NLA the expression given in Eq. (2.6) was checked initially at the first three perturbative orders [70–74]. A rigorous proof of gluon Reggeisation, based on some stringent self-consistency conditions (*bootstrap* conditions [75–77]), was subsequently given with full NLA accuracy.

2.3 The amplitude in multi-Regge kinematics

The gluon Reggeisation governs amplitudes with colour-octet states and negative signature in the t -channel. In the BFKL approach, amplitudes with other quantum numbers can be obtained by using s -channel unitarity relations, where the contribution of order s is given by the MRK. Large logarithms come from the integration over longitudinal momenta of the final-state particles. In an elastic process $A + B \rightarrow A'B'$, according to the Cutkosky rule [78] and to the unitarity relation in the s -channel, the imaginary part of the elastic scattering amplitude $\mathcal{A}_{AB}^{A'B'}$ can be presented as

$$\text{Im}_s \mathcal{A}_{AB}^{A'B'} = \frac{1}{2} \sum_{n=0}^{\infty} \sum_{\{f\}} \int \left| \mathcal{A}_{AB}^{\tilde{A}\tilde{B}n} \right|^2 d\Phi_{\tilde{A}\tilde{B}n}, \quad (2.9)$$

where $\mathcal{A}_{AB}^{\tilde{A}\tilde{B}n}$ is the amplitude for the production of $n + 2$ particles (see Fig. 2.2) with momenta k_i , $i = 0, 1, \dots, n, n + 1$ in the process $A + B \rightarrow \tilde{A} + \tilde{B} + n$, while $d\Phi_{\tilde{A}\tilde{B}n}$ represents the intermediate phase-space element and $\sum_{\{f\}}$ is over the discrete quantum numbers $\{f\}$ of the intermediate particles. The initial particle momenta p_A and p_B are assumed to be equal to $p_A = p_1 + (m_A^2/s)p_2$ and $p_B = p_2 + (m_B^2/s)p_1$, respectively. For any momentum k_i the Sudakov decomposition is satisfied by the relation

$$k_i = \beta_i p_1 + \alpha_i p_2 + k_{i\perp}, \quad (2.10)$$

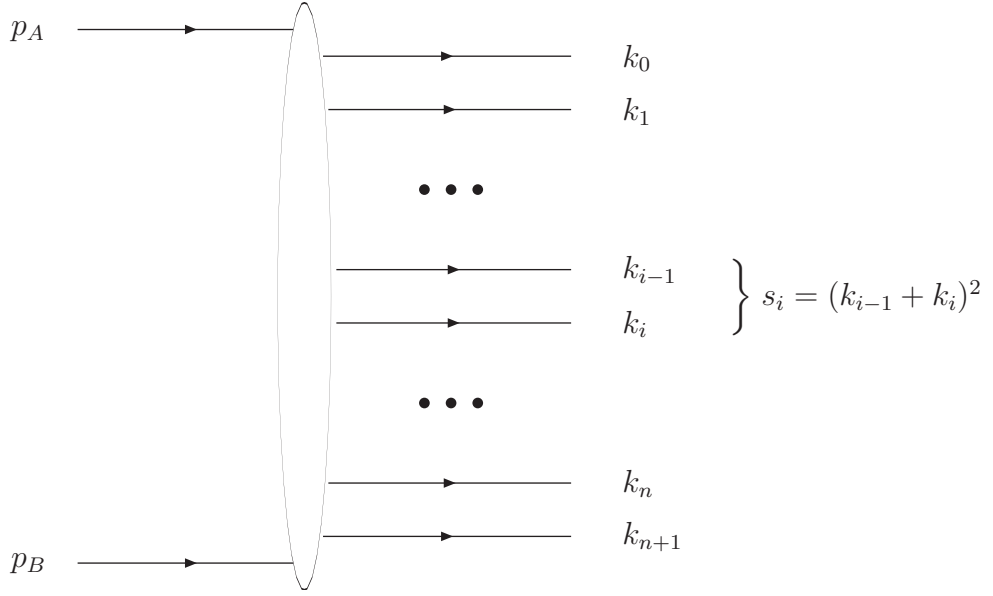


Figure 2.2: Diagrammatic representation of the s -channel unitarity relation.

where p_1 and p_2 are light-like vectors and $(p_1 + p_2)^2 = 2p_1 \cdot p_2 = s$,

$$\alpha_i \beta_i = \frac{k_i^2 - k_{i\perp}^2}{s} = \frac{k_i^2 + \vec{k}_i^2}{s}, \quad (2.11)$$

with $\vec{k}_{i\perp}$ transverse component with respect to the plane generated by p_1 and p_2 , and $k_{i\perp}^2 = -\vec{k}_i^2$.

The Sudakov decomposition allows us to write the following expression for the phase space:

$$\begin{aligned} d\Phi_{\tilde{A}\tilde{B}n} &= \frac{2}{s} (2\pi)^D \delta \left(1 + \frac{m_A^2}{s} - \sum_{i=0}^{n+1} \alpha_i \right) \delta \left(1 + \frac{m_B^2}{s} - \sum_{i=0}^{n+1} \beta_i \right) \\ &\times \delta^{D-2} \left(\sum_{i=0}^{n+1} k_{i\perp} \right) \frac{d\beta_{n+1}}{2\beta_{n+1}} \frac{d\alpha_0}{2\alpha_0} \prod_{i=0}^n \frac{d\beta_i}{2\beta_i} \prod_{i=1}^{n+1} \frac{d^{D-2}k_{i\perp}}{(2\pi)^{D-1}}, \end{aligned} \quad (2.12)$$

where $p_{\tilde{A}} = k_0$; $p_{\tilde{B}} = k_{n+1}$. In the unitarity condition (Eq. (2.9)), the dominant contribution ($\sim s$) in the LLA is given by the region of limited (not growing with s) transverse momenta of produced particles. As we said, large logarithms come from the integration over longitudinal momenta of the produced

particles. In particular, we have a logarithm of s for every particle produced according to MRK. By definition, in this kinematics transverse momenta of the produced particles are limited and their Sudakov variables α_i and β_i are strongly ordered in the rapidity space, having so

$$\begin{aligned}\alpha_{n+1} &\gg \alpha_n \cdots \gg \alpha_0, \\ \beta_0 &\gg \beta_1 \cdots \gg \beta_{n+1}.\end{aligned}\tag{2.13}$$

Eqs. (2.10) and (2.13) ensure the squared invariant masses of neighbouring particles,

$$s_i = (k_{i-1} + k_i)^2 \approx s\beta_{i-1}\alpha_i = \frac{\beta_{i-1}}{\beta_i} \left(k_i^2 + \vec{k}_i^2 \right),\tag{2.14}$$

to be large with respect to the squared transverse momenta:

$$s_i \gg \vec{k}_i^2 \sim |t_i| = q_i^2,\tag{2.15}$$

with

$$t_i = q_i^2 \approx q_{i\perp}^2 = -\vec{q}_i^2\tag{2.16}$$

and

$$\prod_{i=1}^{n+1} s_i = s \prod_{i=1}^n \left(k_i^2 + \vec{k}_i^2 \right).\tag{2.17}$$

In order to obtain the large logarithm from the integration over β_i for each produced particle in the phase space given in Eq. (2.12), the amplitude in the r.h.s. in Eq. (2.9) must not decrease with the growth of the invariant masses. This is true only when there are exchanges of vector particles (gluons) in all channels with momentum transfers $q_{i=1,\dots,n+1}$ with

$$q_i = p_a - \sum_{j=0}^{i-1} k_j = - \left(p_B - \sum_{l=i}^{n+1} k_l \right)\tag{2.18}$$

$$\simeq \beta_i p_1 - \alpha_{i-1} p_2 - \sum_{j=0}^{i-1} k_{j\perp}$$

and

$$q_i^2 \simeq q_{i\perp}^2 = -\bar{q}_i^2 \quad (2.19)$$

The dominant amplitudes at every expansion order can be diagrammatically represented as in Fig. 2.3. Multi-particle amplitudes show a complicated analytical structure even in MRK (see Refs. [79–82]). Fortunately, only real parts of these amplitudes are used in the BFKL approach in NLA as well as in LLA. Considering just the real parts, it is possible to write [83]

$$\begin{aligned} \mathcal{A}_{\tilde{A}\tilde{B}}^{\tilde{A}\tilde{B}n} &= 2s \Gamma_{\tilde{A}\tilde{A}}^{c_1} \left(\prod_{i=1}^n \gamma_{c_i c_{i+1}}^{P_i}(q_i, q_{i+1}) \left(\frac{s_i}{s_R} \right)^{\omega(t_i)} \frac{1}{t_i} \right) \\ &\times \frac{1}{t_{n+1}} \left(\frac{s_{n+1}}{s_R} \right)^{\omega(t_{n+1})} \Gamma_{\tilde{B}\tilde{B}}^{c_{n+1}} \end{aligned} \quad (2.20)$$

with s_R being an arbitrary energy scale, irrelevant at LLA. Here $\omega(t)$ and $\Gamma_{p/p}^a$ are the gluon Regge trajectory and the PPR (see Eq. (2.9)), while $\gamma_{c_i c_{i+1}}^{P_i}$ are the Reggeon-Reggeon-Particle (RRP) vertices, *i.e.* the effective vertices for the production of particles P_i with momenta $q_i - q_{i+1}$ in collisions of Reggeised gluons with momenta q_i and $-q_{i+1}$ and colour indices c_i and c_{i+1} , respectively. In the LLA only one gluon can be produced in the RRP vertex. For this reason, final-state particles are massless. The Reggeon-Reggeon-Gluon (RRG) vertex takes the form [7–10]

$$\gamma_{c_i c_{i+1}}^{G_i}(q_i, q_{i+1}) = g_s T_{c_i c_{i+1}}^{d_i} e_{\mu}^*(k_i) C^{\mu}(q_{i+1}, q_i), \quad (2.21)$$

where $T_{c_i c_{i+1}}^{d_i}$ are the matrix elements of the $SU(N_c)$ group generators in the adjoint representation, d_i is the colour index of the produced gluon with polarisation vector $e_{\mu}^*(k_i)$, $k_i = q_i - q_{i+1}$ its momentum and

$$C^{\mu}(q_{i+1}, q_i) = -q_i^{\mu} - q_{i+1}^{\mu} + p_1^{\mu} \left(\frac{q_i^2}{k_i \cdot p_1} + 2 \frac{k_i \cdot p_2}{p_1 \cdot p_2} \right) \quad (2.22)$$

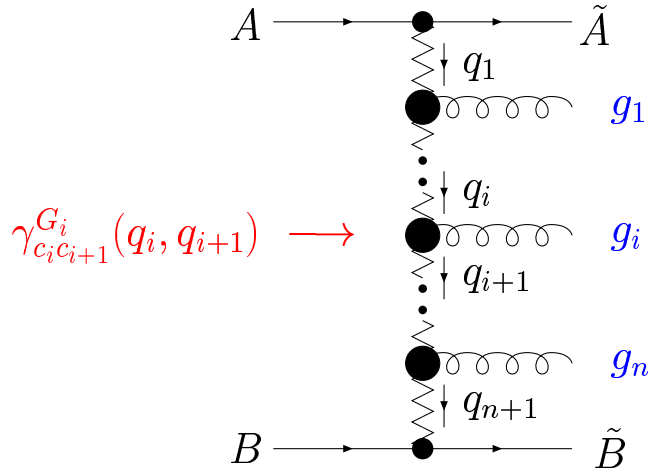


Figure 2.3: Diagrammatic representation of the amplitude $A_{AB}^{\tilde{A}\tilde{B}n}$.

$$\times -p_2^\mu \left(\frac{q_{i+1}^2}{k_i \cdot p_2} + 2 \frac{k_i \cdot p_1}{p_1 \cdot p_2} \right).$$

The structure of C^μ given in Eq. (2.22) reflects the current conservation property $(k_i)_\mu C^\mu = 0$, which permits to choose an arbitrary gauge for each of the produced gluons. Let us introduce now the following decomposition:

$$T_{c_i c_{i+1}}^{d_i} \left(T_{c_i c_{i+1}}^{d_i} \right)^* = \sum_R c_R \langle c_i c'_i | \hat{\mathcal{P}}_R | c_{i+1} c'_{i+1} \rangle \quad (2.23)$$

where $\hat{\mathcal{P}}_R$ is the projection operator of the two-gluon colour states on the irreducible representation R of the colour group. For the singlet (vacuum) and antisymmetric octet (gluon) representations one has respectively

$$\langle c_i c'_i | \hat{\mathcal{P}}_0 | c_{i+1} c'_{i+1} \rangle = \frac{\delta_{c_i c'_i} \delta_{c_{i+1} c'_{i+1}}}{N_c^2 - 1} \quad (2.24)$$

and

$$\langle c_i c'_i | \hat{\mathcal{P}}_8 | c_{i+1} c'_{i+1} \rangle = \frac{f_{ac_i c'_i} f_{ac_{i+1} c'_{i+1}}}{N_c}, \quad (2.25)$$

where f_{abc} are the (SUN_c) structure constants. It is possible to prove that

$$c_0 = N_c, \quad c_8 = \frac{N_c}{2}. \quad (2.26)$$

Using the decomposition given in Eq. (2.23), we can write

$$\begin{aligned} & \sum_{G_i} \gamma_{c_i c_{i+1}}^{G_i}(q_i, q_{i+1}) \left(\gamma_{c_i c_{i+1}}^{G_i}(q_i, q_{i+1}) \right)^* \\ &= 2(2\pi)^{D-1} \sum_{\mathbf{R}} \left\langle c_i c'_i \left| \hat{\mathcal{P}}_{\mathbf{R}} \right| c_{i+1} c'_{i+1} \right\rangle \mathcal{K}_{\mathbf{r}}^{(\mathbf{R})}(\vec{q}_i, \vec{q}_{i+1}; \vec{q}) \end{aligned} \quad (2.27)$$

where the sum is taken over colour and polarisation states of the produced gluon and $\mathcal{K}_{\mathbf{r}}^{(\mathbf{R})}(\vec{q}_i, \vec{q}_{i+1}; \vec{q})$ is the so-called *real part* of the kernel.

2.3.1 The BFKL equation

The BFKL equation at LLA is obtained from the amplitude given in Eq. (2.20), using the unitarity relation (see Eq. (2.9)) for the s -channel imaginary part of the elastic amplitude, which, according to the decomposition in Eq. (2.23) can be written as

$$\mathcal{A}_{AB}^{A'B'} = \sum_{\mathbf{R}} (\mathcal{A}_{\mathbf{R}})_{AB}^{A'B'} , \quad (2.28)$$

where $(\mathcal{A}_{\mathbf{R}})_{AB}^{A'B'}$ is the part of the scattering amplitude corresponding to a definite irreducible representation \mathbf{R} of the colour group in the t -channel. Using the amplitude (2.20) in the unitarity relation (2.9) for the s -channel imaginary part of the elastic scattering amplitude, one obtain an expression which can be factorised [68] in the following way (see Fig. 2.4):

$$\begin{aligned} \text{Im} (\mathcal{A}_{\mathbf{R}})_{AB}^{A'B'} &= \frac{s}{(2\pi)^{D-2}} \int \frac{d^{D-2}q_1}{\vec{q}_1^2 (\vec{q}_1 - \vec{q})^2} \int \frac{d^{D-2}q_2}{\vec{q}_2^2 (\vec{q}_2 - \vec{q})^2} \\ &\times \sum_{\nu} \Phi_{A'A}^{(\mathbf{R}, \nu)}(\vec{q}_1; \vec{q}, s_0) \int_{\delta-i\infty}^{\delta+i\infty} \frac{d\omega}{2\pi i} \left[\left(\frac{s}{s_0} \right)^{\omega} G_{\omega}^{(\mathbf{R})}(\vec{q}_1, \vec{q}_2, \vec{q}) \right] \Phi_{B'B}^{(\mathbf{R}, \nu)}(-\vec{q}_2; -\vec{q}, s_0) . \end{aligned} \quad (2.29)$$

Here \vec{q}_1 and \vec{q}_2 are the transverse momenta of the Reggeised gluons, while s_0 is an arbitrary energy scale introduced in order to define the partial wave expansion of the scattering amplitudes via the (inverse) *Mellin transform* (see

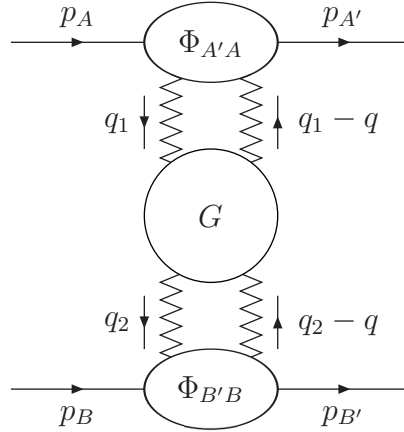


Figure 2.4: Diagrammatic representation of the imaginary part of the BFKL amplitude.

Appendix A for further details), while the ν index identifies the state in the irreducible representation R . $\Phi_{p'p}^{(R,\nu)}$ are the so-called impact factors, obtained through the convolution of two PPR vertices. $G_{\omega}^{(R)}$, defined via a Mellin transform, is the Green's function for scattering of two Reggeised gluons and is universal (it does not depend on the particular process). Conversely, the impact factors are specific of the particles on the external lines and can be expressed through the imaginary part of the particle-Reggeon scattering amplitudes, in the form

$$\Phi_{p'p}^{(R,\nu)}(\vec{q}_R; \vec{q}; s_0) = \int \frac{d s_{\text{PR}}}{2\pi s} \text{Im} \mathcal{A}_{p'p}^{(R,\nu)}(p_p, q_R; \vec{q}; s_0) \theta(s_{\Lambda} - s_{\text{PR}}) \quad (2.30)$$

$$- \frac{1}{2} \int \frac{d^{D-2} q'}{\vec{q}'^2 (\vec{q}' - \vec{q})^2} \Phi_{p'p}^{(R,\nu)\text{B}}(\vec{q}', \vec{q}) \mathcal{K}_r^{(R)\text{B}}(\vec{q}', \vec{q}_R) \ln \left(\frac{s_{\Lambda}^2}{(\vec{q}' - \vec{q}_R) s_0} \right),$$

where $s_{\text{PR}} = (q_p - q_R)^2$ is the squared particle-Reggeon invariant mass and $\text{Im} \mathcal{A}_{p'p}^{(R,\nu)}$ is the s_{PR} -channel imaginary part of the scattering amplitude of the particle P with momentum p_p off the Reggeon with momentum q_R , while q is the transferred momentum. This definition is valid both in the LLA and in the NLA. The parameter s_{Λ} , which plays the role of a cutoff for the s_{PR} -integration, is introduced to separate the contributions from MRK and QMRK and must be

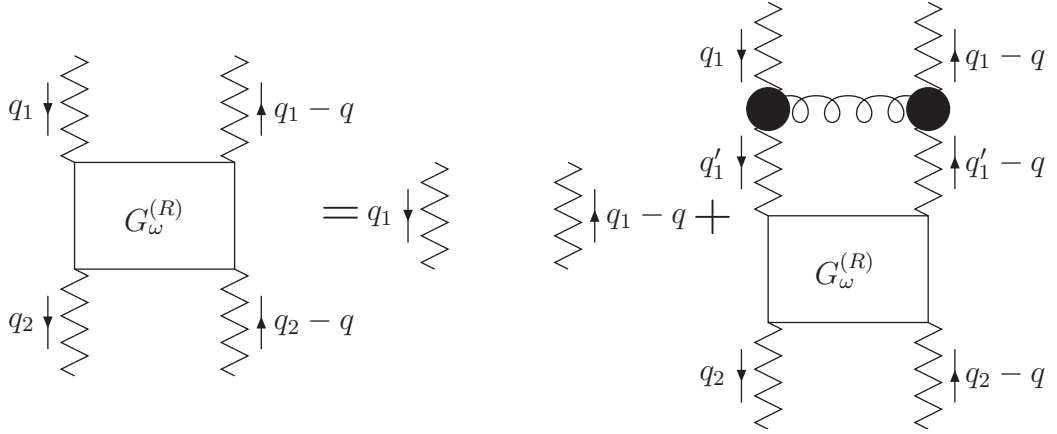


Figure 2.5: Diagrammatic representation of the generalised BFKL integral equation.

considered in the limit $s_\Lambda \rightarrow +\infty$. In this way, the second term in the r.h.s. of Eq. (2.30) works as a counterterm for the large s_{PR} . The Green's function obeys the following integral equation (Fig. 2.5), known as *generalised BFKL equation*:

$$\begin{aligned} \omega G_\omega^{(R)}(\vec{q}_1, \vec{q}_2; \vec{q}) &= \vec{q}_1^2 (\vec{q}_1 - \vec{q})^2 \delta^{(D-2)}(\vec{q}_1 - \vec{q}_2) \\ &+ \int \frac{d^{D-2} q_{1\perp}'}{\vec{q}_1'^2 (\vec{q}_1' - \vec{q})^2} \mathcal{K}^{(R)}(\vec{q}_1, \vec{q}_1'; \vec{q}) G_\omega^{(R)}(\vec{q}_1', \vec{q}_2; \vec{q}), \end{aligned} \quad (2.31)$$

where the kernel

$$\begin{aligned} \mathcal{K}^{(R)}(\vec{q}_1, \vec{q}_2; \vec{q}) &= (\omega(q_{1\perp}^2) + \omega((q_1 - q)_\perp^2)) \vec{q}_1^2 (\vec{q}_1 - \vec{q})^2 \delta^{(D-2)}(\vec{q}_1 - \vec{q}_2) \\ &+ \mathcal{K}_r^{(R)}(\vec{q}_1, \vec{q}_2; \vec{q}) \end{aligned} \quad (2.32)$$

consists of two parts: the first one is the so-called *virtual part* and is expressed in terms of the gluon Regge trajectory; the second one, known as *real part* (see Fig. 2.6), is related to the real particle production and reads:

$$\begin{aligned} \mathcal{K}_r^{(R)}(\vec{q}_i, \vec{q}_{i+1}; \vec{q}) &= -\frac{g^2 c_R}{2(2\pi)^{D-1}} C^\mu(q_{i+1}, q_i) C_\mu(q_{i+1} - q, q_i - q) \\ &= \frac{g^2 c_R}{(2\pi)^{D-1}} \left(\frac{\vec{q}_i^2 (\vec{q}_{i+1} - \vec{q})^2 + \vec{q}_{i+1}^2 (\vec{q}_i - \vec{q})^2}{(\vec{q}_i - \vec{q}_{i+1})^2} - \vec{q}^2 \right). \end{aligned} \quad (2.33)$$

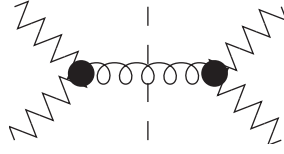


Figure 2.6: Diagrammatic representation of the real part of the BFKL kernel at the Born level.



Figure 2.7: Diagrammatic representations of replacements $\Gamma_{p'p}^{c(\text{Born})} \rightarrow \Gamma_{p'p}^{c(1\text{-loop})}$ (a) and $\Gamma_{c_i c_{i+1}}^{g(\text{Born})} \rightarrow \Gamma_{c_i c_{i+1}}^{g(1\text{-loop})}$ (b).

If $R = 0$ (colour-singlet representation) the Eq. (2.31) is called *BFKL equation*. The BFKL equation iterative: knowing the kernel in the Born level, it permits to get all the LLA terms of the Green's function. Similarly, knowing all the NLA corrections to the gluon trajectory and to the real part of the kernel, one can get all the NLA terms of the Green's function. In order to obtain a full amplitude the impact factors are needed, which depend on the process though and have to be calculated time by time at the requested perturbative accuracy. Furthermore, in most cases impact factors encode non-perturbative objects for real processes, *e.g.* the PDF of the of the parton emitted from the initial state parent hadron and/or the FF describing the detected hadron in the final state within collinear factorisation (in the case of processes with identified particles in the final state). Impact factors are known in the NLA just for few processes.

2.3.2 The BFKL equation in the NLA

In order to derive the BFKL equation in the NLA, gluon Reggeisation is assumed to be valid to all orders of perturbation theory. As we said, it has been recently shown that Reggeisation is fulfilled also in the NLA, through the

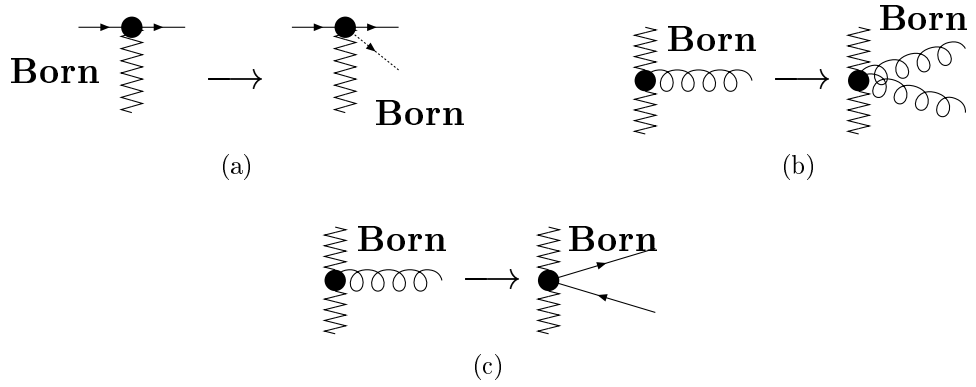


Figure 2.8: Diagrammatic representations of replacements $\Gamma_{P'P}^{\mathcal{C}(\text{Born})} \rightarrow \Gamma_{\{f\}P}^{\mathcal{C}(\text{Born})}$ (a), $\gamma_{c_i c_{i+1}}^{\mathcal{G}(\text{Born})} \rightarrow \gamma_{c_i c_{i+1}}^{\mathcal{Q}\bar{\mathcal{Q}}(\text{Born})}$ (b) and $\gamma_{c_i c_{i+1}}^{\mathcal{G}(\text{Born})} \rightarrow \gamma_{c_i c_{i+1}}^{\mathcal{G}\mathcal{G}(\text{Born})}$ (c).

study of the bootstrap conditions [75–77]. In the NLA, where all terms of the type $\alpha_s[\alpha_s \ln(s)]^n$ need be collected, the PPR vertex in Eq. (2.6) assumes the following expression:

$$\Gamma_{P'P} = \delta_{\lambda P, \lambda P'} \Gamma_{PP}^{(+)} + \delta_{\lambda P', -\lambda P} \Gamma_{PP}^{(-)}. \quad (2.34)$$

In this approximation a term in which the helicity of the scattering particle P is not conserved appears. To obtain production amplitudes in the NLA it is sufficient to take one of the vertices or the trajectory in Eq. (2.20) in the NLO. In the LLA, the Reggeised gluon trajectory is needed at 1-loop accuracy and the only contribution to the real part of the kernel is from the production of one gluon at Born level in the collision of two Reggeons (K_{RRG}^B) [68]. In the NLA the gluon trajectory is taken in the NLO (2-loop accuracy [70–74]) and the real part includes the contributions coming from: one-gluon (K_{RRG}^1) [84], two-gluon (K_{RRGG}^B) [14, 85–87], and quark-antiquark pair ($K_{RRQ\bar{Q}}^B$) [13, 88–90] production at Born level [68].

The first set of corrections is realised by performing, only in one place, one of the following replacements in the production amplitude (see Eq. (2.20))

entering the s-channel unitarity relation:

$$\Gamma_{P/P}^{\mathcal{C}(\text{Born})} \rightarrow \Gamma_{P/P}^{\mathcal{C}(1\text{-loop})}, \quad \gamma_{c_i c_{i+1}}^{\mathcal{G}_i(\text{Born})} \rightarrow \gamma_{c_i c_{i+1}}^{\mathcal{G}_i(1\text{-loop})}, \quad (2.35)$$

diagrammatically shown in Fig. 2.7. The second set of corrections consists in allowing the production in the s-channel intermediate state of one pair of particles with rapidities of the same order of magnitude, both in the central or in the fragmentation region (QMRK). This implies one replacement among the following in the production amplitude:

$$\Gamma_{P/P}^{\mathcal{C}(\text{Born})} \rightarrow \Gamma_{\{f\}P}^{\mathcal{C}(\text{Born})}, \quad \gamma_{c_i c_{i+1}}^{\mathcal{G}_i(\text{Born})} \rightarrow \gamma_{c_i c_{i+1}}^{\mathcal{Q}\bar{\mathcal{Q}}(\text{Born})}, \quad \gamma_{c_i c_{i+1}}^{\mathcal{G}_i(\text{Born})} \rightarrow \gamma_{c_i c_{i+1}}^{\mathcal{G}\mathcal{G}(\text{Born})}. \quad (2.36)$$

Here $\Gamma_{\{f\}P}$ stands for the production of a state containing an extra-particle in the fragmentation region of the particle P in the scattering off the Reggeon, $\gamma_{c_i c_{i+1}}^{\mathcal{Q}\bar{\mathcal{Q}}(\text{Born})}$ and $\gamma_{c_i c_{i+1}}^{\mathcal{G}\mathcal{G}(\text{Born})}$ are the effective vertices for the production of a quark-antiquark pair and of a two-gluon pair, respectively, in the collision of two Reggeons. This second set of replacements is shown in Fig. 2.8.

2.3.3 The BFKL cross section

The total cross section and many other physical observables are directly related to the imaginary part of the forward scattering amplitude ($\vec{q} = 0$) via the optical theorem. The cross section can be expressed by

$$\sigma(s) = \frac{\text{Im}_s \mathcal{A}_{AB}^{AB}}{s}, \quad (2.37)$$

with $\text{Im}_s \mathcal{A}_{AB}^{AB}$ given in Eq. (2.29). It is possible to make the following redefinition of the Green's function:

$$G_\omega(\vec{q}_1, \vec{q}_2) = \frac{G_\omega^{(0)}(\vec{q}_1, \vec{q}_2; 0)}{\vec{q}_1^2 \vec{q}_2^2}, \quad (2.38)$$

where $\vec{q}_{1,2}$ are two-dimensional vectors and $G_\omega^{(0)}(\vec{q}_1, \vec{q}_2; 0)$ is the forward Green's function in the singlet-colour representation which obeys the BFKL equation

given in Eq. (2.31) with $R = 0$. This leads to a simplification of the expressions of the BFKL equation and of the BFKL kernel (2.32), which now read

$$\omega G_\omega(\vec{q}_1, \vec{q}_2) = \delta^{D-2}(\vec{q}_1 - \vec{q}_2) + \int d^{D-2}\vec{q} \mathcal{K}(\vec{q}_1, \vec{q}) G_\omega(\vec{q}, \vec{q}_2) \quad (2.39)$$

and

$$\mathcal{K}(\vec{q}_1, \vec{q}_2) = \frac{\mathcal{K}^{(0)}(\vec{q}_1, \vec{q}_2; 0)}{\vec{q}_1^2 \vec{q}_2^2} = 2 \omega(-\vec{q}_1^2) \delta^{(D-2)}(\vec{q}_1 - \vec{q}_2) + \mathcal{K}_r(\vec{q}_1, \vec{q}_2), \quad (2.40)$$

respectively. Here $\omega(-\vec{q}^2)$ is the gluon Regge trajectory given in Eq. (2.8). Due to scale invariance of the kernel, we can take its eigenfunctions as powers of one of the two squared momenta $q_{1,2}^2$, say $(\vec{q}_2^2)^{\gamma-1}$ with γ being a complex number. Denoting the corresponding eigenvalues as $\frac{N\alpha_s}{\pi} \chi^B(\gamma)$, we can write:

$$\int d^{D-2}q_2 \mathcal{K}(\vec{q}_1, \vec{q}_2) (\vec{q}_2^2)^{\gamma-1} = \frac{N\alpha_s}{\pi} \chi^B(\gamma) (\vec{q}_1^2)^{\gamma-1}, \quad (2.41)$$

with [7–10]

$$\chi^B(\gamma) = 2\psi(1) - \psi(\gamma) - \psi(1 - \gamma), \quad \psi(\gamma) = \Gamma'(\gamma)/\Gamma(\gamma). \quad (2.42)$$

The set of functions $(\vec{q}_2^2)^{\gamma-1}$ with $\gamma = 1/2 + i\nu$, $-\infty < \nu < \infty$ is complete and represent the eigenfunctions of the LO BFKL kernel averaged on the azimuthal angle between \vec{q}_1 and \vec{q}_2 . Taking its projection onto them in Eq. (2.29), one can find the following simple expression for the cross section:

$$\begin{aligned} \sigma(s) &= \frac{1}{(2\pi)^2} \int \frac{d^2\vec{q}_1}{\vec{q}_1^2} \Phi_1(\vec{q}_1, s_0) \int \frac{d^2\vec{q}_2}{\vec{q}_2^2} \Phi_2(-\vec{q}_2, s_0) \\ &\times \int_{\delta-i\infty}^{\delta+i\infty} \frac{d\omega}{2\pi i} \left(\frac{s}{s_0}\right)^\omega G_\omega(\vec{q}_1, \vec{q}_2), \end{aligned} \quad (2.43)$$

which holds with NLA accuracy. All momenta entering this expression are defined on the transverse plane and are therefore two-dimensional. $\Phi_{1,2}$ are the NLO impact factors specific of the process. From this equation it is possible

to see that if the Green's function G_ω has a pole at ω' , the cross section at LLA takes the form

$$\sigma^{(\text{LLA})} \sim \frac{s^{\omega_p^B}}{\sqrt{\ln s}}, \quad \omega' \equiv \omega_p^B, \quad (2.44)$$

where ω_p^B is the ($t = 0$)-intercept of the Regge trajectory that rules the asymptotic behaviour in s of the amplitude with exchange of the vacuum quantum numbers in the t -channel. It is equal to $4N_c(\alpha_s/\pi)\ln 2$, which implies violation of the Froissart bound [56], giving rise to a power-like behaviour of cross section with energy. The BFKL unitarity restoration is an open issue, which goes beyond the scope of this thesis. We mention here some of the solution methods proposed so far: the Balitsky–Kovchegov (BK) scheme [91,92], which generalises the BFKL evolution equation (2.31) through the inclusion of non-linear terms that tame the growth of the cross section; the Bartels–Kwiecinski–Praszalowicz (BKP) method [81,93], which introduces composite states of several Reggeised gluons; approaches based on gauge-invariant effective field theories for the Reggeised gluon interactions [94,95].

Besides the unitarity issue, there is another important question that should be contemplated, *i.e.* whether the characteristic growth with energy of sufficiently inclusive cross sections, which represents the most striking prediction of the BFKL Pomeron, could be observed in actual and forthcoming LHC analyses. This possibility will be examined in the course of our study on inclusive dijet production (see Section 3.6).

As we saw in Section 2.3.1, the Green's function G_ω takes care of the universal, energy-dependent part of the amplitude and obeys the BFKL equation (2.31).

In this section we derive a general form for the cross section in the so-called (ν, n) -representation (for more details, see Refs. [48,49]), which will provide

us with the starting point of our further analysis. First of all, it is convenient to work in the transverse momentum representation, defined by

$$\hat{q}|\vec{q}_i\rangle = \vec{q}_i|\vec{q}_i\rangle, \quad \langle\vec{q}_1|\vec{q}_2\rangle = \delta^{(2)}(\vec{q}_1 - \vec{q}_2), \quad (2.45)$$

$$\langle A|B\rangle = \langle A|\vec{k}\rangle\langle\vec{k}|B\rangle = \int d^2k A(\vec{k})B(\vec{k}).$$

In this representation, the total cross section given in Eq. (2.43) takes the simple form

$$\sigma = \frac{1}{(2\pi)^2} \int_{\delta-i\infty}^{\delta+i\infty} \frac{d\omega}{2\pi i} \left(\frac{s}{s_0}\right)^\omega \langle \frac{\Phi_1}{\vec{q}_1^2} | \hat{G}_\omega | \frac{\Phi_2}{\vec{q}_2^2} \rangle. \quad (2.46)$$

The kernel of the operator \hat{K} becomes

$$K(\vec{q}_2, \vec{q}_1) = \langle \vec{q}_2 | \hat{K} | \vec{q}_1 \rangle \quad (2.47)$$

and the equation for the Green's function reads

$$\hat{1} = (\omega - \hat{K})\hat{G}_\omega, \quad (2.48)$$

its solution being

$$\hat{G}_\omega = (\omega - \hat{K})^{-1}. \quad (2.49)$$

The kernel is given as an expansion in the strong coupling,

$$\hat{K} = \bar{\alpha}_s \hat{K}^0 + \bar{\alpha}_s^2 \hat{K}^1, \quad (2.50)$$

where

$$\bar{\alpha}_s \equiv \frac{N_c}{\pi} \alpha_s \quad (2.51)$$

and N_c is the number of colours. In Eq. (2.50) \hat{K}^0 is the BFKL kernel in the leading order (LO), while \hat{K}^1 represents the NLO correction.

To determine the cross section with NLA accuracy we need an approximate solution of Eq. (2.49). With the required accuracy this solution is

$$\begin{aligned} \hat{G}_\omega &= (\omega - \bar{\alpha}_s \hat{K}^0)^{-1} \\ &+ (\omega - \bar{\alpha}_s \hat{K}^0)^{-1} \left(\bar{\alpha}_s^2 \hat{K}^1 \right) (\omega - \bar{\alpha}_s \hat{K}^0)^{-1} + \mathcal{O} \left[\left(\bar{\alpha}_s^2 \hat{K}^1 \right)^2 \right]. \end{aligned} \quad (2.52)$$

In Eq. (2.41) we gave the expressions for the eigenfunctions of the LO kernel averaged on the azimuthal angle. In the general case the basis of eigenfunctions of the LO kernel,

$$\begin{aligned} \hat{K}^0 |n, \nu\rangle &= \chi(n, \nu) |n, \nu\rangle, \\ \chi(n, \nu) &= 2\psi(1) - \psi\left(\frac{n}{2} + \frac{1}{2} + i\nu\right) - \psi\left(\frac{n}{2} + \frac{1}{2} - i\nu\right), \end{aligned} \quad (2.53)$$

is given by the following set of functions:

$$\langle \vec{q} | n, \nu \rangle = \frac{1}{\pi\sqrt{2}} \left(\vec{q}^2 \right)^{i\nu - \frac{1}{2}} e^{in\phi}, \quad (2.54)$$

which now depend not only on ν , but also on the integer n , called *conformal spin*. Here ϕ is the azimuthal angle of the vector \vec{q} counted from some fixed direction in the transverse space, $\cos \phi \equiv q_x / |\vec{q}|$. Then, the orthonormality and completeness conditions take the form

$$\langle n', \nu' | n, \nu \rangle = \int \frac{d^2\vec{q}}{2\pi^2} \left(\vec{q}^2 \right)^{i\nu - i\nu' - 1} e^{i(n-n')\phi} = \delta(\nu - \nu') \delta_{nn'} \quad (2.55)$$

and

$$\hat{1} = \sum_{n=-\infty}^{\infty} \int_{-\infty}^{\infty} d\nu |n, \nu\rangle \langle n, \nu|. \quad (2.56)$$

The action of the full NLO BFKL kernel on these functions may be ex-

pressed as follows:

$$\begin{aligned} \hat{K}|n, \nu\rangle &= \bar{\alpha}_s(\mu_R)\chi(n, \nu)|n, \nu\rangle \\ &+ \bar{\alpha}_s^2(\mu_R)\left(\chi^{(1)}(n, \nu) + \frac{\beta_0}{4N_c}\chi(n, \nu)\ln(\mu_R^2)\right)|n, \nu\rangle \\ &+ \bar{\alpha}_s^2(\mu_R)\frac{\beta_0}{4N_c}\chi(n, \nu)\left(i\frac{\partial}{\partial\nu}\right)|n, \nu\rangle, \end{aligned} \quad (2.57)$$

where μ_R is the renormalisation scale of the QCD coupling; the first term represents the action of LO kernel, while the second and the third ones stand for the diagonal and the non-diagonal parts of the NLO kernel and we have used

$$\beta_0 = \frac{11N_c}{3} - \frac{2n_f}{3}, \quad (2.58)$$

where n_f is the number of active quark flavours.

The function $\chi^{(1)}(n, \nu)$, calculated in Ref. [96] (see also Ref. [97]), is conveniently represented in the form

$$\chi^{(1)}(n, \nu) = -\frac{\beta_0}{8N_c}\left(\chi^2(n, \nu) - \frac{10}{3}\chi(n, \nu) - i\chi'(n, \nu)\right) + \bar{\chi}(n, \nu), \quad (2.59)$$

where

$$\begin{aligned} \bar{\chi}(n, \nu) &= -\frac{1}{4}\left[\frac{\pi^2 - 4}{3}\chi(n, \nu) - 6\zeta(3) - \chi''(n, \nu) + 2\phi(n, \nu)\right. \\ &+ 2\phi(n, -\nu) + \frac{\pi^2 \sinh(\pi\nu)}{2\nu \cosh^2(\pi\nu)}\left(\left(3 + \left(1 + \frac{n_f}{N_c^3}\right)\frac{11 + 12\nu^2}{16(1 + \nu^2)}\right)\delta_{n0}\right. \\ &\left.\left. - \left(1 + \frac{n_f}{N_c^3}\right)\frac{1 + 4\nu^2}{32(1 + \nu^2)}\delta_{n2}\right)\right], \end{aligned} \quad (2.60)$$

and

$$\begin{aligned} \phi(n, \nu) &= -\int_0^1 dx \frac{x^{-1/2+iv+n/2}}{1+x} \left[\frac{1}{2}\left(\psi'\left(\frac{n+1}{2}\right) - \zeta(2)\right)\right. \\ &\left.+ \text{Li}_2(x) + \text{Li}_2(-x) + \ln x \left(\psi(n+1) - \psi(1) + \ln(1+x) + \sum_{k=1}^{\infty} \frac{(-x)^k}{k+n}\right)\right] \end{aligned} \quad (2.61)$$

$$\begin{aligned}
 & + \sum_{k=1}^{\infty} \frac{x^k}{(k+n)^2} (1 - (-1)^k) \Big] \\
 & = \sum_{k=0}^{\infty} \frac{(-1)^{k+1}}{k + (n+1)/2 + iv} [\psi'(k+n+1) - \psi'(k+1) \\
 & + (-1)^{k+1} (\beta'(k+n+1) + \beta'(k+1)) \\
 & - \frac{1}{k + (n+1)/2 + iv} (\psi(k+n+1) - \psi(k+1))] ,
 \end{aligned}$$

$$\beta'(z) = \frac{1}{4} \left[\psi' \left(\frac{z+1}{2} \right) - \psi' \left(\frac{z}{2} \right) \right] , \quad (2.62)$$

$$\text{Li}_2(x) = - \int_0^x dt \frac{\ln(1-t)}{t} . \quad (2.63)$$

Here and below $\chi'(n, \nu) \equiv d\chi(n, \nu)/d\nu$ and $\chi''(n, \nu) \equiv d^2\chi(n, \nu)/d^2\nu$.

The projection of the impact factors onto the eigenfunctions of the LO BFKL kernel, *i.e.* the transfer to the (ν, n) -representation, is done as follows:

$$\frac{\Phi_1(\vec{q}_1)}{\vec{q}_1^2} = \sum_{n=-\infty}^{+\infty} \int_{-\infty}^{+\infty} d\nu \Phi_1(\nu, n) \langle n, \nu | \vec{q}_1 \rangle , \quad (2.64)$$

$$\frac{\Phi_2(-\vec{q}_2)}{\vec{q}_2^2} = \sum_{n=-\infty}^{+\infty} \int_{-\infty}^{+\infty} d\nu \Phi_2(\nu, n) \langle \vec{q}_2 | n, \nu \rangle ,$$

$$\Phi_1(\nu, n) = \langle \frac{\Phi_1(\vec{q}_1)}{\vec{q}_1^2} | n, \nu \rangle \equiv \int d^2q_1 \frac{\Phi_1(\vec{q}_1)}{\vec{q}_1^2} \frac{1}{\pi\sqrt{2}} (\vec{q}_1^2)^{iv-\frac{1}{2}} e^{in\phi_1} , \quad (2.65)$$

$$\Phi_2(\nu, n) = \langle n, \nu | \frac{\Phi_2(-\vec{q}_2)}{\vec{q}_2^2} \rangle \equiv \int d^2q_2 \frac{\Phi_2(-\vec{q}_2)}{\vec{q}_2^2} \frac{1}{\pi\sqrt{2}} (\vec{q}_2^2)^{-iv-\frac{1}{2}} e^{-in\phi_2} .$$

The impact factors can be represented as an expansion in α_s ,

$$\Phi_{1,2}(\vec{q}) = \alpha_s(\mu_R) \left[v_{1,2}(\vec{q}) + \bar{\alpha}_s(\mu_R) v_{1,2}^{(1)}(\vec{q}) \right] \quad (2.66)$$

and

$$\Phi_{1,2}(\mathbf{n}, \nu) = \alpha_s(\mu_R) \left[c_{1,2}(\mathbf{n}, \nu) + \bar{\alpha}_s(\mu_R) c_{1,2}^{(1)}(\mathbf{n}, \nu) \right]. \quad (2.67)$$

To obtain our representation of the cross section, the matrix element of the BFKL Green's function is needed. According to Eq. (2.52), one has

$$\begin{aligned} \langle \mathbf{n}, \nu | \hat{G}_\omega | \mathbf{n}', \nu' \rangle &= \delta_{\mathbf{n}, \mathbf{n}'} \left[\delta(\nu - \nu') \left(\frac{1}{\omega - \bar{\alpha}_s(\mu_R) \chi(\mathbf{n}, \nu)} \right. \right. \\ &+ \frac{1}{(\omega - \bar{\alpha}_s(\mu_R) \chi(\mathbf{n}, \nu))^2} \left(\bar{\alpha}_s^2(\mu_R) (\bar{\chi}(\mathbf{n}, \nu) \right. \\ &+ \frac{\beta_0}{8N_c} (-\chi^2(\mathbf{n}, \nu) + \frac{10}{3} \chi(\mathbf{n}, \nu) + 2\chi(\mathbf{n}, \nu) \ln \mu_R^2 + i \frac{d}{d\nu} \chi(\mathbf{n}, \nu)) \left. \right) \left. \right) \\ &+ \frac{\frac{\beta_0}{4N_c} \bar{\alpha}_s^2(\mu_R) \chi(\mathbf{n}, \nu')}{(\omega - \bar{\alpha}_s(\mu_R) \chi(\mathbf{n}, \nu)) (\omega - \bar{\alpha}_s(\mu_R) \chi(\mathbf{n}, \nu'))} \left(i \frac{d}{d\nu'} \delta(\nu - \nu') \right) \left. \right]. \end{aligned} \quad (2.68)$$

Inserting twice the unity operator, written according to the completeness condition given in Eq. (2.56), into Eq. (2.46), we get

$$\begin{aligned} \sigma &= \frac{1}{(2\pi)^2} \sum_{\mathbf{n}=-\infty}^{\infty} \int_{-\infty}^{\infty} d\nu \sum_{\mathbf{n}'=-\infty}^{\infty} \int_{-\infty}^{\infty} d\nu' \int_{\delta-i\infty}^{\delta+i\infty} \frac{d\omega}{2\pi i} \left(\frac{1}{s_0} \right)^\omega \\ &\langle \frac{\Phi_1}{\bar{q}_1^2} | \mathbf{n}, \nu \rangle \langle \mathbf{n}, \nu | \hat{G}_\omega | \mathbf{n}', \nu' \rangle \langle \mathbf{n}', \nu' | \frac{\Phi_2}{\bar{q}_2^2} \rangle, \end{aligned} \quad (2.69)$$

and, after some algebra and integration by parts, finally

$$\begin{aligned} \sigma &= \frac{1}{(2\pi)^2} \sum_{\mathbf{n}=-\infty}^{\infty} \int_{-\infty}^{\infty} d\nu \left(\frac{s}{s_0} \right)^{\bar{\alpha}_s(\mu_R) \chi(\mathbf{n}, \nu)} \\ &\alpha_s^2(\mu_R) c_1(\mathbf{n}, \nu) c_2(\mathbf{n}, \nu) \left[1 + \bar{\alpha}_s(\mu_R) \left(\frac{c_1^{(1)}(\mathbf{n}, \nu)}{c_1(\mathbf{n}, \nu)} + \frac{c_2^{(1)}(\mathbf{n}, \nu)}{c_2(\mathbf{n}, \nu)} \right) \right. \\ &+ \bar{\alpha}_s^2(\mu_R) \ln \frac{s}{s_0} \left\{ \bar{\chi}(\mathbf{n}, \nu) + \frac{\beta_0}{8N_c} \chi(\mathbf{n}, \nu) \right. \\ &\left. \left. \left(-\chi(\mathbf{n}, \nu) + \frac{10}{3} + 2 \ln \mu_R^2 + i \frac{d}{d\nu} \ln \frac{c_1(\mathbf{n}, \nu)}{c_2(\mathbf{n}, \nu)} \right) \right\} \right]. \end{aligned} \quad (2.70)$$

In order to assess the relative weight of NLA corrections with respect to the LLA contribution, one can confront $\chi^{(1)}(n, \nu)$ (Eq. (2.59)) with $\chi(n, \nu)$ (Eq. (2.53)) for $n = 0$ and $\nu = 0$, *i.e.* for the point in the (ν, n) -space which determines the energy asymptotic behaviour in the LLA case. The result found for the ratio $|\chi^{(1)}(0, 0)/\chi(0, 0)|$ is large ($\simeq 6.5$) [11, 12], thus leading to instabilities in the BFKL perturbative expansion, which have to be controlled through some optimisation procedure. In Section 2.4 we will discuss one of them, which represent perhaps the most effective tool to quench the oscillating behaviour of the BFKL series.

2.3.3.1 Representation equivalence

The expression for the cross section given in Eq. (2.70) is valid both in the LLA and in the NLA. However, it is not the only possible one. Actually, several NLA-equivalent expressions can be adopted. One can consider alternative representations aiming at catching some of the unknown next-to-NLA corrections. Here we show two examples, which have been used in recent phenomenological analyses (for more details, see Ref. [36]):

- the so-called *exponentiated* representation,

$$\begin{aligned} \sigma^{\text{exp}} &= \frac{1}{(2\pi)^2} \sum_{n=-\infty}^{\infty} \int_{-\infty}^{\infty} d\nu \alpha_s^2(\mu_R) c_1(n, \nu) c_2(n, \nu) \\ &\times \left(\frac{s}{s_0} \right)^{\bar{\alpha}_s(\mu_R) \chi + \bar{\alpha}_s^2(\mu_R) \left\{ \bar{\chi} + \frac{\beta_0}{8N_c} \chi \left(-\chi + \frac{10}{3} + 2 \ln \mu_R^2 + i \frac{d}{d\nu} \ln \frac{c_1(n, \nu)}{c_2(n, \nu)} \right) \right\}} \\ &\times \left[1 + \bar{\alpha}_s(\mu_R) \left(\frac{c_1^{(1)}(n, \nu)}{c_1(n, \nu)} + \frac{c_2^{(1)}(n, \nu)}{c_2(n, \nu)} \right) \right]; \end{aligned} \quad (2.71)$$

- the exponentiated representation with an extra, irrelevant in the NLA term, given by the product of the NLO corrections of the two impact

factors,

$$\begin{aligned}
 \sigma^{\text{exp}(c)} &= \frac{1}{(2\pi)^2} \sum_{n=-\infty}^{\infty} \int_{-\infty}^{\infty} d\nu \alpha_s^2(\mu_R) c_1(n, \nu) c_2(n, \nu) \\
 &\times \left(\frac{s}{s_0} \right)^{\bar{\alpha}_s(\mu_R) \chi + \bar{\alpha}_s^2(\mu_R) \left\{ \bar{\chi} + \frac{\beta_0}{8N_c} \chi \left(-\chi + \frac{10}{3} + 2 \ln \mu_R^2 + i \frac{d}{d\nu} \ln \frac{c_1(n, \nu)}{c_2(n, \nu)} \right) \right\}} \\
 &\times \left[1 + \bar{\alpha}_s(\mu_R) \left(\frac{c_1^{(1)}(n, \nu)}{c_1(n, \nu)} + \frac{c_2^{(1)}(n, \nu)}{c_2(n, \nu)} \right) \right. \\
 &\left. + \alpha_s^2(\mu_R) \left(\frac{c_1^{(1)}(n, \nu)}{c_1(n, \nu)} \frac{c_2^{(1)}(n, \nu)}{c_2(n, \nu)} \right) \right].
 \end{aligned} \tag{2.72}$$

In Eqs. (2.71) and (2.72) is the LO kernel eigenvalue given in (2.53). In our calculations for Mueller–Navelet jet (see Chapter 3) and dihadron (see Chapter 3) production processes, we will adopt the exponentiated representation (Eq. (2.71)).

2.4 The BLM optimisation procedure

It is well known that the BFKL approach is plagued by large NLA corrections (see the discussion at the end of Section 2.3.3), both in the kernel of the Green’s function and in the process-dependent impact factors, as well as by large uncertainties in the renormalisation scale setting. As an example, the NLA BFKL corrections for the $n = 0$ conformal spin are with opposite sign with respect to the LLA results and large in absolute value. All that calls for some optimisation procedure of the perturbative series, which can consist in (i) including some pieces of the (unknown) next-to-NLA corrections, such as those dictated by renormalisation group, as in *collinear improvement* [33, 43, 98–109], or by energy-momentum conservation [110], or (ii) suppressing the emission of gluons which are close by in rapidity in the BFKL framework (*rapidity*

veto approach [111, 112]), and/or (iii) suitably choosing the values of the energy and renormalisation scales, which, though arbitrary within the NLO, can have a sizeable numerical impact through subleading terms. Common optimisation methods are those inspired by the *principle of minimum sensitivity* (PMS) [113, 114], the *fast apparent convergence* (FAC) [115–117] and the *Brodsky–Lepage–Mackenzie method* (BLM) [118–122].

In this Section we present and discuss the widely-used BLM approach, which relies on the removal of the renormalisation scale ambiguity by absorbing the non-conformal β_0 -terms into the running coupling. It is known that after BLM scale setting, the QCD perturbative convergence can be greatly improved due to the elimination of renormalon terms in the perturbative QCD series. Moreover, with the BLM scale setting, the BFKL Pomeron intercept has a weak dependence on the virtuality of the Reggeised gluon [121, 122].

We provide, as result, an exact implementation of the BLM method, together with two other, approximated ones, which were used earlier in the literature of the BLM method for different semi-hard processes (see a more detailed discussion in [38]).

We consider the BLM scale setting for the separate contributions to the cross section, specified in Eq. (2.70) by different values of n , denoted in the following by \mathcal{C}_n . The starting point of our considerations is the expression for \mathcal{C}_n in the $\overline{\text{MS}}$ scheme (see Eq. (2.70)),

$$\begin{aligned} \mathcal{C}_n &= \frac{1}{(2\pi)^2} \int_{-\infty}^{\infty} d\nu \left(\frac{s}{s_0} \right)^{\bar{\alpha}_s(\mu_R)\chi(n,\nu)} \alpha_s^2(\mu_R) c_1(n,\nu) c_2(n,\nu) \\ &\times \left[1 + \bar{\alpha}_s(\mu_R) \left(\frac{c_1^{(1)}(n,\nu)}{c_1(n,\nu)} + \frac{c_2^{(1)}(n,\nu)}{c_2(n,\nu)} \right) \right. \\ &\left. + \bar{\alpha}_s^2(\mu_R) \ln \frac{s}{s_0} \left\{ \bar{\chi}(n,\nu) + \frac{\beta_0}{8N_c} \chi(n,\nu) \right\} \right] \end{aligned} \quad (2.73)$$

$$\times \left(-\chi(\mathbf{n}, \nu) + \frac{10}{3} + 2 \ln \mu_R^2 + i \frac{d}{d\nu} \ln \frac{c_1(\mathbf{n}, \nu)}{c_2(\mathbf{n}, \nu)} \right) \Bigg] .$$

In the r.h.s. of this expression we have terms $\sim \alpha_s$ originated from the NLO corrections to the impact factors, and terms $\sim \alpha_s^2 \ln(s/s_0)$ coming from NLA corrections to the BFKL kernel. In the latter case, the terms proportional to the QCD β -function are explicitly shown. For our further consideration of the BLM scale setting, similar contributions have to be separated also from the NLO impact factors.

In fact, the contribution to an NLO impact factor that is proportional to β_0 is universally expressed through the LO impact factor,

$$v^{(1)}(\vec{q}) = v(\vec{q}) \frac{\beta_0}{4N_c} \left(\ln \left(\frac{\mu_R^2}{\vec{q}^2} \right) + \frac{5}{3} \right) + \dots , \quad (2.74)$$

where the dots stand for the other terms, not proportional to β_0 . This statement becomes evident if one considers the part of the strong coupling renormalisation proportional to n_f and related to the contributions of light quark flavours. Such contribution to the NLO impact factor originates only from diagrams with the light quark loop insertion in the Reggeised gluon propagator. The results for such contributions can be found, for instance, in Eq. (5.1) of [123]. Tracing there the terms $\sim n_f$ and performing the QCD charge renormalisation, one can indeed confirm (Eq. (2.74)).

Transforming Eq. (2.74) to the ν -representation according to Eq. (2.65), we obtain

$$\begin{aligned} \tilde{c}_1^{(1)}(\nu, \mathbf{n}) &= \frac{\beta_0}{4N_c} \left[+i \frac{d}{d\nu} c_1(\nu, \mathbf{n}) + \left(\ln \mu_R^2 + \frac{5}{3} \right) c_1(\nu, \mathbf{n}) \right] , \\ \tilde{c}_2^{(1)}(\nu, \mathbf{n}) &= \frac{\beta_0}{4N_c} \left[-i \frac{d}{d\nu} c_2(\nu, \mathbf{n}) + \left(\ln \mu_R^2 + \frac{5}{3} \right) c_2(\nu, \mathbf{n}) \right] , \end{aligned} \quad (2.75)$$

and

$$\frac{\tilde{c}_1^{(1)}}{c_1} + \frac{\tilde{c}_2^{(1)}}{c_2} = \frac{\beta_0}{4N_c} \left[i \frac{d}{d\nu} \ln \left(\frac{c_1}{c_2} \right) + 2 \left(\ln \mu_R^2 + \frac{5}{3} \right) \right] . \quad (2.76)$$

It is convenient to introduce the function $f(\nu)$, defined through

$$i \frac{d}{d\nu} \ln \left(\frac{c_1}{c_2} \right) \equiv 2 [f(\nu) - \ln(Q_1 Q_2)] , \quad (2.77)$$

that depends on the given process, where $Q_{1,2}$ denote here the hard scales which enter the impact factors $c_{1,2}$. The specific form of the function $f(\nu)$ depends on the particular process.

Now, we present again our result for the generic observable \mathcal{C}_n , showing explicitly all contributions proportional to the QCD β -function, *i.e.* also those originating from the impact factors:

$$\mathcal{C}_n = \frac{1}{(2\pi)^2} \int_{-\infty}^{\infty} d\nu \left(\frac{s}{s_0} \right)^{\bar{\alpha}_s(\mu_R) \chi(n, \nu)} \alpha_s^2(\mu_R) c_1(n, \nu) c_2(n, \nu) \quad (2.78)$$

$$\times \left[1 + \bar{\alpha}_s(\mu_R) \left(\frac{\bar{c}_1^{(1)}(n, \nu)}{c_1(n, \nu)} + \frac{\bar{c}_2^{(1)}(n, \nu)}{c_2(n, \nu)} + \frac{\beta_0}{2N_c} \left(\frac{5}{3} + \ln \frac{\mu_R^2}{Q_1 Q_2} + f(\nu) \right) \right) \right. \\ \left. + \bar{\alpha}_s^2(\mu_R) \ln \frac{s}{s_0} \left\{ \bar{\chi}(n, \nu) + \frac{\beta_0}{4N_c} \chi(n, \nu) \left(-\frac{\chi(n, \nu)}{2} + \frac{5}{3} + \ln \frac{\mu_R^2}{Q_1 Q_2} + f(\nu) \right) \right\} \right] ,$$

where $\bar{c}_{1,2}^{(1)} \equiv c_{1,2}^{(1)} - \tilde{c}_{1,2}^{(1)}$. We note that the dependence of Eq. (2.78) on the scale μ_R is subleading: performing in Eq. (2.78) the replacement

$$\alpha_s(\mu_R) = \alpha_s(\mu'_R) \left(1 - \bar{\alpha}_s(\mu'_R) \frac{\beta_0}{2N_c} \ln \frac{\mu_R}{\mu'_R} \right) , \quad (2.79)$$

one indeed obtains the same expression as before with the new scale μ'_R at the place of the old one μ_R , plus some additional contributions which are beyond the NLA accuracy.

As the next step, we perform a finite renormalisation from the $\overline{\text{MS}}$ to the physical MOM scheme, that means:

$$\alpha_s^{\overline{\text{MS}}} = \alpha_s^{\text{MOM}} \left(1 + \frac{\alpha_s^{\text{MOM}}}{\pi} T \right) , \quad (2.80)$$

with

$$\Upsilon = \Upsilon^\beta + \Upsilon^{\text{conf}}, \quad (2.81)$$

$$\Upsilon^\beta = -\frac{\beta_0}{2} \left(1 + \frac{2}{3} I \right),$$

$$\Upsilon^{\text{conf}} = \frac{C_A}{8} \left[\frac{17}{2} I + \frac{3}{2} (I-1) \xi + \left(1 - \frac{1}{3} I \right) \xi^2 - \frac{1}{6} \xi^3 \right],$$

where $C_A \equiv N_c$ is the colour factor associated with gluon emission from a gluon, $I = -2 \int_0^1 dx \frac{\ln(x)}{x^2-x+1} \simeq 2.3439$ and ξ is a gauge parameter, fixed at zero in the following.

Inserting Eq. (2.80) into Eq. (2.78) and expanding the result, we obtain, within NLA accuracy,

$$\begin{aligned} \mathcal{C}_n^{\text{MOM}} &= \frac{1}{(2\pi)^2} \int_{-\infty}^{\infty} d\nu \left(\frac{s}{s_0} \right)^{\bar{\alpha}_s^{\text{MOM}}(\mu_R) \chi(n, \nu)} \left(\alpha_s^{\text{MOM}}(\mu_R) \right)^2 \\ &\times c_1(n, \nu) c_2(n, \nu) \left[1 + \bar{\alpha}_s^{\text{MOM}}(\mu_R) \left\{ \frac{\bar{c}_1^{(1)}(n, \nu)}{c_1(n, \nu)} + \frac{\bar{c}_2^{(1)}(n, \nu)}{c_2(n, \nu)} + \frac{2\Upsilon^{\text{conf}}}{N_c} \right. \right. \\ &+ \left. \frac{\beta_0}{2N_c} \left(\frac{5}{3} + \ln \frac{\mu_R^2}{Q_1 Q_2} + f(\nu) - 2 \left(1 + \frac{2}{3} I \right) \right) \right\} \\ &+ \left(\bar{\alpha}_s^{\text{MOM}}(\mu_R) \right)^2 \ln \frac{s}{s_0} \left\{ \bar{\chi}(n, \nu) + \frac{\Upsilon^{\text{conf}}}{N_c} \chi(n, \nu) \right. \\ &+ \left. \left. \frac{\beta_0}{4N_c} \chi(n, \nu) \left(-\frac{\chi(n, \nu)}{2} + \frac{5}{3} + \ln \frac{\mu_R^2}{Q_1 Q_2} + f(\nu) - 2 \left(1 + \frac{2}{3} I \right) \right) \right\} \right]. \end{aligned} \quad (2.82)$$

The optimal scale μ_R^{BLM} is the value of μ_R that makes the expression proportional to β_0 vanish. We thus have

$$\begin{aligned} \mathcal{C}_n^\beta &= \frac{1}{(2\pi)^2} \int_{-\infty}^{\infty} d\nu \left(\frac{s}{s_0} \right)^{\bar{\alpha}_s^{\text{MOM}}(\mu_R^{\text{BLM}}) \chi(n, \nu)} \left(\alpha_s^{\text{MOM}}(\mu_R^{\text{BLM}}) \right)^3 \\ &\times c_1(n, \nu) c_2(n, \nu) \frac{\beta_0}{2N_c} \left[\frac{5}{3} + \ln \frac{(\mu_R^{\text{BLM}})^2}{Q_1 Q_2} + f(\nu) - 2 \left(1 + \frac{2}{3} I \right) \right] \end{aligned} \quad (2.83)$$

$$\begin{aligned}
 & + \bar{\alpha}_s^{\text{MOM}}(\mu_R^{\text{BLM}}) \ln \frac{s}{s_0} \frac{\chi(\mathbf{n}, \nu)}{2} \\
 & \times \left[-\frac{\chi(\mathbf{n}, \nu)}{2} + \frac{5}{3} + \ln \frac{(\mu_R^{\text{BLM}})^2}{Q_1 Q_2} + f(\nu) - 2 \left(1 + \frac{2}{3} \text{I} \right) \right] = 0.
 \end{aligned}$$

In the r.h.s. of Eq. (2.83) we have two groups of contributions. The first one originates from the β_0 -dependent part of NLO impact factor (2.74) and also from the expansion of the common α_s^2 pre-factor in Eq. (2.78) after expressing it in terms of α_s^{MOM} . The other group are the terms proportional to $\bar{\alpha}_s^{\text{MOM}} \ln s/s_0$. These contributions are those β_0 -dependent terms that are proportional to $\ln s/s_0$ in Eq. (2.78) and also the one coming from the expansion of the $(s/s_0)^{\bar{\alpha}_s \chi(\mathbf{n}, \nu)}$ factor in Eq. (2.78) after expressing it in terms of α_s^{MOM} .

The solution of Eq. (2.83) gives us the value of BLM scale. Note that this solution depends on the energy (on the ratio s/s_0). Such scale setting procedure is a direct application of the original BLM approach to semi-hard processes. Finally, our expression for the observable reads

$$\begin{aligned}
 c_n^{\text{BLM}} &= \frac{1}{(2\pi)^2} \int_{-\infty}^{\infty} d\nu \left(\frac{s}{s_0} \right)^{\bar{\alpha}_s^{\text{MOM}}(\mu_R^{\text{BLM}}) \left[\chi(\mathbf{n}, \nu) + \bar{\alpha}_s^{\text{MOM}}(\mu_R^{\text{BLM}}) \left(\bar{\chi}(\mathbf{n}, \nu) + \frac{\Gamma^{\text{conf}}}{N_c} \chi(\mathbf{n}, \nu) \right) \right]} \\
 & \times \left(\alpha_s^{\text{MOM}}(\mu_R^{\text{BLM}}) \right)^2 c_1(\mathbf{n}, \nu) c_2(\mathbf{n}, \nu) \\
 & \times \left[1 + \bar{\alpha}_s^{\text{MOM}}(\mu_R^{\text{BLM}}) \left\{ \frac{\bar{c}_1^{(1)}(\mathbf{n}, \nu)}{c_1(\mathbf{n}, \nu)} + \frac{\bar{c}_2^{(1)}(\mathbf{n}, \nu)}{c_2(\mathbf{n}, \nu)} + \frac{2\Gamma^{\text{conf}}}{N_c} \right\} \right],
 \end{aligned} \tag{2.84}$$

where we put at the exponent the terms $\sim \bar{\alpha}_s^{\text{MOM}} \ln s/s_0$, which is allowed within the NLA accuracy (see Section 2.3.3.1).

Eq. (2.83) can be solved only numerically. For this reason, we give also two analytic approximate approaches to the BLM scale setting. We consider the BLM scale as a function of ν and chose it in order to make vanish either the first or the second ($\sim \bar{\alpha}_s^{\text{MOM}} \ln s/s_0$) group of terms in the Eq. (2.83). In these

two cases one gets simpler analytical expressions for the BLM scales which do not depend on the energy. We thus have:

- case (a)

$$\left(\mu_{R,a}^{\text{BLM}}\right)^2 = Q_1 Q_2 \exp \left[2 \left(1 + \frac{2}{3} I \right) - f(\nu) - \frac{5}{3} \right], \quad (2.85)$$

$$\begin{aligned} \mathcal{C}_n^{\text{BLM},a} &= \frac{1}{(2\pi)^2} \int_{-\infty}^{\infty} d\nu \left(\alpha_s^{\text{MOM}}(\mu_{R,a}^{\text{BLM}}) \right)^2 c_1(\mathbf{n}, \nu) c_2(\mathbf{n}, \nu) \quad (2.86) \\ &\times \left(\frac{s}{s_0} \right)^{\bar{\alpha}_s^{\text{MOM}}(\mu_{R,a}^{\text{BLM}}) \left[\chi + \bar{\alpha}_s^{\text{MOM}}(\mu_{R,a}^{\text{BLM}}) \left(\bar{\chi} + \frac{\Gamma^{\text{conf}}}{N_c} \chi - \frac{\beta_0}{8N_c} \chi^2 \right) \right]} \\ &\times \left[1 + \bar{\alpha}_s^{\text{MOM}}(\mu_{R,a}^{\text{BLM}}) \left\{ \frac{\bar{c}_1^{(1)}(\mathbf{n}, \nu)}{c_1(\mathbf{n}, \nu)} + \frac{\bar{c}_2^{(1)}(\mathbf{n}, \nu)}{c_2(\mathbf{n}, \nu)} + \frac{2\Gamma^{\text{conf}}}{N_c} \right\} \right], \end{aligned}$$

which corresponds to the removal of the β_0 -dependent terms in the impact factors;

- case (b)

$$\left(\mu_{R,b}^{\text{BLM}}\right)^2 = Q_1 Q_2 \exp \left[2 \left(1 + \frac{2}{3} I \right) - f(\nu) - \frac{5}{3} + \frac{1}{2} \chi(\nu, \mathbf{n}) \right], \quad (2.87)$$

$$\begin{aligned} \mathcal{C}_n^{\text{BLM},b} &= \frac{1}{(2\pi)^2} \int_{-\infty}^{\infty} d\nu \left(\alpha_s^{\text{MOM}}(\mu_{R,b}^{\text{BLM}}) \right)^2 c_1(\mathbf{n}, \nu) c_2(\mathbf{n}, \nu) \quad (2.88) \\ &\times \left(\frac{s}{s_0} \right)^{\bar{\alpha}_s^{\text{MOM}}(\mu_{R,b}^{\text{BLM}}) \left[\chi + \bar{\alpha}_s^{\text{MOM}}(\mu_{R,b}^{\text{BLM}}) \left(\bar{\chi} + \frac{\Gamma^{\text{conf}}}{N_c} \chi \right) \right]} \\ &\times \left[1 + \bar{\alpha}_s^{\text{MOM}}(\mu_{R,b}^{\text{BLM}}) \left\{ \frac{\bar{c}_1^{(1)}(\mathbf{n}, \nu)}{c_1(\mathbf{n}, \nu)} + \frac{\bar{c}_2^{(1)}(\mathbf{n}, \nu)}{c_2(\mathbf{n}, \nu)} + \frac{2\Gamma^{\text{conf}}}{N_c} + \frac{\beta_0}{4N_c} \chi(\mathbf{n}, \nu) \right\} \right], \end{aligned}$$

which corresponds to the removal of the β_0 -dependent terms in the BFKL kernel.

Note that the two approximated approaches (a) and (b) discussed above and given in Eqs. (2.86) and (2.88), could be applicable only to processes characterised by a real-valued function $f(\nu)$. For some processes this is not the case. In particular, the inclusive dihadron production (see Chapter 4), is described by a complex-valued function, $f^*(\nu) = f(-\nu)$ (Eq. (4.11)). In such cases one can use only the exact-scale fixing method which relies on the numerical solution of Eq. (2.83).

Appendix A

The Mellin transform

R.H. Mellin was a Finnish mathematician who studied under K. Weierstrass. He is accredited as the developer of the integral transform

$$\mathbf{M}[f](\omega) \equiv \mathcal{F}(\omega) = \int_0^{+\infty} k^{\omega-1} f(k) dk, \quad (\text{A.1})$$

known as *Mellin transform*. Here f is a complex function of the real variable k and ω is a complex variable. The inverse transform is given by

$$\mathbf{M}^{-1}[F](k) \equiv f(k) = \frac{1}{2\pi i} \int_{c-i\infty}^{c+i\infty} k^{-\omega} \mathcal{F}(\omega) d\omega, \quad (\text{A.2})$$

where the line integral is taken over the line $\omega = c$ in the complex- ω plane. Conditions under which this inversion is valid are given in the Mellin inversion theorem. In particular, if $\mathcal{F}(\omega)$ is analytic in the strip $a < \text{Re } \omega < b$, and if it tends to zero uniformly as $\text{Im } \omega \rightarrow \pm\infty$ for any real value $c \mid a < c < b$, then we can recover $f(k)$ from $\mathcal{F}(\omega)$ via the inverse transform. The functions $\mathcal{F}(\omega)$ and $f(k)$ are called a Mellin transform pair.

There is a relation between the Mellin transform $\mathbf{M}[f](\omega)$ and the two-sided Laplace transform $\mathbf{L}[f](\omega)$. In fact, by letting $k = e^{-x}$, $dk = -e^{-x} dx$, the transform becomes

$$\mathbf{M}[f](\omega) = \int_{-\infty}^{+\infty} k^{\omega x} f(e^{-x}) dx \equiv \mathbf{L}[f](\omega). \quad (\text{A.3})$$

Conversely, one can get the two-sided Laplace transform from the Mellin transform by

$$\mathbf{L}[f](\omega) = \mathbf{M}[f(-\ln x)](\omega). \quad (\text{A.4})$$

It is also possible to define the Fourier transform $\mathbf{F}[f](\beta)$ in terms of the Mellin transform and vice versa by setting $\omega = \alpha + 2\pi i\beta$, with α and β real, and letting again $k = e^{-x}$:

$$\mathbf{M}[f](\omega) = \int_{-\infty}^{+\infty} f(e^{-x})e^{-\alpha x}e^{-2\pi i\beta x}dx \equiv \mathbf{F}[k^\alpha f(k)](\beta). \quad (\text{A.5})$$

An important example of Mellin transform is the relation between the Riemann function $R(k)$ and the Riemann zeta function $\zeta(\omega)$ (see Ref. [124] for further details):

$$R(k) = \lim_{y \rightarrow +\infty} \frac{1}{2\pi i} \int_{2-iy}^{2+iy} \frac{k^\omega}{\omega} \ln(\zeta(\omega)) d\omega, \quad (\text{A.6})$$

and

$$\frac{\ln(\zeta(\omega))}{\omega} = \int_1^{+\infty} R(k)k^{-\omega-1}dk. \quad (\text{A.7})$$

A.1 Properties of the Mellin transform

A list of some general properties of the Mellin transform is given below (to know more, see for instance Refs. [125–130]).

1. Scaling

$$\begin{aligned} \mathbf{M}[f(\xi k)](\omega) &= \int_0^{+\infty} f(\xi k)k^{\omega-1}d\omega \\ &= \xi^{-\omega} \int_0^{+\infty} f(x)x^{\omega-1}dx = \xi^{-\omega}\mathcal{F}(\omega). \end{aligned} \quad (\text{A.8})$$

2. Multiplication by k^ξ

$$\mathbf{M} \left[k^\xi f(k) \right] (\omega) = \int_0^{+\infty} f(k) k^{\omega+\xi-1} dk = \mathcal{F}(\omega + \xi). \quad (\text{A.9})$$

3. Raising the independent variable to a real power

$$\begin{aligned} \mathbf{M} \left[f(k^\xi) \right] (\omega) &= \int_0^{+\infty} f(k^\xi) k^{\omega-1} dk \\ &= \int_0^{+\infty} f(x) x^{\frac{x-1}{\xi}} \left(\frac{1}{\xi} x^{\frac{1}{\xi}-1} \right) dx = \xi^{-1} \mathcal{F} \left(\frac{\omega}{\xi} \right), \quad \xi > 0. \end{aligned} \quad (\text{A.10})$$

4. Inverse of the independent variable

$$\mathbf{M} \left[k^{-1} f(k^{-1}) \right] (\omega) = \mathcal{F}(1 - \omega). \quad (\text{A.11})$$

5. Multiplication by $\ln(k)$

$$\mathbf{M} [\ln(k) f(k)] (\omega) = \frac{d}{d\omega} \mathcal{F}(\omega). \quad (\text{A.12})$$

6. Multiplication by a power of $\ln(k)$

$$\mathbf{M} [(\ln(k))^n f(k)] (\omega) = \frac{d^n}{d\omega^n} \mathcal{F}(\omega). \quad (\text{A.13})$$

7. Derivative

$$\mathbf{M} \left[f^{(n)}(k) \right] (\omega) = (-1)^n \frac{\Gamma(\omega)}{\Gamma(\omega - n)} \mathcal{F}(\omega - n). \quad (\text{A.14})$$

8. Derivative multiplied by the independent variable

$$\mathbf{M} \left[k^n f^{(n)}(k) \right] (\omega) = (-1)^n \frac{\Gamma(\omega + n)}{\Gamma(\omega)} \mathcal{F}(\omega). \quad (\text{A.15})$$

9. Integral

$$\mathbf{M} \left[\int_0^k f(k') dk' \right] (\omega) = -\frac{1}{\omega} \mathbf{M} \left[\int_0^k f(k') dk' \right] (\omega + 1). \quad (\text{A.16})$$

10. Convolution

$$\mathbf{M}[f(k)g(k)](\omega) = \frac{1}{2\pi i} \int_{c-i\infty}^{c+i\infty} \mathcal{F}(\omega') \mathcal{G}(\omega - \omega') d\omega'. \quad (\text{A.17})$$

11. Multiplicative convolution

$$\mathbf{M}[f \diamond g](\omega) \equiv \mathbf{M} \left[\int_0^{+\infty} f\left(\frac{k}{k'}\right) g(k') \frac{dk'}{k'} \right](\omega) = \mathcal{F}(\omega) \mathcal{G}(\omega). \quad (\text{A.18})$$

Chapter 3

Mueller–Navelet jets

As we anticipated in the Introduction 1, Mueller–Navelet jet production has been one of the so far most studied semi-hard processes, having allowed the possibility to define infrared-safe observables whose theoretical predictions (see for instance Refs. [34,36]) are in a very good agreement with experimental data [44].

The analysis given in this Chapter, devoted to address the open issues in the Mueller–Navelet sector, is based on the work done in Refs. [36,46,47] and presented in Refs. [131,132].

3.1 Theoretical framework

In this Section the BFKL cross section and the azimuthal corrections for the Mueller–Navelet jet process are presented.

3.1.1 Inclusive dijet production in proton-proton collisions

The reaction under exam is the inclusive production of two jets (a *dijet* system) in proton-proton collisions

$$p(p_1) + p(p_2) \rightarrow \text{jet}(k_{J_1}) + \text{jet}(k_{J_2}) + X, \quad (3.1)$$

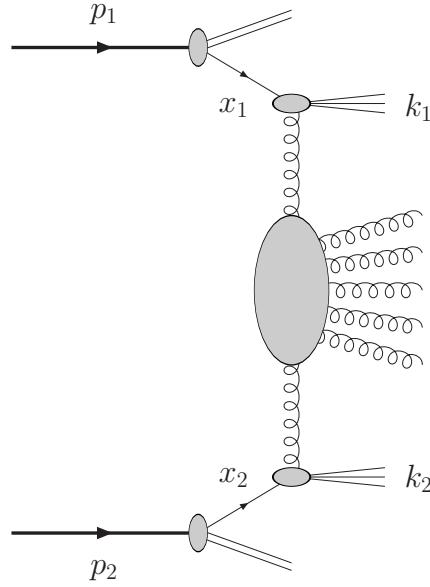


Figure 3.1: Mueller–Navelet jet production process in multi-Regge kinematics.

where the two jets are characterised by high transverse momenta, $\vec{k}_{J_1}^2 \sim \vec{k}_{J_2}^2 \gg \Lambda_{\text{QCD}}^2$ and large separation in rapidity; p_1 and p_2 are taken as Sudakov vectors (see Eq. (2.10)) satisfying $p_1^2 = p_2^2 = 0$ and $2(p_1 p_2) = s$, working at leading twist and neglecting the proton mass and other power suppressed corrections.

At LHC energies, the theoretical description of this reaction lies at the crossing point of two distinct approaches: collinear factorisation and BFKL resummation. On one side, at leading twist the process can be seen as the hard scattering of two partons, each emitted by one of the colliding hadrons according to the appropriate PDF, see Fig. 3.1. Collinear factorisation takes care to systematically resum the logarithms of the hard scale, through the standard DGLAP evolution of the PDFs and the fixed-order radiative corrections to the parton scattering cross section. The other resummation mechanism at work, justified by the large center-of-mass energy \sqrt{s} available at the LHC, is the BFKL resummation of energy logarithms, which are so large to compensate the small QCD coupling and must therefore be accounted for to all orders of

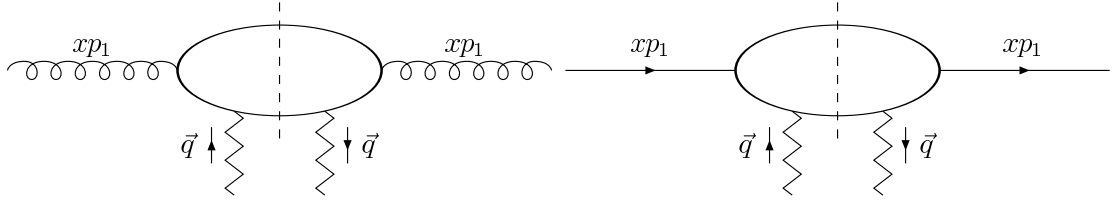


Figure 3.2: Schematic view of the forward gluon (left) and the forward quark (right) impact factor. Here p_1 is the proton momentum, x_1 is the fraction of proton momentum carried by the parton and \vec{q} is the transverse momentum of the incoming Reggeised gluon.

perturbation.

The expression of the cross section (Eq. (2.70)), which takes the form a convolution between two, process-dependent impact factors and a process-independent Green's function, is valid for a fully inclusive process, *i.e.* without any particle/object identified/tagged in the final state. By demanding the tagging of two forward jets, each of them produced in the fragmentation region of the respective parent proton, we are relaxing the inclusiveness condition requested in Eq. (2.70). This has an impact on the form of the process-dependent part of the cross section, namely the forward jet impact factors (also known as jet vertices).

The starting point is provided by the impact factors for the colliding partons, calculated with NLO accuracy in Refs. [20,21] (see Fig. 3.2). To obtain the impact factor for a tagged forward jet (see Fig. 3.3), the first step is to 'open' one of the integrations over the intermediate-state phase space to allow one parton to generate the jet¹. Then, according to QCD collinear factorisation, take the convolution with the parent parton PDFs. The jet can be formed by one parton in LO and by one or two partons when the process is considered in

¹This is achieved by introducing into the phase-space integration a suitably defined function which identifies the jet momentum with the momentum of one parton or with the sum of the two or more parton momenta when the jet is originated from the a multi-parton intermediate state

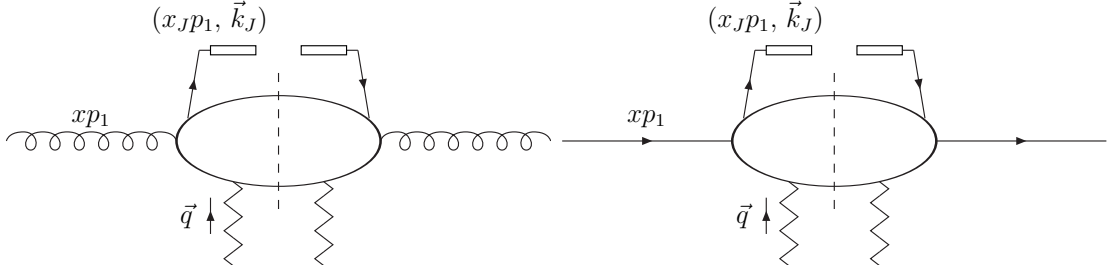


Figure 3.3: Schematic view of the vertex for the forward jet production in the case of incoming gluon (left) or quark (right). Here p_1 is the proton momentum, x is the fraction of proton momentum carried by the gluon/quark, $x_J p_1$ is the longitudinal jet momentum, \vec{k}_J is the transverse jet momentum and \vec{q} is the transverse momentum of the incoming Reggeised gluon.

NLO. In the simplest case, the jet momentum is identified with the momentum of the parton in the intermediate state k by the following jet function [133]:

$$S_J^{(2)}(\vec{k}; x) = \delta(x - x_J) \delta^{(2)}(\vec{k} - \vec{k}_J), \quad (3.2)$$

where x is the fraction of proton momentum carried by the quark, x_J is the longitudinal fraction of the jet momentum and \vec{k}_J is the transverse jet momentum. We get the expression for the jet impact factor, differential with respect to the variables parameterising the jet phase space, at the LO level as

$$\frac{d\Phi_J^{(0)}(\vec{q})}{dx_J dk_J} = 2\pi\alpha_s \sqrt{\frac{2C_F}{C_A}} \int_0^1 dx \left(\frac{C_A}{C_F} f_g(x) + \sum_{a=q, \bar{q}} f_a(x) \right) S_J^{(2)}(\vec{q}; x), \quad (3.3)$$

given as the sum of the gluon and all possible quark and antiquark PDF contributions $f_g(x)$, $f_a(x)$. In Eq. (3.3) C_F is the colour factor associated with gluon emission from a quark, $C_F = (N_c^2 - 1)/(2N_c)$. The last step to do is to project Eq. (3.3) onto the eigenfunctions (Eq. (2.54)) of the LO BFKL kernel (2.53), *i.e.* transfer to the (ν, n) -representation (see Section 2.3.3). The expression for the LO forward jet vertex will be given in Eq. (3.8) of Section 3.1.3.

In the NLO case, both the one-loop virtual corrections to the amplitude with one parton state and the terms coming from the two-partons final-state

amplitude have to be taken into account. In this last case, when the jet originates from a state of two partons, we need another jet selection function $S_j^{(3)}$, whose explicit form depends on the chosen jet algorithm. We will use the NLO jet vertex calculated in the *small-cone* approximation [134, 135], *i.e.* for small jet-cone aperture in the rapidity-azimuthal angle plane, which allow to get a simple analytic result in the (ν, n) -representation (see Eq. (B.1)).

3.1.2 Dijet cross section and azimuthal correlations

In QCD collinear factorisation the cross section of the process (3.1) reads

$$\begin{aligned} \frac{d\sigma}{dx_{J_1} dx_{J_2} d^2k_{J_1} d^2k_{J_2}} &= \sum_{r,s=q,\bar{q},g} \int_0^1 dx_1 \int_0^1 dx_2 f_r(x_1, \mu_F) f_s(x_2, \mu_F) \quad (3.4) \\ &= \frac{d\hat{\sigma}_{r,s}(x_1 x_2 s, \mu_F)}{dx_{J_1} dx_{J_2} d^2k_{J_1} d^2k_{J_2}}, \end{aligned}$$

where the r, s indices specify the parton types (quarks $q = u, d, s, c, b$; anti-quarks $\bar{q} = \bar{u}, \bar{d}, \bar{s}, \bar{c}, \bar{b}$; or gluon g), $f_i(x, \mu_F)$ denotes the initial proton PDFs; $x_{1,2}$ are the longitudinal fractions of the partons involved in the hard subprocess, while $x_{J_{1,2}}$ are the jet longitudinal fractions; μ_F is the factorisation scale; $d\hat{\sigma}_{r,s}(x_1 x_2 s, \mu_F)$ is the partonic cross section for the production of jets and $x_1 x_2 s \equiv \hat{s}$ is the squared center-of-mass energy of the parton-parton collision subprocess (see Fig. 3.1).

The cross section of the process can be presented as (see Section 2.3.3 for the details of the derivation)

$$\frac{d\sigma}{dy_{J_1} dy_{J_2} d|\vec{k}_{J_1}| d|\vec{k}_{J_2}| d\phi_{J_1} d\phi_{J_2}} = \frac{1}{(2\pi)^2} \left[\mathcal{C}_0 + \sum_{n=1}^{\infty} 2 \cos(n\phi) \mathcal{C}_n \right], \quad (3.5)$$

where $\phi = \phi_{J_1} - \phi_{J_2} - \pi$, while \mathcal{C}_0 gives the total cross section and the other coefficients \mathcal{C}_n determine the distribution of the azimuthal angle of the two jets.

Since the main object of the present analysis is the impact of jet produced in the central region on azimuthal coefficients, we will concentrate just on one representation for \mathcal{C}_n , out of the many possible NLA-equivalent options (see Section. 2.3.3.1 for a discussion). In particular, we will use the exponentiated representation together with the BLM optimisation method, whose details are given in Section 2.4 on scale μ_R and the factorisation scale μ_F . In our calculation we will use the exact implementation of BLM method, given in Eq. (2.84), together with the two approximate, semianalytic (a) and (b) cases (Eqs. (2.85) and (2.87), respectively), in order to keep contact with previous applications of BLM method where approximate approaches were used.

3.1.3 BLM scale setting

In this Section the expressions for the azimuthal coefficients \mathcal{C}_n , using the BLM prescription (see Section 2.4) are given. For the approximated (a) (Eq. (2.86)) and (b) (Eq. (2.88)) cases, we present also the expressions in the fixed-order DGLAP approach at the NLO, which will be used in the phenomenology Section 3.3. The $\mathcal{C}_n^{\text{DGLAP}}$ coefficients are nothing but the truncation of the respective BFKL expressions \mathcal{C}_n up to inclusions of NLO terms.

Introducing, for the sake of brevity, the definitions

$$Y = y_{J_1} - y_{J_2} = \ln \frac{x_{J_1} x_{J_2} s}{|\vec{k}_{J_1}| |\vec{k}_{J_2}|}, \quad Y_0 = \ln \frac{s_0}{|\vec{k}_{J_1}| |\vec{k}_{J_2}|}, \quad (3.6)$$

we will present in what follows the three different expressions for the coefficients \mathcal{C}_n .

- case “exact”

We remember that the BLM optimal scale μ_R^{BLM} is defined as the value of μ_R that makes all contributions to the considered observables which are proportional to the QCD β - function, β_0 , vanish, such that Eq. (2.83) is satisfied.

After that we have the following expression for our observables:

$$\begin{aligned} \mathcal{C}_n &= \frac{x_{J_1} x_{J_2}}{|\vec{k}_{J_1}| |\vec{k}_{J_2}|} \int_{-\infty}^{+\infty} d\nu e^{(Y-Y_0)\bar{\alpha}_s^{\text{MOM}}(\mu_R^{\text{BLM}}) \left[\chi + \bar{\alpha}_s^{\text{MOM}}(\mu_R^{\text{BLM}}) \left(\bar{\chi} + \frac{T^{\text{conf}}}{N_c} \chi \right) \right]} \\ &\times (\alpha_s^{\text{MOM}}(\mu_R^{\text{BLM}}))^2 c_1(n, \nu, |\vec{k}_{J_1}|, x_{J_1}) c_2(n, \nu, |\vec{k}_{J_2}|, x_{J_2}) \\ &\times \left[1 + \alpha_s^{\text{MOM}}(\mu_R^{\text{BLM}}) \left\{ \frac{\bar{c}_1^{(1)}(n, \nu, |\vec{k}_{J_1}|, x_{J_1})}{c_1(n, \nu, |\vec{k}_{J_1}|, x_{J_1})} + \frac{\bar{c}_2^{(1)}(n, \nu, |\vec{k}_{J_2}|, x_{J_2})}{c_2(n, \nu, |\vec{k}_{J_2}|, x_{J_2})} + \frac{2T^{\text{conf}}}{N_c} \right\} \right]. \end{aligned} \quad (3.7)$$

In the above equation, α_s^{MOM} is the QCD coupling in the physical momentum subtraction (MOM) scheme, related to $\alpha_s^{\overline{\text{MS}}}$ by the finite renormalisation given in Eq. (2.80), while $\bar{\alpha}_s^{\text{MOM}} = N_c/\pi \alpha_s^{\text{MOM}}$ as in Eq. (2.51), with N_c the number of colours. Then,

$$c_1(n, \nu, |\vec{k}|, x) = 2 \sqrt{\frac{C_F}{C_A}} (\vec{k}^2)^{i\nu-1/2} \left(\frac{C_A}{C_F} f_g(x, \mu_F) + \sum_{a=q, \bar{q}} f_a(x, \mu_F) \right) \quad (3.8)$$

and

$$c_2(n, \nu, |\vec{k}|, x) = \left[c_1(n, \nu, |\vec{k}|, x) \right]^*, \quad (3.9)$$

are the LO jet vertices in the ν -representation (see Eq. (3.3) for the corresponding expression in the momentum space) and $\chi = \chi(n, \nu)$ is the eigenvalue of the LO BFKL kernel (Eq. (2.53)). Note that, since $c_{1,2}$ do not depend on ν , the $f(\nu)$ function, whose general expression is given in Eq. (2.77), is zero for this process. The remaining objects are related to the NLO corrections of the BFKL kernel, ($\bar{\chi}(n, \nu)$, given in Eq. (2.60)) and of the jet vertices in the small-cone approximation ($c_{1,2}^{(1)}(n, \nu, |\vec{k}_{J_{1,2}}|, x_{J_{1,2}})$, given in Eq. (B.1) of Appendix B. The functions $\bar{c}_{1,2}^{(1)}(n, \nu, |\vec{k}_{J_{1,2}}|, x_{J_{1,2}})$ are the same as $c_{1,2}^{(1)}(n, \nu, |\vec{k}_{J_{1,2}}|, x_{J_{1,2}})$ with all terms proportional to β_0 removed.

- case (a)

$$(\mu_{R,a}^{\text{BLM}})^2 = k_{J_1} k_{J_2} \exp \left[2 \left(1 + \frac{2}{3} I \right) - \frac{5}{3} \right],$$

with

$$\begin{aligned} \mathcal{C}_n^{(a)} &= \frac{x_{J_1} x_{J_2}}{|\vec{k}_{J_1}| |\vec{k}_{J_2}|} \int_{-\infty}^{+\infty} d\nu e^{(Y-Y_0) \left[\bar{\alpha}_s^{\text{MOM}}(\mu_{R,a}^{\text{BLM}}) \chi + (\bar{\alpha}_s^{\text{MOM}}(\mu_{R,a}^{\text{BLM}}))^2 \left(\bar{\chi} + \frac{\Gamma^{\text{conf}}}{N_c} \chi - \frac{\beta_0}{8N_c} \chi^2 \right) \right]} \quad (3.10) \\ &\times (\alpha_s^{\text{MOM}}(\mu_{R,a}^{\text{BLM}}))^2 c_1(\mathbf{n}, \nu, |\vec{k}_{J_1}|, x_{J_1}) c_2(\mathbf{n}, \nu, |\vec{k}_{J_2}|, x_{J_2}) \\ &\times \left[1 + \alpha_s^{\text{MOM}}(\mu_{R,a}^{\text{BLM}}) \left\{ \frac{\bar{c}_1^{(1)}(\mathbf{n}, \nu, |\vec{k}_{J_1}|, x_{J_1})}{c_1(\mathbf{n}, \nu, |\vec{k}_{J_1}|, x_{J_1})} + \frac{\bar{c}_2^{(1)}(\mathbf{n}, \nu, |\vec{k}_{J_2}|, x_{J_2})}{c_2(\mathbf{n}, \nu, |\vec{k}_{J_2}|, x_{J_2})} + \frac{2\Gamma^{\text{conf}}}{N_c} \right\} \right]; \end{aligned}$$

$$\begin{aligned} \mathcal{C}_n^{\text{DGLAP (a)}} &= \frac{x_{J_1} x_{J_2}}{|\vec{k}_{J_1}| |\vec{k}_{J_2}|} \int_{-\infty}^{+\infty} d\nu \alpha_s^2 c_1(\mathbf{n}, \nu, |\vec{k}_{J_1}|, x_{J_1}) c_2(\mathbf{n}, \nu, |\vec{k}_{J_2}|, x_{J_2}) \quad (3.11) \\ &\times \left[1 + \frac{2}{\pi} \alpha_s \Gamma^{\text{conf}} + \bar{\alpha}_s (Y - Y_0) \chi \right. \\ &\left. + \alpha_s \left(\frac{\bar{c}_1^{(1)}(\mathbf{n}, \nu, |\vec{k}_{J_1}|, x_{J_1})}{c_1(\mathbf{n}, \nu, |\vec{k}_{J_1}|, x_{J_1})} + \frac{\bar{c}_2^{(1)}(\mathbf{n}, \nu, |\vec{k}_{J_2}|, x_{J_2})}{c_2(\mathbf{n}, \nu, |\vec{k}_{J_2}|, x_{J_2})} \right) \right], \end{aligned}$$

• case (b)

$$(\mu_{R,b}^{\text{BLM}})^2 = k_{J_1} k_{J_2} \exp \left[2 \left(1 + \frac{2}{3} I \right) - \frac{5}{3} + \frac{1}{2} \chi(\mathbf{n}, \nu) \right],$$

with

$$\begin{aligned} \mathcal{C}_n^{(b)} &= \frac{x_{J_1} x_{J_2}}{|\vec{k}_{J_1}| |\vec{k}_{J_2}|} \int_{-\infty}^{+\infty} d\nu e^{(Y-Y_0) \left[\bar{\alpha}_s^{\text{MOM}}(\mu_{R,b}^{\text{BLM}}) \chi + (\bar{\alpha}_s^{\text{MOM}}(\mu_{R,b}^{\text{BLM}}))^2 \left(\bar{\chi} + \frac{\Gamma^{\text{conf}}}{N_c} \chi \right) \right]} \quad (3.12) \\ &\times (\alpha_s^{\text{MOM}}(\mu_{R,b}^{\text{BLM}}))^2 c_1(\mathbf{n}, \nu, |\vec{k}_{J_1}|, x_{J_1}) c_2(\mathbf{n}, \nu, |\vec{k}_{J_2}|, x_{J_2}) \\ &\times \left[1 + \alpha_s^{\text{MOM}}(\mu_{R,b}^{\text{BLM}}) \left\{ \frac{\bar{c}_1^{(1)}(\mathbf{n}, \nu, |\vec{k}_{J_1}|, x_{J_1})}{c_1(\mathbf{n}, \nu, |\vec{k}_{J_1}|, x_{J_1})} + \frac{\bar{c}_2^{(1)}(\mathbf{n}, \nu, |\vec{k}_{J_2}|, x_{J_2})}{c_2(\mathbf{n}, \nu, |\vec{k}_{J_2}|, x_{J_2})} + \frac{2\Gamma^{\text{conf}}}{N_c} + \frac{\beta_0}{4N_c} \chi \right\} \right], \end{aligned}$$

$$\begin{aligned} \mathcal{C}_n^{\text{DGLAP (b)}} &= \frac{x_{J_1} x_{J_2}}{|\vec{k}_{J_1}| |\vec{k}_{J_2}|} \int_{-\infty}^{+\infty} d\nu \alpha_s^2 c_1(\mathbf{n}, \nu, |\vec{k}_{J_1}|, x_{J_1}) c_2(\mathbf{n}, \nu, |\vec{k}_{J_2}|, x_{J_2}) \quad (3.13) \\ &\times \left[1 + \alpha_s (\mu_R) \left(\frac{\beta_0}{4\pi} \chi + 2 \frac{\Gamma^{\text{conf}}}{\pi} \right) + \bar{\alpha}_s (Y - Y_0) \chi \right] \end{aligned}$$

$$+ \alpha_s \left(\frac{\bar{c}_1^{(1)}(\mathbf{n}, \nu, |\vec{k}_{J_1}|, x_{J_1})}{c_1(\mathbf{n}, \nu, |\vec{k}_{J_1}|, x_{J_1})} + \frac{\bar{c}_2^{(1)}(\mathbf{n}, \nu, |\vec{k}_{J_2}|, x_{J_2})}{c_2(\mathbf{n}, \nu, |\vec{k}_{J_2}|, x_{J_2})} \right) \Big].$$

Note that, in the above equations the scale s_0 entering Y_0 is the artificial energy scale introduced in the BFKL approach to perform the Mellin transform from the s -space to the complex angular momentum plane and cancels in the full expression, up to terms beyond the NLA. In our analysis it will always be fixed at the “natural” value $Y_0 = 0$, given by the kinematical of Mueller–Navelet process.

Although the final expressions in Eqs. (3.7), (3.10), (3.11), (3.12), and (3.13) are given in terms of α^{MOM} in the MOM scheme, it is possible to use analogous expressions in the $\overline{\text{MS}}$ scheme. The way to do that is to start from the general expressions, then perform the change of scheme $\overline{\text{MS}} \rightarrow \text{MOM}$ as an intermediate step, and finally, after setting the BLM scales, go back again to the $\overline{\text{MS}}$ scheme. From a practical point of view, one obtains the expressions in the $\overline{\text{MS}}$ scheme, starting from MOM, by making the change

$$\Upsilon^{\text{conf}} \rightarrow -\Upsilon^\beta, \quad (3.14)$$

with Υ^β given in Eq. (2.81), in the expressions cited above. In Sections 3.2 and 3.3 we will give predictions for our observables in the $\overline{\text{MS}}$ scheme.

3.1.4 Integration over the final-state phase space

In order to match the kinematical cuts used by the CMS collaboration (see for instance Ref. [44]), we will consider the *integrated coefficients* given by

$$\int_{y_{J_2}^{\min}}^{y_{J_2}^{\max}} dy_{J_2} \int_{k_{J_1}^{\min}}^{\infty} dk_{J_1} \int_{k_{J_2}^{\min}}^{\infty} dk_{J_2} \delta(y_{J_1} - y_{J_2} - Y) \quad (3.15)$$

$$\times \mathcal{C}_n(y_{J_1}, y_{J_2}, k_{J_1}, k_{J_2})$$

and their ratios $R_{nm} \equiv C_n/C_m$. Among them, the ratios of the form R_{n0} have a simple physical interpretation, being the azimuthal correlations $\langle \cos(n\phi) \rangle$. We will take jet rapidities in the range delimited by $y_{J_1}^{\min} = y_{J_2}^{\min} = -4.7$ and $y_{J_1}^{\max} = y_{J_2}^{\max} = 4.7$ and study the dependence of the R_{nm} ratios as function of the jet rapidity separation $Y \equiv y_{J_1} - y_{J_2}$. Concerning the jet transverse momenta $k_{J_{1,2}}$, differently from most previous analyses, we make several different choices, which include *asymmetric* cuts (see the next three Sections for further details). The jet-cone size R entering the NLO-jet vertices is fixed at the value $R = 0.5$ and, as anticipated, $Y_0 = 0$. Finally, we will consider two characteristic values for the center-of-mass energy, *i.e.* $\sqrt{s} = 7$ TeV, for which experimental analyses with *symmetric* configuration for the outgoing jet momenta already exist (see Section 3.2), and $\sqrt{s} = 13$ TeV.

3.2 Theory versus experiment

In this Section we present the analysis of Ref. [36], in which predictions for the R_{10} , R_{20} , R_{30} , R_{21} and R_{32} are given and compared with recent CMS data at 7 TeV [44]. BLM scale optimisation, in both variants (a) (Eq. (3.10)) and (b) (Eq. (3.12)) is used, while final calculations are done in the $\overline{\text{MS}}$. We remember that the expressions above cited are given in the MOM scheme and it is possible to obtain the analogous ones in the $\overline{\text{MS}}$ through the substitution $T^{\text{conf}} \rightarrow -T^\beta$, with T^{conf} and T^β given in Eq. (2.81).

Results are reported in Table 3.1 and in Fig. 3.4. We clearly see that the pure LLA calculations (*i.e.* considering just the LO kernel contribution and neglecting the NLO corrections to the impact factors) overestimate the decorrelation by far in all R_{nm} ratios. Introducing NLA BFKL corrections and using the BLM method we can see that, except for the ratio C_1/C_0 , the agreement with exper-

imental data becomes very good, for both variants (a) and (b), at the larger values of Y .

Meanwhile, it would be also useful to address, on the experimental side, some possible issues which could be sources of mismatch with the way in which Mueller–Navelet jets are defined in theory and that are not easy to be revealed in the comparison with theoretical predictions, for being the latter affected in their turn by systematic effects of the same amount. We list below two of them.

- The use of *symmetric* cuts in the values of $k_{J_i}^{\min}$ maximises the contribution of the Born term in C_0 , which is present for back-to-back jets (see Fig. 3.5) only and is expected to be large, therefore making less visible the effect of the BFKL resummation in all observables involving C_0 . The use of *asymmetric* cuts can reduce the contribution of the Born term and enhance effects with additional undetected hard gluon radiation, which makes the visibility of BFKL effect more clear in comparison to the descriptions based on fixed-order DGLAP approach.
- In data analysis defining the Y value for a given final state with two jets, the rapidity of one of the two jets could be so small, say $|y_{J_i}| \lesssim 2$, that this jet is actually produced in the central region, rather than in one of the two forward regions. The longitudinal momentum fractions of the parent partons that generate a central jet are very small, and one can naturally expect sizable corrections to the vertex of this jet, due to the fact that the collinear factorisation approach used in the derivation of the result for jet vertex is not designed for the region of small x .

These issues are addressed in Sections 3.3 and 3.4, respectively.

Table 3.1: R_{10} , R_{20} , R_{30} , R_{21} , and R_{32} with the BLM method, in both variants (a) (Eq. (3.10)) and (b) (Eq. (3.12)).

Y	C_1/C_0		C_2/C_0		C_3/C_0		C_2/C_1		C_3/C_2	
	(a)	(b)	(a)	(b)	(a)	(b)	(a)	(b)	(a)	(b)
3	0.960	0.962	0.819	0.821	0.687	0.696	0.853	0.853	0.839	0.848
4	0.890	0.892	0.684	0.696	0.548	0.555	0.768	0.780	0.798	0.797
5	0.837	0.818	0.582	0.587	0.427	0.434	0.696	0.713	0.733	0.744
6	0.744	0.744	0.447	0.483	0.320	0.335	0.627	0.649	0.686	0.694
7	0.685	0.680	0.387	0.403	0.246	0.261	0.566	0.593	0.636	0.647
8	0.660	0.641	0.339	0.348	0.202	0.213	0.513	0.544	0.596	0.611
9	0.760	0.663	0.367	0.344	0.207	0.201	0.483	0.519	0.563	0.583

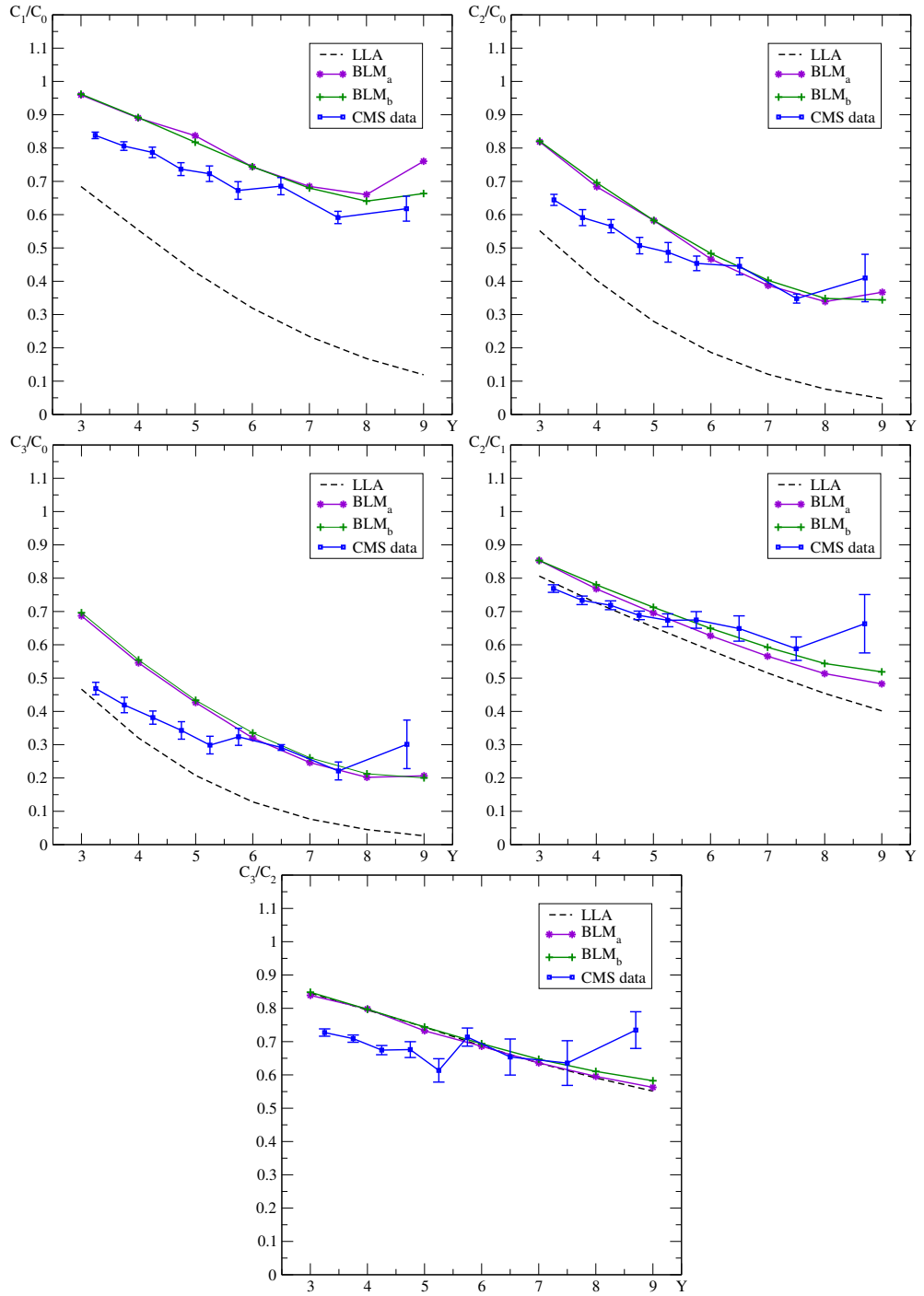


Figure 3.4: Y -dependence of R_{10} , R_{20} , R_{30} , R_{21} , and R_{32} at $\sqrt{s} = 7$ TeV [44] in the symmetric configuration $k_{J_{1,2}}^{\min} = 35$ GeV. Results were obtained with the two variants (a) (Eq. (3.10)) and (b) (Eq. (3.12)) of the BLM method. The dashed line gives the LLA BFKL result.

3.3 BFKL versus high-energy DGLAP

3.3.1 Motivation

As we saw at the end of Section 3.2, the effect of Born contribution to the cross section C_0 , present only for back-to-back jets (see Fig. 3.5), is maximised when *symmetric* cuts in the values of the forward jet transverse momenta are used; on the contrary, in the case of *asymmetric* cuts, the Born term is suppressed and the effects of the additional undetected hard gluon radiation is enhanced, thus making more visible the BFKL resummation, in comparison to descriptions based on the fixed-order DGLAP approach, in all observables involving C_0 .

For this purpose, we compare predictions for several azimuthal correlations and their ratios obtained, on one side, by a fixed-order DGLAP calculation at the NLO and, on the other side, by BFKL resummation in the NLA.

We remember that our implementation of the NLO DGLAP calculation is an approximate one. We just use here NLA BFKL expressions, given in Eqs. (3.11) and (3.13), for the observables that are truncated to the $\mathcal{O}(\alpha_s^3)$ order. In this way we take into account the leading power asymptotic of the exact NLO DGLAP prediction and neglect terms that are suppressed by the inverse powers of the energy of the parton-parton collisions. Such approach is legitimate in the region of large Y which we consider here. The exact implementation of NLO DGLAP for Mueller–Navelet jets is important, because it allows to understand better the region of applicability of our approach, but it requires more involved Monte Carlo calculations. We use the BLM scheme in both semi-analytic (a) (Eq. (2.86)) and (b) (Eq. (2.88)) cases in order to compare BFKL (Eqs. (3.10) and (3.12) with DGLAP (Eqs. (3.11) and (3.11) predictions. As done in Section 3.2, we perform all calculations in the $\overline{\text{MS}}$ scheme. We remember

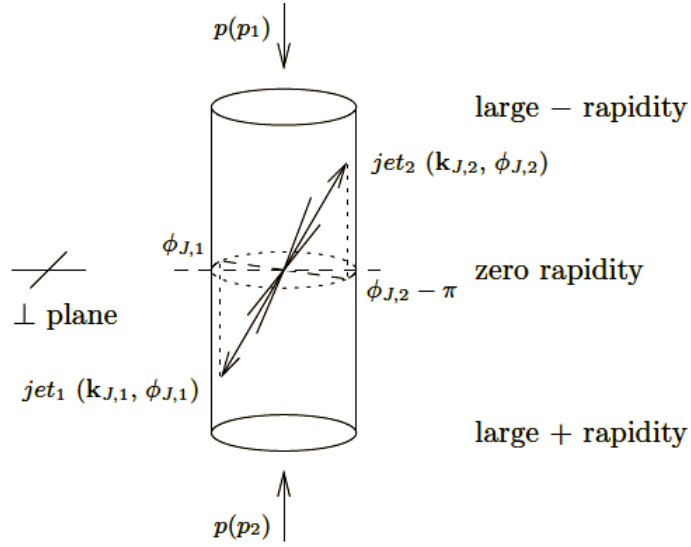


Figure 3.5: Mueller–Navelet jets at LLA: a back-to-back dijet reaction. Picture from Ref. [29].

that all the four expressions above cited are given in the MOM scheme and it is possible to obtain the analogous ones in the $\overline{\text{MS}}$ through the substitution $\Upsilon^{\text{conf}} \rightarrow -\Upsilon^\beta$, with Υ^{conf} and Υ^β given in (2.81).

Another important benefit from the use of *asymmetric* cuts, pointed out in [35], is that the effect of violation of the energy-momentum conservation in the NLA is strongly suppressed with respect to what happens in the LLA.

3.3.2 Results and discussion

We study the Y -dependence of ratios R_{nm} of the integrated coefficients given in Eq. (3.15), fixing the center-of-mass energy at $\sqrt{s} = 7$ TeV and making two *asymmetric* choices for the jet transverse momenta:

1. $k_{J_1}^{\text{min}} = 35$ GeV, $k_{J_2}^{\text{min}} = 45$ GeV;
2. $k_{J_1}^{\text{min}} = 35$ GeV, $k_{J_2}^{\text{min}} = 50$ GeV.

We summarise our results in Tables 3.2 and 3.3 and in Figs. 3.6 and 3.7. We can clearly see that, at $Y = 9$, BFKL and DGLAP, in both variants (a)

(Eq. (3.10)) and (b) (Eq. (3.12)) of the BLM setting, give quite different predictions for the all considered ratios except C_1/C_0 ; at $Y = 6$ this happens in fewer cases, while at $Y = 3$ BFKL and DGLAP cannot be distinguished with given uncertainties. In particular, taking one of the cuts at 35 GeV (as done by the CMS collaboration [44]) and the other at 45 GeV or 50 GeV, we can clearly see that predictions from BFKL and DGLAP become separate for most azimuthal correlations and ratios between them, this effect being more and more visible as the rapidity gap between the jets, Y , increases. In other words, in this kinematics the additional undetected parton radiation between the jets which is present in the resummed BFKL series, in comparison to just one undetected parton allowed by the NLO DGLAP approach, makes its difference and leads to more azimuthal angle decorrelation between the jets, in full agreement with the original proposal of Mueller and Navelet.

This result was not unexpected: the use of *symmetric* cuts for jet transverse momenta maximises the contribution of the Born term, which is present for back-to-back jets only and is expected to be large, therefore making less visible the effect of the BFKL resummation. This phenomenon could be at the origin of the instabilities observed in the NLO fixed-order calculations of Refs. [136,137].

One may argue that using *disjoint* intervals for the two jet transverse momenta would be an even cleaner setup. However, since the majority of dijet events are characterised by the lowest possible values for the jet transverse momenta in the selected range, our setup with two different lower cuts but overlapping intervals is not effectively different from the setup with *disjoint* transverse momenta ranges. Furthermore, independently of the cutoff procedure, there is a non-escapable limitation, namely that the actual energies of partonic subprocesses at the LHC are not much larger than the final-object transverse momenta and, therefore, not too many additional hard parton emissions can

occur. This implies that, even after *asymmetric* or *disjoint* configurations in the transverse momentum space, the BFKL and the full NLO DGLAP approaches are not expected to be largely different.

Table 3.2: Ratios C_n/C_m at 7 TeV and for $k_{J_1}^{\min} = 35$ GeV and $k_{J_2}^{\min} = 45$ GeV.

	Y	BFKL _(a)	DGLAP _(a)	BFKL _(b)	DGLAP _(b)
C_1/C_0	3.0	0.963(21)	1.003(44)	0.964(17)	1.021(78)
	6.0	0.7426(43)	0.884(61)	0.7433(30)	0.914(91)
	9.0	0.897(15)	0.868(16)	0.714(10)	0.955(50)
C_2/C_0	3.0	0.80(2)	0.948(43)	0.812(15)	0.949(75)
	6.0	0.4588(32)	0.726(56)	0.4777(26)	0.702(81)
	9.0	0.4197(79)	0.710(15)	0.3627(50)	0.850(48)
C_3/C_0	3.0	0.672(18)	0.876(41)	0.684(13)	0.838(70)
	6.0	0.3095(26)	0.566(45)	0.3282(21)	0.435(68)
	9.0	0.2275(72)	0.558(13)	0.2057(29)	0.717(44)
C_2/C_1	3.0	0.831(18)	0.945(43)	0.842(16)	0.929(72)
	6.0	0.6178(43)	0.821(66)	0.6427(34)	0.768(91)
	9.0	0.4677(63)	0.817(18)	0.5079(56)	0.890(51)
C_3/C_2	3.0	0.839(22)	0.924(45)	0.843(17)	0.883(76)
	6.0	0.6745(64)	0.780(71)	0.6869(52)	0.62(11)
	9.0	0.542(15)	0.787(21)	0.5670(59)	0.844(56)

Table 3.3: Ratios C_n/C_m at 7 TeV and for $k_{j_1}^{\min} = 35$ GeV and $k_{j_2}^{\min} = 50$ GeV.

	Y	BFKL _(a)	DGLAP _(a)	BFKL _(b)	DGLAP _(b)
C_1/C_0	3.0	0.961(23)	1.006(46)	0.964(15)	1.034(89)
	6.0	0.7360(49)	0.869(58)	0.7357(25)	0.89(12)
	9.0	1.0109(61)	0.857(16)	0.7406(46)	0.958(56)
C_2/C_0	3.0	0.788(21)	0.946(44)	0.801(14)	0.950(85)
	6.0	0.4436(37)	0.698(53)	0.4626(19)	0.611(98)
	9.0	0.4568(50)	0.695(15)	0.3629(23)	0.862(54)
C_3/C_0	3.0	0.653(19)	0.868(43)	0.669(12)	0.814(79)
	6.0	0.2925(31)	0.530(42)	0.3115(15)	0.320(57)
	9.0	0.2351(35)	0.551(17)	0.1969(17)	0.748(50)
C_2/C_1	3.0	0.820(21)	0.940(44)	0.832(15)	0.918(81)
	6.0	0.6027(51)	0.803(64)	0.6288(26)	0.69(12)
	9.0	0.4518(35)	0.811(18)	0.4900(24)	0.899(57)
C_3/C_2	3.0	0.829(26)	0.917(46)	0.835(17)	0.857(85)
	6.0	0.6595(82)	0.759(70)	0.6733(36)	0.52(11)
	9.0	0.5146(85)	0.793(23)	0.5426(38)	0.869(62)

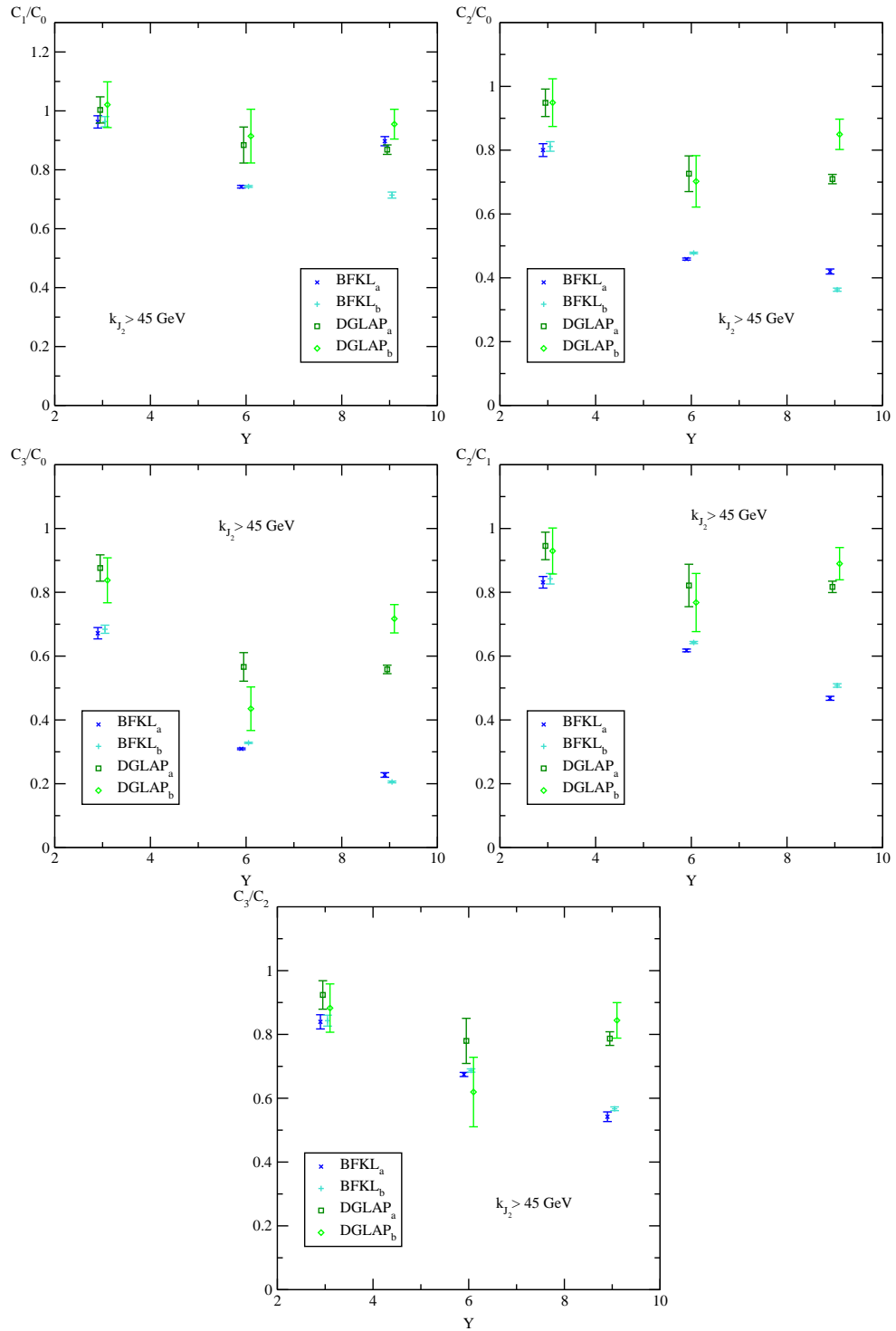


Figure 3.6: Y -dependence of several ratios C_m/C_n for $k_{J_1}^{\min} = 35$ GeV and $k_{J_2}^{\min} = 45$ GeV, for BFKL and high-energy DGLAP in the two variants (a) (Eq. (3.10)) and (b) (Eq. (3.12)) of the BLM method and for $\sqrt{s} = 7$ TeV (data points have been slightly shifted along the horizontal axis for the sake of readability).

3.3. BFKL versus high-energy DGLAP

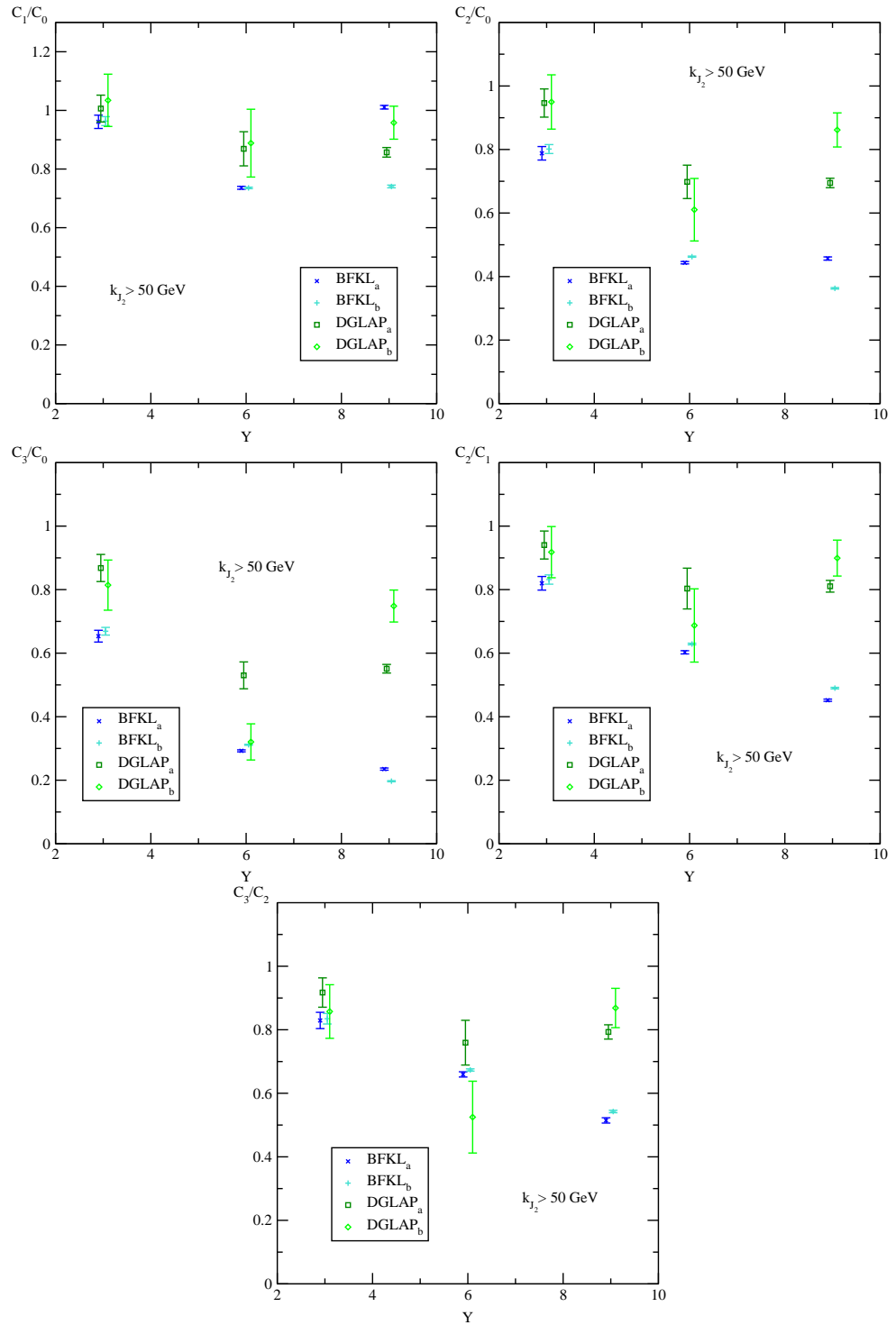


Figure 3.7: Y -dependence of several ratios C_m/C_n for $k_{J_1}^{\min} = 35$ GeV and $k_{J_2}^{\min} = 50$ GeV, for BFKL and high-energy DGLAP in the two variants (a) (Eq. (3.10)) and (b) (Eq. (3.12)) of the BLM method and for $\sqrt{s} = 7$ TeV (data points have been slightly shifted along the horizontal axis for the sake of readability).

3.4 Central rapidity range exclusion

3.4.1 Motivation

In the last Section we studied the effect of using *asymmetric* cuts for the jet transverse momenta, comparing full NLA BFKL predictions with fixed-order DGLAP calculations in the high-energy limit. Here we want to deal with another issue, which deserves some care and has not been taken into consideration both in theoretical and experimental analyses so far. As anticipated in the discussion at the end of Section 3.2, in defining the jet rapidity separation Y for a given final state with two jets, the rapidity of one of the two jets could be so small, say $|y_{J_i}| \lesssim 2$, that this jet is actually produced in the central region, rather than in one of the two forward regions. Since the longitudinal momentum fractions of the parent partons x that generate such central jet are very small, one can naturally expect sizable corrections to the vertex of this jet, due to the fact that the collinear factorisation approach used in the derivation of the result for jet vertex could not be accurate enough in our kinematical region, where x values can be as small as, $x \sim 10^{-3}$.

The use of collinear factorisation methods in the case of central jet production in our kinematical range deserves some discussion. On one hand, at $x \sim 10^{-3}$ and at scales of the order of the jet transverse momenta which we consider here, $\sim 20 \div 40$ GeV, PDFs are well constrained, mainly from DIS HERA data. On the other hand, in this kinematical region PDF parameterisations extracted in next-to-NLO (NNLO) and in NLO approximations start to differ one from the other, which indicates that NNLO effects become essential in the DIS cross sections. The situation with central jet production in proton-proton collisions may be different. Recently, in Ref. [138] results for NNLO corrections to the dijet production originated from the gluonic subprocesses were presented.

In the region $|y_{J_{1,2}}| < 0.3$ and for jet transverse momenta ~ 100 GeV, the account of NNLO effects leads to an increase of the cross section by ~ 25 . For our kinematics, featuring smaller jet transverse momenta and “less inclusive” coverage of jet rapidities, one could expect even larger NNLO corrections.

Conceptually, instead of the collinear approach, for jets produced in the central rapidity region (at very small x) a promising approach would be to use a *high-energy factorisation* scheme (often also referred as k_T -factorisation) [90, 139–141] together with the NLO central jet vertex calculated in Ref. [142]².

We suggest to compare BFKL theory predictions with data in a region where theoretical uncertainties related to other kind of physics are most possibly reduced. Therefore we propose to return to the original Mueller–Navelet idea, to study the inclusive production of two forward jets separated by a large rapidity gap, and to remove from the analysis those regions where jets are produced at central rapidities.

As a contribution to the assessment of this effect, in this Section we will study the Y -dependence of several azimuthal correlations and ratios among them, imposing an additional constraint, that the rapidity of a Mueller–Navelet jet cannot be smaller than a given value. Then we will compare this option with the case when the constraint is absent.

3.4.2 Phase-space constraints

In order to exclude events where, for a given Y , one of the two jets is produced in the central region, we need to slightly modify the definition of the

²For the discussion of different approaches to factorisation for dijet production see, *e.g.*, the recent review paper [143].

integrated coefficients given in Eq. (3.15) in the following way:

$$\begin{aligned}
 C_n &= \int_{y_{J_1}^{\min}}^{y_{J_1}^{\max}} dy_1 \int_{y_{J_2}^{\min}}^{y_{J_2}^{\max}} dy_2 \int_{k_{J_1}^{\min}}^{\infty} dk_{J_1} \int_{k_{J_2}^{\min}}^{\infty} dk_{J_2} \delta(y_{J_1} - y_{J_2} - Y) \\
 &\times \theta(|y_{J_1}| - y_{\max}^C) \theta(|y_{J_2}| - y_{\max}^C) c_n(y_{J_1}, y_{J_2}, k_{J_1}, k_{J_2}) .
 \end{aligned} \tag{3.16}$$

In Eq. (3.16), the two step-functions force the exclusion of jets whose rapidity is smaller than a cutoff value, given by y_{\max}^C , which delimits the central rapidity region (see Fig. 3.8 for a schematic view).

As for the values of y_{\max}^C , we will consider three cases: $y_{\max}^C = 0$, which means no exclusion from jets in the central region, as in all the numerical analyses so far; $y_{\max}^C = 1.5$, corresponding to a central region with size equal to about one third of the maximum possible rapidity span $Y = 9.4$ and $y_{\max}^C = 2.5$, a control value, to check the stability of our results.

Concerning the jet transverse momenta, differently from most previous analyses, we make the following five choices, which include *asymmetric* cuts:

1. $k_{J_1}^{\min} = 20 \text{ GeV}$, $k_{J_2}^{\min} = 20 \text{ GeV}$;
2. $k_{J_1}^{\min} = 20 \text{ GeV}$, $k_{J_2}^{\min} = 30 \text{ GeV}$;
3. $k_{J_1}^{\min} = 20 \text{ GeV}$, $k_{J_2}^{\min} = 35 \text{ GeV}$;
4. $k_{J_1}^{\min} = 20 \text{ GeV}$, $k_{J_2}^{\min} = 40 \text{ GeV}$;
5. $k_{J_1}^{\min} = 35 \text{ GeV}$, $k_{J_2}^{\min} = 35 \text{ GeV}$;

We will give the first phenomenological predictions for the ratios $R_{nm} \equiv C_n/C_m$ at center-of-mass energy $\sqrt{s} = 13 \text{ TeV}$, using the BLM scheme in its exact implementation (Eq. (3.7)). We will perform also some calculations with these approximate schemes (a) (Eq. (3.10)) and (b) (Eq. (3.12)), in order to get

an idea about the inaccuracy of our predictions coming from such approximate implementations of the BLM scale setting. Differently from Sections 3.2 and 3.3, all calculations are done in the MOM renormalisation scheme.

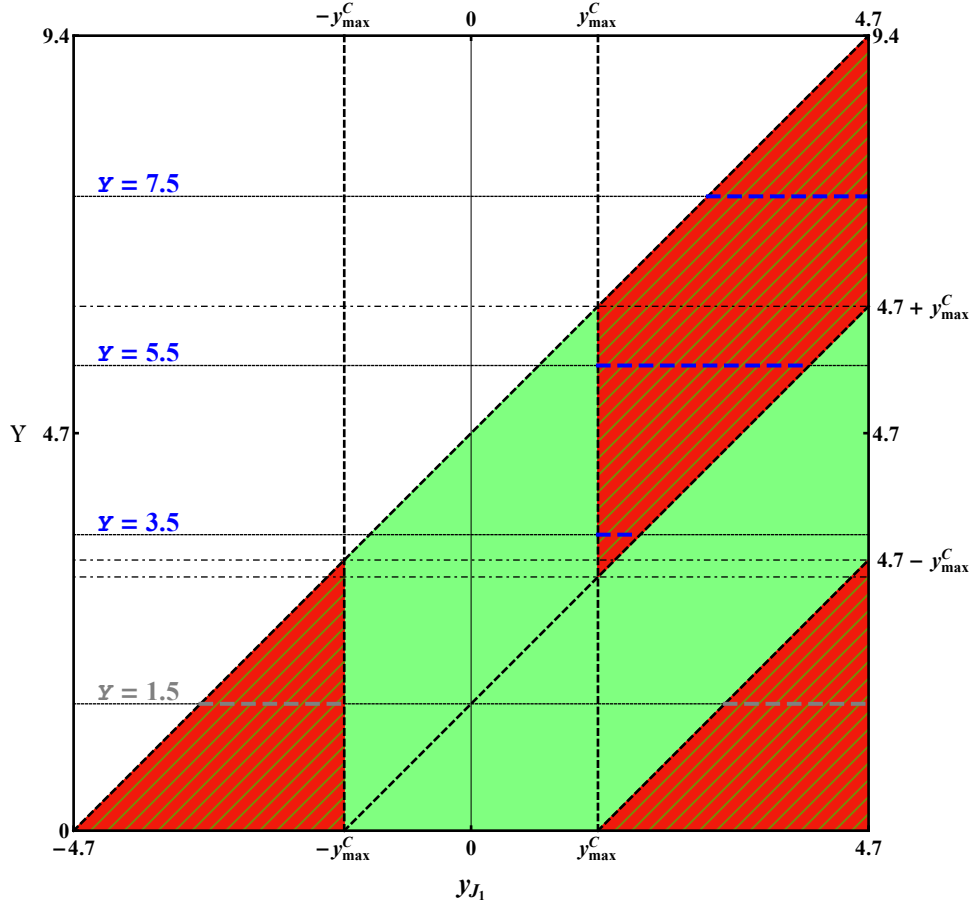


Figure 3.8: Central rapidity range exclusion in the (y_{J_1}, Y) phase-subspace for Mueller–Navelet jets. The green triangle represents the area bounded by the kinematical cuts on y_{J_1} and y_{J_2} , while the red striped area is the region allowed by imposing the constraint on the central rapidity $y_{J_{1,2}} \geq y_{\max}^C$. Finally, for any given value of Y , the y_{J_1} integration is done over the blue dashed segment.

3.4.3 Results and discussion

We summarise our results in Tables 3.4–3.10 and in Figs. 3.9–3.15. From Table 3.4 (and Fig. 3.9) we can see that the different variants of implementation

of the BLM method give predictions which deviate at the level of ~ 10 for C_0 and at the level of ~ 5 for R_{10} , while they basically agree within errors for all other ratios R_{nm} . For this reason, all remaining Tables (and Figures) refer to the “exact” BLM case only. Table 3.5 (and Fig. 3.10) show, quite reasonably, that for all choices of the cuts on jet transverse momenta, the larger is y_{\max}^C , the lower is the total cross section C_0 , up the value of Y is reached where the presence of cut of the central rapidity region becomes ineffective. All remaining Tables (and Figures) unanimously show that all ratios R_{nm} remain unaffected by the cut on the central rapidity region, over the entire region of values of Y . This is obvious for the values of Y large enough to be insensitive to the very presence of a non-zero y_{\max}^C , but it is unexpectedly true also for the lower values of Y .

The latter point means that in our approach, *i.e.* NLA BFKL with BLM optimisation, the cut on jet central rapidities leads to a proportional reduction of both the total cross section, C_0 , and the other coefficients C_1, C_2, C_3 , which parameterise the azimuthal angle distribution. In other words in our approach, the central cut only reduces the value of the total cross section, but does not affect the azimuthal angle distribution of dijets. It would be very interesting to study whether such feature remains true also in other approaches, both within the BFKL approach, but using different ideæ about the inclusion of the physics beyond NLA, and also in other, non-BFKL schemes, like fixed-order DGLAP or approaches using k_T -factorisation [90, 139–141] for the central jet production.

Table 3.4: C_0 [nb] and ratios C_n/C_m for $k_{J_1}^{\min} = k_{J_2}^{\min} = 20$ GeV, $y_{\max}^C = 2.5$, $\sqrt{s} = 13$ TeV, and for the three variants of the BLM method (see Fig. 3.9).

	Y	BLM _a	BLM _b	BLM _{exact}
C_0	5.5	1353.2(5.6)	1413.2(3.2)	1318(16)
	6.5	1778(23)	1877(13)	1720(49)
	7.5	834.6(2.8)	893.7(2.0)	803.4(6.6)
	8.5	140.06(25)	152.03(18)	133.91(78)
	9.0	32.97(10)	36.16(12)	31.46(20)
C_1/C_0	5.5	0.7641(68)	0.7434(37)	0.775(19)
	6.5	0.674(17)	0.6546(87)	0.686(37)
	7.5	0.6005(44)	0.5775(22)	0.6104(99)
	8.5	0.5339(19)	0.5092(11)	0.5422(64)
	9.0	0.5091(27)	0.4823(23)	0.5174(65)
C_2/C_0	5.5	0.4371(52)	0.4315(29)	0.450(18)
	6.5	0.336(11)	0.3357(53)	0.3329(19)
	7.5	0.2638(27)	0.2625(13)	0.2611(35)
	8.5	0.2052(11)	0.20452(59)	0.1939(49)
	9.0	0.1835(14)	0.1827(11)	0.1674(14)
C_3/C_0	5.5	0.2761(45)	0.2691(26)	0.3019(68)
	6.5	0.1934(74)	0.1907(37)	0.210(18)
	7.5	0.1383(20)	0.13708(80)	0.144(29)
	8.5	0.09796(70)	0.09765(31)	0.095(17)
	9.0	0.08378(90)	0.08361(63)	0.0775(13)
C_2/C_1	5.5	0.5721(71)	0.5804(42)	0.580(24)
	6.5	0.499(15)	0.5128(76)	0.484(27)
	7.5	0.4393(47)	0.4546(19)	0.4278(55)
	8.5	0.3844(21)	0.4017(11)	0.3576(91)
	9.0	0.3605(23)	0.3788(19)	0.3236(27)
C_3/C_2	5.5	0.632(13)	0.6236(74)	0.671(26)
	6.5	0.575(25)	0.568(12)	0.634(55)
	7.5	0.5241(93)	0.5221(32)	0.5509(92)
	8.5	0.4773(41)	0.4775(18)	0.492(16)
	9.0	0.4565(55)	0.4577(29)	0.4627(59)

Table 3.5: Values of C_0 [nb] from the exact BLM method (Eq. 3.7) at $\sqrt{s} = 13$ TeV, for all choices of the cuts on jet transverse momenta and of the central rapidity region (see Fig. 3.10).

$k_{J_1}^{\min}$	$k_{J_2}^{\min}$	Y	$y_{\max}^C = 0$	$y_{\max}^C = 1.5$	$y_{\max}^C = 2.5$
20 GeV	20 GeV	3.5	46100(950)	5498(110)	-
		4.5	20410(290)	8200(130)	-
		5.5	8270(130)	6120(110)	1318(16)
		6.5	2902(31)	2902(31)	1720(49)
		7.5	803.4(6.6)	803.4(6.6)	803.4(6.6)
		8.5	133.91(78)	133.91(78)	133.91(78)
		9.0	31.46(20)	31.46(20)	31.46(20)
20 GeV	30 GeV	3.5	15000(270)	1842(27)	-
		4.5	6734(73)	2779(33)	-
		5.5	2701(51)	2030(34)	442.3(3.4)
		6.5	919.8(9.2)	919.8(9.2)	555(13)
		7.5	240.8(1.6)	240.8(1.6)	240.8(1.6)
		8.5	36.44(13)	36.44(13)	36.44(13)
		9.0	7.801(53)	7.801(53)	7.801(53)
20 GeV	35 GeV	3.5	8090(160)	1050(20)	-
		4.5	3793(54)	1598(21)	-
		5.5	1534(26)	1169(16)	256.0(2.1)
		6.5	520.6(6.2)	520.6(6.2)	318.5(6.9)
		7.5	134.2(1.1)	134.2(1.1)	134.2(1.1)
		8.5	19.422(98)	19.422(98)	19.422(98)
		9.0	3.9601(23)	3.9601(23)	3.9601(23)
20 GeV	40 GeV	3.5	4627(86)	595.3(7.3)	-
		4.5	2137(31)	912(10)	-
		5.5	872(13)	668(10)	146.68(94)
		6.5	295.4(2.7)	295.4(2.7)	181.6(4.1)
		7.5	74.75(37)	74.75(37)	74.75(37)
		8.5	10.362(30)	10.362(30)	10.362(30)
		9.0	1.9980(45)	1.9980(45)	1.9980(45)
35 GeV	35 GeV	3.5	4286(36)	544.7(6.0)	-
		4.5	1618(13)	690.9(3.3)	-
		5.5	555.2(4.1)	429.0(3.6)	94.48(13)
		6.5	161.8(1.2)	161.8(1.2)	101.5(1.1)
		7.5	35.70(16)	35.70(16)	35.70(16)
		8.5	4.2843(98)	4.2843(98)	4.2843(98)
		9.0	0.7579(23)	0.7579(23)	0.7579(23)

3.4. Central rapidity range exclusion

Table 3.6: Values of C_1/C_0 from the exact BLM method (Eq. 3.7) at $\sqrt{s} = 13$ TeV, for all choices of the cuts on jet transverse momenta and of the central rapidity region (see Fig. 3.11).

$k_{J_1}^{\min}$	$k_{J_2}^{\min}$	Y	$y_{\max}^C = 0$	$y_{\max}^C = 1.5$	$y_{\max}^C = 2.5$
20 GeV	20 GeV	3.5	0.988(37)	0.975(35)	-
		4.5	0.885(25)	0.874(27)	-
		5.5	0.785(25)	0.778(31)	0.775(19)
		6.5	0.692(18)	0.692(18)	0.686(37)
		7.5	0.6104(99)	0.6104(99)	0.6104(99)
		8.5	0.5423(64)	0.5423(64)	0.5423(64)
		9.0	0.5174(64)	0.5174(64)	0.5174(64)
20 GeV	30 GeV	3.5	1.004(31)	0.989(28)	-
		4.5	0.896(18)	0.886(20)	-
		5.5	0.799(27)	0.792(27)	0.783(10)
		6.5	0.710(13)	0.710(13)	0.702(33)
		7.5	0.6321(83)	0.6321(83)	0.6321(83)
		8.5	0.5717(45)	0.5717(45)	0.5717(45)
		9.0	0.5543(70)	0.5543(70)	0.5543(70)
20 GeV	35 GeV	3.5	1.051(37)	1.005(33)	-
		4.5	0.907(24)	0.892(24)	-
		5.5	0.803(28)	0.795(22)	0.788(13)
		6.5	0.712(16)	0.712(16)	0.704(31)
		7.5	0.636(10)	0.636(10)	0.636(10)
		8.5	0.5803(56)	0.5803(56)	0.5803(56)
		9.0	0.5679(74)	0.5679(74)	0.5679(74)
20 GeV	40 GeV	3.5	1.043(35)	1.021(22)	-
		4.5	0.916(25)	0.899(20)	-
		5.5	0.808(22)	0.798(24)	0.791(10)
		6.5	0.714(12)	0.714(12)	0.705(31)
		7.5	0.6383(64)	0.6383(64)	0.6383(64)
		8.5	0.5875(35)	0.5875(35)	0.5875(35)
		9.0	0.5804(25)	0.5804(25)	0.5804(25)
35 GeV	35 GeV	3.5	0.963(16)	0.952(18)	-
		4.5	0.883(14)	0.8722(82)	-
		5.5	0.798(13)	0.792(12)	0.7866(22)
		6.5	0.718(11)	0.718(11)	0.709(16)
		7.5	0.6478(53)	0.6478(53)	0.6478(53)
		8.5	0.5972(26)	0.5972(26)	0.5972(26)
		9.0	0.5886(33)	0.5886(33)	0.5886(33)

Table 3.7: Values of C_2/C_0 from the exact BLM method (Eq. 3.7) at $\sqrt{s} = 13$ TeV, for all choices of the cuts on jet transverse momenta and of the central rapidity region (see Fig. 3.12).

$k_{J_1}^{\min}$	$k_{J_2}^{\min}$	Y	$y_{\max}^C = 0$	$y_{\max}^C = 1.5$	$y_{\max}^C = 2.5$
20 GeV	20 GeV	3.5	0.749(25)	0.730(30)	-
		4.5	0.594(23)	0.581(24)	-
		5.5	0.458(13)	0.454(27)	0.450(18)
		6.5	0.350(13)	0.350(13)	0.332(19)
		7.5	0.2611(35)	0.2611(35)	0.2611(35)
		8.5	0.1939(49)	0.1939(49)	0.1939(49)
		9.0	0.1674(14)	0.1674(14)	0.1674(14)
20 GeV	30 GeV	3.5	0.727(27)	0.719(26)	-
		4.5	0.575(15)	0.565(17)	-
		5.5	0.450(20)	0.443(21)	0.4398(98)
		6.5	0.3483(94)	0.3483(94)	0.343(24)
		7.5	0.2683(53)	0.2683(53)	0.2683(53)
		8.5	0.2083(30)	0.2083(30)	0.2083(30)
		9.0	0.1872(39)	0.1872(39)	0.1872(39)
20 GeV	35 GeV	3.5	0.750(22)	0.714(29)	-
		4.5	0.563(20)	0.555(20)	-
		5.5	0.435(11)	0.430(17)	0.4268(40)
		6.5	0.337(12)	0.337(12)	0.331(20)
		7.5	0.2602(32)	0.2602(32)	0.2602(32)
		8.5	0.2059(37)	0.2059(37)	0.2059(37)
		9.0	0.1874(15)	0.1874(15)	0.1874(15)
20 GeV	40 GeV	3.5	0.727(21)	0.710(19)	-
		4.5	0.560(17)	0.546(16)	-
		5.5	0.4225(99)	0.420(20)	0.4158(75)
		6.5	0.3276(91)	0.3276(91)	0.321(23)
		7.5	0.2528(22)	0.2528(22)	0.2528(22)
		8.5	0.2021(26)	0.2021(26)	0.2021(26)
		9.0	0.18712(7)	0.18712(7)	0.18712(7)
35 GeV	35 GeV	3.5	0.778(16)	0.766(16)	-
		4.5	0.642(12)	0.6321(85)	-
		5.5	0.5260(94)	0.510(12)	0.5051(20)
		6.5	0.4038(86)	0.4038(86)	0.398(13)
		7.5	0.3109(45)	0.3109(45)	0.3109(45)
		8.5	0.2379(25)	0.2379(25)	0.2379(25)
		9.0	0.2112(37)	0.2112(37)	0.2112(37)

3.4. Central rapidity range exclusion

Table 3.8: Values of C_3/C_0 from the exact BLM method (Eq. 3.7) at $\sqrt{s} = 13$ TeV, for all choices of the cuts on jet transverse momenta and of the central rapidity region (see Fig. 3.13).

$k_{J_1}^{\min}$	$k_{J_2}^{\min}$	Y	$y_{\max}^C = 0$	$y_{\max}^C = 1.5$	$y_{\max}^C = 2.5$
20 GeV	20 GeV	3.5	0.593(22)	0.577(19)	-
		4.5	0.432(13)	0.425(14)	-
		5.5	0.308(12)	0.305(15)	0.3019(68)
		6.5	0.2139(67)	0.2139(67)	0.210(18)
		7.5	0.1439(29)	0.1439(29)	0.1439(29)
		8.5	0.0954(17)	0.0954(17)	0.0954(17)
		9.0	0.0775(13)	0.0775(13)	0.0775(13)
20 GeV	30 GeV	3.5	0.551(26)	0.544(14)	-
		4.5	0.3950(88)	0.3896(97)	-
		5.5	0.281(13)	0.278(12)	0.276(3)
		6.5	0.1973(48)	0.1973(48)	0.194(14)
		7.5	0.1389(49)	0.1389(49)	0.1389(49)
		8.5	0.0944(13)	0.0944(13)	0.0944(13)
		9.0	0.0795(25)	0.0795(25)	0.0795(25)
20 GeV	35 GeV	3.5	0.555(19)	0.528(15)	-
		4.5	0.377(11)	0.3724(94)	-
		5.5	0.2652(90)	0.263(10)	0.2599(30)
		6.5	0.1842(48)	0.1842(48)	0.184(11)
		7.5	0.1272(24)	0.1272(24)	0.1272(24)
		8.5	0.0888(11)	0.0888(11)	0.0888(11)
		9.0	0.0756(12)	0.0756(12)	0.0756(12)
20 GeV	40 GeV	3.5	0.529(18)	0.520(21)	-
		4.5	0.364(10)	0.3585(79)	-
		5.5	0.2496(80)	0.249(11)	0.2400(40)
		6.5	0.1717(41)	0.1717(41)	0.171(13)
		7.5	0.1188(18)	0.1188(18)	0.1188(18)
		8.5	0.0836(66)	0.0836(66)	0.0836(66)
		9.0	0.0720(52)	0.0720(52)	0.0720(52)
35 GeV	35 GeV	3.5	0.6478(76)	0.6360(95)	-
		4.5	0.4983(75)	0.4887(40)	-
		5.5	0.3690(55)	0.3652(69)	0.3613(84)
		6.5	0.2648(47)	0.2648(47)	0.2596(93)
		7.5	0.1838(17)	0.1838(17)	0.1838(17)
		8.5	0.1257(16)	0.1257(16)	0.1257(16)
		9.0	0.1043(12)	0.1043(12)	0.1043(12)

Table 3.9: Values of C_2/C_1 from the exact BLM method (Eq. 3.7) at $\sqrt{s} = 13$ TeV, for all choices of the cuts on jet transverse momenta and of the central rapidity region (see Fig. 3.14).

$k_{J_1}^{\min}$	$k_{J_2}^{\min}$	Y	$y_{\max}^C = 0$	$y_{\max}^C = 1.5$	$y_{\max}^C = 2.5$
20 GeV	20 GeV	3.5	0.759(21)	0.749(28)	-
		4.5	0.671(26)	0.665(28)	-
		5.5	0.583(17)	0.583(37)	0.580(24)
		6.5	0.506(21)	0.506(21)	0.484(27)
		7.5	0.4278(55)	0.4278(55)	0.4278(55)
		8.5	0.3576(91)	0.3576(91)	0.3576(91)
		9.0	0.3236(27)	0.3236(27)	0.3236(27)
20 GeV	30 GeV	3.5	0.724(23)	0.727(25)	-
		4.5	0.642(15)	0.638(18)	-
		5.5	0.563(23)	0.559(27)	0.561(11)
		6.5	0.491(13)	0.491(13)	0.489(34)
		7.5	0.4245(83)	0.4245(83)	0.4245(83)
		8.5	0.3644(54)	0.3644(54)	0.3644(54)
		9.0	0.3377(67)	0.3377(67)	0.3377(67)
20 GeV	35 GeV	3.5	0.713(19)	0.710(24)	-
		4.5	0.622(21)	0.623(22)	-
		5.5	0.542(14)	0.542(22)	0.5414(50)
		6.5	0.473(17)	0.473(17)	0.470(29)
		7.5	0.4095(50)	0.4095(50)	0.4095(50)
		8.5	0.3548(63)	0.3548(63)	0.3548(63)
		9.0	0.3299(31)	0.3299(31)	0.3299(31)
20 GeV	40 GeV	3.5	0.697(18)	0.695(16)	-
		4.5	0.612(17)	0.607(17)	-
		5.5	0.523(10)	0.526(24)	0.5256(96)
		6.5	0.459(12)	0.459(12)	0.455(33)
		7.5	0.3960(33)	0.3960(33)	0.3960(33)
		8.5	0.3441(45)	0.3441(45)	0.3441(45)
		9.0	0.3224(12)	0.3224(12)	0.3224(12)
35 GeV	35 GeV	3.5	0.809(16)	0.805(14)	-
		4.5	0.728(14)	0.7247(98)	-
		5.5	0.659(13)	0.644(14)	0.6421(27)
		6.5	0.562(12)	0.563(12)	0.561(19)
		7.5	0.4799(67)	0.4799(67)	0.4799(67)
		8.5	0.3984(40)	0.3984(40)	0.3984(40)
		9.0	0.3588(61)	0.3588(61)	0.3588(61)

3.4. Central rapidity range exclusion

Table 3.10: Values of C_3/C_2 from the exact BLM method (Eq. 3.7) at $\sqrt{s} = 13$ TeV, for all choices of the cuts on jet transverse momenta and of the central rapidity region (see Fig. 3.15).

$k_{J_1}^{\min}$	$k_{J_2}^{\min}$	Y	$y_{\max}^C = 0$	$y_{\max}^C = 1.5$	$y_{\max}^C = 2.5$
20 GeV	20 GeV	3.5	0.792(22)	0.790(26)	-
		4.5	0.727(30)	0.731(32)	-
		5.5	0.673(24)	0.672(49)	0.671(26)
		6.5	0.611(28)	0.611(28)	0.634(55)
		7.5	0.5509(92)	0.5509(92)	0.5509(92)
		8.5	0.492(16)	0.492(16)	0.492(16)
		9.0	0.4627(59)	0.4627(59)	0.4627(59)
20 GeV	30 GeV	3.5	0.758(37)	0.756(23)	-
		4.5	0.687(18)	0.689(22)	-
		5.5	0.625(32)	0.629(36)	0.628(11)
		6.5	0.566(18)	0.567(18)	0.566(54)
		7.5	0.518(22)	0.518(22)	0.518(22)
		8.5	0.4530(93)	0.4530(93)	0.4530(93)
		9.0	0.424(17)	0.424(17)	0.424(17)
20 GeV	35 GeV	3.5	0.741(19)	0.740(23)	-
		4.5	0.670(24)	0.671(23)	-
		5.5	0.609(15)	0.610(32)	0.6090(25)
		6.5	0.547(21)	0.547(21)	0.555(43)
		7.5	0.4887(75)	0.4887(75)	0.4887(75)
		8.5	0.4312(86)	0.4312(86)	0.4312(86)
		9.0	0.4033(50)	0.4033(50)	0.4033(50)
20 GeV	40 GeV	3.5	0.728(19)	0.732(32)	-
		4.5	0.650(18)	0.657(18)	-
		5.5	0.591(15)	0.592(34)	0.578(13)
		6.5	0.524(17)	0.524(17)	0.532(56)
		7.5	0.4700(63)	0.4700(63)	0.4700(63)
		8.5	0.4134(62)	0.4134(62)	0.4134(62)
		9.0	0.3850(25)	0.3850(25)	0.3850(25)
35 GeV	35 GeV	3.5	0.832(13)	0.830(11)	-
		4.5	0.776(14)	0.7731(94)	-
		5.5	0.701(13)	0.716(18)	0.7152(27)
		6.5	0.656(16)	0.656(16)	0.652(31)
		7.5	0.5912(88)	0.5912(88)	0.5912(88)
		8.5	0.5284(96)	0.5284(96)	0.5284(96)
		9.0	0.4939(11)	0.4939(11)	0.4939(11)

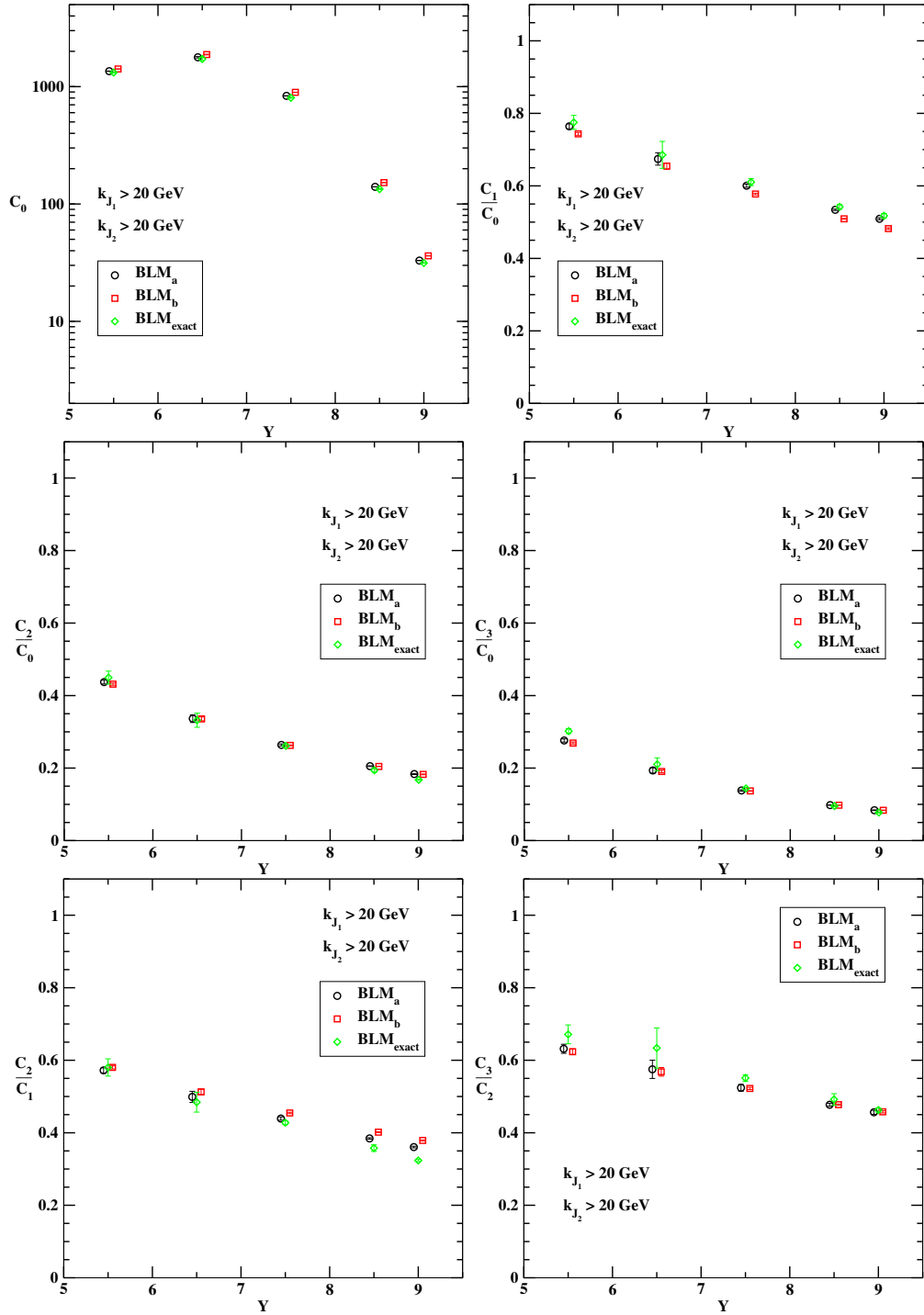


Figure 3.9: Y -dependence of C_0 and of several ratios C_m/C_n for $k_{J_1}^{\min} = k_{J_2}^{\min} = 20$ GeV, $|y_{J_1}| > 2.5$ and for $\sqrt{s} = 13$ TeV, from the three variants of the BLM method (data points have been slightly shifted along the horizontal axis for the sake of readability; see Table 3.4).

3.4. Central rapidity range exclusion

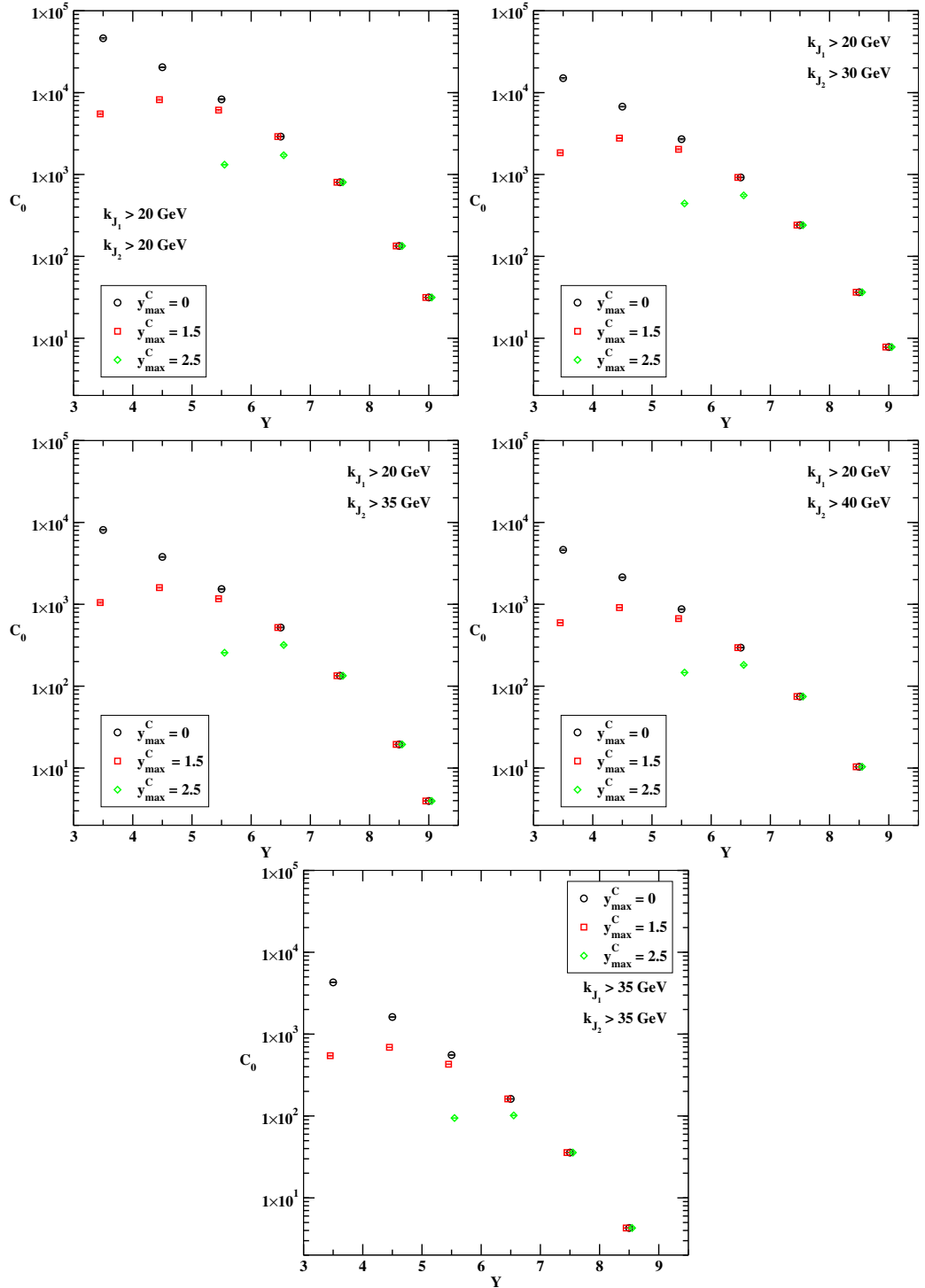


Figure 3.10: Y -dependence of C_0 from the exact BLM method (Eq. 3.7), for all choices of the cuts on jet transverse momenta and of the central rapidity region, and for $\sqrt{s} = 13$ TeV (data points have been slightly shifted along the horizontal axis for the sake of readability; see Table 3.5).

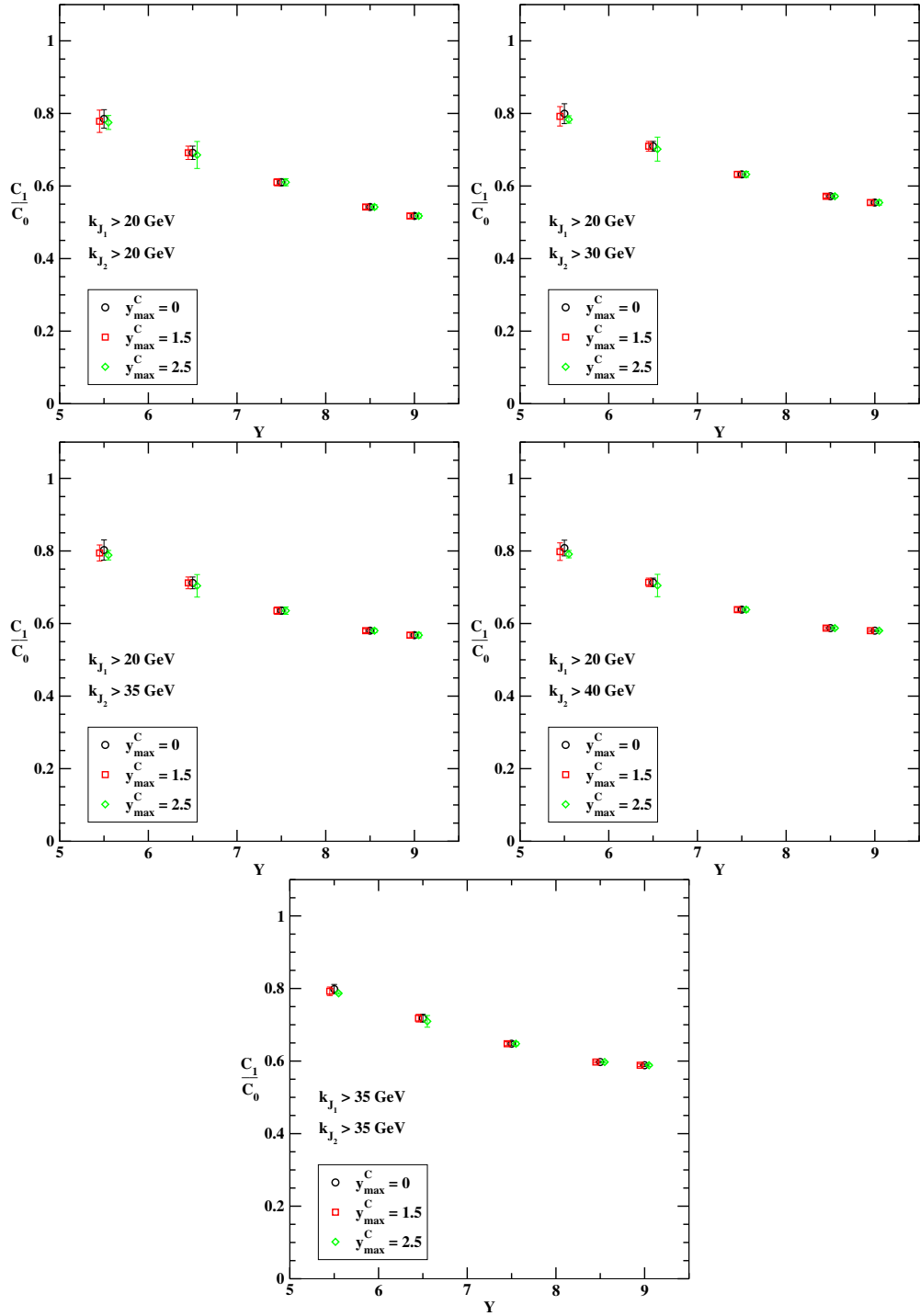


Figure 3.11: Y -dependence of C_1/C_0 from the exact BLM method (Eq. 3.7), for all choices of the cuts on jet transverse momenta and of the central rapidity region, and for $\sqrt{s} = 13$ TeV (data points have been slightly shifted along the horizontal axis for the sake of readability; see Table 3.6).

3.4. Central rapidity range exclusion

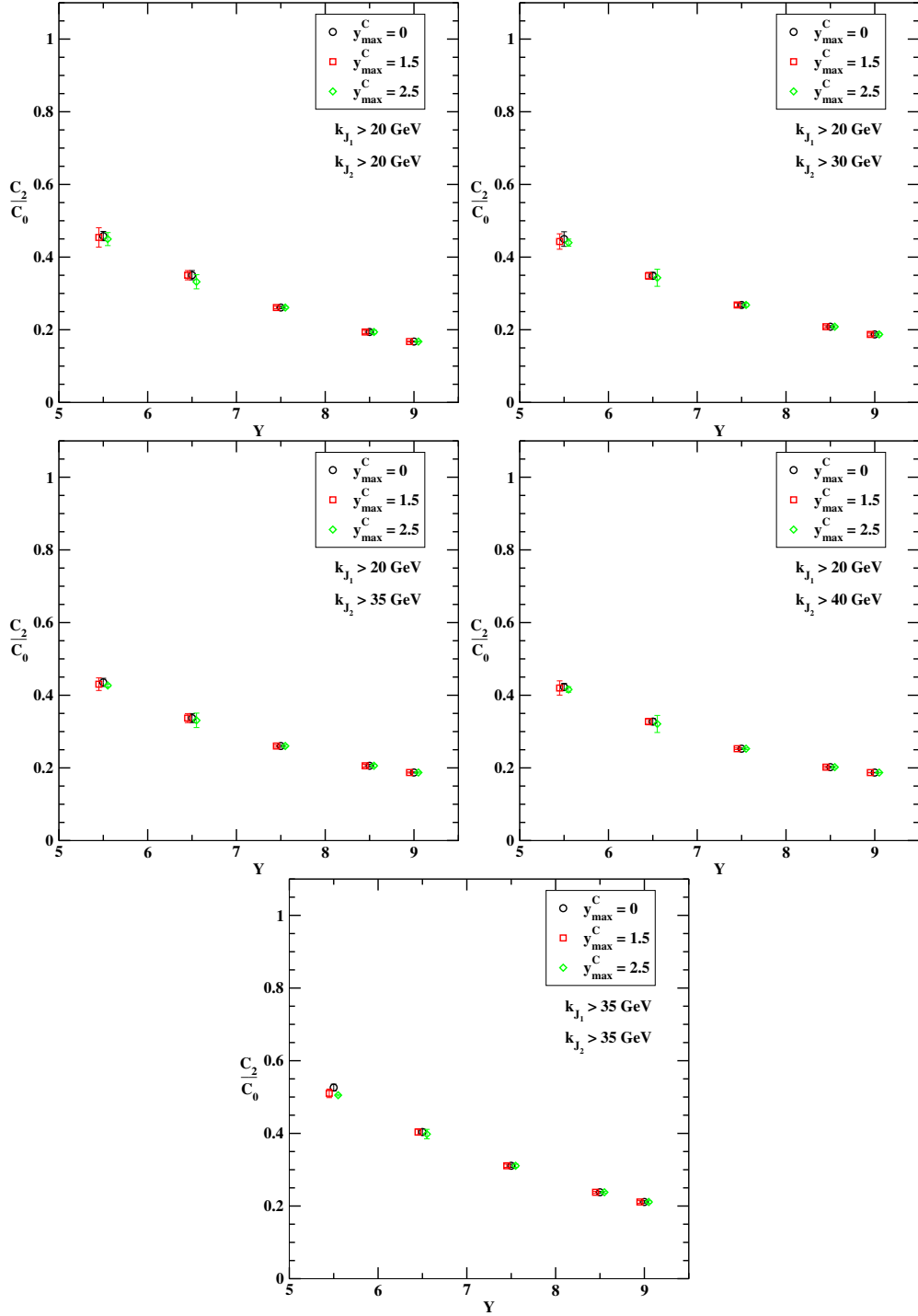


Figure 3.12: Y -dependence of C_2/C_0 from the exact BLM method (Eq. 3.7), for all choices of the cuts on jet transverse momenta and of the central rapidity region, and for $\sqrt{s} = 13$ TeV (data points have been slightly shifted along the horizontal axis for the sake of readability; see Table 3.7).

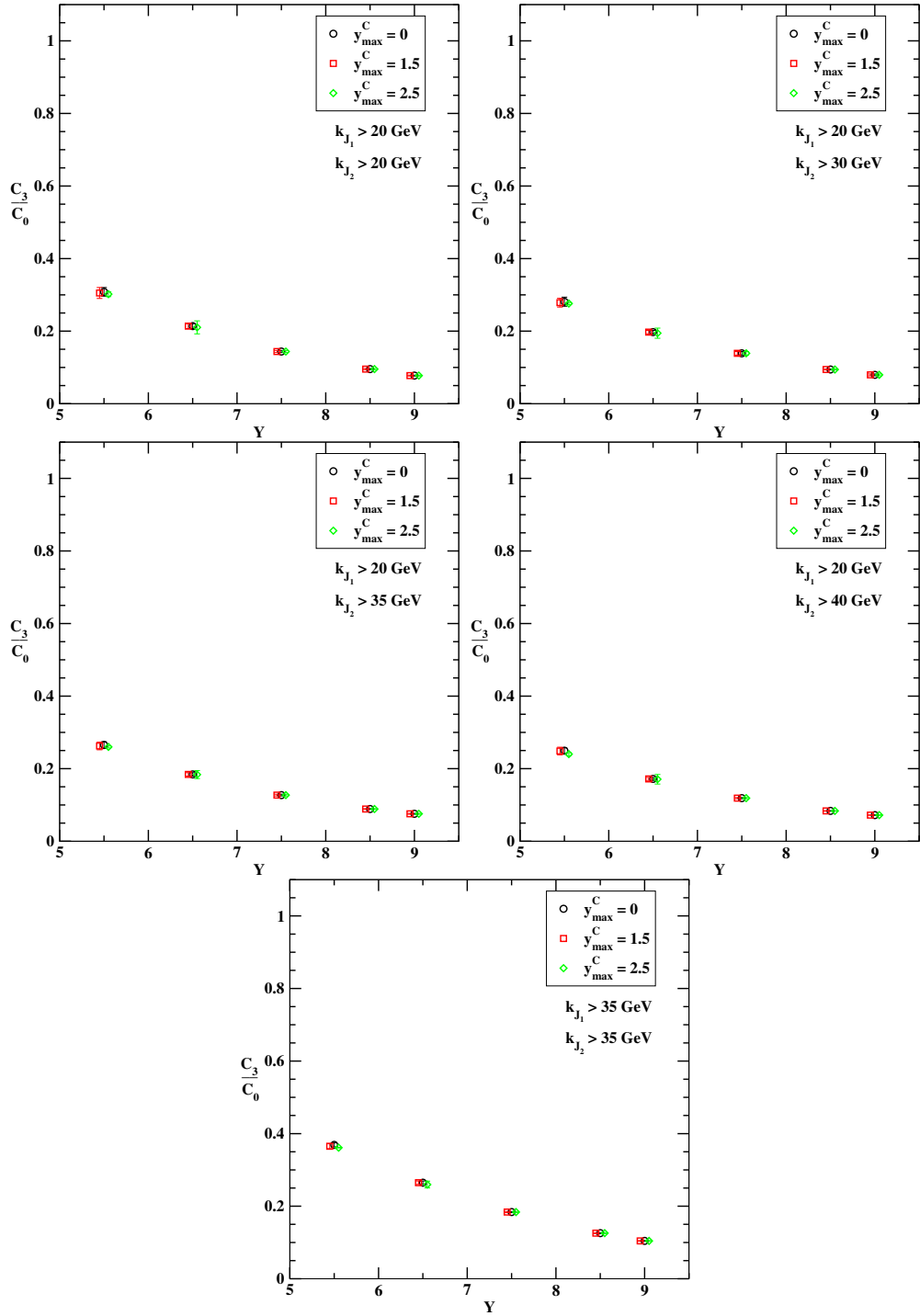


Figure 3.13: Y -dependence of C_3/C_0 from the exact BLM method (Eq. 3.7), for all choices of the cuts on jet transverse momenta and of the central rapidity region, and for $\sqrt{s} = 13$ TeV (data points have been slightly shifted along the horizontal axis for the sake of readability; see Table 3.8).

3.4. Central rapidity range exclusion

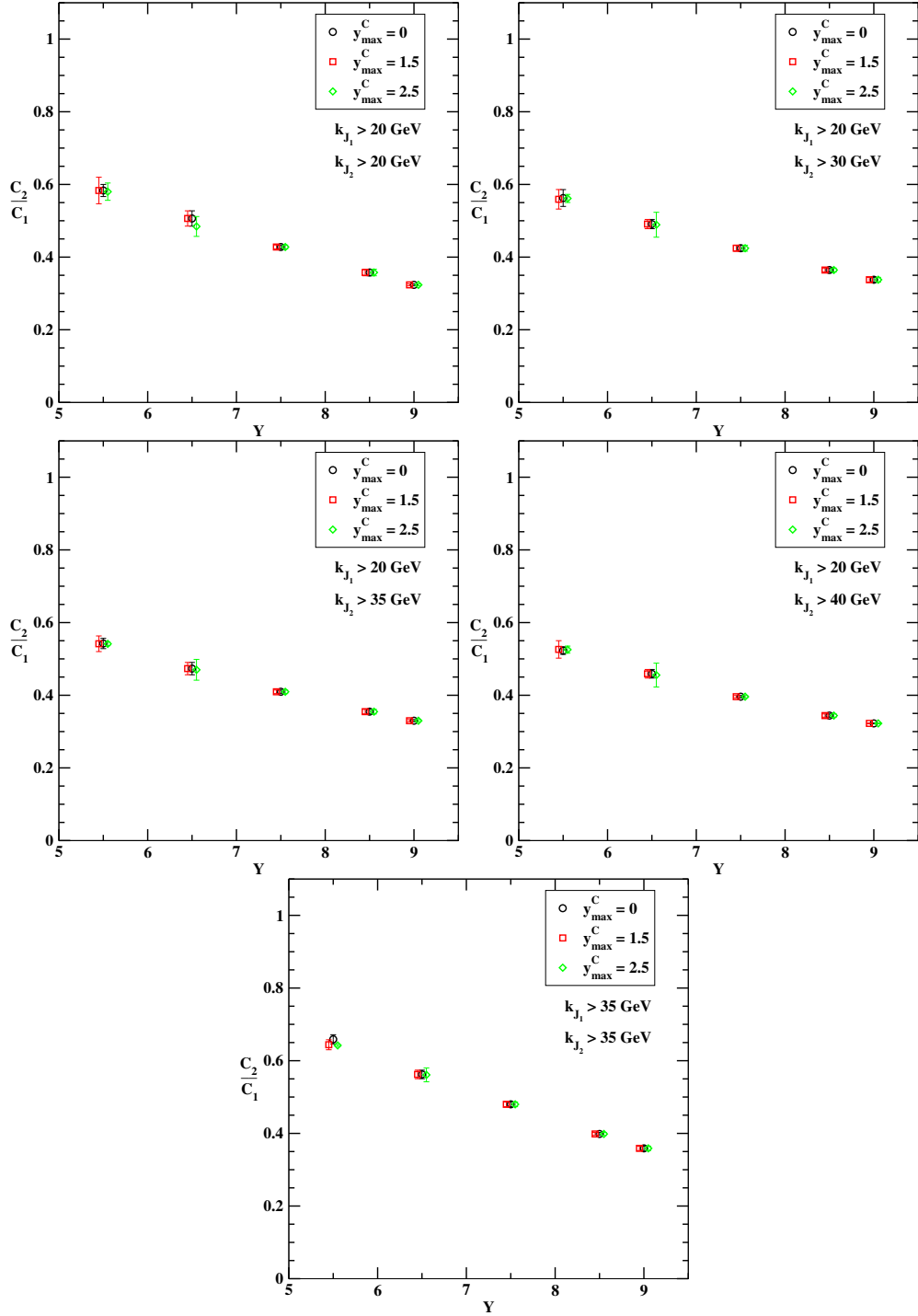


Figure 3.14: Y -dependence of C_2/C_1 from the exact BLM method (Eq. 3.7), for all choices of the cuts on jet transverse momenta and of the central rapidity region, and for $\sqrt{s} = 13$ TeV (data points have been slightly shifted along the horizontal axis for the sake of readability; see Table 3.9).

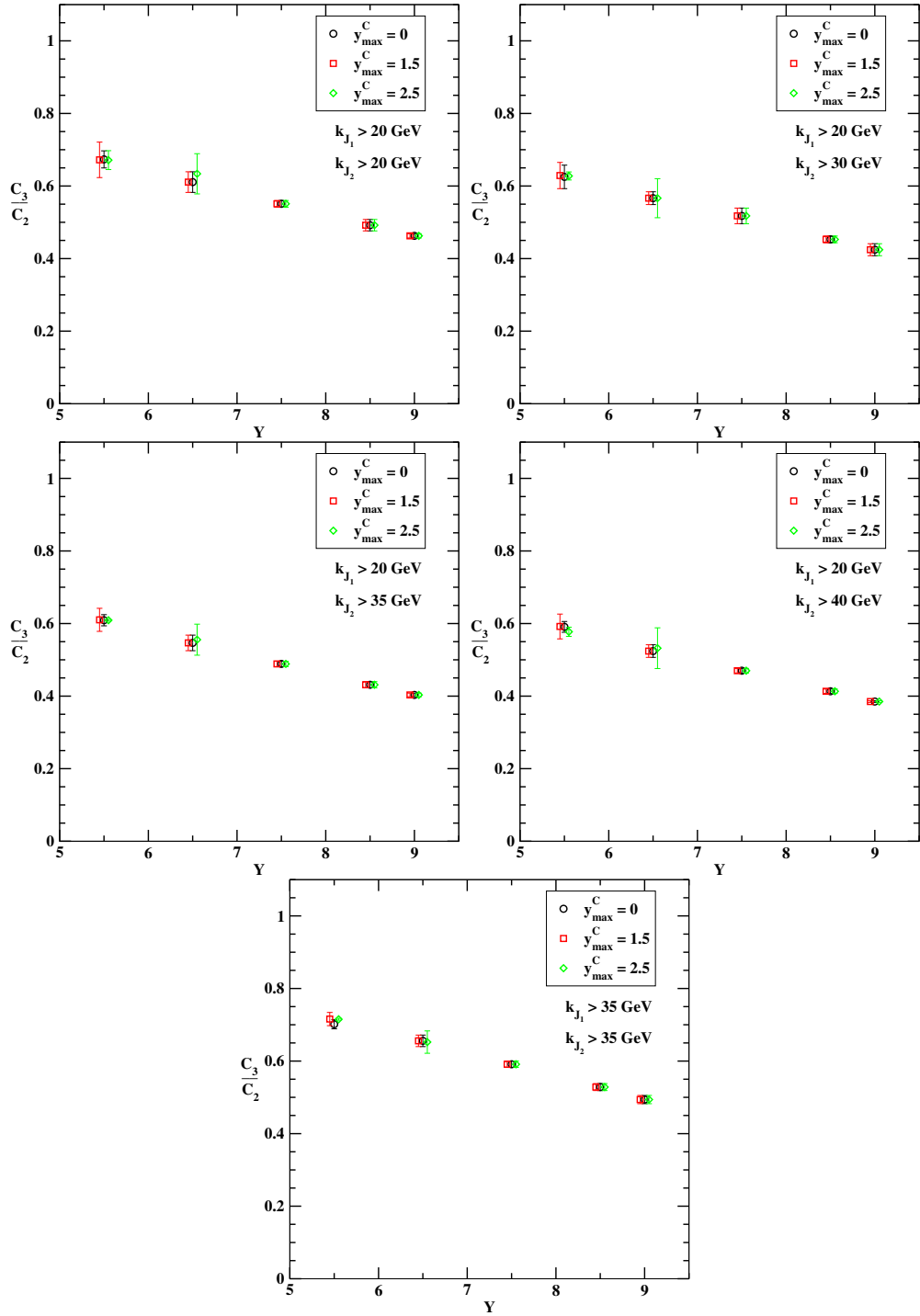


Figure 3.15: Y -dependence of C_3/C_2 from the exact BLM method (Eq. 3.7), for all choices of the cuts on jet transverse momenta and of the central rapidity region, and for $\sqrt{s} = 13$ TeV (data points have been slightly shifted along the horizontal axis for the sake of readability; see Table 3.10).

3.5 Numerical specifics

In this Section the numerical specifics for all the calculations done in Sections 3.3 and 3.4 are discussed.

3.5.1 Used tools

All numerical calculations were implemented in FORTRAN, using the corresponding interfaces for the NLO MSTW 2008 PDFs [144] and the two-loop running coupling with $\alpha_s(M_Z) = 0.11707$ with five quark flavours active. Now there exist updated PDF parameterisations, including the NLO MMHT 2014 set [145], which is the successor of the MSTW 2008 analysis. Here we continue to use MSTW 2008 PDFs because in our kinematical range the difference between MSTW 2008 and the updated MMHT 2014 PDFs is very small. Also, we want to keep the opportunity to compare our results at 13 TeV with our previous calculations at 7 TeV without introducing any other source of discrepancy related to the change of the PDF set. Numerical integrations and the computation of the polygamma functions were performed using specific CERN program libraries [146]. Furthermore, we used slightly modified versions of the Chyp [147] and Psi [148] routines in order to perform the calculation of the Gauss hypergeometric function ${}_2F_1$ and of the real part of the ψ function, respectively.

3.5.2 Uncertainty estimation

There are three main sources of uncertainty in our calculation:

- The first source of uncertainty is the numerical 4-dimensional integration over the variables $|\vec{k}_{J_1}|$, $|\vec{k}_{J_2}|$, y_{J_1} and ν and was directly estimated by Dadmul integration routine [146].

- The second one is the one-dimensional integration over the longitudinal momentum fraction ζ , entering the expression for the NLO impact factors $c_{1,2}^{(1)}(n, \nu, |\vec{k}_{J_{1,2}}|, x_{J_{1,2}})$ (see Appendix B). This integration was performed by using the `WGauss` routine [146]. At first, we fixed the best value of the input accuracy parameter `EPS` by making comparisons between separate `FORTRAN` and `MATHEMATICA` calculations of the impact factor. Then, we verified that, under variations by factors of 10 or 1/10 of the `EPS` parameter, the C_n^{BFKL} and C_n^{DGLAP} coefficients change by less than 1 permille.
- The third one is related to the upper cutoff in the integrations over $|\vec{k}_{J_1}|$, $|\vec{k}_{J_2}|$ and ν . We fixed $k_{J_1}^{\text{max}} = k_{J_2}^{\text{max}} = 60$ GeV as in Ref. [32], where it was shown that the contribution to the integration from the omitted region is negligible. Concerning the ν -integration, we fixed the upper cutoff $\nu^{\text{max}} = 30$ for the calculation of the C_n^{BFKL} coefficients, after verifying that a larger value does not change the result in appreciable way.

The C_n^{DGLAP} coefficients show a more pronounced sensitivity to ν^{max} , due to the fact that the oscillations in the integrand in Eqs. (3.11) and (3.13) are not dumped by the exponential factor as in the BFKL expressions (2.85) and (2.87). For the same reason, the computational time of C_n^{DGLAP} is much larger than for C_n^{BFKL} . We found that the best compromise was to set $\nu^{\text{max}} = 50$. We checked in some sample cases, mostly at $Y = 6$ and 9, that, putting ν^{max} at 60, ratios C_m/C_n change always less than 1%, in spite of the fact that the single coefficients C_n change in a more pronounced way.

Of the three main sources of uncertainty, the first one is, by far, the most significant, therefore the error bars of all data presented in this work are just those given by the `Dadmul` integration. We checked, however, using some trial

functions which mimic the behaviour of the true integrands involved in this work, that the error given by the Dadmul integration is a large overestimate of the true one. We are therefore confident that our error estimation is quite conservative.

3.6 Summary

In this Chapter we have considered the Mueller–Navelet jet production process at the LHC at the two values for center-of-mass energy of 7 TeV and 13 TeV and for several and distinct kinematical configurations for the transverse momenta of the detected jets.

First, we have shown how BFKL predictions [36] taken at $\sqrt{s} = 7$ TeV, for *symmetric* cuts for the transverse momenta ($k_{J_{1,2}\text{min}} = 35$ GeV) and with the renormalisation and the factorization scales optimised according to the BLM method, are in a very good agreement with experimental data [44]. Then, we have addressed some of the open questions raised in recent phenomenological works (see Section 3.2).

On one side [46], we compared predictions for several azimuthal correlations and ratios between them at $\sqrt{s} = 7$ TeV, both in full NLA BFKL approach and in fixed-order NLO DGLAP. Differently from current experimental analyses of the same process, we have used *asymmetric* cuts for the transverse momenta of the detected jets. In particular, taking one of the cuts at 35 GeV (as done by the CMS collaboration [44]) and the other at 45 GeV or 50 GeV, we can clearly see that predictions from BFKL and DGLAP become separate for most azimuthal correlations and ratios between them, this effect being more and more visible as the rapidity gap between the jets, Y , increases. In other words, in this kinematics the additional undetected parton radiation between the jets

which is present in the resummed BFKL series, in comparison to just one undetected parton allowed by the NLO DGLAP approach, makes its difference and leads to more azimuthal angle decorrelation between the jets, in full agreement with the original proposal of Mueller and Navelet. Another important benefit from the use of *asymmetric* cuts, pointed out in [35], is that the effect of violation of the energy-momentum conservation in the NLA is strongly suppressed with respect to what happens in the LLA. All these considerations persuade us to strongly suggest experimental collaborations to consider also *asymmetric* cuts in jet transverse momenta in all future analyses of Mueller–Navelet jet production process.

On the other side [47], we performed the first analysis at $\sqrt{s} = 13$ TeV, studying the jet azimuthal correlations in five different configurations for the jet transverse momenta, which include *asymmetric* cuts. Differently from all previous studies of the same kind, we considered in our analysis the effect of excluding the possibility that one of the two detected jets be produced in the central rapidity region. Central jets originate from small- x partons, and the collinear approach for the description of the Mueller–Navelet jet vertices may not hold at small x . The outcome of our analysis is that, for two reasonable ways to define the extension of the central region: (i) the total cross section, C_0 , is strongly reduced by the “exclusion cuts” in the range ($Y < 5.5$) where they are effective; (ii) on the other hand, in the same kinematics, the difference with respect to the case of no central rapidity exclusion is invisible in azimuthal correlations and in ratios between them. We believe that it would be very interesting to confront these conclusions with the forthcoming LHC analysis at 13 TeV.

As anticipated in Section 2.3.3, it would be interesting to figure out whether the growth with energy of the cross section, a characteristic feature of the BFKL

resummation, can be observed in the Mueller–Navelet jet reaction. First of all, the relevant observable for such investigation is the ϕ -averaged cross section \mathcal{C}_0 , which, however, is affected by theoretical ambiguities coming from the choice of the representation (see Section 2.3.3.1) and the scale setting procedure (see Section 2.4). The possible experimental measurement of \mathcal{C}_0 would be extremely helpful in discriminating among the several NLA-equivalent options. Even in case the theoretical ambiguities in the definition of \mathcal{C}_0 were cleared up, the search for the growth in the jet rapidity interval Y of the cross section and the subsequent extraction of the Pomeron intercept would be hindered by the fact that, due to collinear factorisation, the hadronic cross section embeds the parent proton PDFs which are responsible of its decrease for increasing Y . To switch off the role of PDFs and thus isolate the Y -dependence of the partonic cross section, one should select final-state configurations so as to keep x constant in the PDFs. The price for that, however, is a too restrictive choice of the ranges for the jet transverse momenta. Indeed, since the dependence of x on the rapidity is exponential (Eq. (3.6)), one should consider ranges for the transverse momenta which are much larger than the ones available at the present and forthcoming LHC energies. Furthermore, there is a principle difficulty in detecting at the LHC clear imprints of a genuine BFKL power asymptotic. As already stated at the end of Section 3.3.2, the limited number of undetected hard partons emitted with LHC kinematics makes BFKL hardly distinguishable from DGLAP when one goes from LLA to NLA, so that it is difficult to say something definite about the intercept. We can only compare our predictions for the cross section with data, to see whether our approach in its present status works or not. Although these issues affect also the other hadroproduction processes investigated in this thesis, dihadron production (see Chapter 4) has better chances to bring us closer to the Regge kinematics for partonic sub-

processes, due to the fact that hadrons can be detected at the LHC at much smaller transverse momenta than jets.

Appendix B

NLO impact factor for the small-cone forward jet

In this Appendix the expression for the NLO correction to the forward jet impact factor in the small-cone limit is given (see Ref. [31] for further details).

In the (ν, n) representation, we have:

$$\begin{aligned}
 c_1^{(1)}(n, \nu, |\vec{k}|, x) &= \frac{1}{\pi} \sqrt{\frac{C_F}{C_A}} \left(\vec{k}^2\right)^{i\nu-1/2} \int_x^1 \frac{d\zeta}{\zeta} \zeta^{-\bar{\alpha}_s(\mu_R)\chi(n, \nu)} \quad (\text{B.1}) \\
 &\left\{ \sum_{a=q, \bar{q}} f_a \left(\frac{x}{\zeta}\right) \left[\left(P_{qq}(\zeta) + \frac{C_A}{C_F} P_{gq}(\zeta) \right) \ln \frac{\vec{k}^2}{\mu_F^2} \right. \right. \\
 &- 2\zeta^{-2\gamma} \ln R \{ P_{qq}(\zeta) + P_{gq}(\zeta) \} - \frac{\beta_0}{2} \ln \frac{\vec{k}^2}{\mu_R^2} \delta(1-\zeta) \\
 &+ C_A \delta(1-\zeta) \left(\chi(n, \gamma) \ln \frac{s_0}{\vec{k}^2} + \frac{85}{18} + \frac{\pi^2}{2} \right. \\
 &\left. \left. + \frac{1}{2} \left(\psi' \left(1 + \gamma + \frac{n}{2} \right) - \psi' \left(\frac{n}{2} - \gamma \right) - \chi^2(n, \gamma) \right) \right) \right. \\
 &+ (1 + \zeta^2) \left\{ C_A \left(\frac{(1 + \zeta^{-2\gamma}) \chi(n, \gamma)}{2(1-\zeta)_+} - \zeta^{-2\gamma} \left(\frac{\ln(1-\zeta)}{1-\zeta} \right)_+ \right) \right. \\
 &\left. \left. + \left(C_F - \frac{C_A}{2} \right) \left[\frac{\bar{\zeta}}{\zeta^2} I_2 - \frac{2 \ln \zeta}{1-\zeta} + 2 \left(\frac{\ln(1-\zeta)}{1-\zeta} \right)_+ \right] \right\} \right. \\
 &\left. + \delta(1-\zeta) \left(C_F \left(3 \ln 2 - \frac{\pi^2}{3} - \frac{9}{2} \right) - \frac{5n_f}{9} \right) + C_A \zeta + C_F \bar{\zeta} \right\}
 \end{aligned}$$

$$\begin{aligned}
 & + \frac{1 + \bar{\zeta}^2}{\bar{\zeta}} \left(C_A \frac{\bar{\zeta}}{\bar{\zeta}} I_1 + 2C_A \ln \frac{\bar{\zeta}}{\bar{\zeta}} + C_F \zeta^{-2\gamma} (\chi(n, \gamma) - 2 \ln \bar{\zeta}) \right) \\
 & + f_g \left(\frac{\chi}{\bar{\zeta}} \right) \frac{C_A}{C_F} \left[\left(P_{gg}(\zeta) + 2n_f \frac{C_F}{C_A} P_{qg}(\zeta) \right) \ln \frac{\vec{k}^2}{\mu_F^2} \right. \\
 & \quad \left. - 2\zeta^{-2\gamma} \ln R (P_{gg}(\zeta) + 2n_f P_{qg}(\zeta)) - \frac{\beta_0}{2} \ln \frac{\vec{k}^2}{4\mu_R^2} \delta(1 - \zeta) \right. \\
 & \quad \left. + C_A \delta(1 - \zeta) \left(\chi(n, \gamma) \ln \frac{s_0}{\vec{k}^2} + \frac{1}{12} + \frac{\pi^2}{6} \right. \right. \\
 & \quad \left. \left. + \frac{1}{2} \left(\psi' \left(1 + \gamma + \frac{n}{2} \right) - \psi' \left(\frac{n}{2} - \gamma \right) - \chi^2(n, \gamma) \right) \right) \right. \\
 & \quad \left. + 2C_A (1 - \zeta^{-2\gamma}) \left(\left(\frac{1}{\bar{\zeta}} - 2 + \zeta \bar{\zeta} \right) \ln \bar{\zeta} + \frac{\ln(1 - \zeta)}{1 - \zeta} \right) \right. \\
 & \quad \left. + C_A \left[\frac{1}{\bar{\zeta}} + \frac{1}{(1 - \zeta)_+} - 2 + \zeta \bar{\zeta} \right] \left((1 + \zeta^{-2\gamma}) \chi(n, \gamma) - 2 \ln \zeta + \frac{\bar{\zeta}^2}{\zeta^2} I_2 \right) \right. \\
 & \quad \left. + n_f \left[2\zeta \bar{\zeta} \frac{C_F}{C_A} + (\zeta^2 + \bar{\zeta}^2) \left(\frac{C_F}{C_A} \chi(n, \gamma) + \frac{\bar{\zeta}}{\zeta} I_3 \right) - \frac{1}{12} \delta(1 - \zeta) \right] \right] \}.
 \end{aligned}$$

Here $\bar{\zeta} = 1 - \zeta$, $\gamma = i\nu - 1/2$, $P_{ij}(\zeta)$ are leading order DGLAP kernels defined as

$$\begin{aligned}
 P_{gq}(z) &= C_F \frac{1 + (1 - z)^2}{z}, \\
 P_{qg}(z) &= T_R [z^2 + (1 - z)^2], \\
 P_{qq}(z) &= C_F \left(\frac{1 + z^2}{1 - z} \right)_+ = C_F \left[\frac{1 + z^2}{(1 - z)_+} + \frac{3}{2} \delta(1 - z) \right], \\
 P_{gg}(z) &= 2C_A \left[\frac{1}{(1 - z)_+} + \frac{1}{z} - 2 + z(1 - z) \right] + \left(\frac{11}{6} C_A - \frac{n_f}{3} \right) \delta(1 - z),
 \end{aligned} \tag{B.2}$$

where C_F is the Casimir operator associated with gluon emission from a quark, $C_F = (N_c^2 - 1)/(2N_c)$ and $T_R = 1/2$ is the colour factor associated with the splitting of a gluon into a quark-antiquark pair. For the $I_{1,2,3}$ functions we have the results:

$$I_2 = \frac{\zeta^2}{\bar{\zeta}^2} \left[\zeta \left(\frac{{}_2F_1(1, 1 + \gamma - \frac{n}{2}, 2 + \gamma - \frac{n}{2}, \zeta)}{\frac{n}{2} - \gamma - 1} - \frac{{}_2F_1(1, 1 + \gamma + \frac{n}{2}, 2 + \gamma + \frac{n}{2}, \zeta)}{\frac{n}{2} + \gamma + 1} \right) \right]$$

$$\begin{aligned}
 & + \zeta^{-2\gamma} \left(\frac{{}_2F_1\left(1, -\gamma - \frac{n}{2}, 1 - \gamma - \frac{n}{2}, \zeta\right)}{\frac{n}{2} + \gamma} - \frac{{}_2F_1\left(1, -\gamma + \frac{n}{2}, 1 - \gamma + \frac{n}{2}, \zeta\right)}{\frac{n}{2} - \gamma} \right) \quad (\text{B.3}) \\
 & + \left(1 + \zeta^{-2\gamma}\right) \left(\chi(n, \gamma) - 2 \ln \bar{\zeta}\right) + 2 \ln \zeta \Big] ,
 \end{aligned}$$

$$I_1 = \frac{\bar{\zeta}}{2\bar{\zeta}} I_2 + \frac{\zeta}{\bar{\zeta}} \left[\ln \zeta + \frac{1 - \zeta^{-2\gamma}}{2} \left(\chi(n, \gamma) - 2 \ln \bar{\zeta}\right) \right] , \quad (\text{B.4})$$

$$I_3 = \frac{\bar{\zeta}}{2\bar{\zeta}} I_2 - \frac{\zeta}{\bar{\zeta}} \left[\ln \zeta + \frac{1 - \zeta^{-2\gamma}}{2} \left(\chi(n, \gamma) - 2 \ln \bar{\zeta}\right) \right] . \quad (\text{B.5})$$

In Eq. (B.1) the *plus-prescription* is introduced, which is defined as

$$\int_a^1 d\zeta \frac{F(\zeta)}{(1-\zeta)_+} = \int_a^1 d\zeta \frac{F(\zeta) - F(1)}{(1-\zeta)} - \int_0^a d\zeta \frac{F(1)}{(1-\zeta)} , \quad (\text{B.6})$$

for any function $F(\zeta)$, regular at $\zeta = 1$. Note that

$$\begin{aligned}
 (1-\zeta)^{2\epsilon-1} &= (1-\zeta)_+^{2\epsilon-1} + \frac{1}{2\epsilon} \delta(1-\zeta) \quad (\text{B.7}) \\
 &= \frac{1}{2\epsilon} \delta(1-\zeta) + \frac{1}{(1-\zeta)_+} + 2\epsilon \left(\frac{\ln(1-\zeta)}{1-\zeta} \right)_+ + \mathcal{O}(\epsilon^2) .
 \end{aligned}$$

The factor $\zeta^{-\bar{\alpha}_s(\mu_R)\chi(n,\gamma)}$ appears in Eq. (B.1) due to extra contributions attributed to the jet vertices, as discussed after Eq. (29) of Ref. [31].

Chapter 4

Dihadron production

In this Chapter the inclusive dihadron production

$$p(p_1) + p(p_2) \rightarrow h_1(k_1) + h_2(k_2) + X \quad (4.1)$$

is investigated, *i.e.* when the two charged light hadrons: $\pi^\pm, K^\pm, p, \bar{p}$ with high transverse momenta and separated by a large interval of rapidity, together with an undetected hadronic system X , are produced in the final state (see Fig. 4.1 for a schematic view).

This process is similar to the Mueller–Navelet jet production and shares with it the underlying theoretical framework, the only obvious difference lying in the vertices describing the dynamics in the proton fragmentation region: instead of the proton-to-jet vertex, the vertex for the proton to identified hadron transition is needed. Such a vertex was considered in [45] within NLA: it was shown there that ultraviolet divergences are taken care of by the renormalisation of the QCD coupling, soft and virtual infrared divergences cancel each other, whereas the surviving infrared collinear ones are compensated by the collinear counterterms related to the renormalisation of PDFs for the initial proton and FFs describing the detected hadron in the final state within collinear factorisation.¹ Hence, infrared-safe NLA predictions for observables

¹The identified hadron production vertex in the NLA was found within the *shockwave* ap-

related to this process are amenable, thus making this process an additional clear channel to test the BFKL dynamics at the LHC. The reaction (4.1) can be considered complementary to Mueller–Navelet jet production, since hadrons can be detected at the LHC at much smaller values of the transverse momentum than jets, thus giving access to a kinematical range outside the reach of the Mueller–Navelet channel.

This Chapter is organised as follows. In Section 4.1 we give the main formulae for cross section and azimuthal correlations (see Section 4.1.2), together with the BLM scale setting (see Section 4.1.4) and the final-state phase space integration (see Section 4.1.3). In Section 4.2 we present a comparison between full LLA and partial NLA BFKL predictions, *i.e.* considering just the NLO kernel corrections and taking the hadron vertices at LLA. Full NLA predictions at 7 and 13 TeV and considering various realistic LHC kinematical constraint are given in Section 4.3. Section 4.4 is devoted to the details on the numerical implementation, together with the study of the effects of using different PDF and FF parameterisations. The section Summary is drawn in Section 4.5.

The analysis given in this Chapter is based on the work done in Refs. [151, 152] and presented in Refs. [153–156].

proach (or *colour glass condensate* effective theory) in [149]. It was used there to study the single inclusive particle production at forward rapidities in proton-nucleus collisions; for recent developments of this line of research, see also [150]. Unfortunately, the comparison between the results of [149] and those of [45] is not simple and straightforward, since the distribution of radiative corrections between the kernel and the impact factor is different in the shockwave and the BFKL frameworks. Non-trivial kernel and impact factor transformations are required for such a comparison. It certainly deserves a separate study, and the consideration of the process (4.1) within both the shockwave and the BFKL resummation schemes seems the best possibility to this purpose.

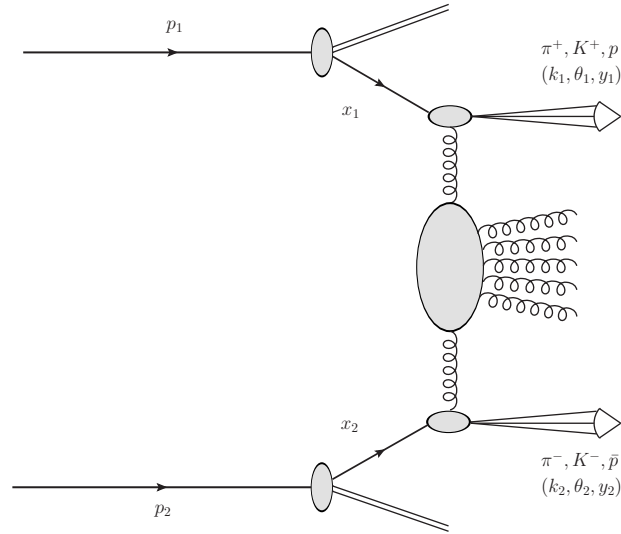


Figure 4.1: Inclusive dihadron production process in multi-Regge kinematics.

4.1 Theoretical framework

In this Section the BFKL cross section and the azimuthal corrections for the inclusive dihadron production process are presented.

4.1.1 Inclusive dihadron production

The process under investigation (see Eq. (4.1) and Fig. 4.1) is the inclusive production of a pair of identified hadrons featuring high transverse momenta, $\vec{k}_1^2 \sim \vec{k}_2^2 \gg \Lambda_{\text{QCD}}^2$ and separated by a large rapidity interval in high-energy proton-proton collisions. The protons' momenta p_1 and p_2 are taken as Sudakov vectors (see Eq. (2.10)) satisfying $p_1^2 = p_2^2 = 0$ and $2(p_1 p_2) = s$, so that the momentum of each hadron can be decomposed as

$$\begin{aligned} k_1 &= \alpha_1 p_1 + \frac{\vec{k}_1^2}{\alpha_1 s} p_2 + k_{1\perp}, & k_{1\perp}^2 &= -\vec{k}_1^2, \\ k_2 &= \alpha_2 p_2 + \frac{\vec{k}_2^2}{\alpha_2 s} p_1 + k_{2\perp}, & k_{2\perp}^2 &= -\vec{k}_2^2. \end{aligned} \quad (4.2)$$

In the center of mass system, the hadrons' longitudinal momentum frac-

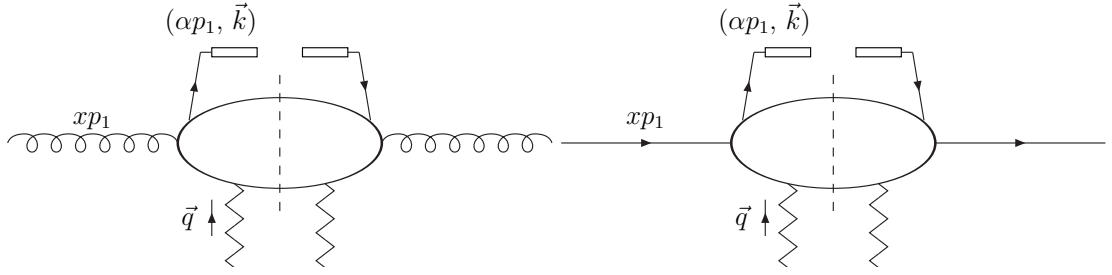


Figure 4.2: Schematic view of the the vertex for the identified hadron production for the case of incoming gluon (left) or quark (right). Here p_1 is the proton momentum, x is the fraction of proton momentum carried by the gluon/quark, $\alpha_h p_1$ is the longitudinal momentum of the hadron h , \vec{k}_h is the transverse hadron momentum and \vec{q} is the transverse momentum of the incoming Reggeised gluon.

tions $\alpha_{1,2}$ are connected to the respective rapidities through the relations $y_1 = \frac{1}{2} \ln \frac{\alpha_1^2 s}{k_1^2}$, and $y_2 = \frac{1}{2} \ln \frac{k_2^2}{\alpha_2^2 s}$, so that $dy_1 = \frac{d\alpha_1}{\alpha_1}$, $dy_2 = -\frac{d\alpha_2}{\alpha_2}$, and $Y = y_1 - y_2 = \ln \frac{\alpha_1 \alpha_2 s}{|\vec{k}_1| |\vec{k}_2|}$, here the space part of the four-vector $p_{1\parallel}$ being taken positive.

By studying Mueller–Navelet jets, we probed the BFKL dynamics through a very inclusive process. Now we require that a couple of hadrons is always identified in the final state, considering so a less inclusive final-state reaction. Following the course taken in the Mueller–Navelet case (see Section 3.1.1), we start from the NLO forward parton impact factors [20,21] (see Fig. 3.2). In order to allow the inclusive production of a given hadron, one of these integrations in the definition of parton impact factors is ‘opened’ (see Fig. 3.2). This means that the integration over the momentum of one of the intermediate-state partons is replaced by the convolution with a suitable FF. The expression for the identified-hadron impact factor with LO accuracy is given below (see Fig. 4.2):

$$\begin{aligned} \frac{d\Phi_h^{(0)}}{\vec{q}^2} &= 2\pi\alpha_s \sqrt{\frac{2C_F}{C_A}} \frac{d\alpha_h d^2\vec{k}}{\vec{k}^2} \int_{\alpha_h}^1 \frac{dx}{x} \delta^{(2)}(\vec{k} - \vec{q}) \\ &\times \left(\frac{C_A}{C_F} f_g(x) D_g^h\left(\frac{\alpha_h}{x}\right) + \sum_{a=q,\bar{q}} f_a(x) D_a^h\left(\frac{\alpha_h}{x}\right) \right), \end{aligned} \quad (4.3)$$

where D_a^h is the FF that describes non-perturbative, large-distance part of the transition from the parton a produced with momentum k and longitudinal fraction x to a hadron with momentum fraction α_h . As we did for the forward jet impact factor, the last step to do is to project Eq. (4.3) onto the eigenfunctions (Eq. (2.54)) of the LO BFKL kernel (2.53), *i.e.* transfer to the (ν, n) -representation (see Section 2.3.3). The expression for the LO forward jet vertex will be given in Eq. (4.7) of Section 4.1.4. In the NLO case, one-loop virtual corrections and two-body final-state contribution have to be considered. The expression of the hadron vertex with NLO accuracy was calculated in Ref. [45]. Its projection on the (ν, n) -space (see Section 2.3.3 for further details) is given in Eq. (4.9) and in Appendix C.

4.1.2 Dihadron cross section and azimuthal correlations

In QCD collinear factorisation the cross section of the process (4.1) reads

$$\frac{d\sigma}{d\alpha_1 d\alpha_2 d^2k_1 d^2k_2} = \sum_{r,s=q,\bar{q},g} \int_0^1 dx_1 \int_0^1 dx_2 f_r(x_1, \mu_F) f_s(x_2, \mu_F) \quad (4.4)$$

$$\times \frac{d\hat{\sigma}_{r,s}(\hat{s}, \mu_F)}{d\alpha_1 d\alpha_2 d^2k_1 d^2k_2},$$

where the r, s indices specify the parton types (quarks $q = u, d, s, c, b$; anti-quarks $\bar{q} = \bar{u}, \bar{d}, \bar{s}, \bar{c}, \bar{b}$; or gluon g), $f_r(x, \mu_F)$ denotes the initial proton PDFs; $x_{1,2}$ are the longitudinal fractions of the partons involved in the hard subprocess, while μ_F is the factorisation scale; $d\hat{\sigma}_{r,s}(\hat{s})$ is the partonic cross section and $x_1 x_2 s \equiv \hat{s}$ is the squared center-of-mass energy of the parton-parton collision subprocess.

In the BFKL approach the cross section can be presented (see Section 2.3.3 for the details of the derivation) as the Fourier sum of the azimuthal coefficients

\mathcal{C}_n , having so:

$$\frac{d\sigma}{dy_1 dy_2 d|\vec{k}_1| d|\vec{k}_2| d\phi_1 d\phi_2} = \frac{1}{(2\pi)^2} \left[\mathcal{C}_0 + \sum_{n=1}^{\infty} 2 \cos(n\phi) \mathcal{C}_n \right], \quad (4.5)$$

where $\phi = \phi_1 - \phi_2 - \pi$, with $\phi_{1,2}$ are the two hadrons' azimuthal angles, while $y_{1,2}$ and $\vec{k}_{1,2}$ are their rapidities and transverse momenta, respectively. The ϕ -averaged cross section \mathcal{C}_0 and the other coefficients $\mathcal{C}_{n \neq 0}$ are given by

$$\begin{aligned} \mathcal{C}_n &\equiv \int_0^{2\pi} d\phi_1 \int_0^{2\pi} d\phi_2 \cos[n(\phi_1 - \phi_2 - \pi)] \frac{d\sigma}{dy_1 dy_2 d|\vec{k}_1| d|\vec{k}_2| d\phi_1 d\phi_2} \quad (4.6) \\ &= \frac{e^Y}{s} \int_{-\infty}^{+\infty} d\nu \left(\frac{\alpha_1 \alpha_2 s}{s_0} \right)^{\bar{\alpha}_s(\mu_R)} \left[\chi + \bar{\alpha}_s(\mu_R) \left(\bar{\chi} + \frac{\beta_0}{8N_c} \chi \left(-\chi + \frac{10}{3} + \ln \frac{\mu_R^4}{\vec{k}_1^2 \vec{k}_2^2} \right) \right) \right] \\ &\times \alpha_s^2(\mu_R) c_1(n, \nu, |\vec{k}_1|, \alpha_1) c_2(n, \nu, |\vec{k}_2|, \alpha_2) \\ &\times \left[1 + \alpha_s(\mu_R) \left(\frac{c_1^{(1)}(n, \nu, |\vec{k}_1|, \alpha_1)}{c_1(n, \nu, |\vec{k}_1|, \alpha_1)} + \frac{c_2^{(1)}(n, \nu, |\vec{k}_2|, \alpha_2)}{c_2(n, \nu, |\vec{k}_2|, \alpha_2)} \right) \right. \\ &\left. + \bar{\alpha}_s^2(\mu_R) \ln \frac{\alpha_1 \alpha_2 s}{s_0} \frac{\beta_0}{8N_c} \chi \left(2 \ln \vec{k}_1^2 \vec{k}_2^2 + i \frac{d \ln \frac{c_1(n, \nu)}{c_2(n, \nu)}}{d\nu} \right) \right]. \end{aligned}$$

Here $\bar{\alpha}_s(\mu_R) = N_c/\pi \alpha_s(\mu_R)$, with N_c the number of colours, $\chi = \chi(n, \nu)$ is the LO BFKL characteristic function defined in (2.53), $c_{1,2}(n, \nu)$ are the LO impact factors in the ν -representation (see Eq. (4.3) for the corresponding expression in the momentum space), that are given as an integral in the parton fraction x , containing the PDFs of the gluon and of the different quark/antiquark flavours in the proton, and the FFs of the detected hadron,

$$\begin{aligned} c_1(n, \nu, |\vec{k}_1|, \alpha_1) &= 2 \sqrt{\frac{C_F}{C_A}} (\vec{k}_1^2)^{i\nu-1/2} \int_{\alpha_1}^1 \frac{dx}{x} \left(\frac{x}{\alpha_1} \right)^{2i\nu-1} \quad (4.7) \\ &\times \left[\frac{C_A}{C_F} f_g(x) D_g^h \left(\frac{\alpha_1}{x} \right) + \sum_{a=q, \bar{q}} f_a(x) D_a^h \left(\frac{\alpha_1}{x} \right) \right] \end{aligned}$$

and

$$c_2(n, \nu, |\vec{k}_2|, \alpha_2) = \left[c_1(n, \nu, |\vec{k}_2|, \alpha_2) \right]^* , \quad (4.8)$$

while

$$\begin{aligned} c_1^{(1)}(n, \nu, |\vec{k}_1|, \alpha_1) &= 2 \sqrt{\frac{C_F}{C_A}} \left(\vec{k}_1^2 \right)^{i\nu - \frac{1}{2}} \frac{1}{2\pi} \int_{\alpha_1}^1 \frac{dx}{x} \int_{\frac{\alpha_1}{x}}^1 \frac{d\zeta}{\zeta} \left(\frac{x\zeta}{\alpha_1} \right)^{2i\nu - 1} \\ &\times \left[\frac{C_A}{C_F} f_g(x) D_g^h \left(\frac{\alpha_1}{x\zeta} \right) C_{gg}(x, \zeta) + \sum_{a=q, \bar{q}} f_a(x) D_a^h \left(\frac{\alpha_1}{x\zeta} \right) C_{qq}(x, \zeta) \right. \\ &\times \left. D_g^h \left(\frac{\alpha_1}{x\zeta} \right) \sum_{a=q, \bar{q}} f_a(x) C_{qg}(x, \zeta) + \frac{C_A}{C_F} f_g(x) \sum_{a=q, \bar{q}} D_a^h \left(\frac{\alpha_1}{x\zeta} \right) C_{gq}(x, \zeta) \right] , \end{aligned} \quad (4.9)$$

and

$$c_2^{(1)}(n, \nu, |\vec{k}_2|, \alpha_2) = \left[c_1^{(1)}(n, \nu, |\vec{k}_2|, \alpha_2) \right]^* \quad (4.10)$$

are the NLO impact factor corrections in the ν -representation. The expressions for the NLO coefficient functions C_{ij} in Eq. (4.9) are given in Appendix C. It is known [38] that contributions to the NLO impact factors that are proportional to the QCD β_0 -function are universally expressed in terms of the LO impact factors of the considered process, through the function $f(\nu)$, defined as follows:

$$\begin{aligned} 2 \ln \mu_R^2 + i \frac{d \ln \frac{c_1(n, \nu)}{c_2(n, \nu)}}{d\nu} &= \ln \frac{\mu_R^4}{\vec{k}_1^2 \vec{k}_2^2} \\ &- 2 \frac{\int_{\alpha_1}^1 \frac{dx}{x} \left(\frac{x}{\alpha_1} \right)^{2i\nu - 1} \log \left(\frac{x}{\alpha_1} \right) \left[\frac{C_A}{C_F} f_g(x) D_g^h \left(\frac{\alpha_1}{x} \right) + \sum_{a=q, \bar{q}} f_a(x) D_a^h \left(\frac{\alpha_1}{x} \right) \right]}{\int_{\alpha_1}^1 \frac{dx}{x} \left(\frac{x}{\alpha_1} \right)^{2i\nu - 1} \left[\frac{C_A}{C_F} f_g(x) D_g^h \left(\frac{\alpha_1}{x} \right) + \sum_{a=q, \bar{q}} f_a(x) D_a^h \left(\frac{\alpha_1}{x} \right) \right]} \\ &- 2 \frac{\int_{\alpha_2}^1 \frac{dx}{x} \left(\frac{x}{\alpha_2} \right)^{-2i\nu - 1} \log \left(\frac{x}{\alpha_2} \right) \left[\frac{C_A}{C_F} f_g(x) D_g^h \left(\frac{\alpha_2}{x} \right) + \sum_{a=q, \bar{q}} f_a(x) D_a^h \left(\frac{\alpha_2}{x} \right) \right]}{\int_{\alpha_2}^1 \frac{dx}{x} \left(\frac{x}{\alpha_2} \right)^{-2i\nu - 1} \left[\frac{C_A}{C_F} f_g(x) D_g^h \left(\frac{\alpha_2}{x} \right) + \sum_{a=q, \bar{q}} f_a(x) D_a^h \left(\frac{\alpha_2}{x} \right) \right]} \\ &\equiv \ln \frac{\mu_R^4}{\vec{k}_1^2 \vec{k}_2^2} + 2f(\nu) . \end{aligned} \quad (4.11)$$

4.1.3 Integration over the final-state phase space

In order to match the actual LHC kinematical cuts, we integrate the coefficients over the phase space for two final-state hadrons,

$$C_n = \int_{y_1^{\min}}^{y_1^{\max}} dy_1 \int_{y_2^{\min}}^{y_2^{\max}} dy_2 \int_{k_1^{\min}}^{\infty} dk_1 \int_{k_2^{\min}}^{\infty} dk_2 C_n(y_1, y_2, k_1, k_2). \quad (4.12)$$

For the integrations over rapidities we consider two distinct ranges:

1. $y_1^{\min} = -y_2^{\max} = -2.4$, $y_1^{\max} = -y_2^{\min} = 2.4$, and $Y \leq 4.8$,
typical for the identified hadron detection at the LHC;
2. $y_1^{\min} = -y_2^{\max} = -4.7$, $y_1^{\max} = -y_2^{\min} = 4.7$, and $Y \leq 9.4$,
similar to those used in the CMS Mueller–Navelet jets analysis.

As minimum transverse momenta we choose $k_1^{\min} = k_2^{\min} = 5$ GeV, which are also realistic values for the LHC. We observe that the minimum transverse momentum in the CMS analysis [44] of Mueller–Navelet jet production is much larger, $k_j^{\min} = 35$ GeV. In our calculations we use the PDF set NLO MSTW 2008 [144] with two different NLO parameterisations for hadron FFs: AKK [157] and HKNS [158] (see Section 4.4 for a related discussion). In the results presented below we sum over the production of charged light hadrons: $\pi^\pm, K^\pm, p, \bar{p}$.

4.1.4 BLM scale setting

In order to find the values of the BLM scales, we introduce the ratios of the BLM to the “natural” scale suggested by the kinematical of the process, $\mu_N = \sqrt{|\vec{k}_1||\vec{k}_2|}$, so that $m_R = \mu_R^{\text{BLM}}/\mu_N$, and look for the values of m_R such that Eq. (2.83) is satisfied.

Then we plug these scales into our expression for the *integrated coefficients* in the BLM scheme (for the derivation see Section 2.4 and Ref. [38]):

$$\begin{aligned}
 C_n &= \int_{y_1^{\min}}^{y_1^{\max}} dy_1 \int_{y_2^{\min}}^{y_2^{\max}} dy_2 \int_{k_1^{\min}}^{\infty} dk_1 \int_{k_2^{\min}}^{\infty} dk_2 \int_{-\infty}^{\infty} dv \frac{e^Y}{s} \\
 &\times e^{Y\bar{\alpha}_s^{\text{MOM}}(\mu_R^{\text{BLM}}) \left[\chi(n, \nu) + \bar{\alpha}_s^{\text{MOM}}(\mu_R^{\text{BLM}}) \left(\bar{\chi}(n, \nu) + \frac{T^{\text{conf}}}{3} \chi(n, \nu) \right) \right]} \\
 &\times \left(\bar{\alpha}_s^{\text{MOM}}(\mu_R^{\text{BLM}}) \right)^2 c_1(n, \nu) c_2(n, \nu) \\
 &\times \left[1 + \bar{\alpha}_s^{\text{MOM}}(\mu_R^{\text{BLM}}) \left\{ \frac{\bar{c}_1^{(1)}(n, \nu)}{c_1(n, \nu)} + \frac{\bar{c}_2^{(1)}(n, \nu)}{c_2(n, \nu)} + \frac{2T^{\text{conf}}}{3} \right\} \right],
 \end{aligned} \tag{4.13}$$

with T^{conf} defined in (2.81). The coefficient C_0 gives the total cross sections and the ratios $C_n/C_0 = \langle \cos(n\phi) \rangle$ determine the values of the mean cosines, or azimuthal correlations, of the produced hadrons. In Eq. (4.13), $\bar{\chi}(n, \nu)$ is the eigenvalue of NLO BFKL kernel given in Eq. (2.59), whereas $\bar{c}_{1,2}^{(1)}$ are the NLA parts of the hadron vertices [45].

We give predictions for C_n by fixing the factorisation scale μ_F in three different ways:

1. $\mu_F = \mu_R = \mu_R^{\text{BLM}}$;
2. $(\mu_F)_{1,2} = |\vec{k}_{1,2}|$;
3. $\mu_F = \mu_R = \mu_N = \sqrt{|\vec{k}_1| |\vec{k}_2|}$.

Note that the option 3., which correspond to “natural” scale selection for both μ_F and μ_R , is used only in the full LLA calculations given in Section 4.2.

In Fig. 4.3 we present the Y -dependence of m_R at $\sqrt{s} = 7, 13$ TeV, for the first few values of n , and for $Y \leq 4.8$. We obtain rather large numbers, $m_R \sim 35$. These values are larger than those obtained previously for similar scale ratios in the case of the Mueller–Navelet jet production process. The difference may

be attributed to the fact that, in the case of dihadron production, we have an additional branching of the parton momenta (described by the detected hadron FFs), and typical transverse momenta of the partons participating in the hard scattering turn to be considerably larger than $|\vec{k}_{1,2}|$, the momenta of the hadrons detected in the final state. We found that typical value of the fragmentation fraction is $z = \alpha_h/\chi \sim 0.4$, which explains the main source of the difference between the values of the BLM scales in the case of dijet and dihadron production. Another source is related to the difference in the function $f(\nu)$, defined in Eq. (4.11), which appears in the expression for the jet- and hadron-vertex in these two reactions, and enters also the definition of the BLM scale: $f(\nu)$ is zero for the jets and non-zero in the dihadron case. The typical m_R values obtained for $4.8 < Y \leq 9.4$ are not very different from those shown here (Fig. 4.3), except that for $n = 3$ we got values four to five times larger than in the region $Y \leq 4.8$. All calculations are done in the MOM scheme. For comparison, we present results for the ϕ -averaged cross section C_0 in the \overline{MS} scheme (as implemented in Eq. (4.6)) for $\sqrt{s} = 7, 13$ TeV and for $Y \leq 4.8, 9.4$. In this case, we choose “natural” values for μ_R , *i.e.* $\mu_R = \mu_N = \sqrt{|\vec{k}_1||\vec{k}_2|}$, and the option 2., *i.e.* $(\mu_F)_{1,2} = |\vec{k}_{1,2}|$ for the factorisation scale.

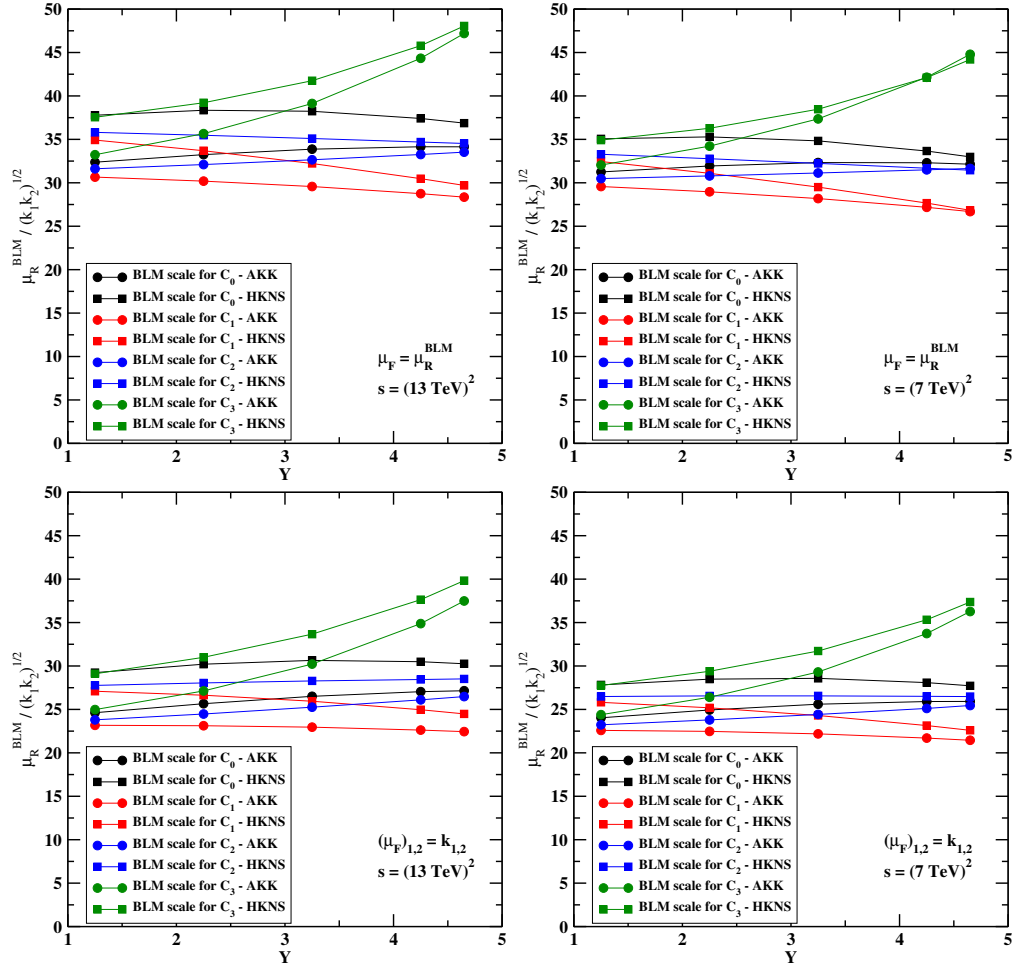


Figure 4.3: BLM scales for the dihadron production versus the rapidity interval Y for the ϕ -averaged cross section C_0 and for the azimuthal coefficients $C_{1,2,3}$. The two choices for the factorisation scale $\mu_F = \mu_R^{\text{BLM}}$ and $(\mu_F)_{1,2} = |\vec{k}_{1,2}|$ are considered, while the center-of-mass energy takes the values $\sqrt{s} = 7, 13$ TeV.

4.2 A first phenomenological analysis

In this Section the first stage of our analysis, with the implementation of a partial NLA BFKL in which we take only the higher-order corrections coming from the kernel and neglecting the NLA parts of hadron vertices, *i.e.* putting $\bar{c}_{1,2}^{(1)} = 0$ in Eq. (4.13).

We found that the difference between our predictions for the C_m/C_n ratios at $\sqrt{s} = 13$ TeV (Fig. 4.4) and the ones at $\sqrt{s} = 13$ TeV (Fig. 4.5), is not larger than 3%. We see on the first caption of Figs. 4.4 and 4.5. the sizeable difference between predictions of the ϕ -averaged cross section C_0 in two cases of selected FFs, AKK and HKNS, which means that the FFs are not well constrained in the required kinematical region. In a similar range the difference between π^\pm and K^\pm AKK and HKNS FFs was recently discussed in Ref. [166]. Our calculation with the AKK FFs gives bigger cross sections, whereas the difference between AKK and HKNS for the azimuthal ratios C_m/C_n is small, since the FFs uncertainties are largely cancelled in the coefficient ratios describing the azimuthal-angle correlations. Our predictions for dihadron production calculated in LLA with the use of the “natural” scale μ_N and our NLA results obtained with the BLM scale setting are different: with NLA BLM we got much lower values of the cross sections and considerably larger predictions for the C_m/C_n . Plots of Figs. 4.4 and 4.5 show that the LLA results with BLM scales lie closer to the NLA BLM ones than LLA results with “natural” scales. The difference between NLA BLM and LLA with BLM scale predictions is due to the account of NLA corrections to the BFKL kernel in the former. This clearly represents a reliability test for the BLM method.

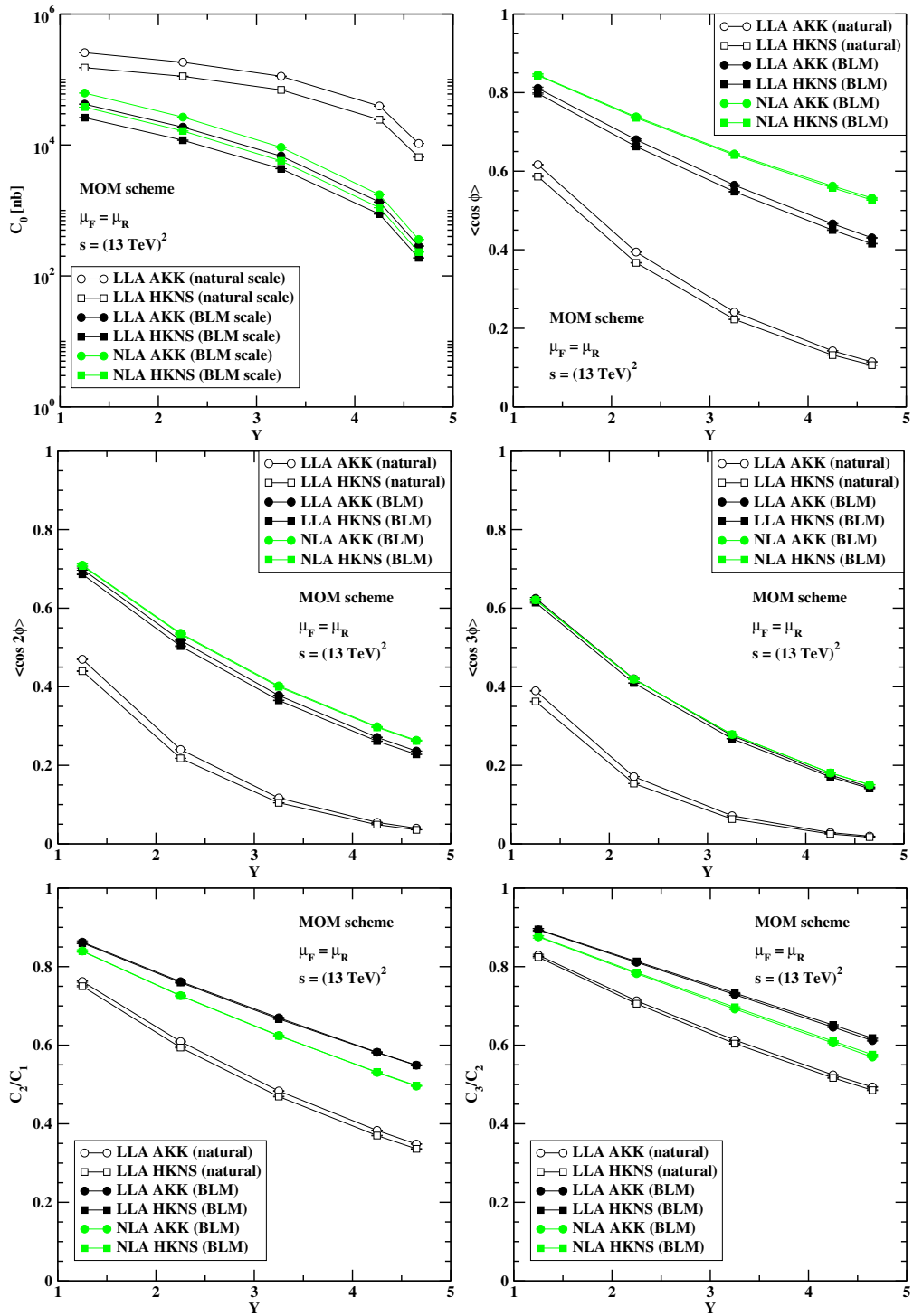


Figure 4.4: Cross section and azimuthal ratios for dihadron production for $\mu_F = \mu_R^{\text{BLM}}$, $\sqrt{s} = 13 \text{ TeV}$, and $Y \leq 4.8$. Here “LLA” means pure leading logarithmic approximation, while “NLA kernel” means inclusion of the NLA corrections from the kernel only. See the text for the definition of “natural” and “BLM” scales.

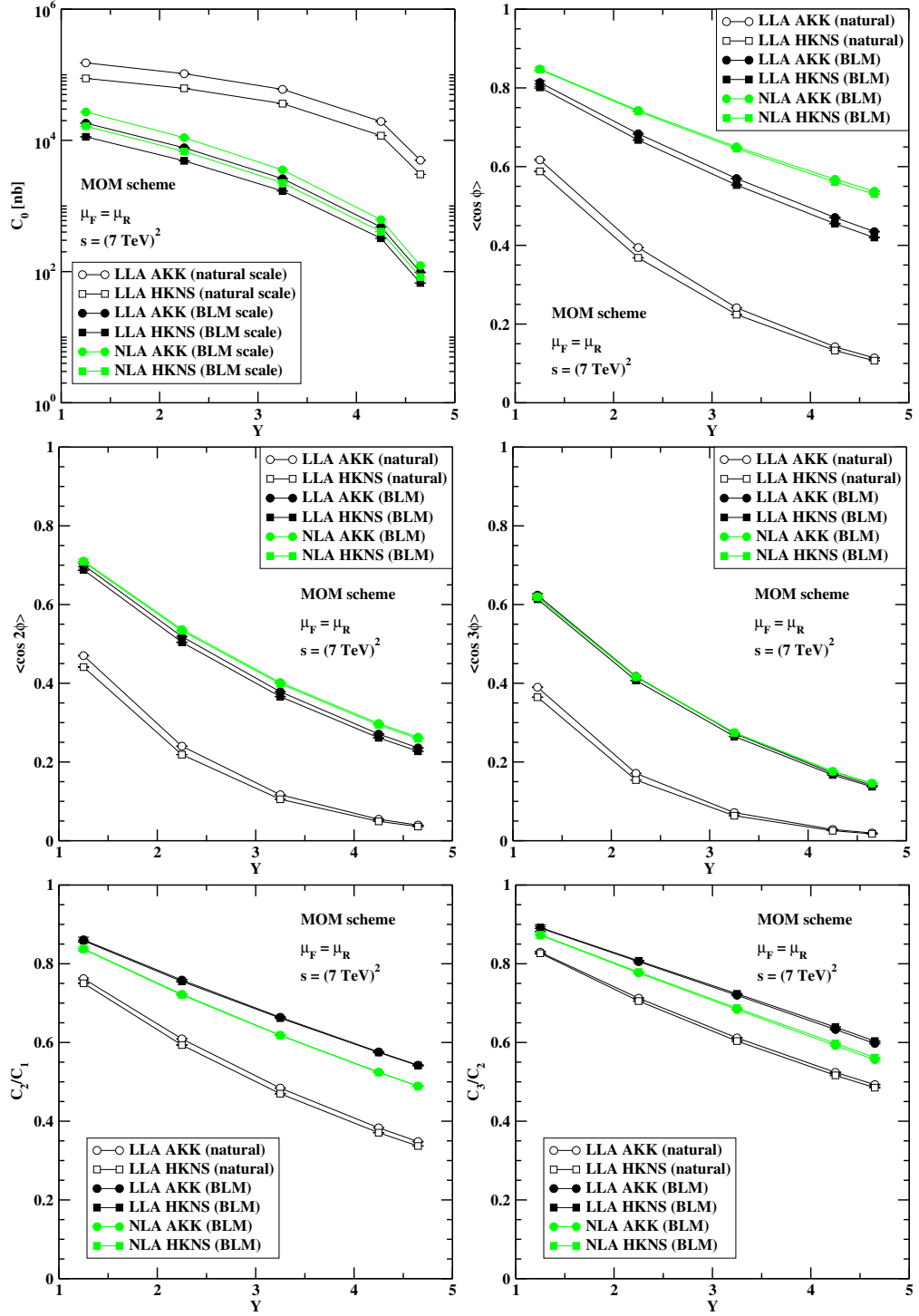


Figure 4.5: Cross section and azimuthal ratios for dihadron production for $\mu_F = \mu_R^{\text{BLM}}$, $\sqrt{s} = 7 \text{ TeV}$, and $Y \leq 4.8$. Here “LLA” means pure leading logarithmic approximation, while “NLA kernel” means inclusion of the NLA corrections from the kernel only. See the text for the definition of “natural” and “BLM” scales.

4.3 Full NLA BFKL calculation

In this section the first analysis for dihadron production in the full NLA BFKL accuracy is presented.

We checked that in our numerical analysis the essential values of x are not too small, $x \sim [10^{-3} \div 10^{-2}]$, and even bigger in the case of the larger $Y \leq 9.4$. This justifies our use of PDFs with the standard DGLAP evolution. Note that our process is not a low- x one, and similarly to the Mueller–Navelet jet production, we are dealing with a dilute partonic system. Therefore possible saturation effects are not important here, and the BFKL dynamics appears only through resummation effects in the hard scattering subprocesses, without influence on the PDF evolution.

In Fig. 4.6 we show our results for C_0 in the $\overline{\text{MS}}$ scheme (as implemented in Eq. (4.6)) for we already specified above the scale settings $\sqrt{s} = 7, 13$ TeV, and in the two cases of $Y \leq 4.8$ and $Y \leq 9.4$. We clearly see that NLA corrections become negative with respect to the LLA prediction when Y grows. Besides, it is interesting to note that the full NLA approach predicts larger values for the cross sections in comparison to the case where only NLA corrections to the BFKL kernel are taken into account. It means that the inclusion into the analysis of the NLA corrections to the hadron vertices makes the predictions for the cross sections somewhat bigger and partially compensates the large negative effect from the NLA corrections to the BFKL kernel.

The other results we presented below are obtained using BLM in the MOM scheme, as it is given in Eq. (4.13). In Figs. 4.7 and 4.8 we present our results for C_0 and for several ratios C_m/C_n at $\sqrt{s} = 13$ and 7 TeV, respectively; μ_F is set equal to μ_R^{BLM} , while $Y \leq 4.8$. It is worth to note that in this case the NLA corrections to C_0 are positive, so they increase the value of the ϕ -averaged

cross section at all values of Y . This is the result of the combination of two distinct effects: on one side, we already saw in Ref. [151] that changing the renormalisation scheme produces a non-exponentiated extra factor in Eq. (4.13) proportional to T^{conf} , and that is positive. On the other side, we found that the C_{gg} coefficient in Eq. (4.9) gives a large and positive contribution to the NLO impact factor. We see also that NLA corrections increase the azimuthal correlations: C_1/C_0 , C_2/C_0 , and C_3/C_0 , while their effect is small with respect to LLA predictions in their ratios, C_2/C_1 and C_3/C_2 . The value of C_1/C_0 for $Y \leq 2.75$ in some cases exceeds 1. We consider this as an effect due to the fact that, at very small Y , which corresponds to the small values of partonic subenergies \hat{s} , we are crossing the applicability limit of the BFKL approach, which systematically neglects any contributions that are suppressed by the powers of \hat{s} .

For comparison, we show in Figs. 4.9 and 4.10 the results for the same observables with the choice of $(\mu_F)_{1,2} = |\vec{k}_{1,2}|$. The patterns we have found are very similar to the previous ones, but we see that the effect of having C_1/C_0 larger than 1 at small Y is reduced. Furthermore, NLA corrections are negative for larger Y values. On the basis of this, we may conclude that, in the $Y \leq 4.8$ kinematical regime, the choice of “natural” scales for μ_F stabilises the results.

In Figs. 4.11 and 4.12 we present our results for C_0 and for several ratios C_m/C_n at $\sqrt{s} = 13$ and 7 TeV respectively; μ_F is set equal to μ_R^{BLM} , while Y lies on a larger range, *i.e.* $Y \leq 9.4$.

For comparison, we show in Figs. 4.13 and 4.14 the results for the same observables with the choice of $(\mu_F)_{1,2} = |\vec{k}_{1,2}|$. We clearly see that, in the case of larger rapidity intervals Y and with the “natural” choice for the factorisation scale, the situation is different in comparison to the $\mu_F = \mu_R^{\text{BLM}}$ choice: the NLA corrections to the cross section C_0 are negative, while the pattern of C_1/C_0

shows a somewhat unexpected “turn-up” at large Y , and these effects are more pronounced for the lower LHC energy, $\sqrt{s} = 7$ TeV. Such a sensitivity to the factorisation scale setting may be an indication of the fact that with the increase of Y values we are moving towards the threshold region, where the energy of detected dihadron system becomes comparable with \sqrt{s} . In this situation the FFs and PDFs are probed in regions that are close to the end-points of their definitions, where they exhibit large dependence on the factorisation scale. From the physical site, in this kinematics the undetected hard-gluon radiation is getting restricted and only radiation of soft gluons is allowed. Soft-gluon radiation can not change the kinematics of the hard subprocess, therefore one expects restoration of the correlation of the detected hadrons in the relative azimuthal angle when we approach the threshold region. It is well known that in this situation large *threshold double logarithms* [159–162] appear in the perturbative series, and such contributions have to be resummed to all orders. Threshold logarithms appear when the parent parton has just enough energy to produce the identified particle in the final state and the unobserved recoiling partonic final state. Resummation in the kinematics where both threshold and BFKL logarithms are important is an interesting task, but it goes well beyond the scope of the present study. Here we just note that pure BFKL predictions in the region of largest Y become rather sensitive to the choice of the factorisation scale.

To better assess the factorization scale dependence, we have considered also the case when μ_F is varied around its “natural” value $\sqrt{|\vec{k}_1||\vec{k}_2|}$ by a factor r taking values in the range 1/2 to four. In Fig. 4.15, as a selection of our results, we present the plots for C_0 and C_1/C_0 at a squared center-of-mass energy of 7 and 13 TeV for the rapidity region $Y \leq 4.8$ and the HKNS parametrization of the fragmentation functions.

It is worth to note that the general features of our predictions for dihadron production are rather similar to those obtained earlier for the Mueller–Navelet jet process. Although the BFKL resummation leads to the growth with energy of the partonic subprocess cross sections, the convolution of the latter with the proton PDFs makes the net effect of a decrease with Y of our predictions. This is due to the fact that, at larger values of Y , PDFs are probed effectively at larger values of x , where they fall very fast. For the dihadron azimuthal correlations we predict a decreasing behaviour with Y . That originates from the increasing amount of hard undetected parton radiation in the final state allowed by the growth of the partonic subprocess energy.

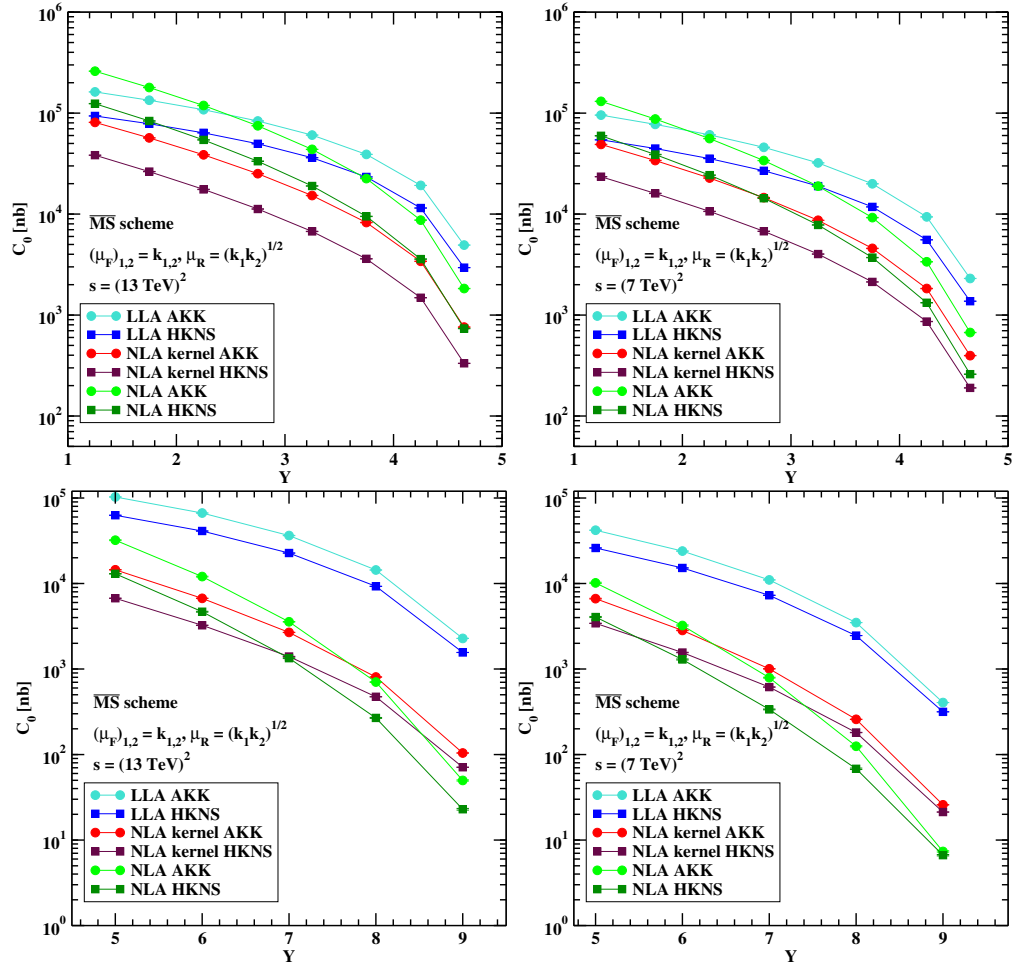


Figure 4.6: Y -dependence of C_0 in the $\overline{\text{MS}}$ scheme (as implemented in Eq. (4.6)) at “natural” scales for μ_R and μ_F , $\sqrt{s} = 7, 13 \text{ TeV}$, and in the two cases of $Y \leq 4.8$ and $Y \leq 9.4$. Here and in the following figure captions “LLA” means pure leading logarithmic approximation, “NLA kernel” means inclusion of the NLA corrections from the kernel only, “NLA” stands for full inclusion of NLA corrections, i.e. both from the kernel and the hadron vertices.

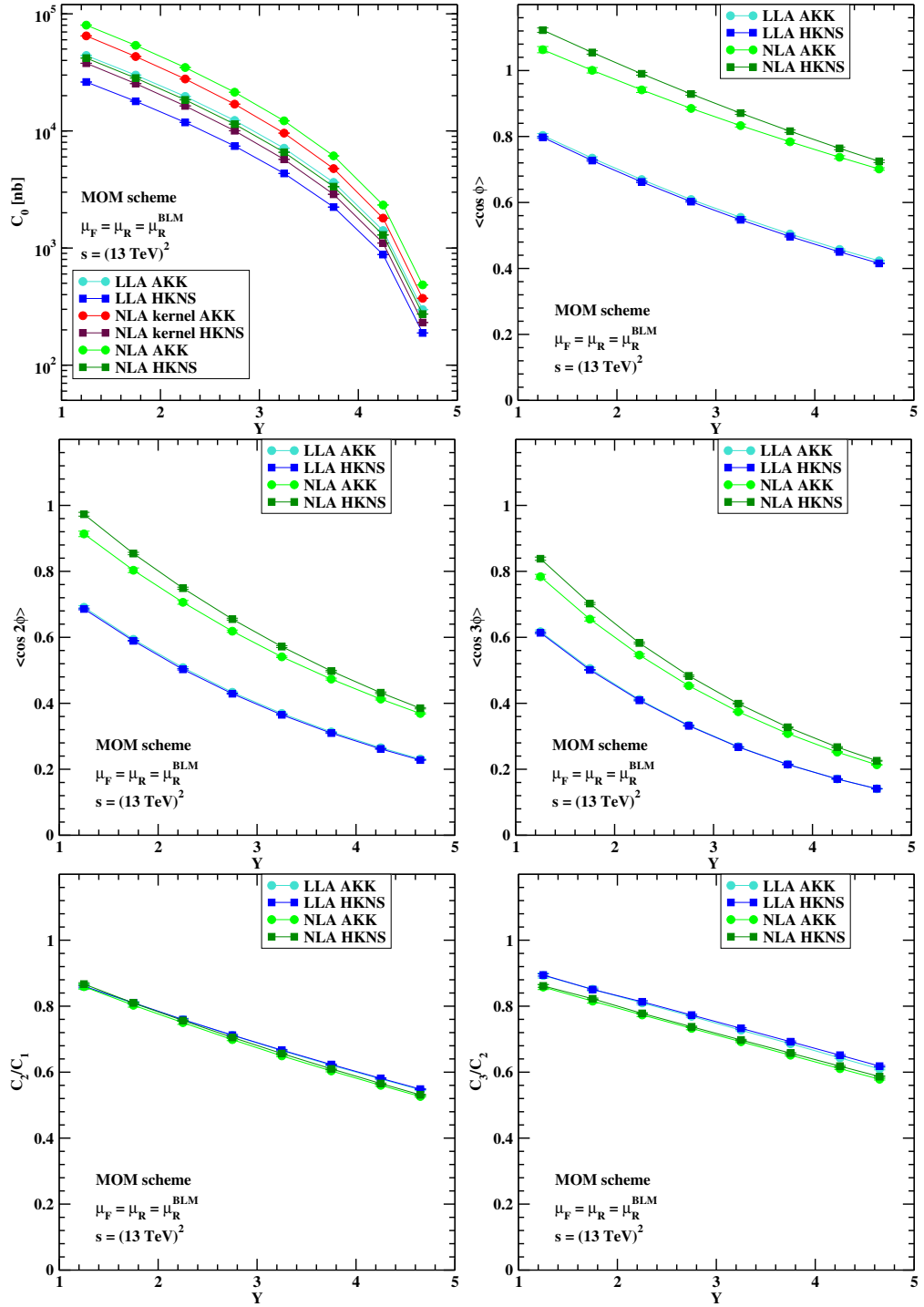


Figure 4.7: Y-dependence of C_0 and of several ratios C_m/C_n for $\mu_F = \mu_R = \mu_R^{\text{BLM}}$, $\sqrt{s} = 13 \text{ TeV}$, and $Y \leq 4.8$.

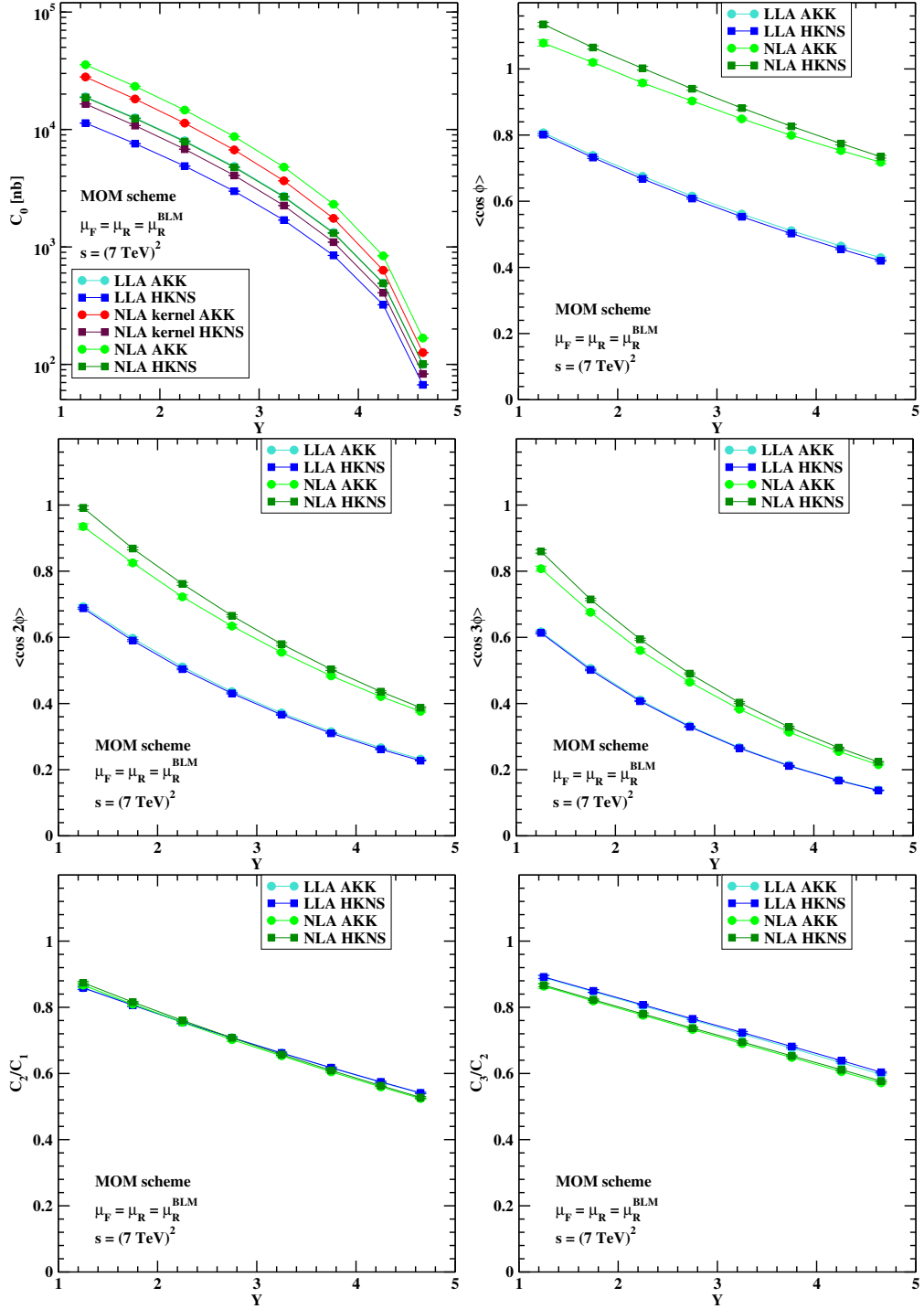


Figure 4.8: Y-dependence of C_0 and of several ratios C_m/C_n for $\mu_F = \mu_R = \mu_R^{\text{BLM}}$, $\sqrt{s} = 7 \text{ TeV}$, and $Y \leq 4.8$.

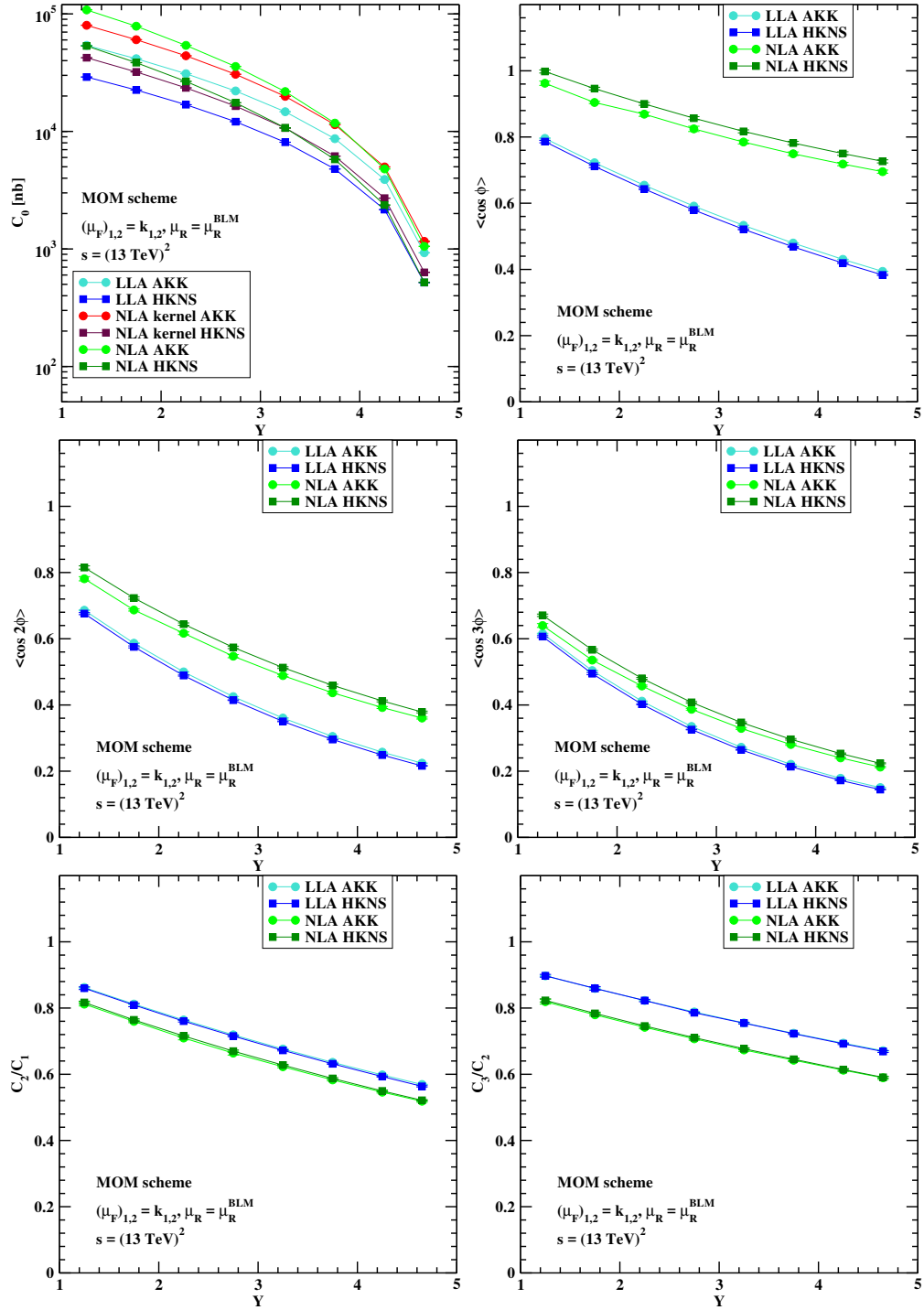


Figure 4.9: Y -dependence of C_0 and of several ratios C_m/C_n for $(\mu_F)_{1,2} = |\vec{k}_{1,2}|$, $\sqrt{s} = 13 \text{ TeV}$, and $Y \leq 4.8$.

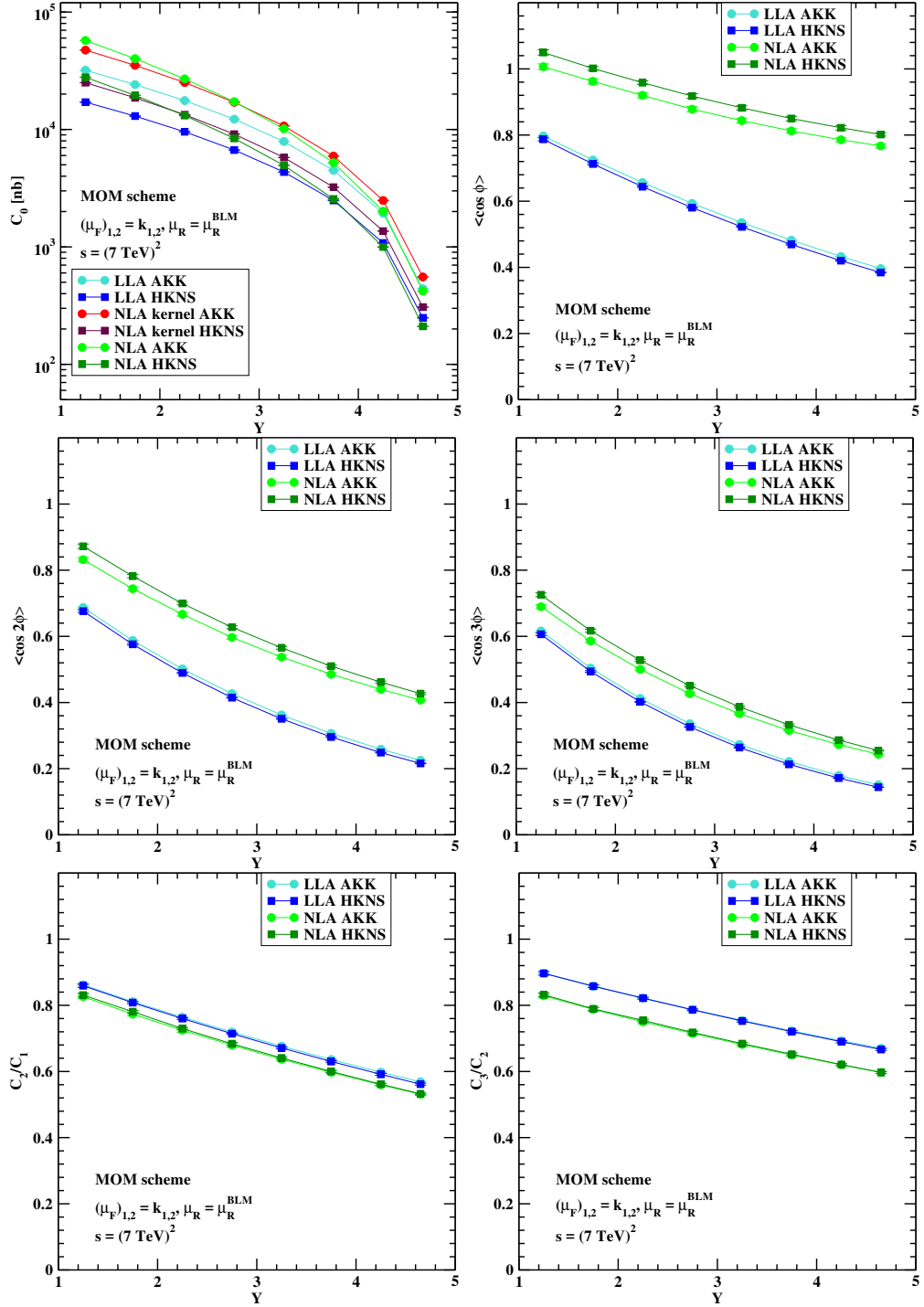


Figure 4.10: Y -dependence of C_0 and of several ratios C_m/C_n for $(\mu_F)_{1,2} = |k_{1,2}|$, $\sqrt{s} = 7$ TeV, and $Y \leq 4.8$.

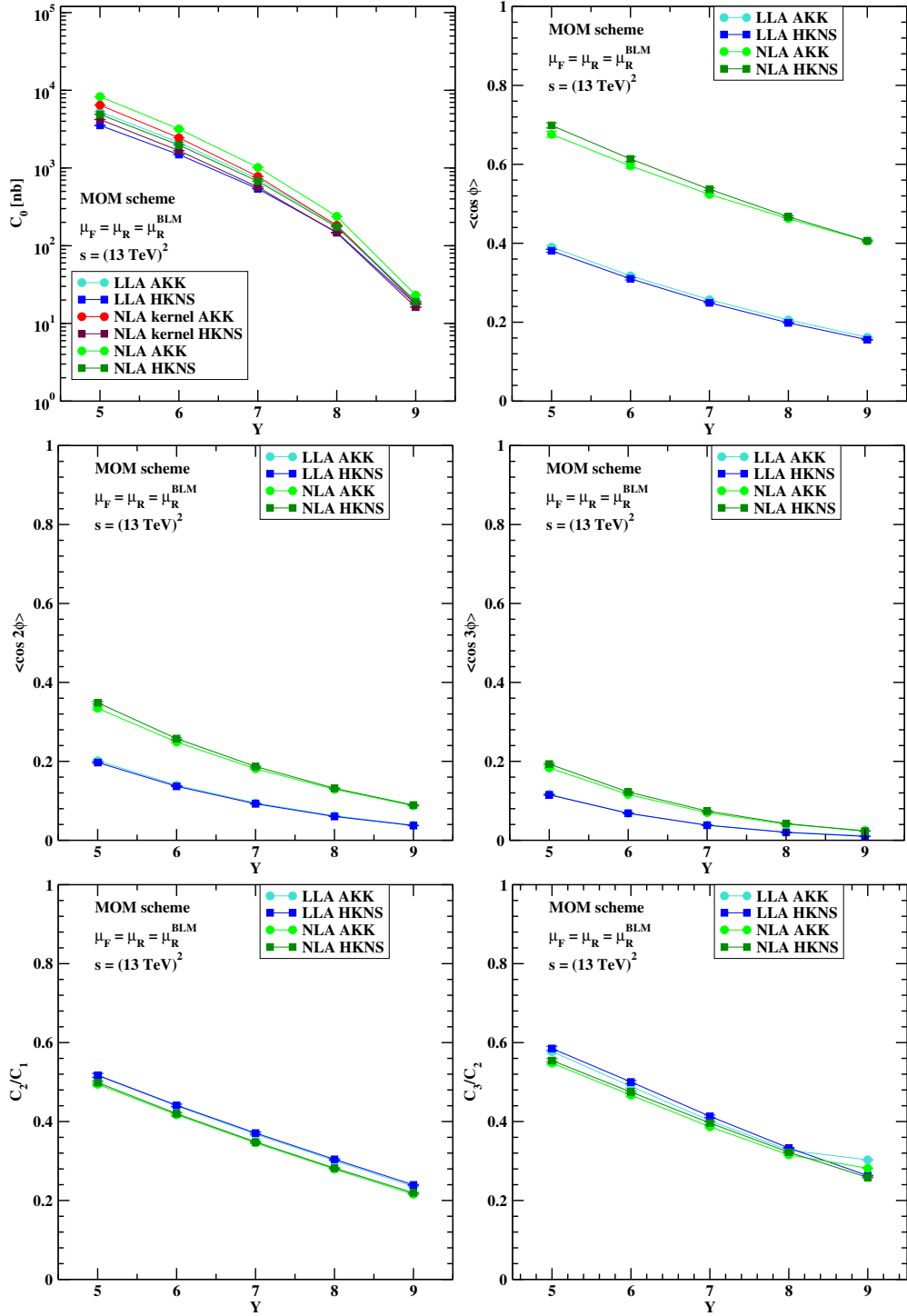


Figure 4.11: Y -dependence of C_0 and of several ratios C_m/C_n for $\mu_F = \mu_R^{\text{BLM}}$, $\sqrt{s} = 13 \text{ TeV}$, and $Y \leq 9.4$.

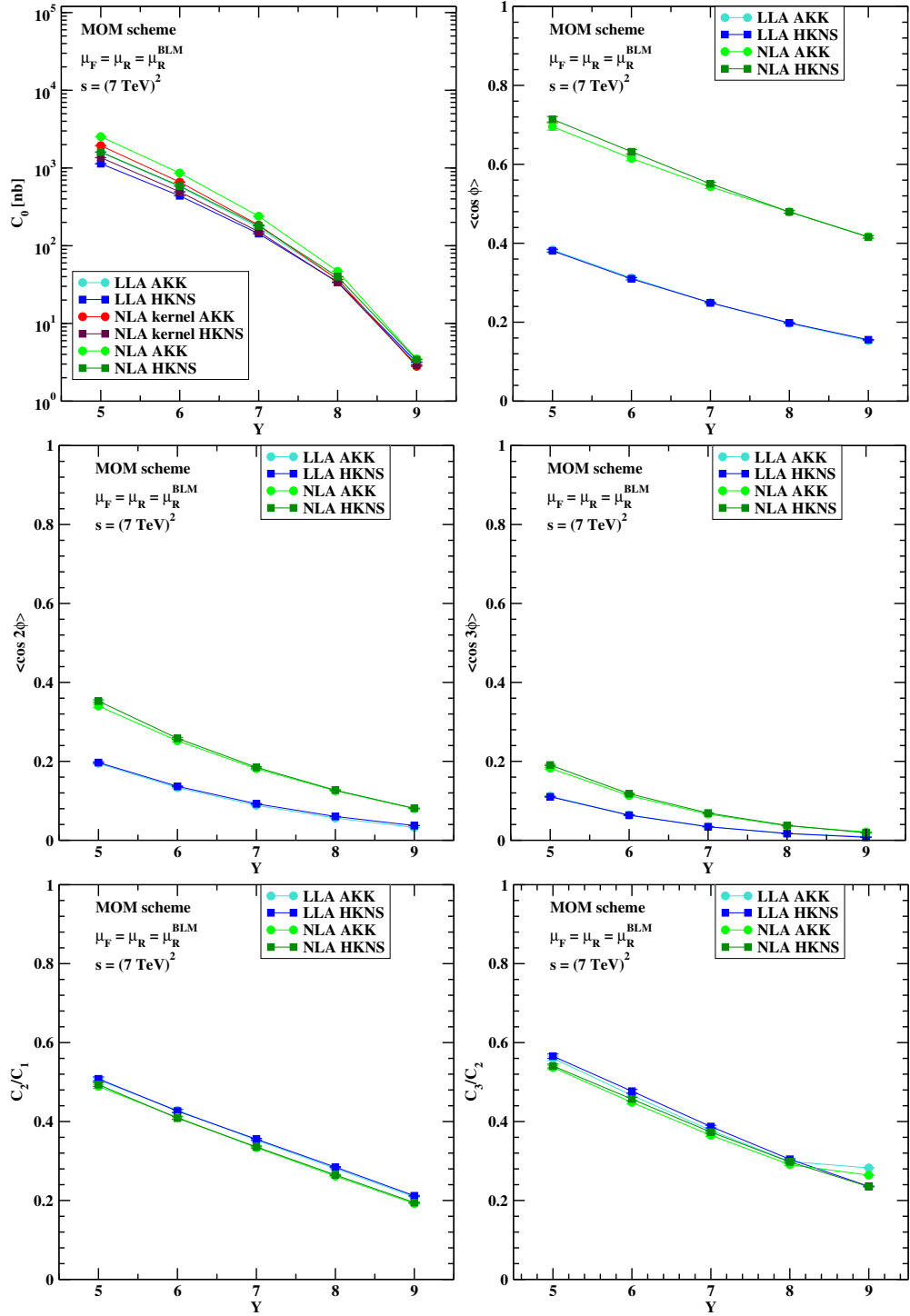


Figure 4.12: Y -dependence of C_0 and of several ratios C_m/C_n for $\mu_F = \mu_R^{\text{BLM}}$, $\sqrt{s} = 7 \text{ TeV}$, and $Y \leq 9.4$.

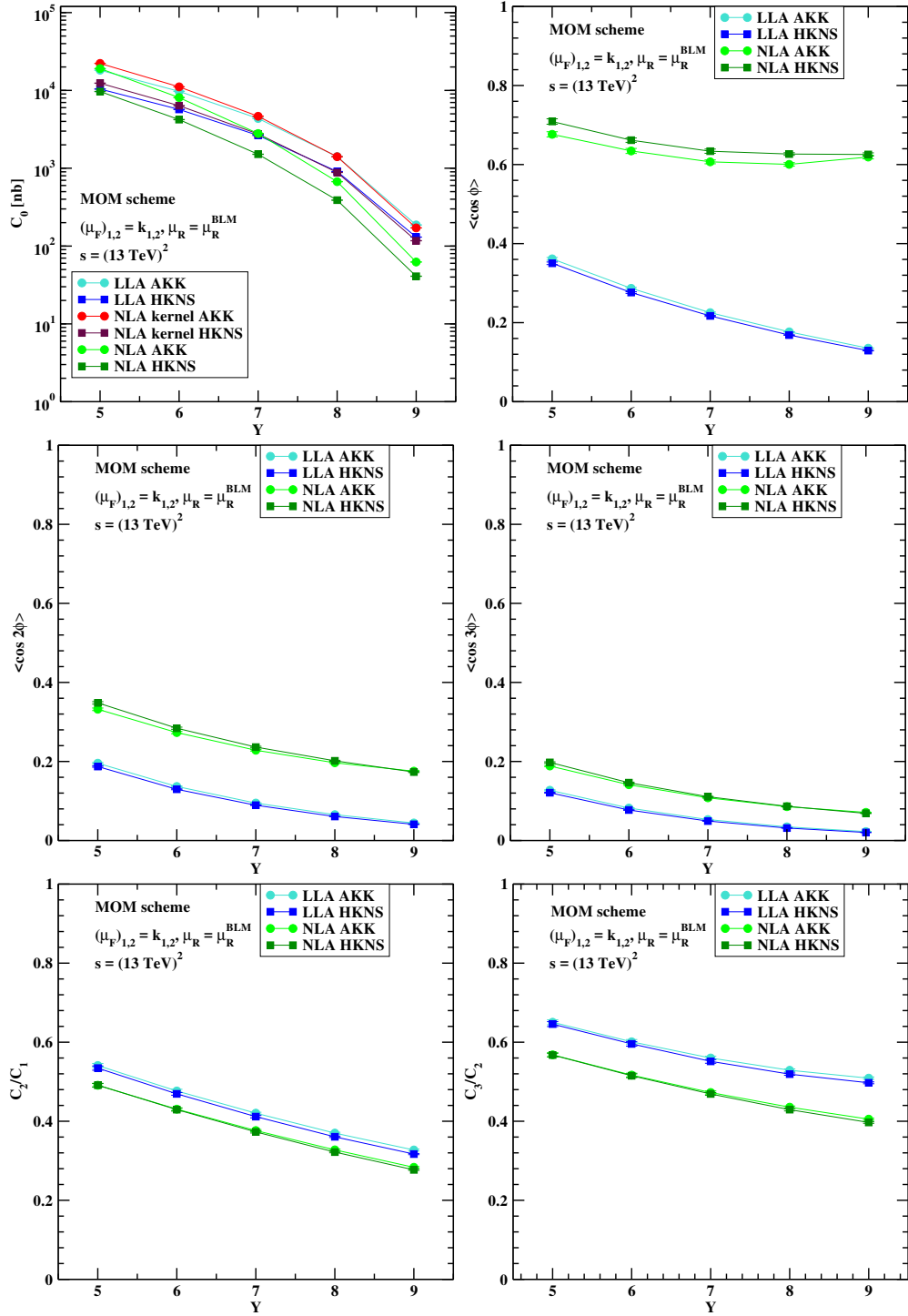


Figure 4.13: Y -dependence of C_0 and of several ratios C_m/C_n for $(\mu_F)_{1,2} = |\vec{k}_{1,2}|$, $\sqrt{s} = 13$ TeV, and $Y \leq 9.4$.

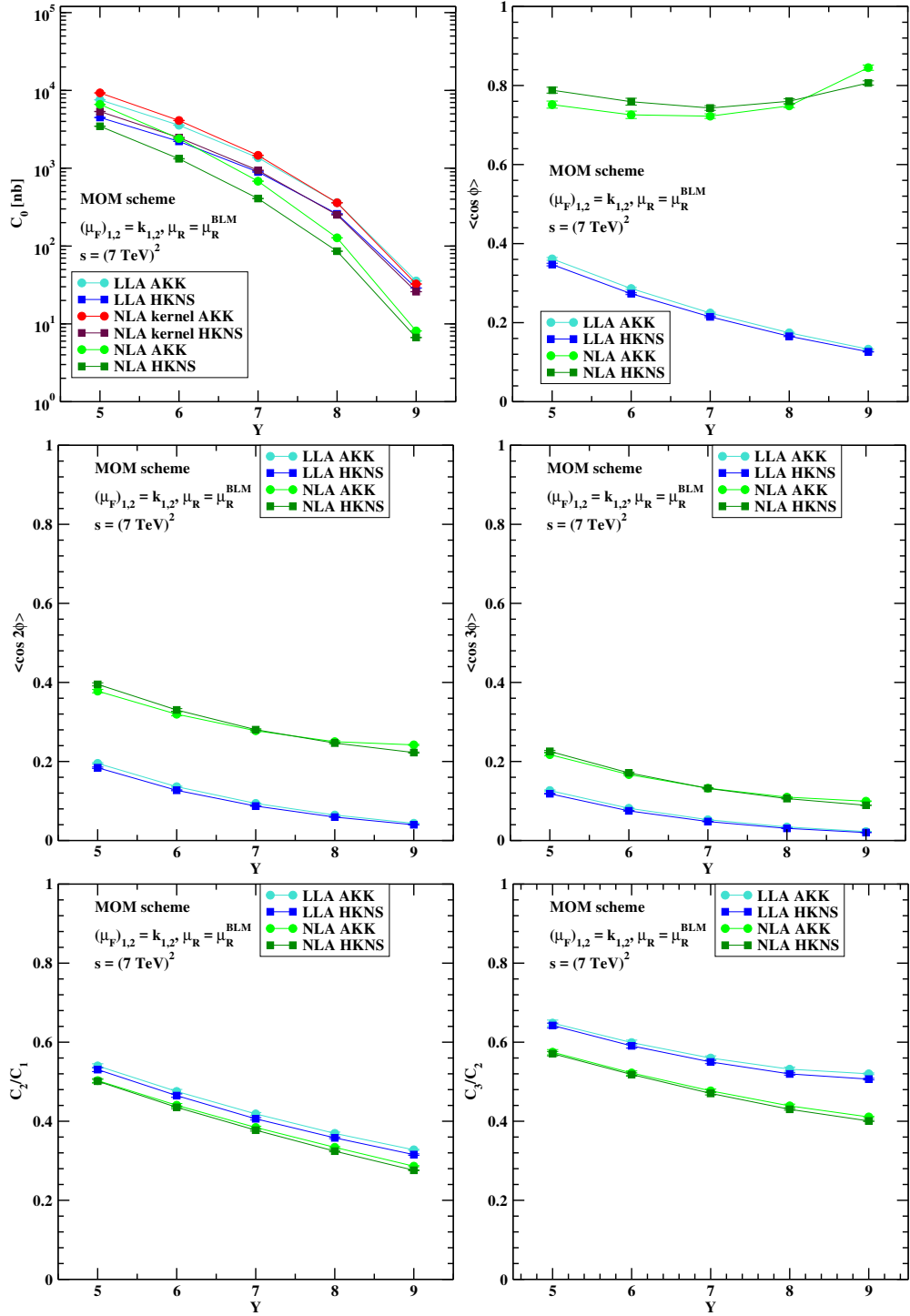


Figure 4.14: Y -dependence of C_0 and of several ratios C_m/C_n for $(\mu_F)_{1,2} = |\vec{k}_{1,2}|$, $\sqrt{s} = 7$ TeV, and $Y \leq 9.4$.

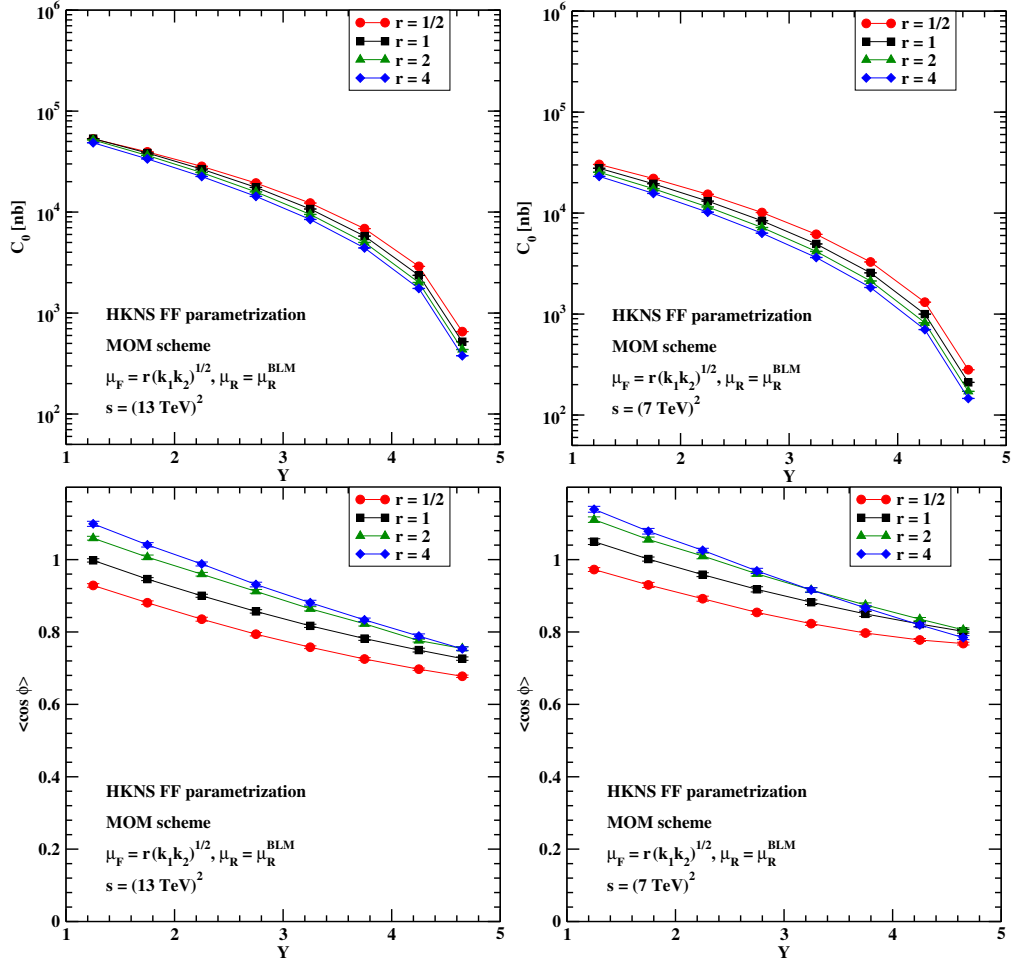


Figure 4.15: Y -dependence of C_0 and of C_1/C_0 for $\mu_F = r\sqrt{|\vec{k}_1||\vec{k}_2|}$, with $r = 1/2, 1, 2, 4$, and $Y \leq 4.8$.

4.4 Numerical specifics

4.4.1 Used tools

All the numerical calculations presented in Section 4.2 and in Section 4.3 were performed in FORTRAN, choosing a two-loop running coupling setup with $\alpha_s(M_Z) = 0.11707$ and five quark flavours. It is known that potential sources of uncertainty could be due to the particular PDF and FF parameterisations used.

For this reason, preliminary tests were done by using three different NLO PDF sets, expressly: MSTW 2008 [144], MMHT 2014 [145], and CT 2014 [163], and convolving them with the three following NLO FF routines: AKK [157], DSS [164, 165], and HNKS [158]. Our tests have shown no significant discrepancy when different PDF sets are used in our kinematical range. In view of this result, in the final calculations the MSTW 2008 PDF set (which was successfully used in various analyses of inclusive semi-hard processes at the LHC, including our previous studies of Mueller–Navelet jets) was selected, together with the FF interfaces mentioned above. The results with the DSS routine are not shown, since they would be hardly distinguishable from those with the HNKS parameterisation.

Specific CERN program libraries [146] were used to evaluate the azimuthal coefficients given in Eq. (4.13), which requires a complicated 8-dimensional numerical integration (the expressions for $\bar{c}_{1,2}^{(1)}$ contain an additional longitudinal fraction integral in comparison to the formulæ for the LLA vertices, given in Eqs. (4.7) and (4.8)). Furthermore, slightly modified versions of the Chyp [147] and Psi [148] routines were used to calculate the Gauss hypergeometric function ${}_2F_1$ and the real part of the ψ function, respectively.

4.4.2 Uncertainty estimation

The most significant uncertainty comes from the numerical 4-dimensional integration over the two transverse momenta $|\vec{k}_{1,2}|$, the rapidity y_1 , and over v . Its effect was directly estimated by Dadmul integration routine [146]. The other three sources of uncertainty, which are respectively: the one-dimensional integration over the parton fraction x needed to perform the convolution between PDFs and FFs in the LO/NLO impact factors (see Eq. (4.7) and (4.9)), the one-dimensional integration over the longitudinal momentum fraction ζ in

the NLO impact factor correction (see Eqs. (4.9)), and the upper cutoff in the numerical integrations over $|\vec{k}_{1,2}|$ and ν , are negligible with respect to the first one. For this reason the error bars of all predictions presented in this work are just those given by the `Dadmul` routine.

4.5 Summary

We studied the inclusive dihadron production process at the LHC within the BFKL approach, giving the first complete phenomenological predictions for cross sections and azimuthal correlation momenta in the full NLA approximation. We implemented the exact version of the BLM optimisation procedure, which requires the choice of renormalisation scale $\mu_R = \mu_R^{\text{BLM}}$ such that it makes completely vanish the NLA terms proportional to the QCD β -function. This procedure leads to rather large values of the scale μ_R^{BLM} and it allows to minimise the size of the NLA corrections in our observables. We considered two center-of-mass energies, $\sqrt{s} = 7, 13$ TeV, and two different ranges for the rapidity interval between the two hadrons in the final state, $Y \leq 4.8$ and $Y \leq 9.4$, which are typical for the last CMS analyses. The first rapidity range we investigated, $Y \leq 4.8$, may look to be not large enough for the dominance of BFKL dynamics. But we see, however, that in this range there are large NLA BFKL corrections, thus indicating that the BFKL resummation is playing here a non-trivial role. To clarify the issue it would be very interesting to confront our predictions with the results of fixed-order NLO DGLAP calculations. But this would require new numerical analysis in our semi-hard kinematical range, because the existing NLO DGLAP results cover the hard kinematical range for the energies of fixed target experiments, see for instance Refs. [167, 168].

As for the hadron's transverse momenta, we imposed the *symmetric* lower

cutoff: $|\vec{k}_{1,2}| \geq 5$ GeV. Considering a region of lower hadron transverse momenta, say $|\vec{k}_{1,2}| \geq 2$ GeV, would lead to even larger values of the cross sections. But it should be noted that in our calculation we use the BFKL method together with leading-twist collinear factorisation, which means that we are systematically neglecting power-suppressed corrections. Therefore, going to smaller transverse momenta we would enter a region where higher-twist effects must be important.

The general features of our predictions for dihadron production are rather similar to those obtained earlier for the Mueller-Navelet jet process. In particular, we observe that the account of NLA BFKL terms leads to much less azimuthal angle decorrelation with increasing Y in comparison to LLA BFKL calculations. As for the difference between the Mueller-Navelet jet and dihadron production processes, we would mention the fact that, contrary to the jets' case, the full account of NLA terms leads in dihadron production to an increase of our predictions for the cross sections in comparison to the LLA BFKL calculation.

We considered the effect of using different parameterisation sets for the PDFs and the FFs, that could potentially give rise to uncertainties which, in principle, are not negligible. We did some preliminary tests devoted to gauge the effect of using different PDF routines, showing that it leads to no significant difference in the results. Then, we investigated the Y -behaviour of our observables by using two different FF parameterisations. Our calculation with the AKK FFs gives bigger cross sections, while the difference between AKK and HKNS is small, since the FFs uncertainties are mostly wiped out in the azimuthal ratios.

We studied the effect of using two different choices for the factorisation scale, $\mu_F = \mu_R^{\text{BLM}}$ and $(\mu_F)_{1,2} = |\vec{k}_{1,2}|$, whereas $\mu_R = \mu_R^{\text{BLM}}$ runs at BLM scales.

We see some difference in predictions within these two approaches, especially for larger values of Y and at the smaller value of the energy $\sqrt{s} = 7$ TeV. In this region, the kinematical restriction for the undetected hard gluon radiation may start to be important, requiring resummation of threshold double logarithms together with BFKL logarithms of energy. In this case, the phase space available for gluon bremsstrahlung vanishes, so that only soft and collinear emission is allowed, resulting in large logarithmic corrections to the partonic cross section. This issue maybe a physical reason for the observed strong dependence on the factorisation scale choice in our pure BFKL approach, and it definitely deserves a further study.

Appendix C

NLO impact factor for the identified hadron

In this Appendix the expressions for the NLO coefficient functions C_{ij} in Eq. (4.9) are given (see Ref. [45] for further details). In particular, we have:

$$\begin{aligned}
C_{gg}(x, \zeta) = & P_{gg}(\zeta) \left(1 + \zeta^{-2\gamma}\right) \ln \left(\frac{\vec{k}_h^2 x^2 \zeta^2}{\mu_F^2 \alpha_h^2}\right) - \frac{\beta_0}{2} \ln \left(\frac{\vec{k}_h^2 x^2 \zeta^2}{\mu_R^2 \alpha_h^2}\right) \quad (C.1) \\
& + \delta(1 - \zeta) \left[C_A \ln \left(\frac{s_0 \alpha_h^2}{\vec{k}_h^2 x^2}\right) \chi(n, \gamma) - C_A \left(\frac{67}{18} - \frac{\pi^2}{2}\right) + \frac{5}{9} n_f \right. \\
& \left. + \frac{C_A}{2} \left(\psi' \left(1 + \gamma + \frac{n}{2}\right) - \psi' \left(\frac{n}{2} - \gamma\right) - \chi^2(n, \gamma)\right) \right] \\
& + C_A \left(\frac{1}{\zeta} + \frac{1}{(1 - \zeta)_+} - 2 + \zeta \bar{\zeta}\right) \\
& \times \left(\chi(n, \gamma)(1 + \zeta^{-2\gamma}) - 2(1 + 2\zeta^{-2\gamma}) \ln \zeta + \frac{\bar{\zeta}^2}{\zeta^2} I_2\right) \\
& + 2 C_A (1 + \zeta^{-2\gamma}) \left(\left(\frac{1}{\zeta} - 2 + \zeta \bar{\zeta}\right) \ln \bar{\zeta} + \left(\frac{\ln(1 - \zeta)}{1 - \zeta}\right)_+\right),
\end{aligned}$$

$$\begin{aligned}
C_{gq}(x, \zeta) = & P_{qg}(\zeta) \left(\frac{C_F}{C_A} + \zeta^{-2\gamma}\right) \ln \left(\frac{\vec{k}_h^2 x^2 \zeta^2}{\mu_F^2 \alpha_h^2}\right) \quad (C.2) \\
& + 2 \zeta \bar{\zeta} T_R \left(\frac{C_F}{C_A} + \zeta^{-2\gamma}\right) + P_{qg}(\zeta) \left(\frac{C_F}{C_A} \chi(n, \gamma) + 2\zeta^{-2\gamma} \ln \frac{\bar{\zeta}}{\zeta} + \frac{\bar{\zeta}}{\zeta} I_3\right),
\end{aligned}$$

$$\begin{aligned}
 C_{qg}(x, \zeta) &= P_{gq}(\zeta) \left(\frac{C_A}{C_F} + \zeta^{-2\gamma} \right) \ln \left(\frac{\vec{k}_h^2 x^2 \zeta^2}{\mu_F^2 \alpha_h^2} \right) \\
 &+ \zeta \left(C_F \zeta^{-2\gamma} + C_A \right) + \frac{1 + \bar{\zeta}^2}{\zeta} \left[C_F \zeta^{-2\gamma} (\chi(n, \gamma) - 2 \ln \zeta) + 2 C_A \ln \frac{\bar{\zeta}}{\zeta} + \frac{\bar{\zeta}}{\zeta} I_1 \right], \quad (C.3)
 \end{aligned}$$

$$\begin{aligned}
 C_{qq}(x, \zeta) &= P_{qq}(\zeta) \left(1 + \zeta^{-2\gamma} \right) \ln \left(\frac{\vec{k}_h^2 x^2 \zeta^2}{\mu_F^2 \alpha_h^2} \right) - \frac{\beta_0}{2} \ln \left(\frac{\vec{k}_h^2 x^2 \zeta^2}{\mu_R^2 \alpha_h^2} \right) \\
 &+ \delta(1 - \zeta) \left[C_A \ln \left(\frac{s_0 \alpha_h^2}{\vec{k}_h^2 x^2} \right) \chi(n, \gamma) + C_A \left(\frac{85}{18} + \frac{\pi^2}{2} \right) - \frac{5}{9} n_f - 8 C_F \right. \\
 &+ \left. \frac{C_A}{2} \left(\psi' \left(1 + \gamma + \frac{n}{2} \right) - \psi' \left(\frac{n}{2} - \gamma \right) - \chi^2(n, \gamma) \right) \right] + C_F \bar{\zeta} (1 + \zeta^{-2\gamma}) \\
 &+ (1 + \zeta^2) \left[C_A (1 + \zeta^{-2\gamma}) \frac{\chi(n, \gamma)}{2(1 - \zeta)_+} + (C_A - 2 C_F (1 + \zeta^{-2\gamma})) \frac{\ln \zeta}{1 - \zeta} \right] \\
 &+ \left(C_F - \frac{C_A}{2} \right) (1 + \zeta^2) \left[2(1 + \zeta^{-2\gamma}) \left(\frac{\ln(1 - \zeta)}{1 - \zeta} \right)_+ + \frac{\bar{\zeta}}{\zeta^2} I_2 \right], \quad (C.4)
 \end{aligned}$$

with the plus-prescription defined in Eq. (B.5).

Here $\gamma = i\nu - 1/2$, while $P_{ij}(\zeta)$ are leading order DGLAP kernels defined in Appendix B. The expressions for the $I_{1,2,3}$ functions are given in Appendix B.

Chapter 5

Three-jet production

In the last two Chapters we investigated semi-hard processes with two objects (jets or charged light hadrons) always tagged in the final state. We started from the expression of the forward parton impact factors [20, 21], ‘opening’ one of the integrations over the intermediate-state phase space to allow one parton to generate the detected object in the final state. Thus, we obtained the expressions for the process-dependent vertex, which have to be convoluted (Eq. (2.70)) with the universal Green’s function in order to get the cross section for the considered processes.

Inclusive multi-jet production represents a further step towards the study of BFKL dynamics in a much more exclusive way. While in the two-body case we modified the expression of the parton impact factors in order to allow the detection of two objects in the fragmentation region of the respective parent proton, in the n -body case we need to suitably generalise our formalism to account for the emission of extra particles in more central regions covered by the LHC detectors. The first advance in this direction, presented in this Chapter, is to propose new observables associated to the inclusive production of three jets: two of them are the original Mueller–Navelet jets, while the third one is tagged in central regions of rapidity.

When a jet central in rapidity is emitted in the final state, it is possible to single out an extra gluon emission by extracting its emission probability from the BFKL kernel. For further details and a more specific discussion, we refer to Refs. [142,169] and to the preliminary discussion given in Section 5.2.5, respectively. The three-jet cross section can be constructed in this way:

$$\begin{aligned}
\sigma^{3\text{-jet}}(s) &= \frac{1}{(2\pi)^2} \int \frac{d^2\vec{q}_1}{\vec{q}_1^2} \int \frac{d^2\vec{q}_2}{\vec{q}_2^2} \Phi_1(\vec{q}_1, s_0) \Phi_2(-\vec{q}_2, s_0) \\
&\times \int d^2\vec{q}_A \int d^2\vec{q}_B \int_{\delta-i\infty}^{\delta+i\infty} \frac{d\omega}{2\pi i} \left(\frac{s}{s_0}\right)^\omega G_\omega(\vec{q}_1, \vec{q}_A) \\
&\times \Phi_C(-\vec{q}_A, \vec{q}_B, s_0) \int_{\delta-i\infty}^{\delta+i\infty} \frac{d\omega'}{2\pi i} \left(\frac{s}{s_0}\right)^{\omega'} G'_{\omega'}(\vec{q}_B, \vec{q}_2),
\end{aligned} \tag{5.1}$$

where $\Phi_{1,2}$ are the two impact factors which describe the two forward/backward jets (as in the Mueller–Navelet case), while Φ_C is the central-jet emission vertex [142]. By selecting one emission to be exclusive we have factorised the Green’s function into two components. Each of them connects one of the external jets to the central one.

We will give predictions for the new azimuthal correlation momenta defined as

$$\mathcal{R}_{PQ}^{MN} = \frac{\langle \cos(M \Delta\phi_{\widehat{AJ}}) \cos(N \Delta\phi_{\widehat{JB}}) \rangle}{\langle \cos(P \Delta\phi_{\widehat{AJ}}) \cos(Q \Delta\phi_{\widehat{JB}}) \rangle}, \tag{5.2}$$

where $\Delta\phi_{\widehat{AJ}}$ and $\Delta\phi_{\widehat{JB}}$ are, respectively, the azimuthal-angle difference between the first and the second (central) jet and between this one and the third jet (see Fig. 5.1). The distribution ratios defined in Eq. (5.2) generalise the \mathcal{R}_{MN} ratios typical of two-body final-state processes, as the previously discussed Mueller–Navelet jet (see Chapter 3) and dihadron (see Chapter 4) production processes, by showing an extra dependence on transverse momentum and rapidity of the central jet. Cross sections are calculated using collinear factorisation to produce

the two most forward/backward jets, taking the convolution of the partonic cross section, which follows the BFKL dynamics, with collinear PDFs included in the forward jet vertex. These two Mueller–Navelet jet vertices are linked to the centrally produced jet via two BFKL Green’s functions. To simplify our predictions, we integrate over the momenta of all produced jets, using current LHC experimental cuts.

This Chapter is organised as follows: In Section 5.1 the main formulæ are given, including a first analysis at partonic level; in Section 5.2 hadronic level predictions are presented, with the inclusion of NLA BFKL corrections together with BLM scales and for three different kinematical configurations (see Sections 5.2.3, 5.2.4 and 5.2.5). The section Summary is given in 6.4.

The analysis given in this Chapter is based on the work done in Refs. [170–172] and presented in Refs. [153, 173–178].

5.1 A new way to probe BFKL

5.1.1 The three-jet cross section

The process under investigation (see Figs. 5.1 and 5.2) is the production of two forward/backward jets, both characterised by high transverse momenta $\vec{k}_{A,B}$ and well separated in rapidity, together with a third jet produced in the central rapidity region and with possible associated minijet production. This corresponds to

$$p(p_1) + p(p_2) \rightarrow j_A(k_A) + j_C(k_J) + j_B(k_B) + \text{minijets} , \quad (5.3)$$

where j_A is the forward jet with transverse momentum \vec{k}_A and rapidity Y_A , j_B is the backward jet with transverse momentum \vec{k}_B and rapidity Y_B and j_C is the central jet with transverse momentum \vec{k}_J and rapidity y_J .

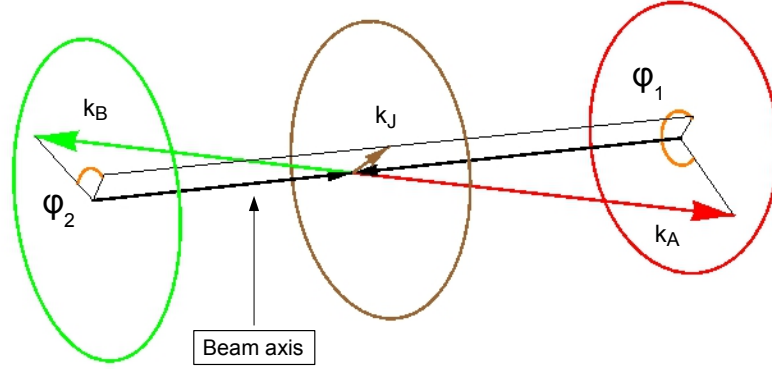


Figure 5.1: Representation of a three-jet event in a generic detector. All three circles are perpendicular to the beam axis.

In collinear factorisation the cross section for the process (5.3) reads

$$\frac{d\sigma^{3\text{-jet}}}{dk_A dY_A d\theta_A dk_B dY_B d\theta_B dk_J dy_J d\theta_J} = \sum_{r,s=q,\bar{q},g} \int_0^1 dx_1 \int_0^1 dx_2 f_r(x_1, \mu_F) f_s(x_2, \mu_F) d\hat{\sigma}_{r,s}^{3\text{-jet}}(\hat{s}, \mu_F), \quad (5.4)$$

where the r, s indices specify the parton types (quarks $q = u, d, s, c, b$; anti-quarks $\bar{q} = \bar{u}, \bar{d}, \bar{s}, \bar{c}, \bar{b}$; or gluon g), $f_{r,s}(x, \mu_F)$ are the initial proton PDFs; $x_{1,2}$ represent the longitudinal fractions of the partons involved in the hard subprocess; $d\hat{\sigma}_{r,s}^{3\text{-jet}}(\hat{s}, \mu_F)$ is the partonic cross section for the production of jets and $x_1 x_2 s \equiv \hat{s}$ is the squared center-of-mass energy of the hard subprocess (see Fig. 5.2). The BFKL dynamics enters in the cross section for the partonic hard subprocess $d\hat{\sigma}_{r,s}^{3\text{-jet}}$ (in the form of two forward Green's functions φ to be described in a while), which can be presented as (from here we start to use the

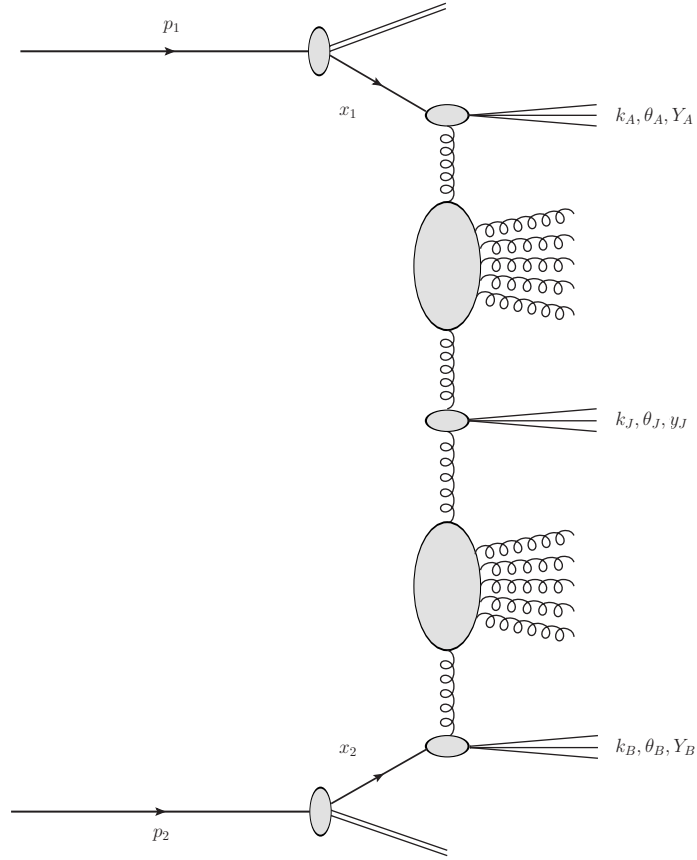


Figure 5.2: Inclusive three-jet production process in multi-Regge kinematics.

notation $k_{A,B,Y} \equiv |\vec{k}_{A,B,Y}|$, which holds in the following):

$$\frac{d\hat{\sigma}_{r,s}^{3\text{-jet}}}{dk_J d\theta_J dy_J} = \frac{\bar{\alpha}_s}{\pi k_J} \int d^2\vec{p}_A \int d^2\vec{p}_B \delta^{(2)}(\vec{p}_A + \vec{k}_J - \vec{p}_B) \quad (5.5)$$

$$\times \varphi(\vec{k}_A, \vec{p}_A, Y_A - y_J) \varphi(\vec{p}_B, \vec{k}_B, y_J - Y_B) ,$$

where $\bar{\alpha}_s = N_c/\pi\alpha_s$, with N_c the number of colours in QCD. In order to lie within MRK, we have considered the ordering in the rapidity of the produced particles $Y_A > y_J > Y_B$, while k_J^2 is always above the experimental resolution scale. $\varphi(\vec{p}, \vec{q}, 0)$ is a suitable redefinition of the BFKL Green's function, which now encode also the momentum two-dimensional delta coming from the LO jet function (Eq. (3.2)). In this way, some pieces of the LO jet vertex (Eq. (3.3))

are encoded in a very useful expression for the Green function, which holds at LLA.

It is possible algebraically manipulate the expression given in Eq. (5.5) in order to find distinct BFKL features. First of all, one can integrate the two-dimensional delta function in Eq. (5.5), to obtain

$$\frac{d\hat{\sigma}_{r,s}^{3\text{-jet}}}{d^2\vec{k}_J dy_J} = \frac{\bar{\alpha}_s}{\pi k_J^2} \int dp^2 d\theta \varphi(\vec{k}_A, \vec{p}, Y_A - y_J) \varphi(\vec{p} + \vec{k}_J, \vec{k}_B, y_J - Y_B). \quad (5.6)$$

Then, the Green's function can be expanded in Fourier components of the azimuthal angle to write:

$$\frac{d\hat{\sigma}_{r,s}^{3\text{-jet}}}{d^2\vec{k}_J dy_J} = \frac{\bar{\alpha}_s}{\pi k_J^2} \sum_{m,n=-\infty}^{+\infty} e^{i(m\theta_A - n\theta_B)} \Omega_{m,n}(\vec{k}_A, \vec{k}_B, Y_A, Y_B, \vec{k}_J, \theta_J, y_J), \quad (5.7)$$

where

$$\begin{aligned} & \Omega_{m,n}(\vec{k}_A, \vec{k}_B, Y_A, Y_B, \vec{k}_J, \theta_J, y_J) \\ &= \int_0^{+\infty} dp p \int_0^{2\pi} d\theta e^{i\left[n \arctan\left(\frac{p \sin \theta + k_J \sin \theta_J}{p \cos \theta + k_J \cos \theta_J}\right) - m\theta\right]} \varphi_m(|\vec{k}_A|, |\vec{p}_A|, Y_A - y_J) \\ & \times \varphi_n\left(\sqrt{p^2 + k_J^2 + 2|\vec{p}||\vec{k}_J| \cos(\theta - \theta_J)}, |\vec{p}_B|, y_J - Y_B\right). \end{aligned} \quad (5.8)$$

Here φ_i is the i -th azimuthal component of the Green's function obtained after the projection on the (ν, n) -space, whose LLA and NLA expressions are given respectively in Eqs. (5.12) and (5.21). Using the relation $\arctan \alpha = \frac{i}{2} \ln\left(\frac{1-i\alpha}{1+i\alpha}\right)$, which holds for any real α , one has

$$\begin{aligned} & \Omega_{m,n}(\vec{k}_A, \vec{k}_B, Y_A, Y_B, \vec{k}_J, \theta_J, y_J) \\ &= \int_0^{+\infty} dp p \int_0^{2\pi} d\theta e^{-im\theta} \left(\frac{pe^{i\theta} + k_J e^{i\theta_J}}{pe^{-i\theta} + k_J e^{-i\theta_J}}\right)^{\frac{n}{2}} \\ & \times \varphi_m(|\vec{k}_A|, |\vec{p}_A|, Y_A - y_J) \\ & \times \varphi_n\left(\sqrt{p^2 + k_J^2 + 2|\vec{p}||\vec{k}_J| \cos(\theta - \theta_J)}, |\vec{p}_B|, y_J - Y_B\right). \end{aligned} \quad (5.9)$$

The dependence on θ_J can be factorised out by making the change of variable $\theta - \theta_J \rightarrow \theta$. The final expression for $\Omega_{m,n}$ reads:

$$\begin{aligned} \Omega_{m,n} \left(\vec{k}_A, \vec{k}_B, Y_A, Y_B, \vec{k}_J, \theta_J, y_J \right) = & \quad (5.10) \\ e^{i(n-m)\theta_J} \int_0^{+\infty} dp p \int_0^{2\pi} d\theta \frac{e^{-im\theta} (pe^{i\theta} + k_J)^n}{\sqrt{\left(p^2 + k_J^2 + 2|\vec{p}||\vec{k}_J| \cos \theta\right)^n}} \\ \varphi_m \left(|\vec{k}_A|, |\vec{p}_A|, Y_A - y_J \right) \varphi_n \left(\sqrt{p^2 + k_J^2 + 2|\vec{p}||\vec{k}_J| \cos \theta}, |\vec{p}_B|, y_J - Y_B \right). \end{aligned}$$

In Sections 5.1.2 and 5.1.3 we investigate the properties of two new, generalised and suitable BFKL observables that the developed formalism allows us to define.

5.1.2 One-cosine projection: *À la* Mueller–Navelet

5.1.2.1 One-cosine azimuthal correlations

The first step is to integrate over the azimuthal angle of the central jet and over the difference in azimuthal angle between the two forward jets, $\Delta\phi = \theta_A - \theta_B - \pi$, to define a quantity similar to the usual Mueller–Navelet case, *i.e.*,

$$\begin{aligned} & \int_0^{2\pi} d\Delta\phi \cos(M\Delta\phi) \int_0^{2\pi} d\theta_J \frac{d\hat{\sigma}_{r,s}^{3\text{-jet}}}{dk_J d\theta_J dy_J} & (5.11) \\ & = \frac{\bar{\alpha}_s}{2\pi} \sum_{L=0}^M \int_0^\infty dp^2 \int_0^{2\pi} d\theta \frac{(-1)^M \binom{M}{L} (k_J^2)^{\frac{L-1}{2}} (p^2)^{\frac{M-L}{2}} \cos(L\theta)}{\sqrt{\left(p^2 + k_J^2 + 2|\vec{p}||\vec{k}_J| \cos \theta\right)^M}} \\ & \times \varphi_M^{(\text{LLA})} \left(|\vec{k}_A|, |\vec{p}|, Y_A - y_J \right) \\ & \times \varphi_M^{(\text{LLA})} \left(\sqrt{p^2 + k_J^2 + 2|\vec{p}||\vec{k}_J| \cos \theta}, |\vec{k}_B|, y_J - Y_B \right), \end{aligned}$$

where $\varphi_n^{(\text{LLA})}$ is the Green's function at LLA

$$\varphi_n^{(\text{LLA})} \left(|\vec{k}|, |\vec{q}|, y \right) = 2 \int_0^\infty dv \cos \left(v \ln \frac{k^2}{q^2} \right) \frac{e^{\bar{\alpha}_s \chi(n,v)y}}{\pi \sqrt{k^2 q^2}}. \quad (5.12)$$

It is worth to note that, since the LO jet vertex (Eq. (3.8)) does not depend on ν , we can let the Green's function encode the ν -integration. This second, suitable redefinition of the Green's function is no more valid when NLO jet vertices (Eq. (B.1)) are considered. One of the experimental observables we want to highlight here corresponds to the mean value of the cosine of $\Delta\phi$ in the recorded events:

$$\langle \cos(M(\Delta\phi)) \rangle_{d\hat{\sigma}_{r,s}^{3\text{-jet}}} = \frac{\int_0^{2\pi} d\Delta\phi \cos(M\Delta\phi) \int_0^{2\pi} d\theta_J \frac{d\hat{\sigma}_{r,s}^{3\text{-jet}}}{d^2\vec{k}_J dy_J}}{\int_0^{2\pi} d\Delta\phi \int_0^{2\pi} d\theta_J \frac{d\hat{\sigma}_{r,s}^{3\text{-jet}}}{d^2\vec{k}_J dy_J}}. \quad (5.13)$$

The perturbative stability (including renormalisation scale dependence) of the mean value defined above can be significantly improved (see Ref. [33] for a related discussion) if the contribution coming from the zero conformal spin, which corresponds to the index $n = 0$ in Eq. (5.12), is removed. This can be achieved by defining the ratios

$$\mathcal{R}_N^M = \frac{\langle \cos(M(\Delta\phi)) \rangle_{d\hat{\sigma}_{r,s}^{3\text{-jet}}}}{\langle \cos(N(\Delta\phi)) \rangle_{d\hat{\sigma}_{r,s}^{3\text{-jet}}}}, \quad (5.14)$$

where we consider M, N as positive integers.

5.1.2.2 Numerical analysis

The observables defined in Eq. (5.14) allow us to perform different kinds of analysis at the partonic level. A first study, where the transverse momenta of the forward jets are fixed to $k_A = 35$ GeV and $k_B = 38$ GeV, done in Ref. [170], is presented in this Section.

The rapidity of the central jet is also fixed to be one half of the rapidity difference between the two forward jets: $y_J = (Y_A - Y_B)/2$ simply because this allows us to connect with the well-known Mueller–Navelet jets. In this way one can study, *e.g.*, the behaviour of the ratio \mathcal{R}_1^2 in Fig. 5.3 for two values of

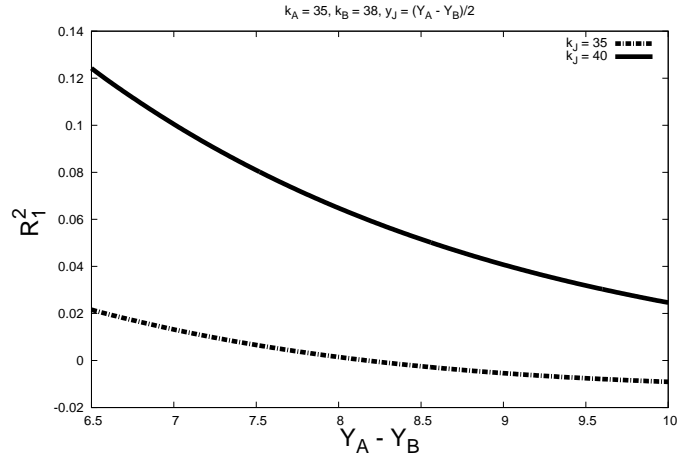


Figure 5.3: A study of the ratio \mathcal{R}_1^2 as defined in Eq. (5.14) for fixed values of the p_t of the two forward jets and two values of the p_t of the tagged central jet, as a function of the rapidity difference between the two forward jets for the rapidity of the central jet chosen as $y_J = (Y_A - Y_B)/2$.

the transverse momentum of the central jet $k_J = 35, 40$ GeV. We see that this ratio decreases as a function of $Y_A - Y_B$. This is a consequence of the increase of the available phase space for inclusive minijet radiation and that the $n = 1$ component decreases which energy slower than the $n = 2$ one.

In the BFKL formalism one has that the larger the n the slower the evolution with rapidity differences. This is very important since it is distinct from other approaches where QCD coherence is introduced as it was shown in Ref. [180].

5.1.3 Two-cosine projection: generalised azimuthal correlations

5.1.3.1 Two-cosine azimuthal correlations

In this Section new observables, whose associated distributions have a very different behaviour to the ones characteristic of the Mueller–Navelet case, are proposed. These new distributions are defined using the projections on the two

relative azimuthal angles formed by each of the forward jets with the central jet,

$$\begin{aligned}\Delta\phi_{\widehat{AJ}} &= \theta_A - \theta_J - \pi \\ \Delta\phi_{\widehat{JB}} &= \theta_J - \theta_B - \pi ,\end{aligned}\tag{5.15}$$

in the form

$$\begin{aligned}& \int_0^{2\pi} d\theta_A \int_0^{2\pi} d\theta_B \int_0^{2\pi} d\theta_J \cos(M\Delta\phi_{\widehat{AJ}}) \cos(N\Delta\phi_{\widehat{JB}}) \frac{d^3\sigma^{3\text{-jet}}}{dk_J d\theta_J dy_J} \\ &= \bar{\alpha}_s \sum_{L=0}^N \binom{N}{L} (k_J^2)^{\frac{L-1}{2}} \int_0^\infty dp^2 (p^2)^{\frac{N-L}{2}} \\ & \times \int_0^{2\pi} d\theta \frac{(-1)^{M+N} \cos(M\theta) \cos((N-L)\theta)}{\sqrt{(p^2 + k_J^2 + 2|\vec{p}||\vec{k}_J| \cos\theta)}^N} \\ & \times \varphi_M^{(\text{LLA})}(|\vec{k}_A|, |\vec{p}|, Y_A - y_J) \\ & \times \varphi_N^{(\text{LLA})}\left(\sqrt{p^2 + k_J^2 + 2|\vec{p}||\vec{k}_J| \cos\theta}, |\vec{k}_B|, y_J - Y_B\right) .\end{aligned}\tag{5.16}$$

The experimentally relevant observable is the mean value in the selected events of the two cosines, *i.e.*

$$\begin{aligned}& \langle \cos(M\Delta\phi_{\widehat{AJ}}) \cos(N\Delta\phi_{\widehat{JB}}) \rangle_{d\hat{\sigma}_{r,s}^{3\text{-jet}}} \\ &= \frac{\int_0^{2\pi} d\theta_A d\theta_B d\theta_J \cos(M\Delta\phi_{\widehat{AJ}}) \cos(N\Delta\phi_{\widehat{JB}}) \frac{d^3\sigma^{3\text{-jet}}}{d^2\vec{k}_J dy_J}}{\int_0^{2\pi} d\theta_A d\theta_B d\theta_J \frac{d^3\sigma^{3\text{-jet}}}{d^2\vec{k}_J dy_J}} .\end{aligned}\tag{5.17}$$

As done in Section 5.1.2.1, in order to have optimal perturbative convergence and eliminate collinear contamination, one can remove the contributions from zero conformal spin by defining the ratios:

$$\mathcal{R}_{PQ}^{MN} = \frac{\langle \cos(P\Delta\phi_{\widehat{AJ}}) \cos(Q\Delta\phi_{\widehat{JB}}) \rangle_{d\hat{\sigma}_{r,s}^{3\text{-jet}}}}{\langle \cos(M\Delta\phi_{\widehat{AJ}}) \cos(N\Delta\phi_{\widehat{JB}}) \rangle_{d\hat{\sigma}_{r,s}^{3\text{-jet}}}}\tag{5.18}$$

and consider $M, N, P, Q > 0$ as integer numbers.

5.1.3.2 Numerical analysis

Working with fixed kinematics, it is possible to investigate many momenta configurations (see Ref. [170]). As an example, the ratios \mathcal{R}_{22}^{11} , \mathcal{R}_{22}^{12} and \mathcal{R}_{22}^{21} are presented in Fig. 5.4, the momenta of the forward jets being fixed to $k_A = 40$ GeV and $k_B = 50$ GeV and their rapidities to $Y_A = 10$ and $Y_B = 0$. For the transverse momentum of the central jet the three values $k_J = 30, 45, 70$ GeV are chosen, the rapidity of the central jet y_J is allowed to take values in the range in between the two rapidities of the forward jets. These distributions are proving the fine structure of the QCD radiation in the high-energy limit. They gauge the relative weights of each conformal spin contribution to the total cross section.

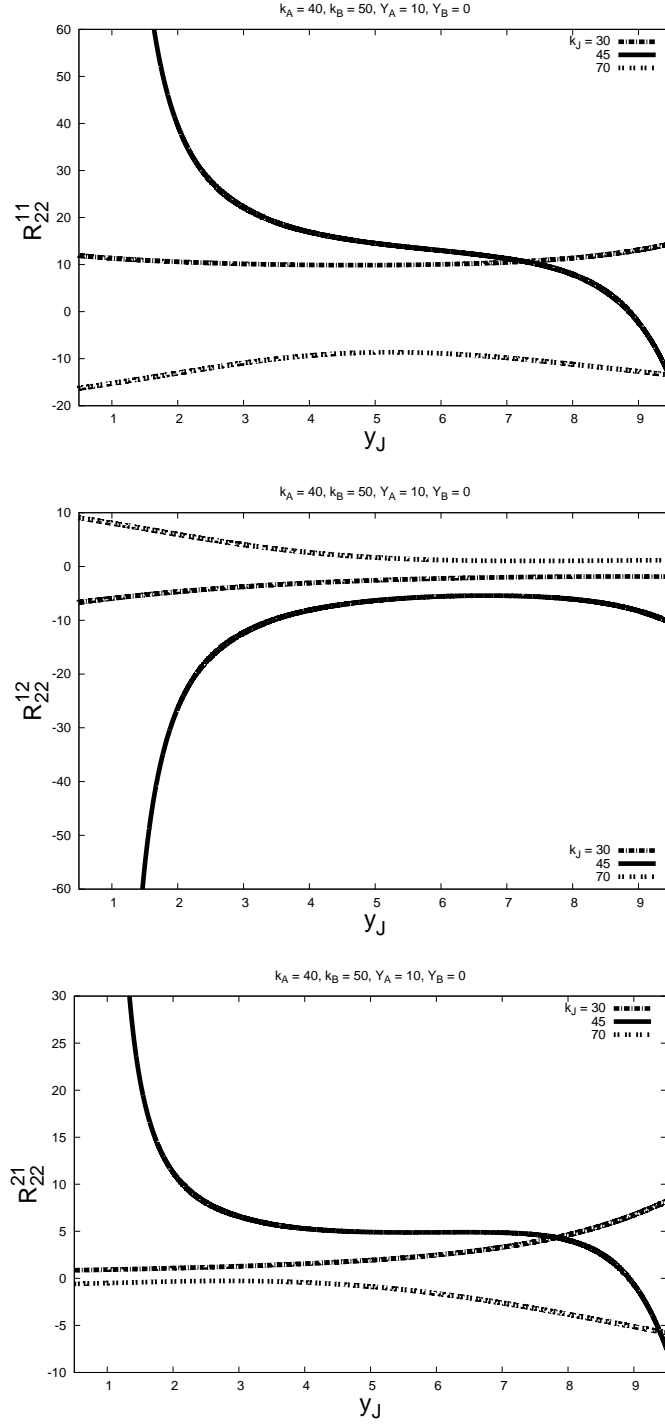


Figure 5.4: A study of the ratios \mathcal{R}_{22}^{11} , \mathcal{R}_{22}^{12} and \mathcal{R}_{22}^{21} as defined in Eq. (5.18) for fixed values of the p_t of the two forward jets and three values of the p_t of the tagged central jet, as a function of the rapidity of the central jet y_J .

5.2 Hadronic level predictions

In Section 5.1 the theoretical setup for the three-jet production in the BFKL approach was built up, and a first study at the partonic level was given. Here we continue and extend our analysis by giving predictions for the generalised azimuthal correlations at the hadronic level. The inclusion of the NLA contributions coming from the higher correction to the BFKL kernel is considered.

5.2.1 A more phenomenological analysis: inclusion of NLA kernel corrections

Using the definition of the LO jet vertex (Eq. (3.8)), the cross section given in Eq. (5.4) can be rewritten, according to Eq. (5.1), as

$$\begin{aligned}
 & \frac{d\sigma^{3\text{-jet}}}{dk_A dY_A d\theta_A dk_B dY_B d\theta_B dk_J dy_J d\theta_J} \\
 &= \frac{8\pi^3 C_F \bar{\alpha}_s^3}{N_c^3} \frac{x_{J_A} x_{J_B}}{k_A k_B k_J} \int d^2\vec{p}_A \int d^2\vec{p}_B \delta^{(2)}(\vec{p}_A + \vec{k}_J - \vec{p}_B) \\
 & \times \left(\frac{N_c}{C_F} f_g(x_{J_A}, \mu_F) + \sum_{r=q,\bar{q}} f_r(x_{J_A}, \mu_F) \right) \\
 & \times \left(\frac{N_c}{C_F} f_g(x_{J_B}, \mu_F) + \sum_{s=q,\bar{q}} f_s(x_{J_B}, \mu_F) \right) \\
 & \times \varphi(\vec{k}_A, \vec{p}_A, Y_A - y_J) \varphi(\vec{p}_B, \vec{k}_B, y_J - Y_B) .
 \end{aligned} \tag{5.19}$$

In MRK characteristic ordering in rapidity is achieved by imposing that $Y_A > y_J > Y_B$, while k_J^2 is always above the experimental resolution scale. $x_{J_{A,B}}$ are the longitudinal momentum fractions of the two external jets, linked to the respective rapidities $Y_{A,B}$ by the relation $x_{A,B} = k_{A,B} e^{\pm Y_{A,B}} / \sqrt{s}$.

Our goal is to study observables for which the BFKL approach will be distinct from other formalisms and also rather insensitive to possible higher-order

corrections. Following the course taken in Section 5.1.3, we focus on new quantities whose associated distributions are different from the ones which characterise the Mueller–Navelet case, though still related to the azimuthal-angle correlations by projecting differential cross section on the two relative azimuthal angles between each external jet and the central one $\Delta\phi_{\widehat{A}J, \widehat{B}}$ defined in Eq. (5.15) (see also Fig. 5.5). Taking into account the factors coming from the jet vertices, it is possible to rewrite the projection of the differential cross section on the azimuthal-angle differences in the form

$$\begin{aligned}
 & \int_0^{2\pi} d\theta_A \int_0^{2\pi} d\theta_B \int_0^{2\pi} d\theta_J \cos(M\Delta\phi_{\widehat{A}J}) \cos(N\Delta\phi_{\widehat{B}}) \\
 & \quad \frac{1}{d\sigma^{3\text{-jet}}} \\
 & \frac{1}{dk_A dY_A d\theta_A dk_B dY_B d\theta_B dk_J dy_J d\theta_J} \\
 & = \frac{8\pi^4 C_F \bar{\alpha}_s^3}{N_C^3} \frac{x_{JA} x_{JB}}{k_A k_B} \left(\frac{N_C}{C_F} f_g(x_{JA}, \mu_F) + \sum_{r=q, \bar{q}} f_r(x_{JA}, \mu_F) \right) \\
 & \times \left(\frac{N_C}{C_F} f_g(x_{JB}, \mu_F) + \sum_{s=q, \bar{q}} f_s(x_{JB}, \mu_F) \right) \sum_{L=0}^N \binom{N}{L} (k_J^2)^{\frac{L-1}{2}} \\
 & \times \int_0^\infty dp^2 (p^2)^{\frac{N-L}{2}} \int_0^{2\pi} d\theta \frac{(-1)^{M+N} \cos(M\theta) \cos((N-L)\theta)}{\sqrt{(p^2 + k_J^2 + 2|\vec{p}||\vec{k}_J| \cos\theta)^N}} \\
 & \times \varphi_M^{(\text{LLA}, \text{NLA})}(|\vec{k}_A|, |\vec{p}|, Y_A - y_J) \\
 & \times \varphi_N^{(\text{LLA}, \text{NLA})} \left(\sqrt{p^2 + k_J^2 + 2|\vec{p}||\vec{k}_J| \cos\theta}, \text{vec}k_B, y_J - Y_B \right).
 \end{aligned} \tag{5.20}$$

In this expression the Green’s function is either at LLA ($\varphi^{(\text{LLA})}$), whose expression is given in Eq. (5.12), or at NLA ($\varphi^{(\text{NLA})}$) accuracy. In particular, at NLA it reads

$$\varphi_n^{(\text{NLA})}(|\vec{k}|, |\vec{q}|, y) = 2 \int_0^\infty d\nu \cos\left(\nu \ln \frac{k^2}{q^2}\right) \frac{e^{\bar{\alpha}_s (\chi(n, \nu) + \bar{\alpha}_s \chi^{(1)}(n, \nu)) Y}}{\pi \sqrt{k^2 q^2}}, \tag{5.21}$$

with $\chi(n, \nu)$ and $\chi^{(1)}(n, \nu)$ given in Eqs. (2.53) and (2.59), respectively.

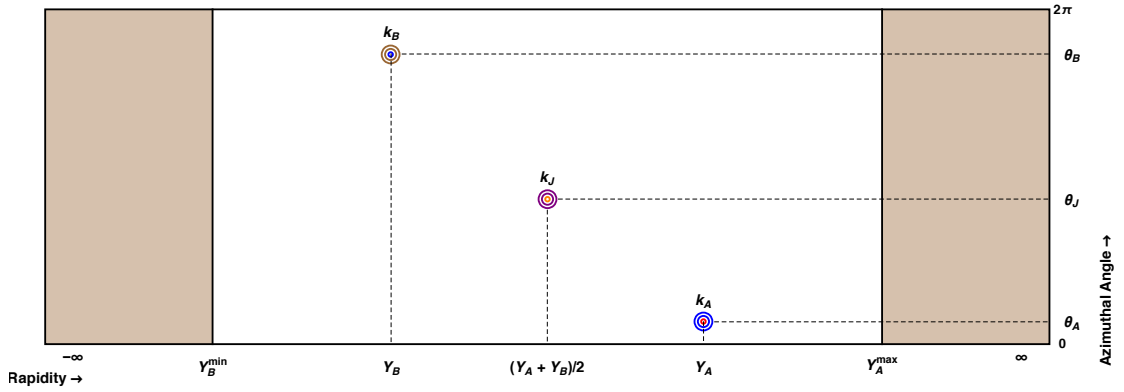


Figure 5.5: A primitive lego plot depicting a three-jet event. k_A is a forward jet with large positive rapidity Y_A and azimuthal angle θ_A , k_B is a forward jet with large negative rapidity Y_B and azimuthal angle θ_B and k_J is a central jet with rapidity Y_J and azimuthal angle θ_J . The fade-brown areas to the left and right highlight the regions in rapidity which are not covered by the standard detectors.

The experimental observables we initially proposed are based on the partonic-level average values (with M, N being positive integers)

$$\mathcal{C}_{MN} = \langle \cos \left(M \Delta \phi_{\widehat{A}J} \right) \cos \left(N \Delta \phi_{\widehat{J}B} \right) \rangle \quad (5.22)$$

$$= \frac{\int_0^{2\pi} d\theta_A d\theta_B d\theta_J \cos \left(M \Delta \phi_{\widehat{A}J} \right) \cos \left(N \Delta \phi_{\widehat{J}B} \right) d\sigma^{3\text{-jet}}}{\int_0^{2\pi} d\theta_A d\theta_B d\theta_J d\sigma^{3\text{-jet}}},$$

whereas, in order to provide testable predictions for the current and future experimental data, we introduce the hadronic-level values C_{MN} after integrating $\mathcal{C}_{M,N}$ over the momenta of the tagged jets, as we will see in the following Sections.

From a more theoretical perspective, it is important to have as good as possible perturbative stability in our predictions (see also Section 5.1.3.1). This can be achieved by removing the contribution stemming from the zero conformal spin, which corresponds to the index $n = 0$ in Eqs. (5.12) and (5.21). We,

therefore, introduce the ratios

$$R_{PQ}^{MN} = \frac{C_{MN}}{C_{PQ}} \quad (5.23)$$

which are free from any $n = 0$ dependence, as long as $M, N, P, Q > 0$. The postulate that Eq. (5.23) generally describes observables with good perturbative stability is under scrutiny in Sections 5.2.3, 5.2.4, and 5.2.5, where we compare LLA and NLA results.

5.2.2 BLM scale setting

In order to make an appropriate choice of the renormalisation scale μ_R , the BLM prescription [118–122] is used. As explained in Section 2.4, it consists of using the MOM scheme and choosing the scale μ_R such that the β_0 -dependence of a given observable vanishes. Applying the BLM prescription leads to the modification of the exponent in Eq. (5.21) in the following way:

$$\bar{\alpha}_s \left(\chi(n, \nu) + \bar{\alpha}_s \chi^{(1)}(n, \nu) \right) Y \rightarrow \bar{\alpha}_s \left(\chi(n, \nu) \left(1 + \frac{\alpha_s}{\pi} T \right) + \bar{\alpha}_s \chi^{(1)}(n, \nu) \right) Y, \quad (5.24)$$

with T given in (2.81). Note that this way to implement BLM is a generalisation of the case (b), given in Eq. (2.87). In the three-jet case, we remove the β_0 dependent factors from the NLA objects present in Eq. (5.20), *i.e.* the NLA Green's functions.

Following this procedure, the renormalisation scale μ_R is fixed at the value

$$(\mu_R^{\text{BLM}})^2 = k_A k_B \exp \left[\frac{1 + 4I}{3} + \frac{1}{2} \chi(n, \nu) \right]. \quad (5.25)$$

In our numerical analysis we consider two cases. In one, we set $\mu_R = \mu_R^{\text{BLM}}$ only in the exponential factor of the Green's function φ_n , while we let the argument of the $\bar{\alpha}_s^3$ in Eq. (5.20) to be at the “natural” scale $\sqrt{k_A k_B}$, that is,

$\bar{\alpha}_s^3 \sqrt{k_A k_B}$. In the second case, we fix $\mu_R = \mu_R^{\text{BLM}}$ everywhere in Eq. (5.20). These two cases lead in general to two different but similar values for our NLA predictions and wherever we present plots we fill the space in between so that we end up having a band instead of a single curve for the NLA observables. The band represents the uncertainty that comes into play after using the BLM prescription since there is no unambiguous way to apply it.

5.2.3 Fixed rapidity kinematics for the central jet

In this Section, results for three generalised ratios, R_{22}^{12} , R_{33}^{12} and R_{33}^{22} are presented, assuming that the central jet is fixed in rapidity at $y_J = (Y_A + Y_B)/2$ (see Fig. 5.5). In particular,

$$C_{MN} = \int_{Y_A^{\min}}^{Y_A^{\max}} dY_A \int_{Y_B^{\min}}^{Y_B^{\max}} dY_B \int_{k_A^{\min}}^{k_A^{\max}} dk_A \int_{k_B^{\min}}^{k_B^{\max}} dk_B \int_{k_J^{\min}}^{k_J^{\max}} dk_J \delta(Y_A - Y_B - Y) \mathcal{C}_{MN}, \quad (5.26)$$

where the forward jet rapidity is taken in the range delimited by $0 < Y_A < 4.7$, the backward jet rapidity in the range $-4.7 < Y_B < 0$, while their difference $Y \equiv Y_A - Y_B$ is kept fixed at definite values in the range $5.5 < Y < 9$.

It is possible to study the ratios R_{PQ}^{MN} in Eq. (5.23) as functions of the rapidity difference Y between the most forward and the most backward jets for a set of characteristic values of M, N, P, Q and for two different center-of-mass energies: $\sqrt{s} = 7$ and $\sqrt{s} = 13$ TeV. Since we are integrating over k_A and k_B , we have the opportunity to impose either *symmetric* or *asymmetric* kinematical cuts, as it has been previously done in Mueller–Navelet studies. Here, and in the next two Sections, we choose to study the *asymmetric* cut which presents certain advantages over the *symmetric* one (see Section 3.3 and Refs. [32, 46]). To be more precise, we set $k_A^{\min} = 35$ GeV, $k_B^{\min} = 50$ GeV, $k_A^{\max} = k_B^{\max} = 60$ GeV throughout the whole analysis.

In order to be as close as possible to the characteristic rapidity ordering of

the MRK, we set the value of the central jet rapidity such that it is equidistant to Y_A and Y_B by imposing the condition $y_J = (Y_A + Y_B)/2$. Moreover, since the tagging of a central jet permits us to extract more exclusive information from our observables, we allow three possibilities for the transverse momentum k_J , that is, $20 \text{ GeV} < k_J < 35 \text{ GeV}$ (bin-1), $35 \text{ GeV} < k_J < 60 \text{ GeV}$ (bin-2) and $60 \text{ GeV} < k_J < 120 \text{ GeV}$ (bin-3). Keeping in mind that the forward/backward jets have transverse momenta in the range $[35 \text{ GeV}, 60 \text{ GeV}]$, restricting the value of k_J within these three bins allows us to see how the ratio R_{PQ}^{MN} changes behaviour depending on the relative size of the central jet momentum when compared to the forward/backward ones. Throughout the whole Section 6.3, we will keep the same setup regarding bin-1, bin-2 and bin-3 which roughly correspond to the cases of k_J being ‘smaller’ than, ‘similar’ to and ‘larger’ than k_A , k_B , respectively.

Finally, apart from the functional dependence of the ratios on Y we will also show the relative corrections when we go from LLA to NLA. To be more precise, we define

$$\delta\chi(\%) = \left(\text{res}^{(\text{LLA})} - \frac{\text{res}^{(\text{BLM-1})} + \text{res}^{(\text{BLM-2})}}{2} \right) \frac{1}{\text{res}^{(\text{LLA})}}. \quad (5.27)$$

$\text{res}^{(\text{BLM-1})}$ is the BLM NLA result for $\mu_R = \mu_R^{\text{BLM}}$ only in the Green’s function while the cubed term of the strong coupling in Eq. (5.20) actually reads $\bar{\alpha}_s^3 = \bar{\alpha}_s^3(\sqrt{k_A k_B})$. $\text{res}^{(\text{BLM-2})}$ is the BLM NLA result for $\mu_R = \mu_R^{\text{BLM}}$ everywhere in Eq. (5.20), therefore, $\bar{\alpha}_s^3 = \bar{\alpha}_s^3(\mu_R^{\text{BLM}})$, as was previously discussed in Section 5.2.1.

In the following, we present our results for R_{22}^{12} , R_{33}^{12} and R_{33}^{22} , with $y_J = (Y_A + Y_B)/2$, collectively in Fig. 5.8 ($\sqrt{s} = 7 \text{ TeV}$) and Fig. 5.9 ($\sqrt{s} = 13 \text{ TeV}$). In the left column we are showing plots for $R_{PQ}^{MN}(Y)$ whereas to the right we are showing the corresponding $\delta\chi(\%)$ between LLA and NLA corrections. The

LLA results are represented with dashed lines whereas the NLA ones with a continuous band. The boundaries of the band are the two different curves we obtain by the two different approaches in applying the BLM prescription. Since there is no definite way to choose one in favour of the other, we allow for any possible value in between and hence we end up with a band. In many cases, as we will see in the following, the two boundaries are so close that the band almost degenerates into a single curve. The red curve (band) corresponds to k_J bounded in bin-1, the green curve (band) to k_J bounded in bin-2 and finally the blue curve (band) to k_J bounded in bin-3. For the $\delta\chi(\%)$ plots we only have three curves, one for each of the three different bins of k_J .

A first observation from inspecting Figs. 5.8 and 5.9 is that the dependence of the different observables on the rapidity difference between k_A and k_B is rather smooth. R_{22}^{12} (top row in Figs. 5.8 and 5.9) at $\sqrt{s} = 7$ TeV and for k_J in bin-1 and bin-3 exhibits an almost linear behaviour with Y both at LLA and NLA, whereas at $\sqrt{s} = 13$ TeV the linear behaviour is extended also for k_J in bin-2. The difference between the NLA BLM-1 and BLM-2 values is small, to the point that the blue and the red bands collapse into a single line which in addition lies very close to the LLA results. When k_J is restricted in bin-2 (green curve/band), the uncertainty from applying the BLM prescription in two different ways seems to be larger. The relative NLA corrections at both colliding energies are very modest ranging from close to 1% for k_J in bin-3 to less than 10% for k_J in the other two bins. R_{33}^{12} (middle row in Figs. 5.8 and 5.9) compared to R_{22}^{12} , shows a larger difference between BLM-1 and BLM-2 values for k_J in bin-1 and bin-2. The ‘green’ corrections lower the LLA estimate whereas the ‘red’ ones make the corresponding LLA estimate less negative. The corrections are generally below 20%, in particular, ‘blue’ $\sim 5\%$, ‘red’ $\sim 10\%$ and ‘green’ $\sim 20\%$. Finally, R_{33}^{22} (bottom row in Figs. 5.8 and 5.9) also shows a larger dif-

ference between BLM-1 and BLM-2 values for k_j in bin-1 and less so for k_j in bin-2. Here, the ‘red’ corrections lower the LLA estimate whereas the ‘green’ ones make the corresponding LLA estimate less negative. The corrections are smaller than the ones for R_{33}^{12} and somehow larger than the corrections for R_{22}^{12} , specifically, ‘blue’ $\sim 5\%$, ‘red’ $\sim 5\%$ and ‘green’ $\sim 15\%$. Noticeably, while for R_{22}^{12} and R_{33}^{12} the corrections are very similar at $\sqrt{s} = 7$ and $\sqrt{s} = 13$ TeV, the ‘green’ R_{33}^{22} receives larger corrections at $\sqrt{s} = 7$ TeV. One important conclusion we would like to draw after comparing Figs. 5.8 and 5.9 is that, in general, for most of the observables there are no striking changes when we increase the colliding energy from 7 to 13 TeV. This indicates that a sort of asymptotic regime has been approached for the kinematical configurations included in our analysis. It also tells us that our observables are really as insensitive as possible to effects which have their origin outside the BFKL dynamics and which normally cannot be isolated (*e.g.* influence from the PDFs) with a possible exclusion at the higher end of the plots, when $Y \sim 8.5 - 9$. There, some of the observables and by that we mean the ‘red’, ‘green’ or ‘blue’ cases of R_{22}^{12} , R_{33}^{12} and R_{33}^{22} , exhibit a more curved rather than linear behaviour with Y at $\sqrt{s} = 7$ TeV.

5.2.4 Dependence of the generalised azimuthal correlations on the central-jet rapidity bin

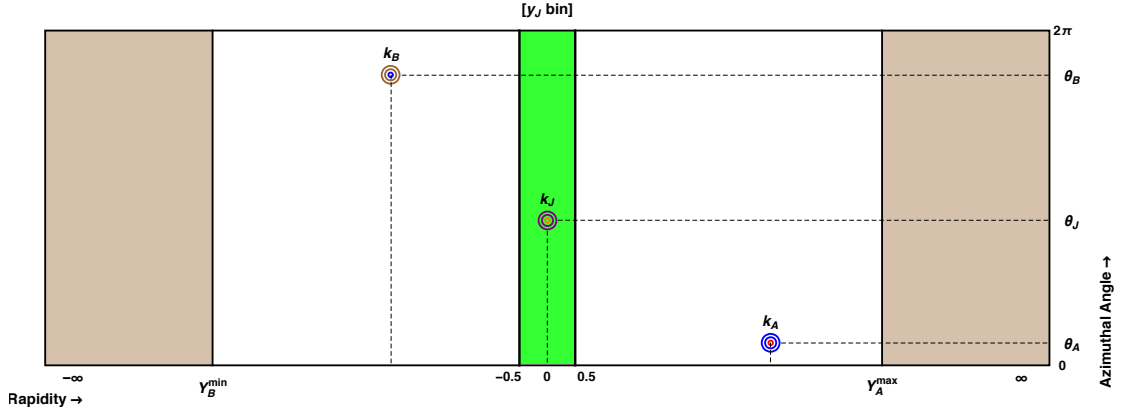


Figure 5.6: A primitive lego plot depicting a three-jet event similar to Fig. 5.5. Here, however, the central jet can take any value in the rapidity range $-0.5 < y_J < 0.5$.

In this Section, everything is kept the same as in Section 5.2.4 with the exemption of the allowed values for y_J (see Fig. 5.6). While in the previous Section $y_J = (Y_A + Y_B)/2$, here y_J is not anymore dependent on the rapidity difference between the outermost jets, Y , and is allowed to take values in a rapidity bin around $y_J = 0$. In particular, $-0.5 < y_J < 0.5$, which in turn means that an additional integration over y_J needs to be considered in Eq. (5.26) with $y_J^{\min} = -0.5$ and $y_J^{\max} = 0.5$:

$$C_{MN}^{(i)} = \int_{y_J^{\min}}^{y_J^{\max}} dy_J \int_{Y_A^{\min}}^{Y_A^{\max}} dY_A \int_{Y_B^{\min}}^{Y_B^{\max}} dY_B \int_{k_A^{\min}}^{k_A^{\max}} dk_A \int_{k_B^{\min}}^{k_B^{\max}} dk_B \int_{k_J^{\min}}^{k_J^{\max}} dk_J \delta(Y_A - Y_B - Y) C_{MN}, \quad (5.28)$$

We define our observables ${}^{(i)}R_{PQ}^{MN}$:

$${}^{(i)}R_{PQ}^{MN} = \frac{C_{MN}^{(i)}}{C_{PQ}^{(i)}}. \quad (5.29)$$

The results for the ${}^{(i)}R_{22}^{12}$, ${}^{(i)}R_{33}^{12}$ and ${}^{(i)}R_{33}^{22}$ are shown in Figs. 5.10 and 5.11. We notice immediately that Fig. 5.8 is very similar to the integrated over y_J observables Fig. 5.10 and the same holds for Figs. 5.9 and 5.11. Therefore, we will not discuss here the individual behaviours of R_{22}^{12} , R_{33}^{12} and R_{33}^{22} with Y , neither the $\delta\chi(\%)$ corrections, since this would only mean to repeat the discussion of Section 5.2.3. We would like only to note that the striking similarity between Fig. 5.8 and Fig. 5.10 and between Fig. 5.9 and Fig. 5.11 was to be expected if we remember that the partonic-level quantities \mathcal{R}_{pQ}^{MN} do not change noticeably if we vary the position in rapidity of the central jet, as long as the position remains ‘sufficiently’ central (see Ref. [170]). This property is very important and we will discuss it more in the next Section. Here, we should stress that the observables as presented in this Section can be readily compared to experimental data.

5.2.5 Dependence of the generalised azimuthal correlations on a forward-, backward- and central-rapidity bin

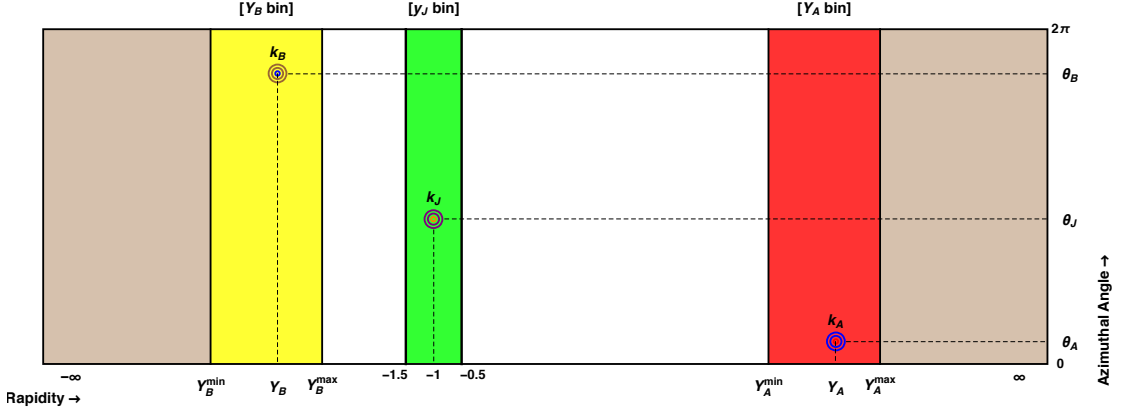


Figure 5.7: A primitive lego plot depicting a three-jet event similar to Figs. 5.5 and 5.6. Here, however, the rapidity of the central jet can take any value in the distinct ranges $y_i - 0.5 < y_J < y_i + 0.5$, where y_i is the central value of the rapidity bin with $y_i = \{-1, -0.5, 0, 0.5, 1\}$. In this figure, $y_i = -1$. Moreover, $Y = Y_A - Y_B$ is not anymore fixed. Instead, the forward jet has a rapidity restricted in the red bin whereas the backward jet in the yellow bin.

In this Section, an alternative kinematical configuration (see Fig. 5.7) for the generalised ratios R_{PQ}^{MN} is presented, whose choice relies on two reasons. The first one is to offer a different setup for which the comparison between theoretical predictions and experimental data might be easier, compared to the previous Section. The second one, to demonstrate that the generalised ratios do capture the Bethe–Salpeter characteristics [179] of the BFKL radiation. The latter needs a detailed explanation.

Let us assume that we have a gluonic ladder exchanged in the t-channel between a forward jet (at rapidity Y_A) and a backward jet (at rapidity Y_B) accounting for minijet activity between the two jets. By gluonic ladder here we mean the Green’s function $\varphi(\vec{p}_A, \vec{p}_B, Y_A - Y_B)$, where \vec{p}_A and \vec{p}_B are the Reggeised momenta connected to the forward and backward jet vertex respectively. It is

known that the following relation holds for the Green's function:

$$\varphi(\vec{p}_A, \vec{p}_B, Y_A - Y_B) = \int d^2\vec{k} \varphi(\vec{p}_A, \vec{k}, Y_A - y) \varphi(\vec{k}, \vec{p}_B, y - Y_B). \quad (5.30)$$

In other words, one may 'cut' the gluonic ladder at any rapidity y between Y_A and Y_B and then integrate over the Reggeised momentum \vec{k} that flows in the t -channel, to recover the initial ladder. Which value of y one chooses to 'cut' the ladder at is irrelevant. Therefore, observables directly connected to a realisation of the r.h.s of Eq. (5.30) should display this y -independence.

In our study actually, we have a very similar picture as the one described in the r.h.s of Eq. (5.30). The additional element is that we do not only 'cut' the gluonic ladder but we also 'insert' a jet vertex for the central jet. This means that the y -independence we discussed above should be present in one form or another. To be precise, we do see the y -independence behaviour but now we have to consider the additional constraint that y cannot take any extreme values, that is, it cannot be close to Y_A or Y_B . For a more detailed discussion of Eq. (5.30), we refer the reader to Appendix D), here we will proceed to present our numerical results.

The kinematical setup now is different than in the previous Sections. We allow Y_A and Y_B to take values such that $(Y_A^{\min} = 3) < Y_A < (Y_A^{\max} = 4.7)$ and $(Y_B^{\min} = -4.7) < Y_B < (Y_B^{\max} = -3)$. Moreover, we allow for the rapidity of the central jet to take values in five distinct rapidity bins of unit width, that is, $y_i - 0.5 < y_J < y_i + 0.5$, with $y_i = \{-1, -0.5, 0, 0.5, 1\}$ and we define the coefficients $C_{MN}^{(i)}(y_i)$ as function of y_i :

$$C_{MN}^{(i)}(y_i) = \int_{y_i-0.5}^{y_i+0.5} dy_J \int_{Y_A^{\min}}^{Y_A^{\max}} dY_A \int_{Y_B^{\min}}^{Y_B^{\max}} dY_B \int_{k_A^{\min}}^{k_A^{\max}} dk_A \int_{k_B^{\min}}^{k_B^{\max}} dk_B \int_{k_J^{\min}}^{k_J^{\max}} dk_J \mathcal{C}_{MN}. \quad (5.31)$$

We denote our observables by ${}^{(i)}R_{PQ}^{MN}$, which are now functions of y_i instead

of Y :

$$R_{PQ}^{MN}(y_i) = \frac{C_{MN}^{(i)}(y_i)}{C_{PQ}^{(i)}(y_i)}. \quad (5.32)$$

We present our results in Figs. 5.12 and 5.13. We see that indeed, the y_i -dependence of the three ratios is very weak. Moreover, the similarity between the $\sqrt{s} = 7$ TeV and $\sqrt{s} = 13$ TeV plots is more striking than in the previous Sections. The relative NLA to LLA corrections seem to be slightly larger here than in the previous Sections. We would like to stress once more that the results in this Section are readily comparable to the experimental data once the same cuts are applied in the experimental analysis.

5.2.6 Numerical tools

The numerical computation of the \mathcal{R}_{PQ}^{MN} ratios presented in Sections 5.2.3, 5.2.4 and 5.2.5 were done both in FORTRAN and in MATHEMATICA (mainly for cross-checks). The NLO MSTW 2008 PDF sets [144] were used ¹ and a two-loop running coupling setup with $\alpha_s(M_Z) = 0.11707$ was chosen with five quark flavours active. An extensive use of the integration routine Vegas [181] was made, as implemented in the Cuba library [182, 183]. Furthermore, Quadpack library [184] and a slightly modified version of the Psi [148] routine were used.

5.3 Summary

The first complete phenomenological analysis for the inclusive three-jet production was presented. New azimuthal-angle-dependent observables, the R_{PQ}^{MN}

¹Other potential sources of uncertainty could be due to the particular PDF sets one uses. One can still argue though that the uncertainty due to different PDF sets does not need to be ascertained before one has gauged how large are the full beyond the LLA corrections to the partonic-level ratios, since it will be overshadowed by the latter. Indeed, from first tries we see no significant difference in the results when we work with different PDF sets and therefore we do not offer any dedicated analysis on that here.

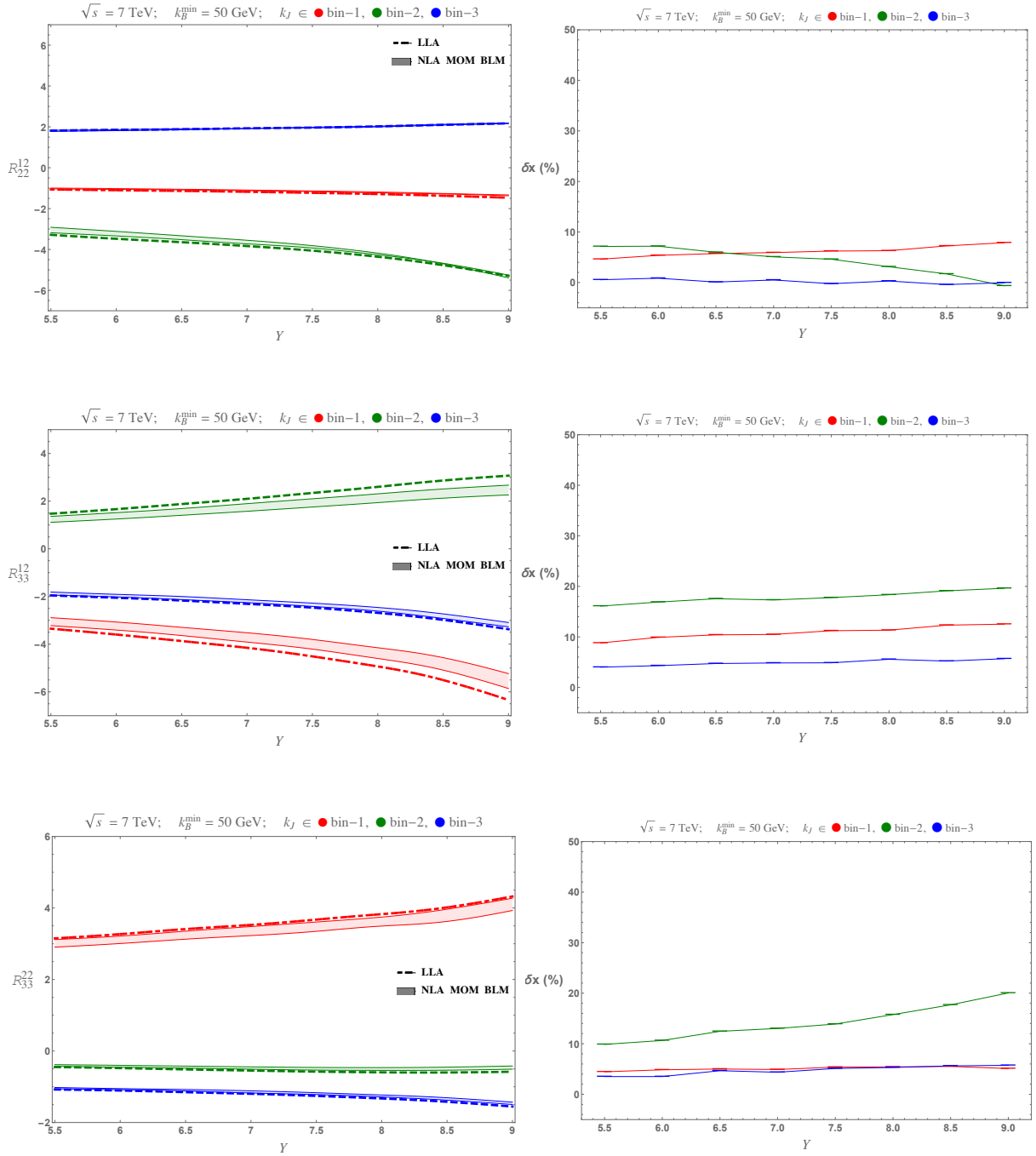


Figure 5.8: LLA and NLA R_{22}^{12} , R_{33}^{12} , and R_{33}^{22} at $\sqrt{s} = 7$ TeV with y_J fixed (left) and the relative NLA to LLA corrections (right).

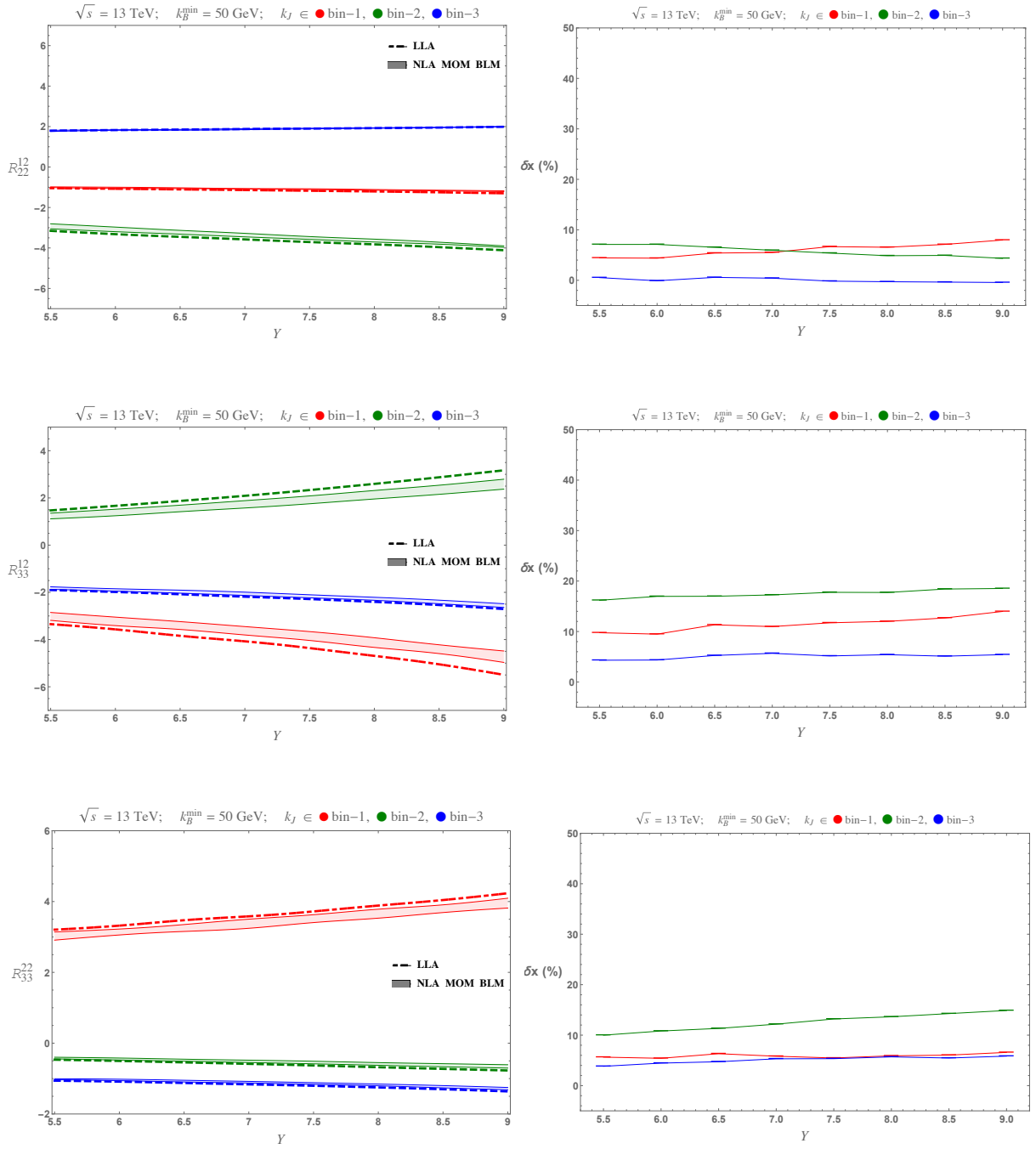


Figure 5.9: Y -dependence of the LLA and NLA R_{22}^{12} , R_{33}^{12} , and R_{33}^{22} at $\sqrt{s} = 13$ TeV with y_J fixed (left) and the relative NLA to LLA corrections (right).

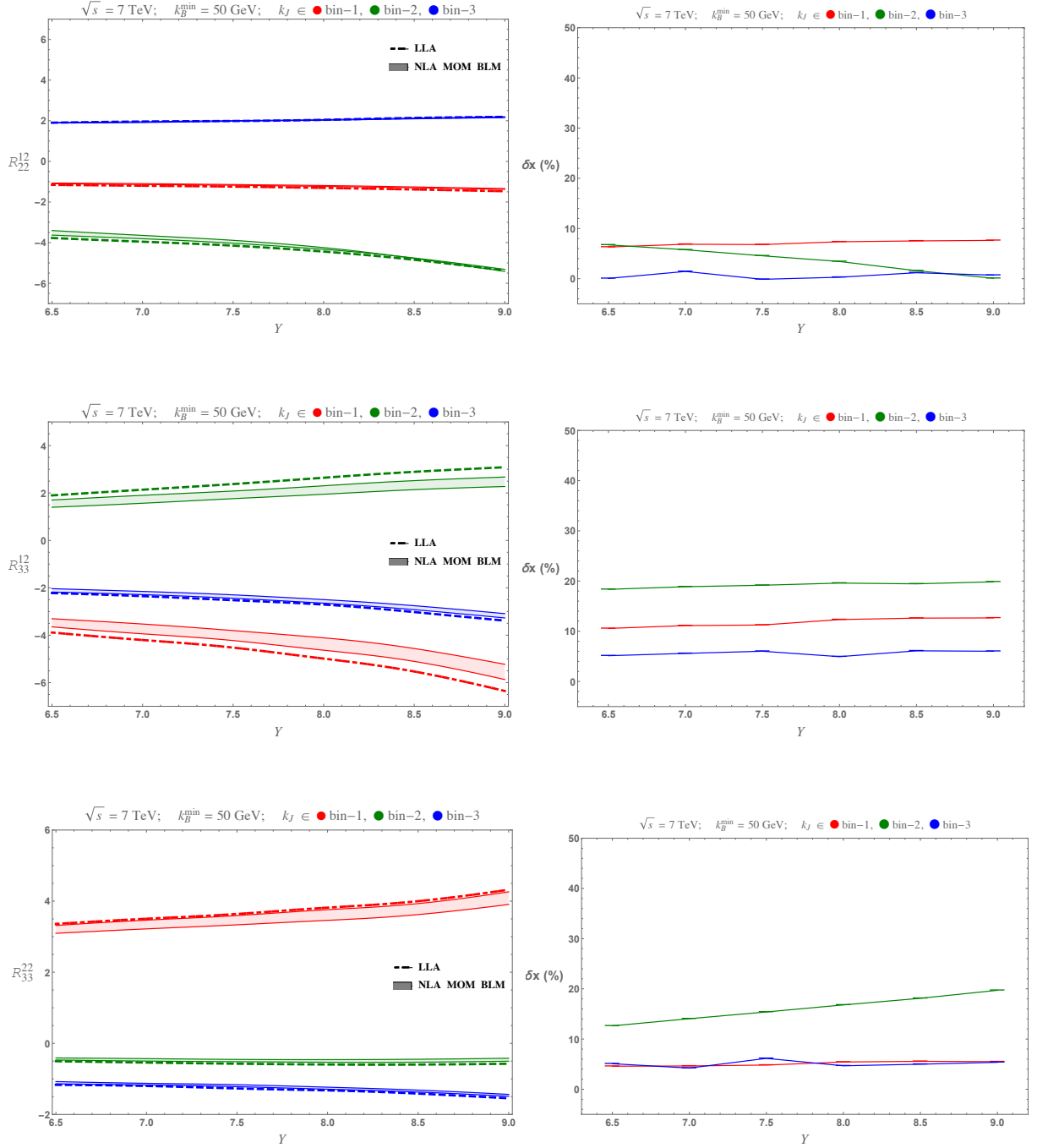


Figure 5.10: LLA and NLA $(i)R_{22}^{12}$, $(i)R_{33}^{12}$, and $(i)R_{33}^{22}$ at $\sqrt{s} = 7$ TeV with y_J integrated over a central rapidity bin (left) and the relative NLA to LLA corrections (right).

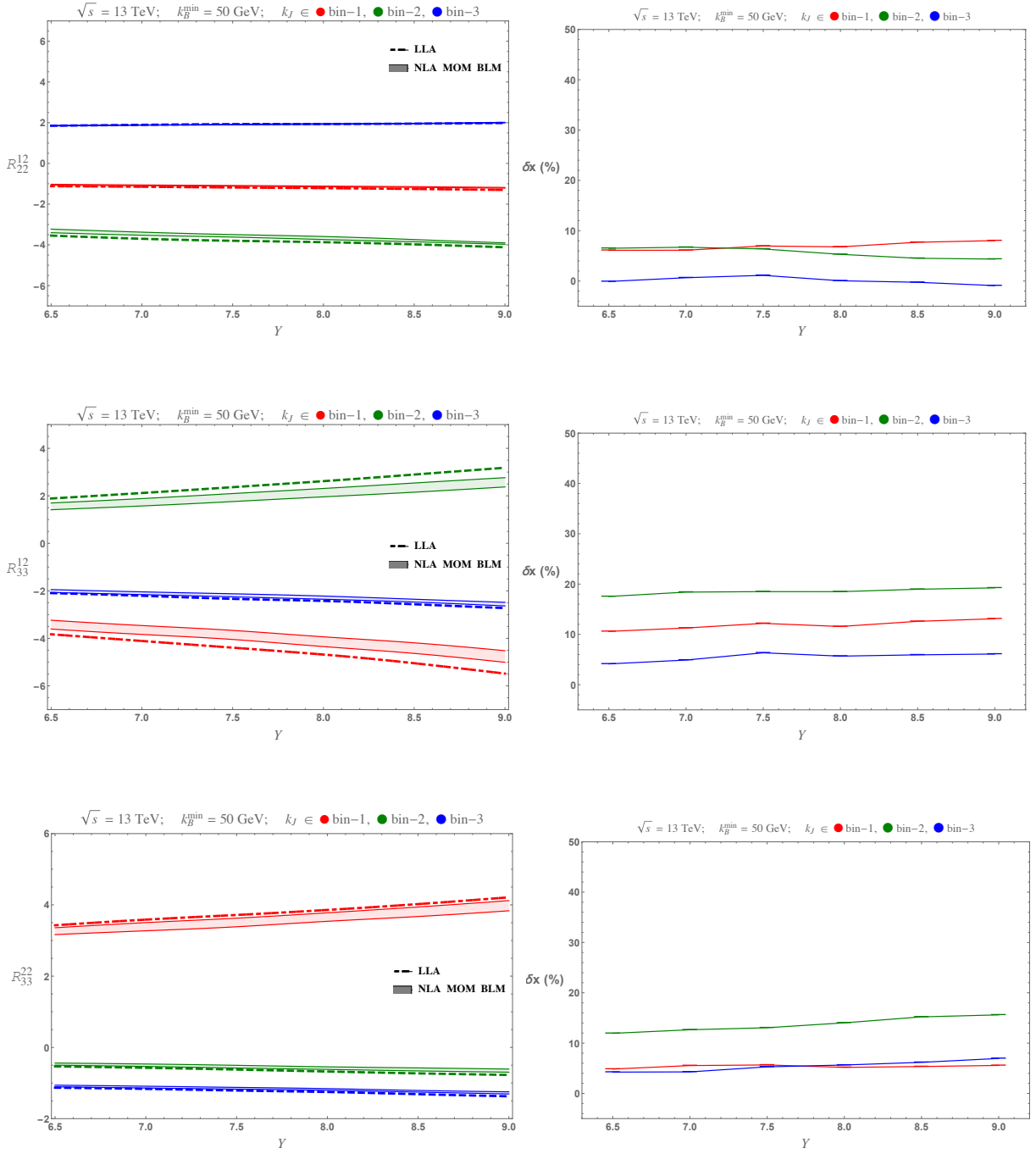


Figure 5.11: LLA and NLA $^{(i)}R_{22}^{12}$, $^{(i)}R_{33}^{12}$, and $^{(i)}R_{33}^{22}$ at $\sqrt{s} = 13$ TeV with y_J integrated over a central rapidity bin (left) and the relative NLA to LLA corrections (right).

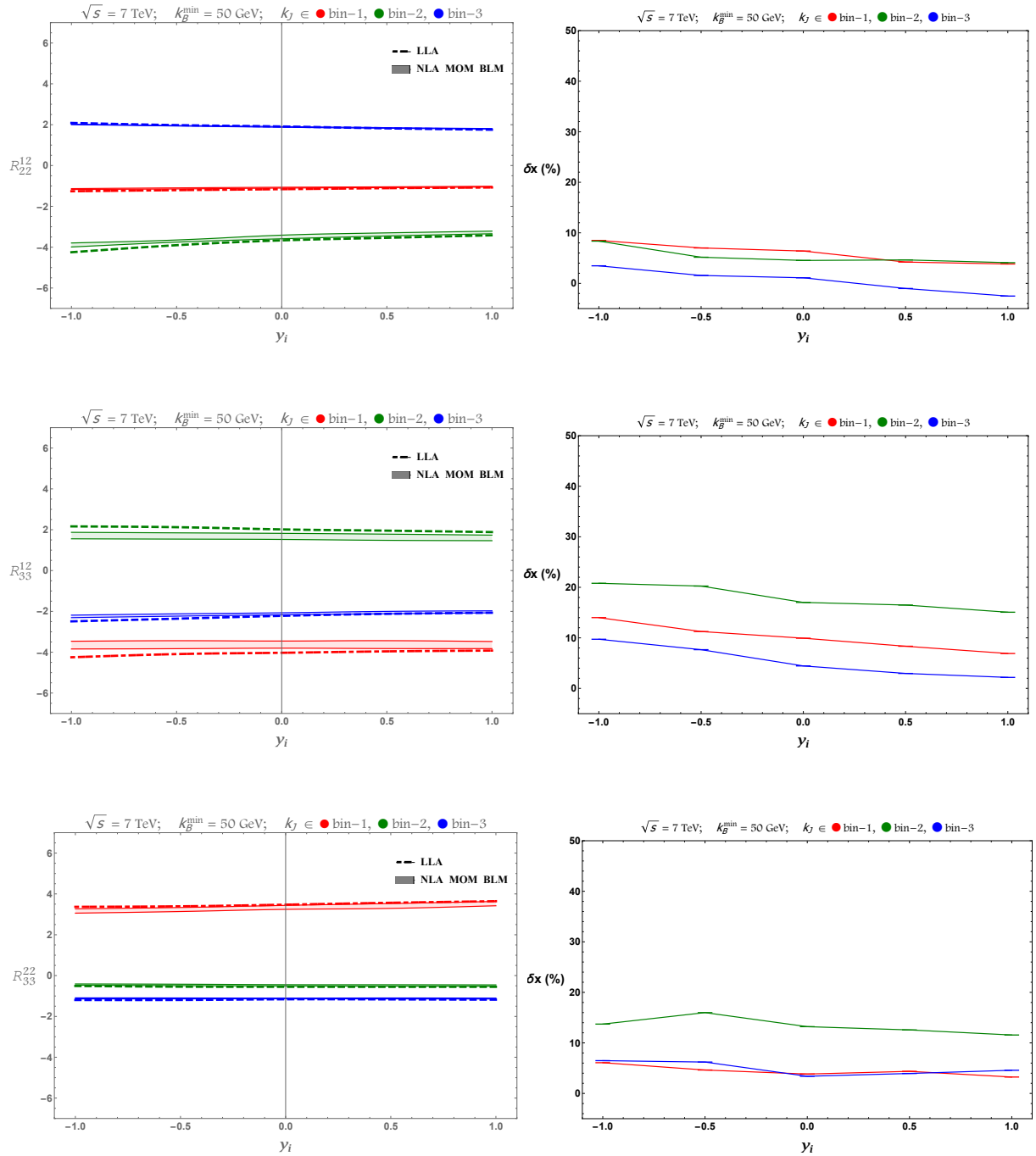


Figure 5.12: y_i -dependence of the LLA and NLA ${}^{(i)}R_{22}^{12}(y_i)$, ${}^{(i)}R_{33}^{12}(y_i)$ and ${}^{(i)}R_{33}^{22}(y_i)$ at $\sqrt{s} = 7$ TeV (left) and the relative NLA to LLA corrections (right).

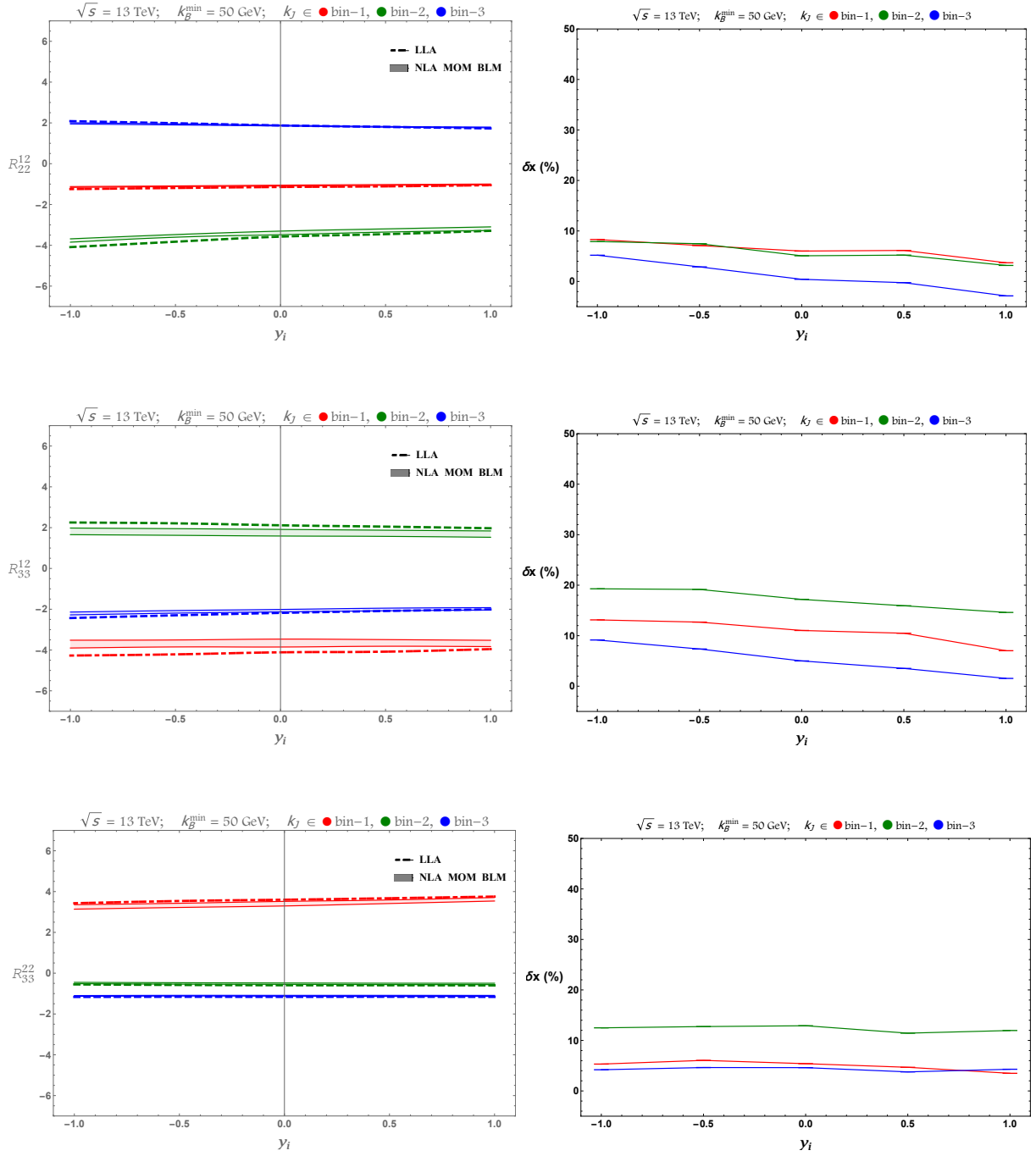


Figure 5.13: y_i -dependence of the LLA and NLA ${}^{(i)}R_{22}^{12}$, ${}^{(i)}R_{33}^{12}$, and ${}^{(i)}R_{33}^{22}$ at $\sqrt{s} = 13$ TeV (left) and the relative NLA to LLA corrections (right).

ratios, were defined first at the partonic level, then extended and studied at the hadronic level, taking in the account of NLA BFKL corrections. Two colliding energies, $\sqrt{s} = 7, 13$ TeV, together with an *asymmetric* kinematical cut with respect to the transverse momentum of the forward (k_A) and backward (k_B) jets were considered. In addition, an extra condition regarding the value of the transverse momentum k_J of the central jet was taken up, dividing the allowed region for k_J into three sub-regions: k_J smaller than $k_{A,B}$, k_J similar to $k_{A,B}$, and k_J larger than $k_{A,B}$.

For a proper study at full NLA, one needs to consider the NLO jet vertices and the NLA Green's functions, with the latter being expected to be of higher relevance. BLM prescription, which has been successful in previous phenomenological analyses [44], was used to choose the values of the renormalisation scale μ_R . It was shown how the R_{PQ}^{MN} ratios change when we vary the rapidity difference Y between k_A and k_B from 5.5 to 9 units for a fixed y_J and from 6.5 to 9 units for $-0.5 < y_J < 0.5$. Both the LLA and NLA results were presented, along with plots that show the relative size of the NLA corrections compared to the LLA ones. An alternative kinematical setup were also investigated, where Y_A and Y_B are allowed to take values such that $3 < Y_A < 4.7$ and $-4.7 < Y_B < -3$, while the rapidity of the central jet takes values in five distinct rapidity bins of unit width, that is, $y_i - 0.5 < y_J < y_i + 0.5$, with $y_i = \{-1, -0.5, 0, 0.5, 1\}$. In this alternative setup, we presented the behaviour of our observables as functions of y_i .

The general conclusion is that the NLA corrections are moderate and our proposed observables exhibit a good perturbative stability. Furthermore, we see that for a wide range of rapidities, the changes we notice when going from 7 TeV to 13 TeV are small which makes us confident that these generalised ratios pinpoint the crucial characteristics of the BFKL dynamics regarding the

azimuthal behaviour of the hard jets in inclusive three-jet production.

It would be very interesting to have an experimental analysis for these observables using previous and current LHC data. We have the strong belief that such an analysis will help us gauge the applicability of the BFKL dynamics in phenomenological studies at present colliding energies.

Appendix D

y_J -independent integrated distributions

In this Appendix it is shown that Eq. (5.30) is fulfilled in our normalisations. We introduce the notation $t = \ln k^2$ to write the Green's function in the form

$$\begin{aligned} & \varphi(t_A, t_B, \theta_A, \theta_B, Y) \\ &= \frac{e^{-\frac{t_A+t_B}{2}}}{\pi^2} \sum_{n=-\infty}^{\infty} e^{in(\theta_A-\theta_B)} \int_0^{\infty} d\nu \cos(\nu(t_A-t_B)) e^{\bar{\alpha}_s \chi(n,\nu)Y}. \end{aligned} \quad (D.1)$$

Making use of $dk = \frac{1}{2}e^{\frac{t}{2}} dt$ and $k dk d\theta = \frac{e^t}{2} d\theta$ we then want to show that

$$\begin{aligned} & \varphi(t_A, t_B, \theta_A, \theta_B, Y) \\ &= \int_0^{2\pi} d\theta \int_{-\infty}^{\infty} dt \frac{e^t}{2} \varphi(t_A, t, \theta_A, \theta, y) \varphi(t, t_B, \theta, \theta_B, Y-y) \\ &= \int_0^{2\pi} d\theta \int_{-\infty}^{\infty} dt \frac{e^t e^{-\frac{t_A+t}{2}}}{\pi^2} \sum_{m=-\infty}^{\infty} e^{im(\theta_A-\theta)} \\ & \times \int_0^{\infty} d\nu \cos(\nu(t_A-t)) e^{\bar{\alpha}_s \chi(m,\nu)y} \\ & \times \frac{e^{-\frac{t+t_B}{2}}}{\pi^2} \sum_{n=-\infty}^{\infty} e^{in(\theta-\theta_B)} \int_0^{\infty} d\mu \cos(\mu(t-t_B)) e^{\bar{\alpha}_s \chi(n,\nu)(Y-y)}. \end{aligned} \quad (D.2)$$

The integration over θ generates a δ_m^n contribution:

$$\begin{aligned} \varphi(t_A, t_B, \theta_A, \theta_B, Y) &= \frac{e^{-\frac{t_A+t_B}{2}}}{\pi^3} \sum_{n=-\infty}^{\infty} e^{in(\theta_A-\theta_B)} \int_0^{\infty} d\nu e^{\bar{\alpha}_s \chi(n, \nu) Y} \\ &\times \int_0^{\infty} d\mu e^{\bar{\alpha}_s \chi(n, \nu)(Y-y)} \int_{-\infty}^{\infty} dt \cos(\nu(t_A - t)) \cos(\mu(t - t_B)) . \end{aligned} \quad (\text{D.3})$$

It can be shown that

$$\begin{aligned} &\int_{-\infty}^{\infty} dt \cos(\nu(t_A - t)) \cos(\mu(t - t_B)) \\ &= \pi (\cos(\nu t_A - \mu t_B) \delta(\nu - \mu) + \cos(\nu t_A + \mu t_B) \delta(\nu + \mu)) , \end{aligned} \quad (\text{D.4})$$

which can be used to write Eq. (D.3) as

$$\begin{aligned} \varphi(t_A, t_B, \theta_A, \theta_B, Y) &= \frac{e^{-\frac{t_A+t_B}{2}}}{2\pi^2} \sum_{n=-\infty}^{\infty} e^{in(\theta_A-\theta_B)} \int_{-\infty}^{\infty} d\nu \int_0^{\infty} d\mu e^{\bar{\alpha}_s \chi(n, \nu)(Y-y)} e^{\bar{\alpha}_s \chi(n, \nu) Y} \\ &\times (\cos(\nu t_A - \mu t_B) \delta(\nu - \mu) + \cos(\nu t_A + \mu t_B) \delta(\nu + \mu)) , \end{aligned} \quad (\text{D.5})$$

and, finally,

$$\begin{aligned} \varphi(t_A, t_B, \theta_A, \theta_B, Y) &= \frac{e^{-\frac{t_A+t_B}{2}}}{\pi^2} \sum_{n=-\infty}^{\infty} e^{in(\theta_A-\theta_B)} \int_0^{\infty} d\mu e^{\bar{\alpha}_s \chi(n, \nu) Y} \cos(\mu(t_A - t_B)) , \end{aligned} \quad (\text{D.6})$$

which is the same as our initial representation for φ in Eq. (D.1). The relation in Eq. (D.2) is remarkable because it holds for any rapidity y .

Chapter 6

Four-jet production

In this Chapter we extend the discussion of Chapter 5 to the case of four jets, which represents our ultimate way to probe the BFKL dynamics through more exclusive processes. We have shown at the beginning of the last Chapter how our formalism can be extended to allow for the tagging of an extra central jet, by picking up its emission probability from the BFKL kernel. We got, as result (Eq. (5.1)), an expression for the three-jet cross section in the form of a double convolution of two Green's functions with three jet vertices, two of them describing the emission of the respective forward/backward jets (*à la* Mueller-Navelet), while the other one being characteristic of the central-jet emission [142]. This procedure can be generalised to the study of n -jet production processes, in which we cut $n - 1$ times the original Green's function to permit the tagging of $n - 2$ extra jets in the central rapidity regions of the detectors. This allows us to extend our discussion by investigating the four-jet production in MRK.

In our analysis we consider the emission of four jets in the final state: one in the forward direction with rapidity Y_A , one in the backward direction with rapidity Y_B and both well-separated in rapidity from the each other, $Y = Y_A - Y_B$ large, along with two more jets tagged in more central regions of the detectors

such that the relative rapidity separation between any two neighbouring jets is actually $Y/3$ respecting thus the MRK ordering. We define and study new generalised azimuthal correlations,

$$\mathcal{R}_{PQR}^{MNL} = \frac{\langle \cos(M\phi_1) \cos(N\phi_2) \cos(L\phi_3) \rangle}{\langle \cos(P\phi_1) \cos(Q\phi_2) \cos(R\phi_3) \rangle}, \quad (6.1)$$

where ϕ_1 , ϕ_2 and ϕ_3 are the azimuthal-angle differences between neighbouring in rapidity jets. In this way we can investigate even more differential distributions in the transverse momenta, azimuthal angles and rapidities of the two central jets, for fixed values of the four momenta of the two forward (originally Mueller–Navelet) jets. The main observable \mathcal{R}_{PQR}^{MNL} proposed at parton level is the extension of the three-jet one, defined in Eq. (5.2), using three cosines instead of two in numerator and denominator.

We make use of the collinear factorisation scheme to produce the two most forward/backward jets and we convolute the partonic differential cross section, which is described by the BFKL dynamics, with collinear parton distribution functions. As done in Section 5, we include in our computation the forward jet vertex. Three BFKL Green’s functions link these two Mueller–Navelet jet-vertices with the more centrally produced jets.

This Chapter is organised as follows: In Section 6.1 the main formulæ are given; in Section 6.2 a first, parton level study is presented; in Section 6.3 the first phenomenological analysis at LLA is shown, using realistic LHC kinematical cuts for the final-state phase space integration. The section Summary is given in 6.4.

The analysis given in this Chapter is based on the work done in Refs. [185, 186] and presented in Refs. [153, 175, 176, 187].

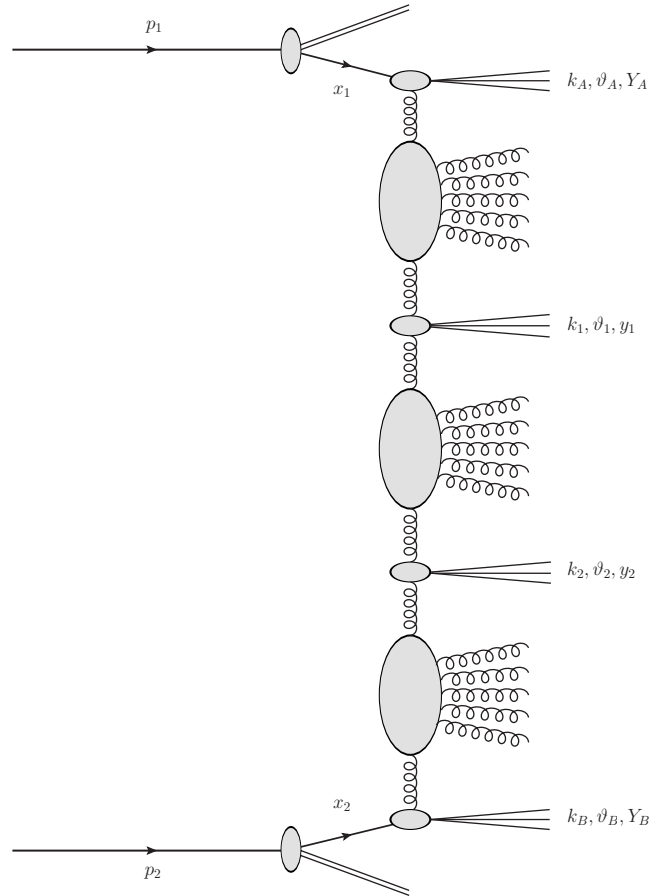


Figure 6.1: *Inclusive four-jet production process in multi-Regge kinematics.*

6.1 Theoretical framework

In this Section the BFKL cross section for the four-jet production process is presented, the main focus lying on the definition of new, generalised and suitable BFKL observables.

6.1.1 The four-jet cross section

The process under exam (see Figs. 6.1 and 6.2) is the production of two forward/backward jets, both characterised by high transverse momenta $\vec{k}_{A,B}$ and well separated in rapidity, together with two more jets produced in the

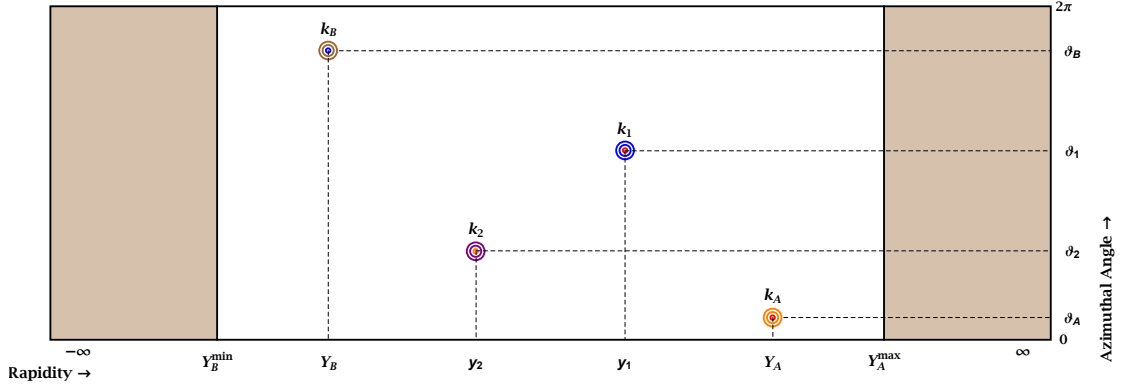


Figure 6.2: A primitive lego plot depicting a four-jet event. k_A is a forward jet with large positive rapidity Y_A and azimuthal angle ϑ_A , k_B is a backward jet with large negative rapidity Y_B and azimuthal angle ϑ_B and k_1 and k_2 are two jets with azimuthal angles ϑ_1 and ϑ_2 respectively and rapidities y_1 and y_2 such that $Y_A - y_1 \sim y_1 - y_2 \sim y_2 - Y_B$.

central rapidity region and with possible associated mini-jet production:

$$p(p_1) + p(p_2) \rightarrow j_A(k_A) + j_1(k_1) + j_2(k_2) + j_B(k_B) + \text{minijets}, \quad (6.2)$$

where j_A is the forward jet with transverse momentum \vec{k}_A and rapidity Y_A , j_B is the backward jet with transverse momentum \vec{k}_B and rapidity Y_B , and with $j_{1,2}$ being the two central jets with transverse momenta $\vec{k}_{1,2}$ and rapidities $y_{1,2}$, such that $Y_A > y_1 > y_2 > Y_B$ according to the ordering characteristic of MRK.

The cross section for the inclusive four-jet production process (6.2) reads in collinear factorisation

$$\begin{aligned} & \frac{d\sigma^{4\text{-jet}}}{dk_A dY_A d\vartheta_A dk_B dY_B d\vartheta_B dk_1 dy_1 d\vartheta_1 dk_2 dy_2 d\vartheta_2} \\ &= \sum_{r,s=q,\bar{q},g} \int_0^1 dx_1 \int_0^1 dx_2 f_r(x_1, \mu_F) f_s(x_2, \mu_F) d\hat{\sigma}_{r,s}^{4\text{-jet}}(\hat{s}, \mu_F), \end{aligned} \quad (6.3)$$

where r, s characterise the partons (gluon g ; quarks $q = u, d, s, c, b$; antiquarks $\bar{q} = \bar{u}, \bar{d}, \bar{s}, \bar{c}, \bar{b}$), $f_{r,s}(x, \mu_F)$ are the parton distribution functions of the protons; $x_{1,2}$ represent the longitudinal fractions of the partons involved in the hard

subprocess; $d\hat{\sigma}_{r,s}^{4\text{-jet}}(\hat{s}, \mu_F)$ is the partonic cross section for the production of jets and $x_1 x_2 s \equiv \hat{s}$ is the partonic squared center-of-mass energy (see Fig. 6.1). The cross section for the partonic hard subprocess $d\hat{\sigma}_{r,s}^{4\text{-jet}}$ can be presented as (from here we start to use the notation $k_{A,B,1,2} \equiv |\vec{k}_{A,B,1,2}|$, which holds in the following):

$$\begin{aligned} \frac{d\hat{\sigma}_{r,s}^{4\text{-jet}}}{d^2\vec{k}_1 dy_1 d^2\vec{k}_2 dy_2} &= \frac{\bar{\alpha}_s^2}{\pi^2 k_1^2 k_2^2} \int d^2\vec{p}_A \int d^2\vec{p}_B \int d^2\vec{p}_1 \int d^2\vec{p}_2 \\ &\times \delta^{(2)}(\vec{p}_A + \vec{k}_1 - \vec{p}_1) \delta^{(2)}(\vec{p}_B - \vec{k}_2 - \vec{p}_2) \\ &\times \varphi(\vec{k}_A, \vec{p}_A, Y_A - y_1) \varphi(\vec{p}_1, \vec{p}_2, y_1 - y_2) \varphi(\vec{p}_B, \vec{k}_B, y_2 - Y_B) , \end{aligned} \quad (6.4)$$

where $\bar{\alpha}_s = N_c/\pi \alpha_s$, with N_c the number of colours. φ are the BFKL Green's functions suitably redefined as explained in Section 5.1. Integrating one of the two two-dimensional delta functions in Eq. (6.4), we have

$$\begin{aligned} \frac{d\hat{\sigma}_{r,s}^{4\text{-jet}}}{d^2\vec{k}_1 dy_1 d^2\vec{k}_2 dy_2} &= \frac{\bar{\alpha}_s^2}{\pi^2 k_1^2 k_2^2} \int d^2\vec{p}_A \int d^2\vec{p}_B \varphi(\vec{k}_A, \vec{p}_A, Y_A - y_1) \\ &\times \varphi(\vec{p}_A + \vec{k}_1, \vec{p}_B - \vec{k}_2, y_1 - y_2) \varphi(\vec{p}_B, \vec{k}_B, y_2 - Y_B) . \end{aligned} \quad (6.5)$$

We can expand the Green's function (whose expression is taken at LLA) in Fourier components on the respective azimuthal angles and write

$$\begin{aligned} \frac{d\hat{\sigma}_{r,s}^{4\text{-jet}}}{d^2\vec{k}_1 dy_1 d^2\vec{k}_2 dy_2} &= \frac{\bar{\alpha}_s^2}{\pi^2 k_1^2 k_2^2} \sum_{m,n,l=-\infty}^{+\infty} e^{i(m\vartheta_A - l\vartheta_B)} \\ &\times \Omega_{m,n,l}(\vec{k}_A, \vec{k}_B, Y_A, Y_B, \vec{k}_1, \vec{k}_2, \vartheta_1, \vartheta_2, y_1, y_2) , \end{aligned} \quad (6.6)$$

where

$$\begin{aligned} &\Omega_{m,n,l}(\vec{k}_A, \vec{k}_B, Y_A, Y_B, \vec{k}_1, \vec{k}_2, \vartheta_1, \vartheta_2, y_1, y_2) \\ &= \int_0^{+\infty} dp_A p_A \int_0^{+\infty} dp_B p_B \int_0^{2\pi} d\phi_A \int_0^{2\pi} d\phi_B e^{in(\phi_1 - \phi_2)} e^{i(l\phi_B - m\phi_A)} \\ &\times \varphi_m^{(\text{LLA})}(|\vec{k}_A|, |\vec{p}_A|, Y_A - y_1) \varphi_l^{(\text{LLA})}(|\vec{p}_B|, |\vec{k}_B|, y_2 - Y_B) \\ &\times \varphi_n^{(\text{LLA})}(|\vec{p}_A + \vec{k}_1|, |\vec{p}_B - \vec{k}_2|, y_1 - y_2) \end{aligned} \quad (6.7)$$

and

$$\begin{aligned}\phi_1 &= \arctan \left(\frac{p_A \sin \phi_A + k_1 \sin \vartheta_1}{p_A \cos \phi_A + k_1 \cos \vartheta_1} \right) \\ \phi_2 &= \arctan \left(\frac{p_B \sin \phi_B - k_2 \sin \vartheta_2}{p_B \cos \phi_B - k_2 \cos \vartheta_2} \right) ;\end{aligned}\quad (6.8)$$

Here $\varphi_i^{(\text{LLA})}$ is the i -th azimuthal component of the LLA Green's function given in Eq. (5.12). It is possible to use the relation $\arctan \alpha = \frac{i}{2} \ln \left(\frac{1-i\alpha}{1+i\alpha} \right)$, with α being a real number, to write

$$\begin{aligned}\Omega_{m,n,l} &\left(\vec{k}_A, \vec{k}_B, Y_A, Y_B, \vec{k}_1, \vec{k}_2, \vartheta_1, \vartheta_2, y_1, y_2 \right) \\ &= \int_0^{+\infty} dp_A p_A \int_0^{+\infty} dp_B p_B \int_0^{2\pi} d\phi_A \int_0^{2\pi} d\phi_B e^{-im\phi_A} e^{il\phi_B} \\ &\quad \left(\frac{p_A e^{i\phi_A} + k_1 e^{i\vartheta_1}}{p_A e^{-i\phi_A} + k_1 e^{-i\vartheta_1}} \right)^{\frac{n}{2}} \left(\frac{p_B e^{-i\phi_B} - k_2 e^{-i\vartheta_2}}{p_B e^{i\phi_B} - k_2 e^{i\vartheta_2}} \right)^{\frac{n}{2}} \\ &\quad \times \varphi_m^{(\text{LLA})} \left(|\vec{k}_A|, |\vec{p}_A|, Y_A - y_1 \right) \varphi_l^{(\text{LLA})} \left(|\vec{p}_B|, |\vec{k}_B|, y_2 - Y_B \right) \\ &\quad \times \varphi_n^{(\text{LLA})} \left(\tilde{p}_{\widehat{A1}}, \tilde{p}_{\widehat{B2}}, y_1 - y_2 \right) ,\end{aligned}\quad (6.9)$$

where

$$\begin{aligned}\tilde{p}_{\widehat{A1}} &= \sqrt{p_A^2 + k_1^2 + 2|\vec{p}_A||\vec{k}_1| \cos(\phi_A - \vartheta_1)} , \\ \tilde{p}_{\widehat{B2}} &= \sqrt{p_B^2 + k_2^2 - 2|\vec{p}_B||\vec{k}_2| \cos(\phi_B - \vartheta_2)} .\end{aligned}\quad (6.10)$$

Making the double change of variables $\phi_A - \vartheta_1 \rightarrow \phi_A$ and $\phi_B - \vartheta_2 \rightarrow \phi_B$, we

obtain the final expression for $\Omega_{m,n,l}$:

$$\begin{aligned}
 & \Omega_{m,n,l} \left(\vec{k}_A, \vec{k}_B, Y_A, Y_B, \vec{k}_1, \vec{k}_2, \vartheta_1, \vartheta_2, y_1, y_2 \right) \\
 &= e^{i(n-m)\vartheta_1} e^{-i(n-l)\vartheta_2} \int_0^{+\infty} dp_A p_A \int_0^{+\infty} dp_B p_B \int_0^{2\pi} d\phi_A \int_0^{2\pi} d\phi_B \\
 & \quad \frac{e^{-im\phi_A} e^{il\phi_B} (p_A e^{i\phi_A} + k_1)^n (p_B e^{-i\phi_B} - k_2)^n}{\sqrt{\left(p_A^2 + k_1^2 + 2|\vec{p}_A||\vec{k}_1| \cos(\phi_A) \right)^n} \sqrt{\left(p_B^2 + k_2^2 - 2|\vec{p}_B||\vec{k}_2| \cos(\phi_B) \right)^n}} \\
 & \times \varphi_m^{(LLA)} \left(|\vec{k}_A|, |\vec{p}_A|, Y_A - y_1 \right) \varphi_l^{(LLA)} \left(|\vec{p}_B|, |\vec{k}_B|, y_2 - Y_B \right) \\
 & \times \varphi_n^{(LLA)} \left(\tilde{p}_1, \tilde{p}_2, y_1 - y_2 \right)
 \end{aligned} \tag{6.11}$$

with

$$\begin{aligned}
 \tilde{p}_1 &= \sqrt{p_A^2 + k_1^2 + 2|\vec{p}_A||\vec{k}_1| \cos(\phi_A)}, \\
 \tilde{p}_2 &= \sqrt{p_B^2 + k_2^2 - 2|\vec{p}_B||\vec{k}_2| \cos(\phi_B)},
 \end{aligned} \tag{6.12}$$

in which the dependence on ϑ_1 and ϑ_2 has been successfully factorised out.

6.1.2 The four-jet azimuthal correlations: partonic level

Following the course taken for the inclusive three-jet production (see Sections 5.1.2 and 5.1.3), our goal is to define and study the behaviour of observables for which the BFKL approach will show distinct features with respect to other formalisms and, if possible, are also quite insensitive to higher-order corrections. We start with the study of a quantity similar to the usual Mueller–Navelet case such that we integrate over the azimuthal angles of the two central jets and over the difference in azimuthal angle between the two forward jets, $\Delta\phi = \vartheta_A - \vartheta_B - \pi$, to define

$$\begin{aligned}
 & \int_0^{2\pi} d\Delta\phi \cos(M\Delta\phi) \int_0^{2\pi} d\vartheta_1 \int_0^{2\pi} d\vartheta_2 \frac{d\sigma^{4\text{-jet}} \left(\vec{k}_A, \vec{k}_B, Y_A - Y_B \right)}{dk_1 dy_1 d\vartheta_1 dk_2 d\vartheta_2 dy_2} \\
 &= \frac{4\bar{\alpha}_s^2}{k_1 k_2} \left(e^{iM\pi} \tilde{Q}_M(\vec{k}_A, \vec{k}_B, Y_A, Y_B, \vec{k}_1, \vec{k}_2, y_1, y_2) + c.c. \right)
 \end{aligned} \tag{6.13}$$

where

$$\begin{aligned}
 & \tilde{\Omega}_n(\vec{k}_A, \vec{k}_B, Y_A, Y_B, \vec{k}_1, \vec{k}_2, y_1, y_2) \\
 &= \int_0^{+\infty} dp_A p_A \int_0^{+\infty} dp_B p_B \int_0^{2\pi} d\phi_A \int_0^{2\pi} d\phi_B \\
 &\times \frac{(p_A + k_1 e^{-i\phi_A})^n (p_B - k_2 e^{i\phi_B})^n}{\sqrt{(p_A^2 + k_1^2 + 2|\vec{p}_A||\vec{k}_1| \cos \phi_A)^n} \sqrt{(p_B^2 + k_2^2 - 2|\vec{p}_B||\vec{k}_2| \cos \phi_B)^n}} \\
 &\times \varphi_n^{(\text{LLA})}(|\vec{k}_A|, |\vec{p}_A|, Y_A - y_1) \varphi_n^{(\text{LLA})}(|\vec{p}_B|, |\vec{k}_B|, y_2 - Y_B) \\
 &\times \varphi_n^{(\text{LLA})} \left(\sqrt{p_A^2 + k_1^2 + 2|\vec{p}_A||\vec{k}_1| \cos \phi_A}, \sqrt{p_B^2 + k_2^2 - 2|\vec{p}_B||\vec{k}_2| \cos \phi_B}, y_1 - y_2 \right).
 \end{aligned} \tag{6.14}$$

The associated experimental observable corresponds to the mean value of the cosine of $\Delta\phi$ in the recorded events:

$$\begin{aligned}
 & \langle \cos(M\Delta\phi) \rangle_{d\hat{\sigma}_{r,s}^{4\text{-jet}}} \\
 &= \frac{\int_0^{2\pi} d\Delta\phi \cos(M\Delta\phi) \int_0^{2\pi} d\vartheta_1 \int_0^{2\pi} d\vartheta_2 \frac{d\sigma^{4\text{-jet}}}{dk_1 dy_1 d\vartheta_1 dk_2 d\vartheta_2 dy_2}}{\int_0^{2\pi} d\Delta\phi \int_0^{2\pi} d\vartheta_1 \int_0^{2\pi} d\vartheta_2 \frac{d\sigma^{4\text{-jet}}}{dk_1 dy_1 d\vartheta_1 dk_2 d\vartheta_2 dy_2}}.
 \end{aligned} \tag{6.15}$$

In order to improve the perturbative stability of our predictions (see Ref. [33] for a related discussion) it is convenient to remove the contribution from the zero conformal spin by defining the ratios

$$\mathcal{R}_N^M = \frac{\langle \cos(M\Delta\phi) \rangle_{d\hat{\sigma}_{r,s}^{4\text{-jet}}}}{\langle \cos(N\Delta\phi) \rangle_{d\hat{\sigma}_{r,s}^{4\text{-jet}}}} \tag{6.16}$$

where M, N are positive integers.

The next step now is to propose new observables, different from those characteristic of the Mueller–Navelet case though still related to azimuthal-angle projections. Let us first define the following azimuthal-angle differences:

$$\begin{aligned}
 \phi_1 &= \vartheta_A - \vartheta_1 - \pi, \\
 \phi_2 &= \vartheta_1 - \vartheta_2 - \pi, \\
 \phi_3 &= \vartheta_2 - \vartheta_B - \pi.
 \end{aligned} \tag{6.17}$$

Then we define

$$\begin{aligned} \mathcal{C}_{MNL} = & \int_0^{2\pi} d\vartheta_A \int_0^{2\pi} d\vartheta_B \int_0^{2\pi} d\vartheta_1 \int_0^{2\pi} d\vartheta_2 \cos(M(\phi_1)) \cos(N(\phi_2)) \quad (6.18) \\ & \times \cos(L(\phi_3)) \frac{d\sigma^{4\text{-jet}}(\vec{k}_A, \vec{k}_B, Y_A - Y_B)}{dk_1 dy_1 d\vartheta_1 dk_2 d\vartheta_2 dy_2}, \end{aligned}$$

where we consider $M, N, L > 0$ and integer. After a bit of algebra we have

$$\begin{aligned} \mathcal{C}_{MNL} = & \frac{2\pi^2 \bar{\alpha}_s^2}{k_1 k_2} (-1)^{M+N+L} (\tilde{\Omega}_{M,N,L} + \tilde{\Omega}_{M,N,-L} + \tilde{\Omega}_{M,-N,L} \quad (6.19) \\ & + \tilde{\Omega}_{M,-N,-L} + \tilde{\Omega}_{-M,N,L} + \tilde{\Omega}_{-M,N,-L} + \tilde{\Omega}_{-M,-N,L} + \tilde{\Omega}_{-M,-N,-L}) \end{aligned}$$

with

$$\begin{aligned} \tilde{\Omega}_{m,n,l} = & \int_0^{+\infty} dp_A p_A \int_0^{+\infty} dp_B p_B \int_0^{2\pi} d\phi_A \int_0^{2\pi} d\phi_B \quad (6.20) \\ & \times \frac{e^{-im\phi_A} e^{il\phi_B} (p_A e^{i\phi_A} + k_1)^n (p_B e^{-i\phi_B} - k_2)^n}{\sqrt{(p_A^2 + k_1^2 + 2|\vec{p}_A||\vec{k}_1| \cos \phi_A)^n} \sqrt{(p_B^2 + k_2^2 - 2|\vec{p}_B||\vec{k}_2| \cos \phi_B)^n}} \\ & \times \varphi_m^{(\text{LLA})}(|\vec{k}_A|, |\vec{p}_A|, Y_A - y_1) \varphi_l^{(\text{LLA})}(|\vec{p}_B|, |\vec{k}_B|, y_2 - Y_B) \\ & \times \varphi_n^{(\text{LLA})}(\sqrt{p_A^2 + k_1^2 + 2|\vec{p}_A||\vec{k}_1| \cos \phi_A}, \sqrt{p_B^2 + k_2^2 - 2|\vec{p}_B||\vec{k}_2| \cos \phi_B}, y_1 - y_2). \end{aligned}$$

In order to drastically reduce the dependence on collinear configurations we can remove the zero conformal spin contribution by defining the following ratios:

$$\mathcal{R}_{PQR}^{MNL} = \frac{\langle \cos(M(\phi_1)) \cos(N(\phi_2)) \cos(L(\phi_3)) \rangle_{d\hat{\sigma}_{r,s}^{4\text{-jet}}}}{\langle \cos(P(\phi_1)) \cos(Q(\phi_2)) \cos(R(\phi_3)) \rangle_{d\hat{\sigma}_{r,s}^{4\text{-jet}}}} \quad (6.21)$$

with integer $M, N, L, P, Q, R > 0$.

6.2 Partonic level analysis

In this section the behaviour of our observables is investigated in many different momenta configurations. In order to cover two characteristic cases,

namely $k_A \sim k_B$ and $k_A < k_B$ (or equivalently $k_A > k_B$) the following two fixed configurations for the transverse momenta of the forward jets have been chosen: $(k_A, k_B) = (40, 50)$ and $(k_A, k_B) = (30, 60)$ GeV. The rapidities of the four tagged jets are fixed to the values $Y_A = 9$, $y_1 = 6$, $Y_2 = 3$, and $Y_B = 0$ whereas the two inner jets can have transverse momenta in the range $20 < k_{1,2} < 80$ GeV. In Fig. 6.3 the results for the normalised coefficients \mathcal{C}_{111} , \mathcal{C}_{112} , \mathcal{C}_{121} and \mathcal{C}_{122} are shown, after they are divided by their respective maximum. The distributions are quite similar for the two configurations here chosen ($(k_A, k_B) = (40, 50)$, $(30, 60)$ GeV) apart from the coefficient \mathcal{C}_{121} which is quite more negative for the latter configuration when the transverse momentum of the first central jet, k_1 , is low. Further coefficients, normalised as above, are calculated in Fig. 6.4 for the cases \mathcal{C}_{211} , \mathcal{C}_{212} , \mathcal{C}_{221} and \mathcal{C}_{222} . Again they are rather similar with the exception of \mathcal{C}_{221} at low p_t of one of the central jets with largest rapidity. Since these coefficients change sign on the parameter space here studied, it is clear that for the associated ratios \mathcal{R}_{PQR}^{MNL} there will be some lines of singularities. We have investigated \mathcal{R}_{212}^{121} , \mathcal{R}_{211}^{212} and \mathcal{R}_{222}^{221} in Fig. 6.5. In this case the configurations $(k_A, k_B) = (40, 50)$, $(30, 60)$ GeV behave quite differently. This is due to the variation of the position of the zeroes of those coefficients \mathcal{C}_{MNP} chosen as denominators in these quantities. It would be very interesting to test if these singularity lines are present in any form in the LHC experimental data. A further set of ratios, \mathcal{R}_{112}^{111} , \mathcal{R}_{122}^{111} , \mathcal{R}_{122}^{112} and \mathcal{R}_{211}^{222} , with their characteristic singular lines, is presented in Fig. 6.6. In general, a very weak dependence on variations of the rapidity of the more central jets $y_{1,2}$ is found for all the observables here presented.

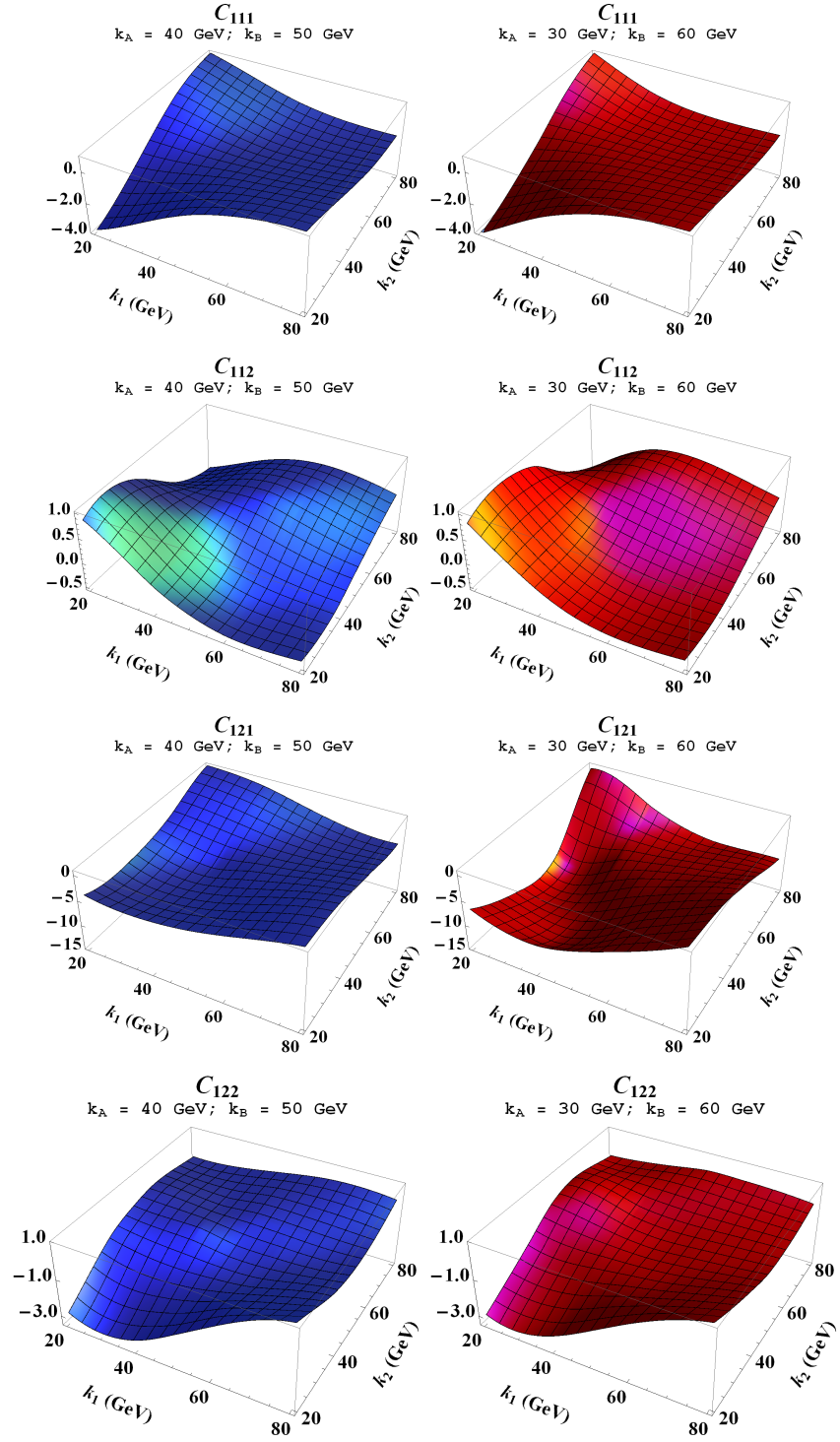


Figure 6.3: $k_{1,2}$ -dependence of the normalised C_{111} , C_{112} , C_{121} and C_{122} for the two selected cases of forward jet transverse momenta k_A and k_B .

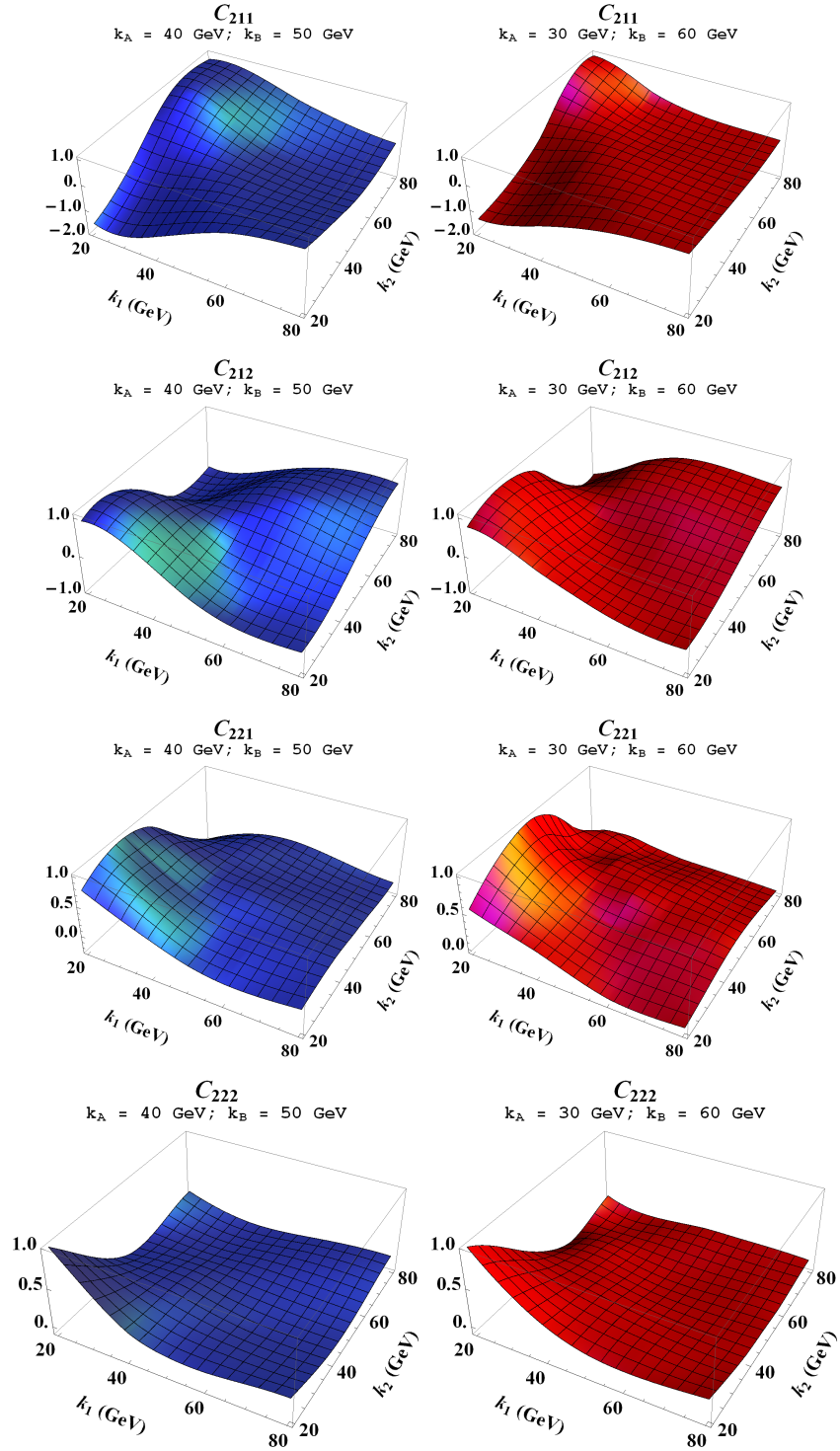


Figure 6.4: $k_{1,2}$ -dependence of the normalised C_{211} , C_{212} , C_{221} and C_{222} for the two selected cases of forward jet transverse momenta k_A and k_B .

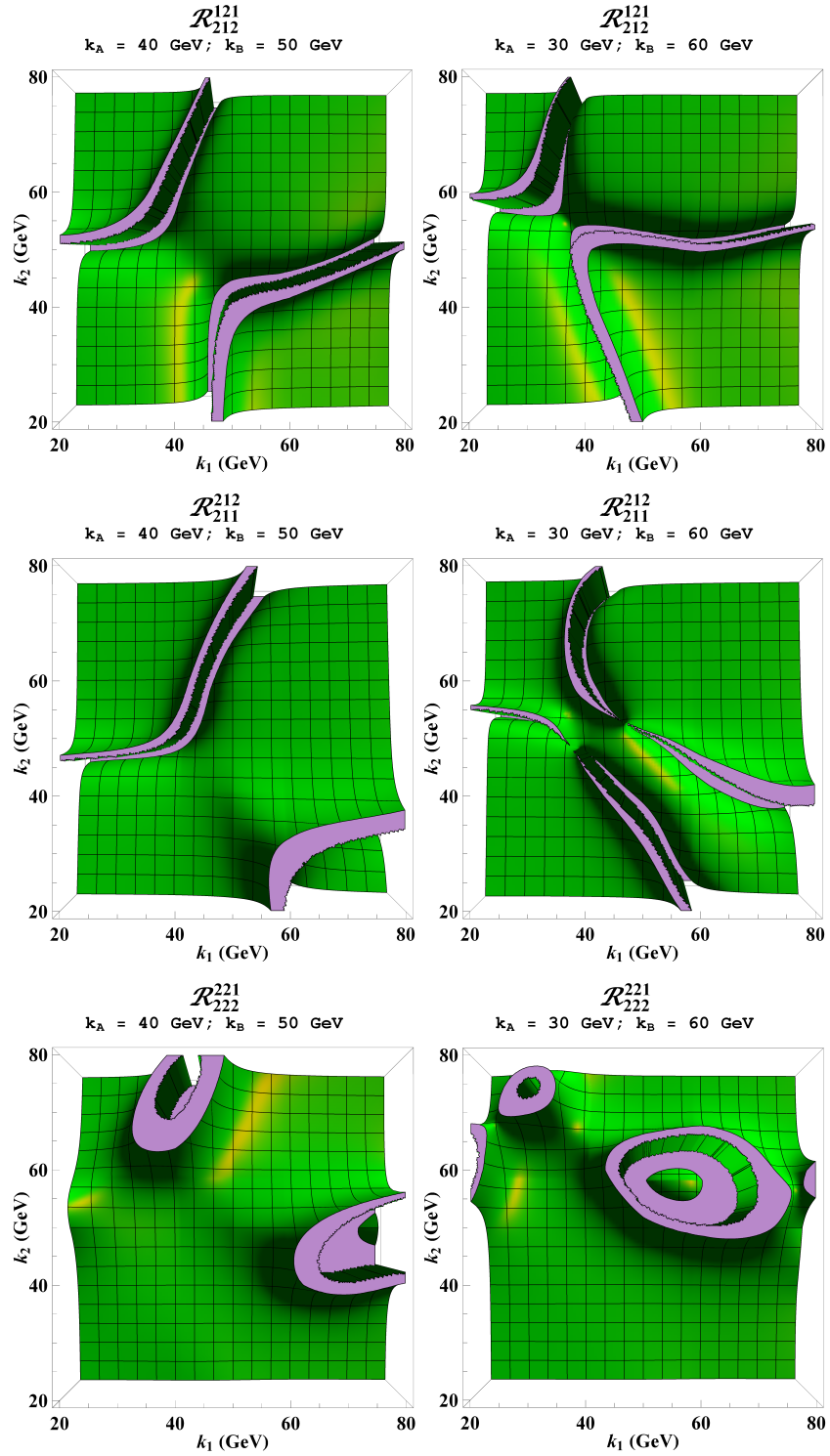


Figure 6.5: $k_{1,2}$ -dependence of \mathcal{R}_{212}^{121} , \mathcal{R}_{211}^{212} and \mathcal{R}_{222}^{221} for the two selected cases of forward/backward jets transverse momenta k_A and k_B .

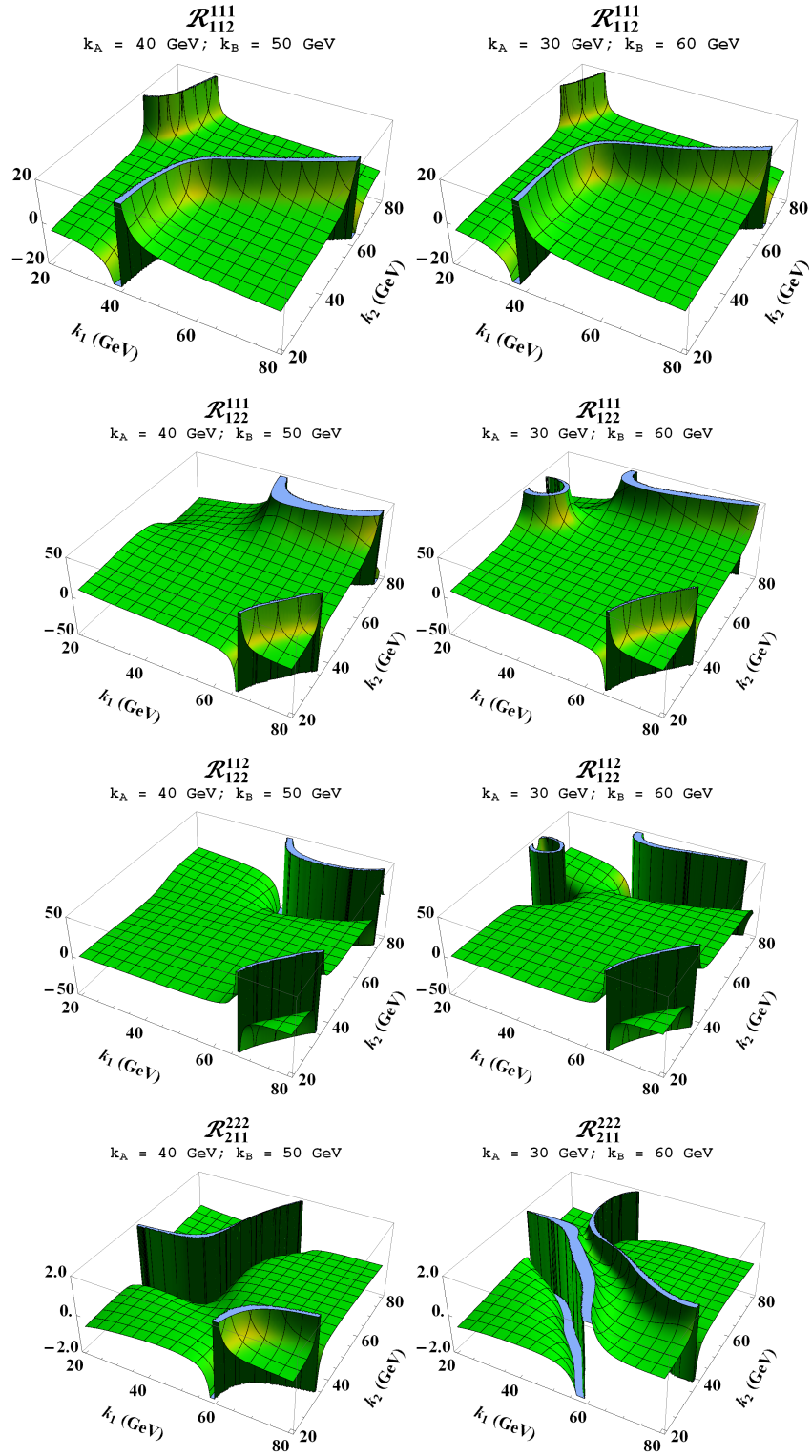


Figure 6.6: $k_{1,2}$ -dependence of \mathcal{R}_{112}^{111} , \mathcal{R}_{122}^{111} , \mathcal{R}_{122}^{112} and \mathcal{R}_{211}^{222} for the two selected cases of forward/backward jets transverse momenta k_A and k_B .

6.3 Hadronic level predictions

In order to perform a more phenomenological analysis it is needed to give predictions at the hadronic level by considering observables built up from the hadronic cross section (see Eq. (6.3)).

6.3.1 The four-jet azimuthal correlations: hadronic level

Making use of the expression for the jet vertex in the LO approximation (Eq. 3.8), the hadronic cross section for the process (6.2) reads

$$\begin{aligned}
& d\sigma^{4\text{-jet}} \\
& \frac{dk_A dY_A d\vartheta_A dk_B dY_B d\vartheta_B dk_1 dy_1 d\vartheta_1 dk_2 dy_2 d\vartheta_2}{N_C^3} \frac{x_{J_A} x_{J_B}}{k_A k_B k_1 k_2} \int d^2\vec{p}_A \int d^2\vec{p}_B \int d^2\vec{p}_1 \int d^2\vec{p}_2 \\
& \times \delta^{(2)}(\vec{p}_A + \vec{k}_1 - \vec{p}_1) \delta^{(2)}(\vec{p}_B - \vec{k}_2 - \vec{p}_2) \\
& \times \left(\frac{N_C}{C_F} f_g(x_{J_A}, \mu_F) + \sum_{r=q,\bar{q}} f_r(x_{J_A}, \mu_F) \right) \\
& \times \left(\frac{N_C}{C_F} f_g(x_{J_B}, \mu_F) + \sum_{s=q,\bar{q}} f_s(x_{J_B}, \mu_F) \right) \\
& \times \varphi(\vec{k}_A, \vec{p}_A, Y_A - y_1) \varphi(\vec{p}_1, \vec{p}_2, y_1 - y_2) \varphi(\vec{p}_B, \vec{k}_B, y_2 - Y_B).
\end{aligned} \tag{6.22}$$

In order to follow a MRK setup we demand, as we did in Section 6.2, that the rapidities of the produced particles obey $Y_A > y_1 > y_2 > Y_B$, while k_1^2 and k_2^2 are well above the resolution scale of the detectors. $x_{J_{A,B}}$ are the longitudinal momentum fractions of the two external jets, connected to the respective rapidities $Y_{A,B}$ by the relation $x_{J_{A,B}} = k_{A,B} e^{\pm Y_{A,B}} / \sqrt{s}$.

Our goal is to define new observables for which the BFKL dynamics would surface in a distinct form. Moreover, we request that our observables should be rather insensitive to possible higher-order corrections. The related experimental observable we propose corresponds to the mean value (with M, N, L

being positive integers)

$$\begin{aligned} \mathcal{C}_{MNL} &= \langle \cos(M\phi_1) \cos(N\phi_2) \cos(L\phi_3) \rangle \\ &= \frac{\int_0^{2\pi} d\vartheta_A \int_0^{2\pi} d\vartheta_B \int_0^{2\pi} d\vartheta_1 \int_0^{2\pi} d\vartheta_2 \cos(M\phi_1) \cos(N\phi_2) \cos(L\phi_3) d\sigma^{4\text{-jet}}}{\int_0^{2\pi} d\vartheta_A d\vartheta_B d\vartheta_1 d\vartheta_2 d\sigma^{4\text{-jet}}}, \end{aligned} \quad (6.23)$$

with ϕ_1 , ϕ_2 and ϕ_3 defined in Eq. (6.17). The numerator in Eq. (6.23) actually reads

$$\begin{aligned} &\int_0^{2\pi} d\vartheta_A \int_0^{2\pi} d\vartheta_B \int_0^{2\pi} d\vartheta_1 \int_0^{2\pi} d\vartheta_2 \cos(M\phi_1) \cos(N\phi_2) \cos(L\phi_3) \\ &\quad d\sigma^{4\text{-jet}} \\ &\times \frac{dk_A dY_A d\vartheta_A dk_B dY_B d\vartheta_B dk_1 dy_1 d\vartheta_1 dk_2 dy_2 d\vartheta_2}{N_C^3} = \\ &\times \frac{16\pi^4 C_F \bar{\alpha}_s^4}{N_C^3} \frac{x_{J_A} x_{J_B}}{k_A k_B k_1 k_2} \int d^2\vec{p}_A \int d^2\vec{p}_B \int d^2\vec{p}_1 \int d^2\vec{p}_2 \\ &\times \delta^{(2)}(\vec{p}_A + \vec{k}_1 - \vec{p}_1) \delta^{(2)}(\vec{p}_B - \vec{k}_2 - \vec{p}_2) \\ &\times \left(\frac{N_C}{C_F} f_g(x_{J_A}, \mu_F) + \sum_{r=q, \bar{q}} f_r(x_{J_A}, \mu_F) \right) \\ &\times \left(\frac{N_C}{C_F} f_g(x_{J_B}, \mu_F) + \sum_{s=q, \bar{q}} f_s(x_{J_B}, \mu_F) \right) \\ &\times (\tilde{\Omega}_{M,N,L} + \tilde{\Omega}_{M,N,-L} + \tilde{\Omega}_{M,-N,L} + \tilde{\Omega}_{M,-N,-L} \\ &\quad + \tilde{\Omega}_{-M,N,L} + \tilde{\Omega}_{-M,N,-L} + \tilde{\Omega}_{-M,-N,L} + \tilde{\Omega}_{-M,-N,-L}). \end{aligned} \quad (6.24)$$

The quantity $\tilde{\Omega}_{m,n,l}$ is simply a convolution of BFKL gluon Green's functions, given in Eq. (6.20).

6.3.2 Integration over the final-state phase space

As anticipated, we would like to consider quantities that are easily measured experimentally and, moreover, we want to eliminate as much as possible any dependence on higher-order corrections. Thus, we need to consider ratios similar to Eq. (6.21), which are defined on a partonic level though. Therefore,

in order to provide testable theoretical predictions against any current and forthcoming experimental data, we proceed in two steps. Firstly, we impose LHC kinematical cuts by integrating \mathcal{C}_{MNL} over the momenta of the tagged jets. More precisely,

$$\begin{aligned} \mathcal{C}_{\text{MNL}} = & \int_{Y_A^{\min}}^{Y_A^{\max}} dY_A \int_{Y_B^{\min}}^{Y_B^{\max}} dY_B \int_{k_A^{\min}}^{k_A^{\max}} dk_A \int_{k_B^{\min}}^{k_B^{\max}} dk_B \int_{k_1^{\min}}^{k_1^{\max}} dk_1 \int_{k_2^{\min}}^{k_2^{\max}} dk_2 \\ & \times \delta(Y_A - Y_B - Y) \mathcal{C}_{\text{MNL}}, \end{aligned} \quad (6.25)$$

where the rapidity Y_A of the most forward jet k_A is restricted to $0 < Y_A < 4.7$ and the rapidity Y_B of the most backward jet k_B is restricted to $-4.7 < Y_B < 0$ while their difference $Y = Y_A - Y_B$ is kept fixed at definite values within the range $6.5 < Y < 9$. Obviously, the last condition on the allowed values of Y makes both the integration ranges over Y_A and Y_B smaller than 4.7 units of rapidity. Secondly, we remove the zeroth conformal spin contribution responsible for any collinear contamination (contributions that originate at φ_0) and we minimise possible higher-order effects by introducing the ratios

$$R_{\text{PQR}}^{\text{MNL}} = \frac{\mathcal{C}_{\text{MNL}}}{\mathcal{C}_{\text{PQR}}}, \quad (6.26)$$

where M, N, L, P, Q, R are positive definite integers.

6.3.3 Numerical analysis

In this Section the results for the ratios $R_{\text{PQR}}^{\text{MNL}}$ in Eq. (6.26) are presented as functions of the rapidity difference Y between the outermost jets for different momenta configurations and for two center-of-mass energies: $\sqrt{s} = 7$ and $\sqrt{s} = 13$ TeV. For the transverse momenta k_A, k_B, k_1 and k_2 the following cuts are imposed:

1.

$$\begin{aligned}
 k_A^{\min} &= 35 \text{ GeV} , \quad k_A^{\max} = 60 \text{ GeV} , \\
 k_B^{\min} &= 45 \text{ GeV} , \quad k_B^{\max} = 60 \text{ GeV} , \\
 k_1^{\min} &= 20 \text{ GeV} , \quad k_1^{\max} = 35 \text{ GeV} , \\
 k_2^{\min} &= 60 \text{ GeV} , \quad k_2^{\max} = 90 \text{ GeV} ;
 \end{aligned} \tag{6.27}$$

2.

$$\begin{aligned}
 k_A^{\min} &= 35 \text{ GeV} , \quad k_A^{\max} = 60 \text{ GeV} , \\
 k_B^{\min} &= 45 \text{ GeV} , \quad k_B^{\max} = 60 \text{ GeV} , \\
 k_1^{\min} &= 25 \text{ GeV} , \quad k_1^{\max} = 50 \text{ GeV} , \\
 k_2^{\min} &= 60 \text{ GeV} , \quad k_2^{\max} = 90 \text{ GeV} .
 \end{aligned} \tag{6.28}$$

To keep things simple, in both cuts, k_2 has been set larger than all the other three-jet momenta, while only the range of k_1 is changed. In the cut defined in Eq. (6.27), k_1 is smaller than all the other three-jet momenta whereas in the cut defined in Eq. (6.28), the allowed k_1 values overlap with the ranges of k_A and k_B .

6.3.3.1 Results and discussion

The results for the ratios R_{221}^{111} , R_{111}^{112} , R_{211}^{112} , R_{111}^{212} , R_{221}^{122} , R_{112}^{221} are shown in Figs. 6.7–6.12. We plot the ratios for the cut defined in Eq. (6.27) with a red dot-dashed line and the ratios for the cut defined in Eq. (6.28) with a blue dashed line. We place the $\sqrt{s} = 7$ TeV results on the top of each figure and the $\sqrt{s} = 13$ TeV results at the bottom.

The functional dependence of the ratios R_{PQR}^{MNL} on the rapidity difference between k_A and k_B is rather smooth. We can further notice that there are

ratios with an almost linear behaviour with Y and with a rather small slope. To be specific, the ratios represented by the blue curve in Fig. 6.7 and the red curve in Figs. 6.8, 6.9 and 6.10 demonstrate this linear behaviour in a striking fashion. Furthermore, whenever a ratio exhibits a linear dependence on Y (for a certain kinematical cut of k_1) at colliding energy 7 TeV, we observe that the ratio maintains almost the exact same linear behaviour (with very similar actual values) at 13 TeV as well.

On the other hand, there are configurations for which the functional dependence on Y is much stronger and far from linear. In Fig. 6.8, the blue curve on the top rises from ~ 1.2 at $Y = 6.5$ to ~ 6.8 at $Y = 9$, whereas in Fig. 6.10 on the top it drops from $\sim (-1.5)$ to $\sim (-4.8)$ for the same variation in Y . Generally, if for some ratio there is a strong functional dependence on Y for a k_1 of intermediate size (blue curve), this dependence is ‘softened’ at higher colliding energy (see plots in Figs. 6.8, 6.9, 6.10 and 6.12). However, for a k_1 of smaller size (red curve), we see that the functional dependence on Y gets stronger at 13 TeV (Figs. 6.7, 6.11 and 6.12), unless of course it exhibits a linear behaviour as was discussed in the previous paragraph.

In all plots presented in Figs. 6.7–6.12, there is no red or blue curve that changes sign in the interval $6.5 < Y < 9$. Moreover, if a ratio R_{PQR}^{MNL} is positive (negative) at 7 TeV, it will continue being positive (negative) at 13 TeV, disregarding the specific functional behaviour on Y .

In contrast to our main observation in Chapter 5 where in general, for most of the three-jet observables R_{PQ}^{MN} there were no significant changes after increasing the colliding energy from 7 to 13 TeV, here we notice that, depending on the kinematical cut, an increase in the colliding energy may lead to a noticeable change to the shape of the functional Y dependence, *e.g.* red curve in Fig. 6.7, blue and red curve in Fig. 6.12. This is a very interesting point for the following

reason. If a BFKL-based analysis for an observable dictates that the latter does not change much when the energy increases, this fact actually indicates that a kind of asymptotia has been reached, *e.g.* the slope of the Green's function plotted as a function of the rapidity for very large rapidities. In asymptotia, the dynamics is driven by pure BFKL effects whereas pre-asymptotic effects are negligible. In the present study, we have a mixed picture. We have ratios that do not really change when the energy increases and other ratios for which a higher colliding energy changes their functional dependence on Y . A crucial point that allows us to speak about pre-asymptotic effects, which in itself infers that BFKL is still the relevant dynamics, was outlined previously in this Section: despite the fact that for some cases we see a different functional dependence on Y after raising the colliding energy, it is important to note that we observe no change of sign for any ratio R_{pQR}^{MNL} . Therefore, the four-jet ratio observables we are studying here are more sensitive to pre-asymptotic effects than the related three-jet ratio observables studied in Chapter 5. Nevertheless, by imposing different kinematical cuts one can change the degree of importance of these effects. To conclude with, carefully combined choice of cuts for the R_{pQR}^{MNL} observables and a detailed confrontation between theoretical predictions and data may turn out to be an excellent way to probe deeper into the BFKL dynamics.

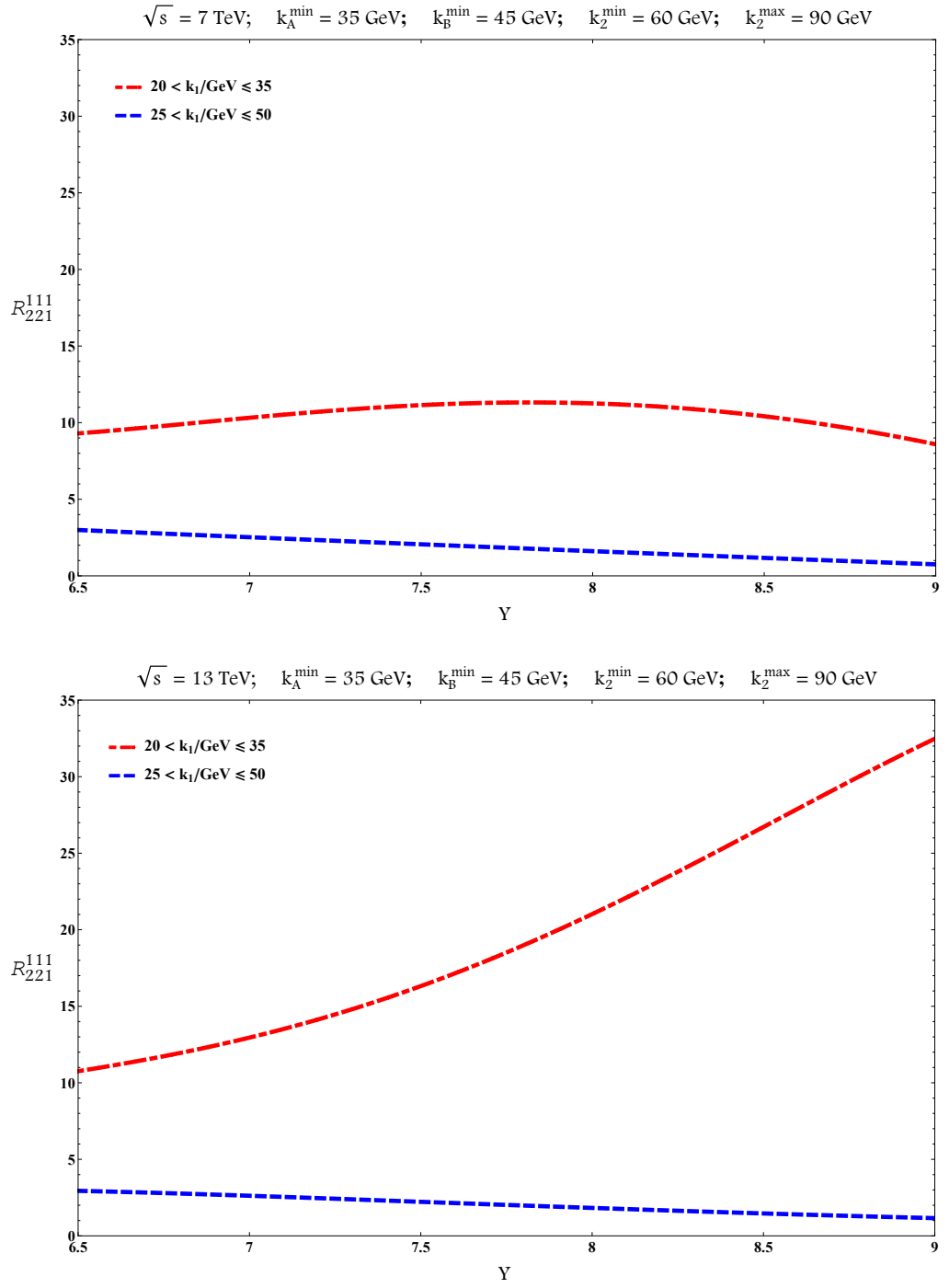


Figure 6.7: Y -dependence of R_{221}^{111} for $\sqrt{s} = 7 \text{ TeV}$ (top) and for $\sqrt{s} = 13 \text{ TeV}$ (bottom).

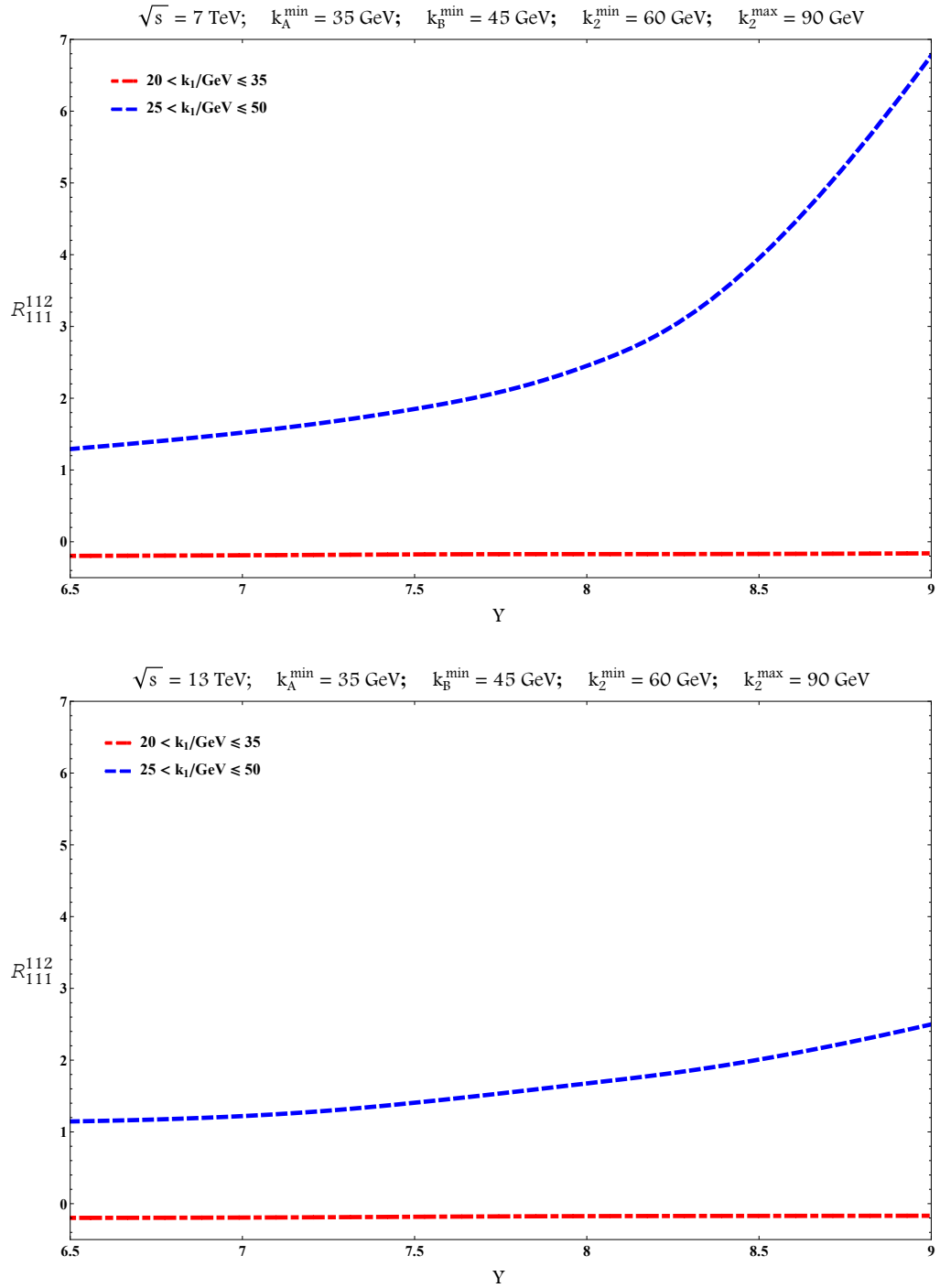


Figure 6.8: Y -dependence of R_{111}^{112} for $\sqrt{s} = 7$ TeV (top) and for $\sqrt{s} = 13$ TeV (bottom).

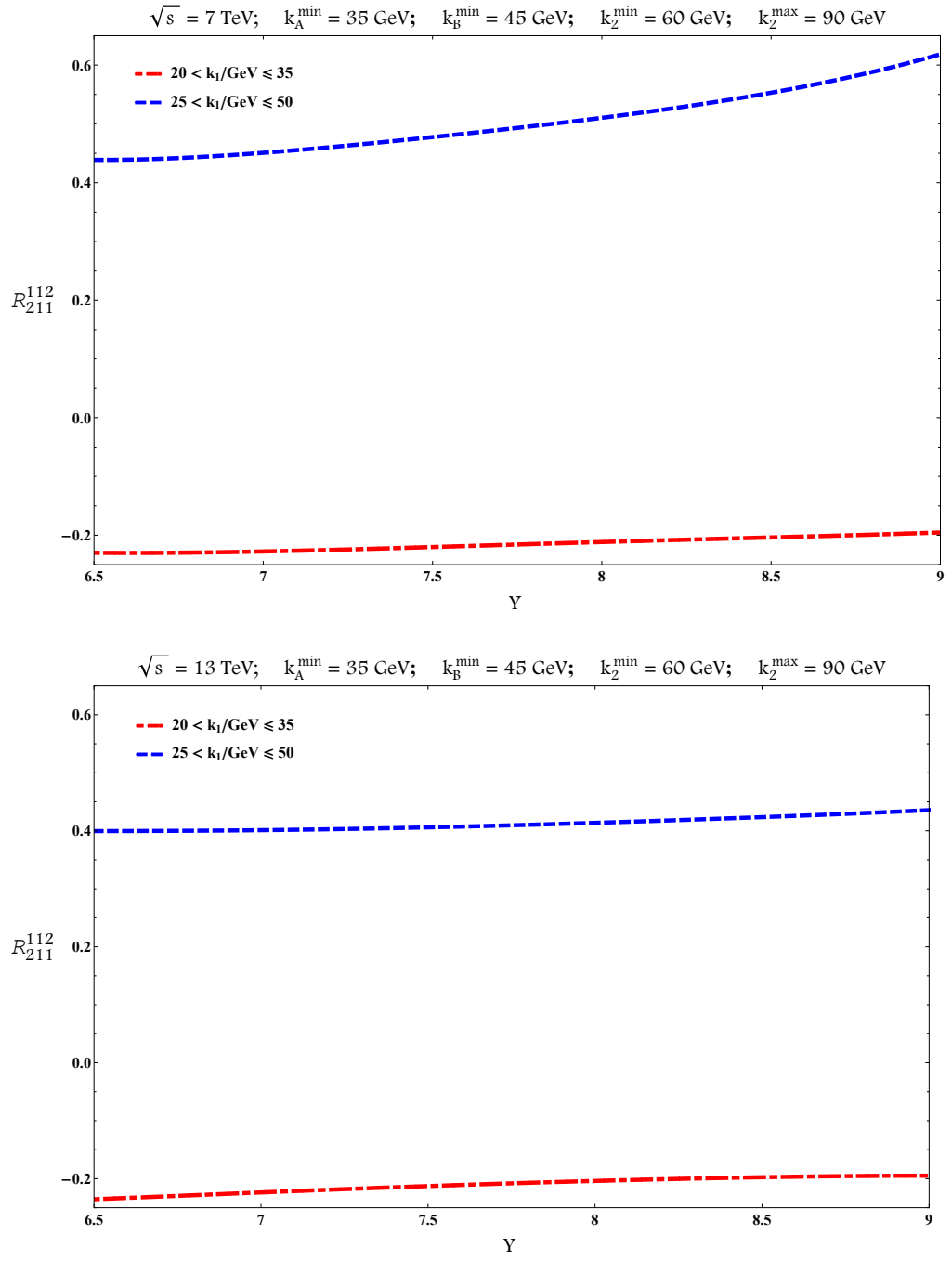


Figure 6.9: Y -dependence of R_{211}^{112} for $\sqrt{s} = 7$ TeV (top) and for $\sqrt{s} = 13$ TeV (bottom).

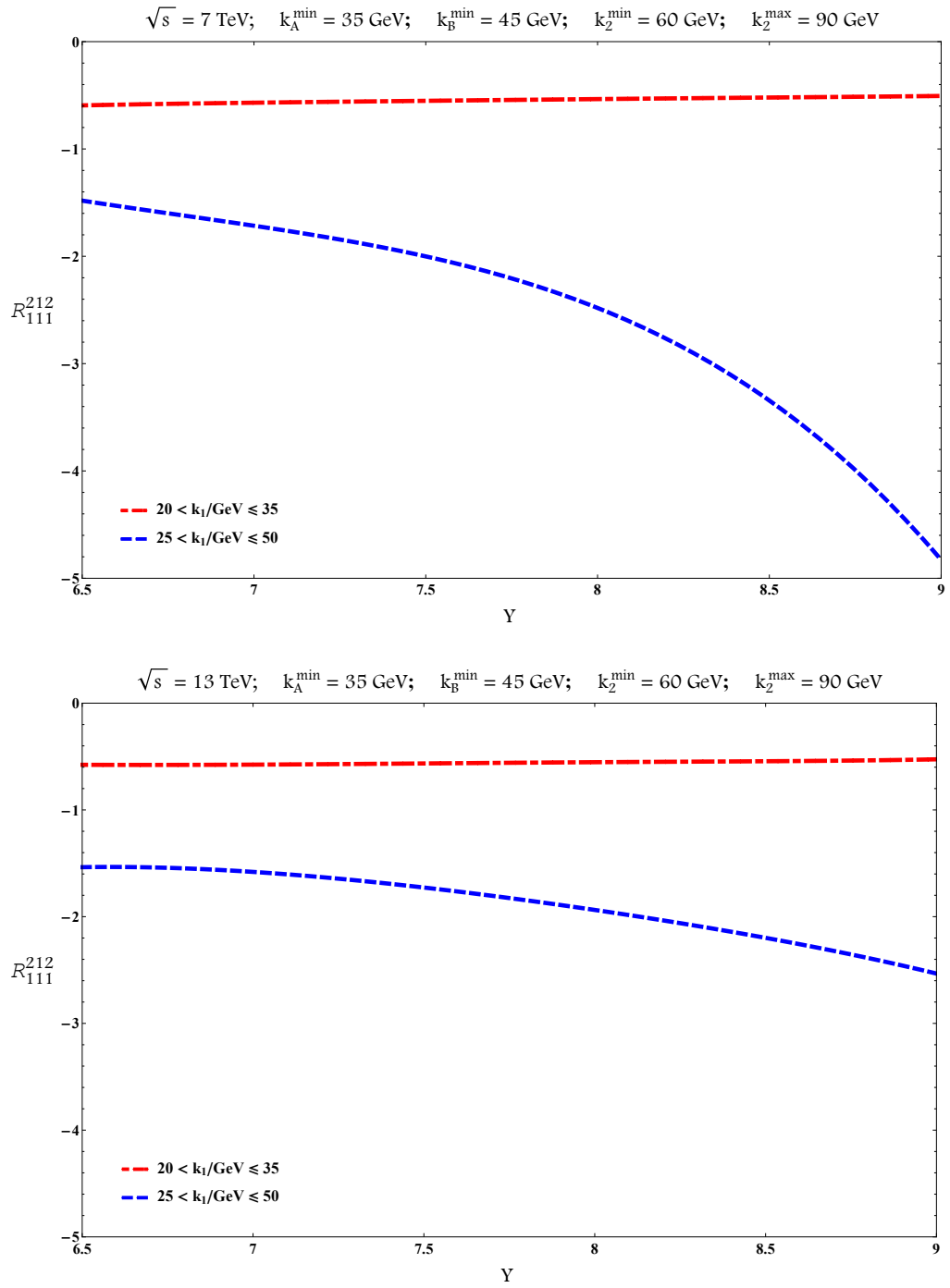


Figure 6.10: Y -dependence of R_{111}^{212} for $\sqrt{s} = 7$ TeV (top) and for $\sqrt{s} = 13$ TeV (bottom).

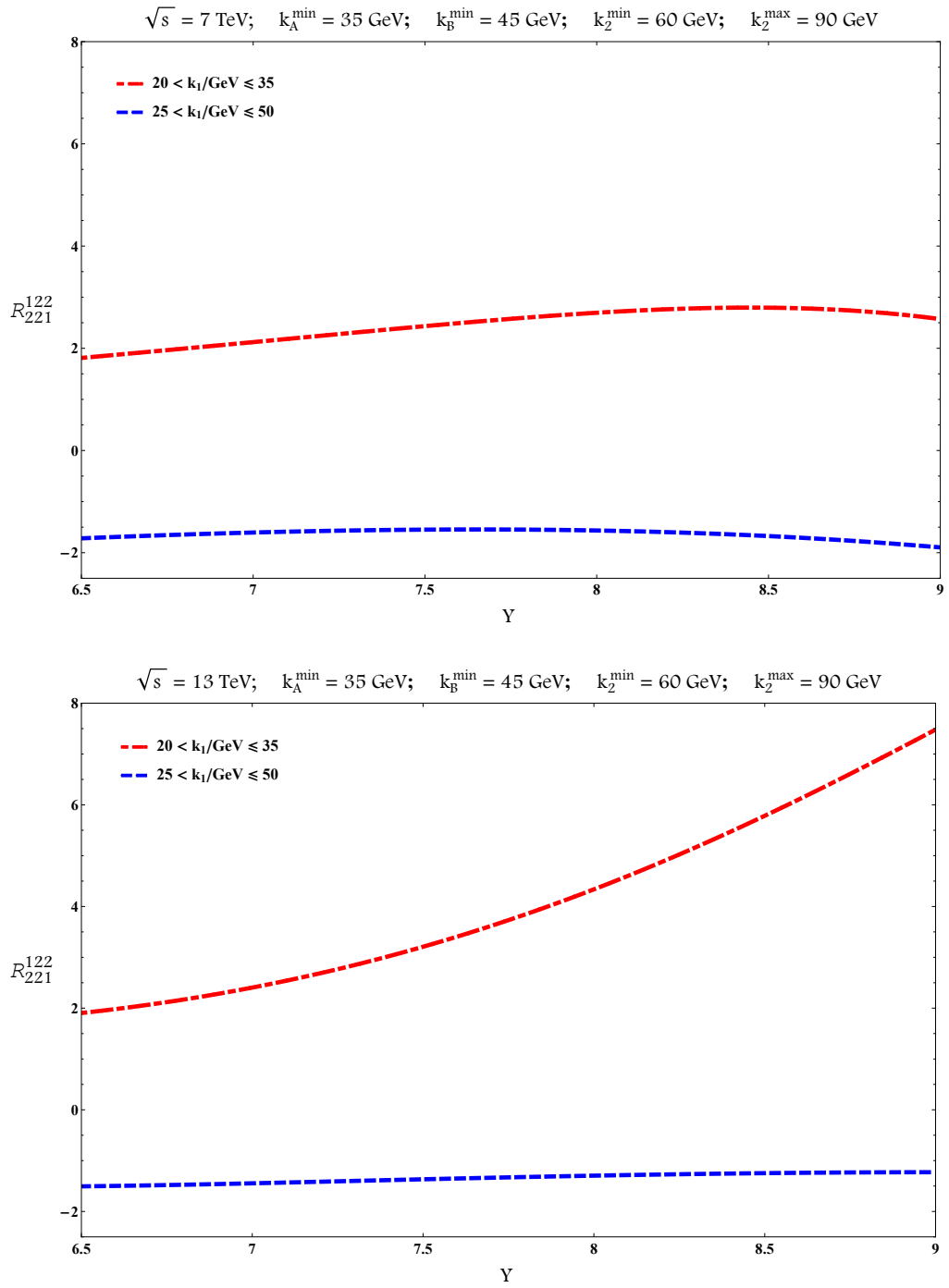


Figure 6.11: Y -dependence of R_{221}^{122} for $\sqrt{s} = 7$ TeV (top) and for $\sqrt{s} = 13$ TeV (bottom).

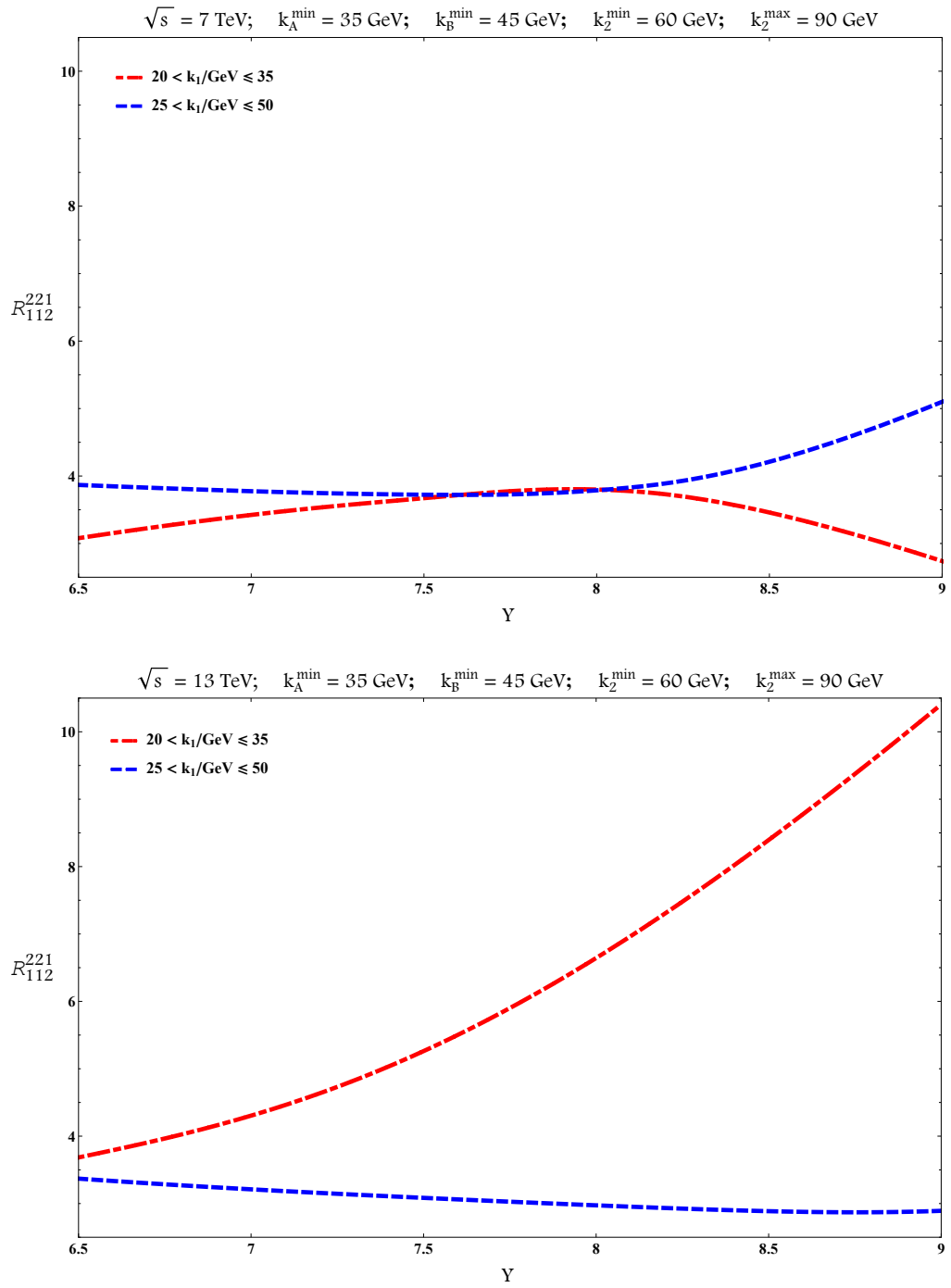


Figure 6.12: Y -dependence of R_{112}^{221} for $\sqrt{s} = 7 \text{ TeV}$ (top) and for $\sqrt{s} = 13 \text{ TeV}$ (bottom).

6.3.3.2 Used tools

The numerical computation of all the observables shown in this Chapter was done in FORTRAN. MATHEMATICA was used for various cross-checks. We used the NLO MSTW 2008 PDF sets [144] whereas regarding the strong coupling a two-loop running coupling setup with $\alpha_s(M_Z) = 0.11707$ and five quark flavours was used. Vegas [181] as implemented in the Cuba library [182, 183] was our main integration routine. We also made use of a modified version of the Psi [148] routine and the library Quadpack [184].

6.4 Summary

New observables were proposed to study four-jet production at hadron colliders in terms of its azimuthal-angle dependences. These correspond to the ratios of correlation functions of products of cosines of azimuthal-angle differences among the tagged jets. A single BFKL ladder approach was used, with inclusive production of two forward/backward and two further, more central, tagged jets. The dependence on the transverse momenta and rapidities of the two central jets is a distinct signal of BFKL dynamics.

The interesting patterns, similar to oscillation modes of a two-dimensional membrane, that the $\mathcal{R}_{PQR}^{\text{MNL}}$ exhibit, are the result of our first analysis at parton level and for final-state fixed kinematics done in Section 6.2. Then (Section 6.3), a full phenomenological study of LHC inclusive four-jet production was presented making use of the BFKL resummation framework. Our study was focused on azimuthal-angle dependent observables, investigating at hadronic level the $\mathcal{R}_{PQR}^{\text{MNL}}$ ratios at two different center-of-mass energies, $\sqrt{s} = 7, 13$ TeV.

An *asymmetric* kinematical cut with respect to the transverse momentum of the most forward (k_A) and most backward (k_B) jets, which is arguably a

more interesting kinematical configuration than a *symmetric* cut, was chosen. The asymmetry was realised by imposing different lower limits to k_A and k_B ($k_A^{\min} = 35$ GeV and $k_B^{\min} = 45$ GeV). Additionally, we demanded for k_2 to be larger than both k_A and k_B whereas the value of the transverse momentum k_1 was allowed to be either smaller than both k_A and k_B or overlapping the k_A and k_B ranges. We presented the dependence of several R_{PQR}^{MNL} on the rapidity interval Y between k_A and k_B . A smooth functional dependence of the ratios on Y seems to be the rule. The ratios we presented show in some cases considerable changes when the colliding energy increases from 7 to 13 TeV which tells us that pre-asymptotic effects do play a role for the azimuthal ratios in inclusive four-jet production.

Chapter 7

Conclusions and Outlook

7.1 Conclusions

We brought exhaustive examples of testable predictions to probe QCD in the high-energy limit through the study of distinct inclusive hadronic processes.

The first reaction (Chapter 3) we investigated is the inclusive production of two jets featuring large transverse momenta and well separated in rapidity, known as Mueller–Navelet jets. We gave predictions [36] with full NLA BFKL accuracy for the jet azimuthal correlations in kinematical ranges already covered by LCH data [44], showing how a fair agreement between theory and experiment is reached when the μ_R and μ_F scales are optimised according to the BLM procedure (Section 2.4). In spite of this, there are still other issues which deserve some care and have not been taken into account both in theoretical and experimental analyses so far.

On one side, the comparison of BFKL-inspired calculations with data needs to be extended to kinematical regimes where the two jets are emitted with *asymmetric* transverse momenta. In this way the Born contribution, which essentially comes from the production of back-to-back jets, is suppressed and

the effects of the additional undetected hard gluon radiation is enhanced, thus giving us the chance to magnify and definitely figure out the size of the BFKL resummation, with respect to descriptions based on the fixed-order DGLAP approach. As a first step in this direction, we compared [46] full NLA BFKL predictions with NLO fixed-order DGLAP calculations in the *high-energy* limit, considering *asymmetric* momentum configurations.

On the other side, for a given value of the jet rapidity separation, the rapidity of one of the two jets could be so small, that this jet is actually produced in the central region, rather than in the fragmentation region of the parent proton. Central jets originate from small- x partons, and the collinear approach for the description of the Mueller–Navelet jet vertices may not hold at small x . Therefore we proposed to return back to the original Mueller–Navelet idea, to study the inclusive production of two forward jets separated by a large rapidity gap, removing from the analysis those regions where jets are produced at central rapidities. This allowed us to give the first phenomenological predictions [47] for Mueller–Navelet jet at the center-of-mass energy of 13 TeV, currently active at the LHC.

The second reaction (Chapter 4) we investigated is the inclusive dihadron production. This process has much in common with the well known Mueller–Navelet jet process. Hadrons can, however, be detected at much smaller values of the transverse momentum than jets, thus allowing us to explore an additional kinematical range, supplementary to the one studied with Mueller–Navelet jets. Furthermore, it has given us the opportunity to constrain not only the PDFs for the initial proton, but also the parton FFs describing the detected hadron in the final state. In a first phenomenological analysis [151], we have shown how the discrepancy between predictions with partial NLA BFKL accuracy and full LLA BFKL calculations is significantly reduced via the use of

the BLM scale setting. Then [152], we gave the first predictions for hadrons' azimuthal correlations at 7 and 13 TeV in the full NLA BFKL approach, considering the effect of choosing different values for the factorisation scale μ_F . We also gauged the uncertainty coming from the use of different PDF and FF parameterisations. Inclusive dihadron production represents so a new suitable channel to get a better understanding of the QCD dynamics in the high-energy limit.

We extended our analysis to the study of more exclusive processes, where one (Chapter 5) or two (Chapter 6) jets are always tagged in the final state in more central regions of the detectors, together with other two forward/backward ones. By demanding a strong ordering in rapidity among the jets, according to MRK, we generalised our formalism to account for high-energy resummation effects. This allowed us to define new, suitable BFKL observables, sensitive to the azimuthal configurations of the tagged extra particles. We started from the partonic level, by giving predictions [170, 185] for azimuthal quantities averaged on the hard cross section. Then, we presented the first phenomenological analyses at hadronic level [171, 186] and for different final-state kinematical ranges, showing the weak dependence of our observables on the rapidity interval between the two outermost jets. Finally [172], we studied the effect of higher-order BFKL corrections, using the BLM method to optimise the renormalisation scale μ_R and considering three distinct setups for the final-state phase space. The general outcome is that the NLA corrections are moderate and our proposed observables exhibit a very good perturbative stability.

In view of all these considerations, we encourage experimental collaborations to consider *asymmetric* configurations in their next Mueller–Navelet jet study, as well as to include inclusive dihadron production and inclusive multi-jet production processes in the program of future analyses at the LHC, making

use of new effective paths to improve our knowledge about the dynamics of strong interactions in the Regge limit.

7.2 Outlook

The study of semi-hard processes is a wide research field, its wealthy phenomenology offering us a faultless chance to test perturbative QCD in the high-energy limit. An ample range of new ideæ can be guessed to extend our understanding of the BFKL dynamics in this kinematical regime. We mention and propose here some possible next studies, which are strictly related to the analysis presented in this thesis.

For all the considered processes, it would be very important to compare our results with fixed-order perturbative calculations based on the DGLAP factorisation, paying particular attention to the Mueller–Navelet and the inclusive dihadron production reactions, where BFKL predictions with full NLA BFKL accuracy have been already provided. Furthermore, we plan to extend our analysis by investigating the effect of using *asymmetric* cuts for the transverse momenta even in the case of hadrons, as well as studying less inclusive reactions where at least one charged light hadron is always tagged in the final state. If, together with the hadron, a forward jet is also emitted, we will have the opportunity to study *hadron-jet* correlations, which clearly enrich the exclusiveness of the process. On one side, the hadron tagging introduces dependence on FFs; on the other side, the larger rapidity values for which jets can be detected with respect to hadrons permit to consider final-state kinematics *asymmetric* also in rapidity.

A further way to disentangle the applicability border of our approach is to make comparisons with some other theoretical predictions which include

higher-twist effects. For the last point, one can consider an alternative, higher-twist production mechanism, related to *multi-parton* interactions in QCD [188–191]. The *double-parton scattering* contribution to the Mueller–Navelet jet production was considered in Refs. [37, 191], using different approaches. It would be very interesting to estimate the effect of the multi-particle interactions also in the other processes we proposed, *i.a.* in the inclusive four-jet production [192–194].

As for the inclusive multi-jet production processes, full NLA BFKL studies are needed [195], as well as comparisons with predictions from the BFKL-inspired Monte Carlo BFKLex [180, 196–202]. Results from general-purpose Monte Carlos tools should also be pursued.

Finally, the inclusion of other resummation effects should be accounted for, such as the threshold-log resummation [159–162] and, in the specific case of Mueller–Navelet jets, the resummation to all orders of logarithms in the jet-cone radius R , which arise when the correspondence between the jet momentum and the original parton’s momentum is strongly affected by radiation at angles larger than R (*micro-jets*) [203, 204].

Bibliography

- [1] S. Mandelstam, *Determination of the pion-nucleon scattering amplitude from dispersion relations and unitarity. General theory*, Phys. Rev. **112** (1958) 1344 doi:[10.1103/PhysRev.112.1344](https://doi.org/10.1103/PhysRev.112.1344). (Cited on page 7.)
- [2] V.N. Gribov, L.N. Lipatov, *Deep inelastic $e p$ scattering in perturbation theory*, Sov. J. Nucl. Phys. **15** (1972) 438. (Cited on pages 7 and 14.)
- [3] V.N. Gribov, L.N. Lipatov, *e^+e^- pair annihilation and deep inelastic $e p$ scattering in perturbation theory*, Sov. J. Nucl. Phys. **15** (1972) 675 [Yad. Fiz. **15** (1972) 1218]. (Cited on pages 7 and 14.)
- [4] L.N. Lipatov, *The parton model and perturbation theory*, Sov. J. Nucl. Phys. **20** (1975) 94 [Yad. Fiz. **20** (1974) 181]. (Cited on pages 7 and 14.)
- [5] G. Altarelli, G. Parisi, *Asymptotic Freedom in Parton Language*, Nucl. Phys. B **126** (1977) 298 doi:[10.1016/0550-3213\(77\)90384-4](https://doi.org/10.1016/0550-3213(77)90384-4). (Cited on pages 7 and 14.)
- [6] Y.L. Dokshitzer, *Calculation of the Structure Functions for Deep Inelastic Scattering and e^+e^- Annihilation by Perturbation Theory in Quantum Chromodynamics*, Sov. Phys. JETP **46** (1977) 641. (Cited on pages 7 and 14.)

- [7] V.S. Fadin, E. Kuraev, L.N. Lipatov, *On the Pomeron Singularity in Asymptotically Free Theories*, Phys. Lett. B **60**, (1975) 50 doi:[10.1016/0370-2693\(75\)90524-9](https://doi.org/10.1016/0370-2693(75)90524-9). (Cited on pages [7](#), [14](#), [15](#), [17](#), [21](#) and [29](#).)
- [8] E. Kuraev, L.N. Lipatov, V.S. Fadin, *Multi-reggeon processes in the Yang-Mills theory*, Zh. Eksp. Teor. Fiz. **71** (1976) 840 [Sov. Phys. JETP **44**, (1976) 443]. (Cited on pages [7](#), [14](#), [15](#), [17](#), [21](#) and [29](#).)
- [9] E. Kuraev, L.N. Lipatov, V.S. Fadin, *The Pomeron Singularity in Non-abelian Gauge Theories*, Zh. Eksp. Teor. Fiz. **72** (1976) 377 [Sov. Phys. JETP **45**, (1977) 199]. (Cited on pages [7](#), [14](#), [17](#), [21](#) and [29](#).)
- [10] I. Balitsky, L.N. Lipatov, *The Pomeron Singularity in Quantum Chromodynamics*, Sov. J. Nucl. Phys. **28**, (1978) 822. (Cited on pages [7](#), [14](#), [17](#), [21](#) and [29](#).)
- [11] V.S. Fadin, L.N. Lipatov, *BFKL pomeron in the next-to-leading approximation*, Phys. Lett. B **429** (1998) 127 doi:[10.1016/S0370-2693\(98\)00473-0](https://doi.org/10.1016/S0370-2693(98)00473-0) [hep-ph/9802290]. (Cited on pages [8](#) and [36](#).)
- [12] M. Ciafaloni, G. Camici, *Energy scale(s) and next-to-leading BFKL equation*, Phys. Lett. B **430** (1998) 349 doi:[10.1016/S0370-2693\(98\)00551-6](https://doi.org/10.1016/S0370-2693(98)00551-6) [hep-ph/9803389]. (Cited on pages [8](#) and [36](#).)
- [13] V.S. Fadin, R. Fiore, A. Papa, *The Quark part of the nonforward BFKL kernel and the 'bootstrap' for the gluon Reggeization*, Phys. Rev. D **60** (1999) 074025 doi:[10.1103/PhysRevD.60.074025](https://doi.org/10.1103/PhysRevD.60.074025) [hep-ph/9812456]. (Cited on pages [8](#) and [27](#).)

- [14] V.S. Fadin, D.A. Gorbachev, *Nonforward color octet BFKL kernel*, JETP Lett. **71** (2000) 222 [Pisma Zh. Eksp. Teor. Fiz. **71** (2000) 322] [Yad. Fiz. **63** (12) (2000) 1] doi:[10.1134/1.568320](https://doi.org/10.1134/1.568320). (Cited on pages 8 and 27.)
- [15] V.S. Fadin, R. Fiore, *Non-forward BFKL Pomeron at next-to-leading order*, Phys. Lett. B **610** (2005) 61 [Erratum: Phys. Lett. B **621** (2005) 61] [hep-ph/0412386] doi:[10.1016/j.physletb.2005.01.062](https://doi.org/10.1016/j.physletb.2005.01.062), doi:[10.1016/j.physletb.2005.06.074](https://doi.org/10.1016/j.physletb.2005.06.074). (Cited on page 8.)
- [16] V.S. Fadin, R. Fiore, *Non-forward NLO BFKL kernel*, Phys. Rev. D **72** (2005) 014018 [hep-ph/0502045] doi:[10.1103/PhysRevD.72.014018](https://doi.org/10.1103/PhysRevD.72.014018). (Cited on page 8.)
- [17] M. Hentschinski, A. Sabio Vera, C. Salas, *The hard to soft Pomeron transition in small x DIS data using optimal renormalization*, Phys. Rev. Lett. **110** (2013) 041601 doi:[10.1103/PhysRevLett.110.041601](https://doi.org/10.1103/PhysRevLett.110.041601) [arXiv:1209.1353 [hep-ph]]. (Cited on page 8.)
- [18] M. Hentschinski, A. Sabio Vera, C. Salas, *Description of F_2 and F_L at small x using a collinearly-improved BFKL resummation*, Phys. Rev. D **87** (2013) 076005 doi:[10.1103/PhysRevD.87.076005](https://doi.org/10.1103/PhysRevD.87.076005) [arXiv:1301.5283 [hep-ph]]. (Cited on page 8.)
- [19] A.H. Mueller, H. Navelet, *An Inclusive Minijet Cross-Section and the Bare Pomeron in QCD*, Nucl. Phys. B **282** (1987) 727 doi:[10.1016/0550-3213\(87\)90705-X](https://doi.org/10.1016/0550-3213(87)90705-X). (Cited on page 8.)
- [20] *The Gluon Impact Factors*, V.S. Fadin, R. Fiore, M.I. Kotsky, A. Papa, Phys. Lett. D **61** (2000) 094005 doi:[10.1103/PhysRevD.61.094005](https://doi.org/10.1103/PhysRevD.61.094005) [arXiv:9908264 [hep-ph]]. (Cited on pages 8, 51, 101 and 132.)

- [21] *The Quark Impact Factors*, V.S. Fadin, R. Fiore, M.I. Kotsky, A. Papa, Phys. Lett. D **61** (2000) 094006 doi:[10.1103/PhysRevD.61.094006](https://doi.org/10.1103/PhysRevD.61.094006) [arXiv:9908265 [hep-ph]]. (Cited on pages [8](#), [51](#), [101](#) and [132](#).)
- [22] M. Ciafaloni, *Energy scale and coherence effects in small x equations*, Phys. Lett. B **429**, (1998) 363 doi:[10.1016/S0370-2693\(98\)00249-4](https://doi.org/10.1016/S0370-2693(98)00249-4) [hep-ph/9801322]. (Cited on page [8](#).)
- [23] M. Ciafaloni and D. Colferai, *K factorization and impact factors at next-to-leading level*, Nucl. Phys. B **538**, (1999) 187 doi:[10.1016/S0550-3213\(98\)00621-X](https://doi.org/10.1016/S0550-3213(98)00621-X) [hep-ph/9806350]. (Cited on page [8](#).)
- [24] J. Bartels, D. Colferai, G.P. Vacca, *The NLO jet vertex for Mueller-Navelet and forward jets: The Quark part*, Eur. Phys. J. C **24** (2002) 83 doi:[10.1007/s100520200919](https://doi.org/10.1007/s100520200919) [hep-ph/0112283]. (Cited on page [8](#).)
- [25] J. Bartels, D. Colferai, G.P. Vacca, *The NLO jet vertex for Mueller-Navelet and forward jets: The Gluon part*, Eur. Phys. J. C **29** (2003) 235 doi:[10.1140/epjc/s2003-01169-5](https://doi.org/10.1140/epjc/s2003-01169-5) [hep-ph/0206290]. (Cited on page [8](#).)
- [26] F. Caporale, D.Yu. Ivanov, B. Murdaca, A. Papa, A. Perri, *The next-to-leading order jet vertex for Mueller-Navelet and forward jets revisited*, JHEP **1202** (2012) 101 doi:[10.1007/JHEP02\(2012\)101](https://doi.org/10.1007/JHEP02(2012)101) [arXiv:1112.3752 [hep-ph]]. (Cited on page [8](#).)
- [27] D.Yu. Ivanov, A. Papa, *The next-to-leading order forward jet vertex in the small-cone approximation*, JHEP **1205** (2012) 086 doi:[10.1007/JHEP05\(2012\)086](https://doi.org/10.1007/JHEP05(2012)086) [arXiv:1202.1082 [hep-ph]]. (Cited on page [8](#).)

- [28] D. Colferai, A. Niccoli, *The NLO jet vertex in the small-cone approximation for kt and cone algorithms*, JHEP **1504** (2015) 071 doi:[10.1007/JHEP04\(2015\)071](https://doi.org/10.1007/JHEP04(2015)071) [arXiv:1501.07442 [hep-ph]]. (Cited on page 8.)
- [29] D. Colferai, F. Schwennsen, L. Szymanowski, S. Wallon, *Mueller Navelet jets at LHC - complete NLL BFKL calculation*, JHEP **1012** (2010) 026 doi:[10.1007/JHEP12\(2010\)026](https://doi.org/10.1007/JHEP12(2010)026) [arXiv:1002.1365 [hep-ph]]. (Cited on pages 9 and 63.)
- [30] M. Angioni, G. Chachamis, J.D. Madrigal, A. Sabio Vera, *Dijet Production at Large Rapidity Separation in N=4 SYM*, Phys. Rev. Lett. **107**, (2011) 191601 doi:[10.1103/PhysRevLett.107.191601](https://doi.org/10.1103/PhysRevLett.107.191601) [arXiv:1106.6172 [hep-th]]. (Cited on page 9.)
- [31] F. Caporale, D.Yu. Ivanov, B. Murdaca, A. Papa, *Mueller–Navelet small-cone jets at LHC in next-to-leading BFKL*, Nucl. Phys. B **877** (2013) 73 doi:[10.1016/j.nuclphysb.2013.09.013](https://doi.org/10.1016/j.nuclphysb.2013.09.013) [arXiv:1211.7225 [hep-ph]]. (Cited on pages 9, 95 and 97.)
- [32] B. Ducloué, L. Szymanowski, S. Wallon, *Confronting Mueller–Navelet jets in NLL BFKL with LHC experiments at 7 TeV*, JHEP **1305** (2013) 096 doi:[10.1007/JHEP05\(2013\)096](https://doi.org/10.1007/JHEP05(2013)096) [arXiv:1302.7012 [hep-ph]]. (Cited on pages 9, 90 and 148.)
- [33] F. Caporale, B. Murdaca, A. Sabio Vera, C. Salas, *Scale choice and collinear contributions to Mueller–Navelet jets at LHC energies*, Nucl. Phys. B **875** (2013) 134 doi:[10.1016/j.nuclphysb.2013.07.005](https://doi.org/10.1016/j.nuclphysb.2013.07.005) [arXiv:1305.4620 [hep-ph]]. (Cited on pages 9, 37, 139 and 174.)
- [34] B. Ducloué, L. Szymanowski, S. Wallon, *Evidence for high-energy resummation effects in Mueller–Navelet jets at the LHC*, Phys. Rev. Lett. **112**

- (2014) 082003 doi:[10.1103/PhysRevLett.112.082003](https://doi.org/10.1103/PhysRevLett.112.082003) [arXiv:1309.3229 [hep-ph]]. (Cited on pages 9 and 49.)
- [35] B. Ducloué, L. Szymanowski, S. Wallon, *Violation of energy-momentum conservation in Mueller–Navelet jets production*, Phys. Lett. B **738** (2014) 311 doi:[10.1016/j.physletb.2014.09.025](https://doi.org/10.1016/j.physletb.2014.09.025) [arXiv:1407.6593 [hep-ph]]. (Cited on pages 9, 63 and 92.)
- [36] F. Caporale, D.Yu. Ivanov, B. Murdaca, A. Papa, *Mueller-Navelet jets in next-to-leading order BFKL: theory versus experiment*, Eur. Phys. J. C **74** (2014) no.10, 3084 Erratum: [Eur. Phys. J. C **75** (2015) no.11, 535] doi:[10.1140/epjc/s10052-014-3084-z](https://doi.org/10.1140/epjc/s10052-014-3084-z), doi:[10.1140/epjc/s10052-015-3754-5](https://doi.org/10.1140/epjc/s10052-015-3754-5) [arXiv:1407.8431 [hep-ph]]. (Cited on pages 9, 36, 49, 58, 91 and 195.)
- [37] B. Ducloué, L. Szymanowski and S. Wallon, *Evaluating the double parton scattering contribution to Mueller–Navelet jets production at the LHC*, Phys. Rev. D **92** (2015) no.7, 076002 doi:[10.1103/PhysRevD.92.076002](https://doi.org/10.1103/PhysRevD.92.076002) [arXiv:1507.04735 [hep-ph]]. (Cited on pages 9 and 199.)
- [38] F. Caporale, D.Yu. Ivanov, B. Murdaca, A. Papa, *Brodsky-Lepage-Mackenzie optimal renormalization scale setting for semi-hard processes*, Phys. Rev. D **91** (2015) no.11, 114009 doi:[10.1103/PhysRevD.91.114009](https://doi.org/10.1103/PhysRevD.91.114009) [arXiv:1504.06471 [hep-ph]]. (Cited on pages 9, 38, 104 and 106.)
- [39] G. Chachamis, *BFKL phenomenology*, arXiv:1512.04430 [hep-ph]. (Cited on page 9.)
- [40] V. Del Duca, C.R. Schmidt, *Dijet production at large rapidity intervals*, Phys. Rev. D **49** (1994) 4510 doi:[10.1103/PhysRevD.49.4510](https://doi.org/10.1103/PhysRevD.49.4510) [hep-ph/9311290]. (Cited on page 9.)

- [41] W.J. Stirling, *Production of jet pairs at large relative rapidity in hadron hadron collisions as a probe of the perturbative pomeron*, Nucl. Phys. B **423** (1994) 56 doi:[10.1016/0550-3213\(94\)90565-7](https://doi.org/10.1016/0550-3213(94)90565-7) [hep-ph/9401266]. (Cited on page 9.)
- [42] A. Sabio Vera, *The Effect of NLO conformal spins in azimuthal angle decorrelation of jet pairs*, Nucl. Phys. B **746** (2006) 1 doi:[10.1016/j.nuclphysb.2006.04.004](https://doi.org/10.1016/j.nuclphysb.2006.04.004) [hep-ph/0602250]. (Cited on page 9.)
- [43] A. Sabio Vera and F. Schwennsen, *The Azimuthal decorrelation of jets widely separated in rapidity as a test of the BFKL kernel*, Nucl. Phys. B **776** (2007) 170 doi:[10.1103/PhysRevLett.77.595](https://doi.org/10.1103/PhysRevLett.77.595) [hep-ph/0702158 [hep-ph]]. (Cited on pages 9 and 37.)
- [44] V. Khachatryan *et al.* [CMS Collaboration], *Azimuthal decorrelation of jets widely separated in rapidity in pp collisions at $\sqrt{s} = 7$ TeV*, JHEP **1608** (2016) 139 doi:[10.1007/JHEP08\(2016\)139](https://doi.org/10.1007/JHEP08(2016)139) [arXiv:1601.06713 [hep-ex]]. (Cited on pages 9, 49, 57, 58, 61, 64, 91, 105, 163 and 195.)
- [45] D.Yu. Ivanov, A. Papa, *Inclusive production of a pair of hadrons separated by a large interval of rapidity in proton collisions*, JHEP **1207** (2012) 045 doi:[10.1007/JHEP07\(2012\)045](https://doi.org/10.1007/JHEP07(2012)045) [arXiv:1205.6068 [hep-ph]]. (Cited on pages 9, 98, 99, 102, 106 and 130.)
- [46] F.G. Celiberto, D.Yu. Ivanov, B. Murdaca, A. Papa, *Mueller–Navelet Jets at LHC: BFKL Versus High-Energy DGLAP*, Eur. Phys. J. C **75** (2015) no.6, 292 doi:[10.1140/epjc/s10052-015-3522-6](https://doi.org/10.1140/epjc/s10052-015-3522-6) [arXiv:1504.08233 [hep-ph]]. (Cited on pages 10, 49, 91, 148 and 196.)
- [47] F.G. Celiberto, D.Yu. Ivanov, B. Murdaca, A. Papa, *Mueller–Navelet jets at 13 TeV LHC: dependence on dynamic constraints in the central rapidity re-*

- gion, Eur. Phys. J. C **76** (2016) no.4, 224 doi:[10.1140/epjc/s10052-016-4053-5](https://doi.org/10.1140/epjc/s10052-016-4053-5) [arXiv:1601.07847 [hep-ph]]. (Cited on pages [10](#), [49](#), [92](#) and [196](#).)
- [48] D.Yu. Ivanov, A. Papa, *Electroproduction of two light vector mesons in the next-to-leading approximation*, Nucl. Phys. B **732** (2006) 183 doi:[10.1016/j.nuclphysb.2005.10.028](https://doi.org/10.1016/j.nuclphysb.2005.10.028) [hep-ph/0508162]. (Cited on page [30](#).)
- [49] D.Yu. Ivanov, A. Papa, *Electroproduction of two light vector mesons in next-to-leading BFKL: Study of systematic effects*, Eur. Phys. J. C **49** (2007) 947 doi:[10.1140/epjc/s10052-006-0180-8](https://doi.org/10.1140/epjc/s10052-006-0180-8) [hep-ph/0610042]. (Cited on page [30](#).)
- [50] T. Regge, *Introduction to complex orbital momenta*, Nuovo Cim. **14** (1959) 951 doi:[10.1007/BF02728177](https://doi.org/10.1007/BF02728177). (Cited on pages [12](#) and [15](#).)
- [51] P.D.B. Collins, *An introduction to Regge Theory and high energy physics*, New York: Cambridge University Press, ISBN-10: 0521110351/ISBN-13: 978-0521110358, 1977 doi:[10.1063/1.3001833](https://doi.org/10.1063/1.3001833). (Cited on page [12](#).)
- [52] V. Barone, E. Predazzi, *High-Energy Particle Diffraction*, Berlin, Heidelberg: Springer, ISBN 10: 3540421076 /ISBN 13: 978-3540421078, 2002 doi:[10.1007/978-3-662-04724-8](https://doi.org/10.1007/978-3-662-04724-8). (Cited on pages [12](#) and [15](#).)
- [53] G.F.P. Chew, S.C. Frautschi, *Principle of Equivalence for All Strongly Interacting Particles Within the S Matrix Framework*, Phys. Rev. Lett. **7** (1961) 394 doi:[10.1103/PhysRevLett.7.394](https://doi.org/10.1103/PhysRevLett.7.394). (Cited on page [12](#).)

- [54] V.N. Gribov, *Partial waves with complex orbital angular momenta and the asymptotic behavior of the scattering amplitude*, Sov. Phys. JETP **14** (1962) 1395 [Zh. Eksp. Teor. Fiz. **41** (1961) 1962]. (Cited on page [12](#).)
- [55] R.G. Newton, *Optical theorem and beyond*, Am. J. Phys. **44** (1976) 639 doi:[10.1119/1.10324](#). (Cited on page [13](#).)
- [56] M. Froissart, *Asymptotic behavior and subtractions in the Mandelstam representation*, Phys. Rev. **123** (1961) 1053 doi:[10.1103/PhysRev.123.1053](#). (Cited on pages [14](#) and [30](#).)
- [57] J.R. Forshaw, D.A. Ross, *Quantum Chromodynamics and the Pomeron*, Cambridge: Cambridge University Press, ISBN 10: 0521568803/ISBN 13: 978-0521568807, 1997 doi:[10.1017/CBO9780511524387](#). (Cited on page [14](#).)
- [58] M. Gell-Mann, M.L. Goldberger, F.E. Low, E. Marx, F. Zachariasen, *Elementary Particles of Conventional Field Theory as Regge Poles. III*, Phys. Rev. B **133** (1964) 145 doi:[PhysRev.133.B145](#). (Cited on page [15](#).)
- [59] B.L. Ioffe, V.S. Fadin, L.N. Lipatov, *Quantum Chromodynamics Perturbative and Nonperturbative Aspects*, Cambridge Monographs on Particle Physics, Nuclear Physics and Cosmology, New York: Cambridge University Press, ISBN 10: 0521631483/ISBN 13: 978-0521631488, 2010 doi:[10.1080/00107514.2011.580051](#). (Cited on page [15](#).)
- [60] S. Mandelstam, *Non-Regge Terms in the Vector-Spinor Theory*, Phys. Rev. B **137** (1965) 949 doi:[10.1103/PhysRev.137.B949](#). (Cited on page [15](#).)

- [61] M.T. Grisaru, H.J. Schnitzer, H.S. Tsao, *Reggeization of yang-mills gauge mesons in theories with a spontaneously broken symmetry*, Phys. Rev. Lett. **30** (1973) 811 doi:[10.1103/PhysRevLett.30.811](https://doi.org/10.1103/PhysRevLett.30.811). (Cited on page 15.)
- [62] M.T. Grisaru, H.J. Schnitzer, H.S. Tsao, *Reggeization of elementary particles in renormalizable gauge theories - vectors and spinors*, Phys. Rev. D **8** (1973) 4498 doi:[10.1103/PhysRevD.8.4498](https://doi.org/10.1103/PhysRevD.8.4498). (Cited on page 15.)
- [63] L.N. Lipatov, *Reggeization of the Vector Meson and the Vacuum Singularity in Nonabelian Gauge Theories*, Sov. J. Nucl. Phys. **23** (1976) 338 [Yad. Fiz. **23** (1976) 642]. (Cited on page 15.)
- [64] V.S. Fadin, V.E. Sherman, *Fermion Reggeization in Nonabelian Calibration Theories*, Pisma Zh. Eksp. Teor. Fiz. **23** (1976) 599. (Cited on page 15.)
- [65] V.S. Fadin, V.E. Sherman, *Processes Involving Fermion Exchange in Nonabelian Gauge Theories*, Zh. Eksp. Teor. Fiz. **72** (1977) 1640. (Cited on page 15.)
- [66] A.V. Bogdan, V. Del Duca, V.S. Fadin, E.W.N. Glover, *The Quark Regge trajectory at two loops*, JHEP **0203** (2002) 032 doi:[10.1088/1126-6708/2002/03/032](https://doi.org/10.1088/1126-6708/2002/03/032) [hep-ph/0201240]. (Cited on page 15.)
- [67] M.I. Kotsky, L.N. Lipatov, A. Principe, M.I. Vyazovsky, *Radiative corrections to the quark gluon Reggeized quark vertex in QCD*, Nucl. Phys. B **648** (2003) 277 doi:[10.1016/S0550-3213\(02\)00967-7](https://doi.org/10.1016/S0550-3213(02)00967-7) [hep-ph/0207169]. (Cited on page 15.)
- [68] V.S. Fadin, *BFKL news*, BUDKER-INP-1998-55 [hep-ph/9807528]. (Cited on pages 17, 23 and 27.)

- [69] V.S. Fadin, L.N. Lipatov, *High-Energy Production of Gluons in a Quasimulti-Regge Kinematics*, JETP Lett. **49** (1989) 352 [Yad. Fiz. **50** (1989) 1141] [Sov. J. Nucl. Phys. **50** (1989) 712]. (Cited on page 18.)
- [70] V.S. Fadin, *Regge trajectory of a gluon in the two loop approximation*, JETP Lett. **61** (1995) 346 [Pisma Zh. Eksp. Teor. Fiz. **61** (1995) 342]. (Cited on pages 18 and 27.)
- [71] V.S. Fadin, R. Fiore, A. Quartarolo, *Reggeization of quark quark scattering amplitude in QCD*, Phys. Rev. D **53** (1996) 2729 doi:[10.1103/PhysRevD.53.2729](https://doi.org/10.1103/PhysRevD.53.2729) [hep-ph/9506432]. (Cited on pages 18 and 27.)
- [72] M.I. Kotsky, V.S. Fadin, *Reggeization of the amplitude of gluon-gluon scattering*, Phys. Atom. Nucl. **59** (1996) 1035 [Yad. Fiz. **59N6** (1996) 1080]. (Cited on pages 18 and 27.)
- [73] V.S. Fadin, M.I. Kotsky, R. Fiore, *Gluon Reggeization in QCD in the next-to-leading order*, Phys. Lett. B **359** (1995) 181 doi:[10.1016/0370-2693\(95\)01016-J](https://doi.org/10.1016/0370-2693(95)01016-J). (Cited on pages 18 and 27.)
- [74] V.S. Fadin, R. Fiore, M.I. Kotsky, *Gluon Regge trajectory in the two loop approximation*, Phys. Lett. B **387** (1996) 593 doi:[10.1016/0370-2693\(96\)01054-4](https://doi.org/10.1016/0370-2693(96)01054-4) [hep-ph/9605357]. (Cited on pages 18 and 27.)
- [75] V.S. Fadin, R. Fiore, M.G. Kozlov, A.V. Reznichenko, *Proof of the multi-Regge form of QCD amplitudes with gluon exchanges in the NLA*, Phys. Lett. B **639** (2006) 74 doi:[10.1016/j.physletb.2006.03.031](https://doi.org/10.1016/j.physletb.2006.03.031) [hep-ph/0602006]. (Cited on pages 18 and 27.)
- [76] M.G. Kozlov, A.V. Reznichenko, V.S. Fadin, *Check of the gluon-Reggeization condition in the next-to-leading order: Quark part*, Phys. Atom. Nucl. **74** (2011)

- 758 [Yad. Fiz. 74 (2011) 784] doi:[10.1134/S1063778811050152](https://doi.org/10.1134/S1063778811050152). (Cited on pages 18 and 27.)
- [77] M.G. Kozlov, A.V. Reznichenko, V.S. Fadin, *Check of the gluon-Reggeization condition in the next-to-leading order: Gluon part*, Phys. Atom. Nucl. 75 (2012) 493 doi:[10.1134/S1063778812030106](https://doi.org/10.1134/S1063778812030106). (Cited on pages 18 and 27.)
- [78] R.E. Cutkosky, *Singularities and discontinuities of Feynman amplitudes*, J. Math. Phys. 1 (1960) 429 doi:[10.1063/1.1703676](https://doi.org/10.1063/1.1703676). (Cited on page 18.)
- [79] J. Bartels, *A Reggeon Calculus for the Production Amplitude. 1.*, Phys. Rev. D 11 (1975) no.10, 2977 doi:[10.1103/PhysRevD.11.2977](https://doi.org/10.1103/PhysRevD.11.2977). (Cited on page 21.)
- [80] J. Bartels, *A Reggeon Calculus for the Production Amplitude. 2.*, Phys. Rev. D 11 (1975) no.10, 2989 doi:[10.1103/PhysRevD.11.2989](https://doi.org/10.1103/PhysRevD.11.2989). (Cited on page 21.)
- [81] J. Bartels, *High-Energy Behavior in a Nonabelian Gauge Theory (II): First Corrections to $T_{n \rightarrow m}$ Beyond the Leading $\ln s$ Approximation*, Nucl. Phys. B 175 (1980) 365 doi:[10.1016/0550-3213\(80\)90019-X](https://doi.org/10.1016/0550-3213(80)90019-X). (Cited on pages 21 and 30.)
- [82] V.S. Fadin, L.N. Lipatov, *Radiative corrections to QCD scattering amplitudes in a multi-Regge kinematics*, Nucl. Phys. B 406 (1993) 259 doi:[10.1016/0550-3213\(93\)90168-O](https://doi.org/10.1016/0550-3213(93)90168-O). (Cited on page 21.)
- [83] V.S. Fadin, R. Fiore, *The Generalized nonforward BFKL equation and the 'bootstrap' condition for the gluon Reggeization in the NLLA*, Phys. Lett. B 440 (1998) 359 doi:[10.1016/S0370-2693\(98\)01099-5](https://doi.org/10.1016/S0370-2693(98)01099-5) [hep-ph/9807472]. (Cited on page 21.)
- [84] V.S. Fadin, L.N. Lipatov, *Higher order corrections to QCD scattering amplitudes in a multi-Regge kinematics*, Nucl. Phys. Proc. Suppl. 29A (1992) 93 doi:[10.1016/0920-5632\(92\)90429-V](https://doi.org/10.1016/0920-5632(92)90429-V). (Cited on page 27.)

- [85] V.S. Fadin, L.N. Lipatov, *Next-to-leading corrections to the BFKL*, Nucl. Phys. B **477** (1996) 767 doi:[10.1016/0550-3213\(96\)00334-3](https://doi.org/10.1016/0550-3213(96)00334-3) [hep-ph/9602287]. (Cited on page 27.)
- [86] V.S. Fadin, M.I. Kotsky, L.N. Lipatov, *One-loop correction to the BFKL kernel from two gluon production*, Phys. Lett. B **415** (1997) 97 doi:[10.1016/S0370-2693\(97\)01210-0](https://doi.org/10.1016/S0370-2693(97)01210-0). (Cited on page 27.)
- [87] M.I. Kotsky, V.S. Fadin, L.N. Lipatov, *Two-gluon contribution to the kernel of the Balitsky-Fadin-Kuraev-Lipatov equation*, Phys. Atom. Nucl. **61** (1998) 641 [Yad. Fiz. **61** (1998) 716]. (Cited on page 27.)
- [88] V.S. Fadin, R. Fiore, A. Flachi, M.I. Kotsky, *Quark-antiquark contribution to the BFKL kernel*, Phys. Lett. B **422** (1998) 287 doi:[10.1016/S0370-2693\(98\)00044-6](https://doi.org/10.1016/S0370-2693(98)00044-6) [hep-ph/9711427]. (Cited on page 27.)
- [89] S. Catani, M. Ciafaloni, F. Hautmann, *Gluon contributions to small x heavy flavor production*, Phys. Lett. B **242** (1990) 97 doi:[10.1016/0370-2693\(90\)91601-7](https://doi.org/10.1016/0370-2693(90)91601-7). (Cited on page 27.)
- [90] S. Catani, M. Ciafaloni, F. Hautmann, *High-energy factorization and small- x heavy flavor production*, Nucl. Phys. B **366** (1991) 135 doi:[10.1016/0550-3213\(91\)90055-3](https://doi.org/10.1016/0550-3213(91)90055-3). (Cited on pages 27, 71 and 74.)
- [91] I. Balitsky, *Operator expansion for high-energy scattering*, Nucl. Phys. B **463** (1996) 99 doi:[10.1016/0550-3213\(95\)00638-9](https://doi.org/10.1016/0550-3213(95)00638-9) [hep-ph/9509348]. (Cited on page 30.)
- [92] Y.V. Kovchegov, *Small x $F(2)$ structure function of a nucleus including multiple pomeron exchanges*, Phys. Rev. D **60** (1999) 034008 doi:[10.1103/PhysRevD.60.034008](https://doi.org/10.1103/PhysRevD.60.034008) [hep-ph/9901281]. (Cited on page 30.)

- [93] J. Kwiecinski, M. Praszalowicz, *Three Gluon Integral Equation and Odd c Singlet Regge Singularities in QCD,* Phys. Lett. **94B** (1980) 413 doi:[10.1016/0370-2693\(80\)90909-0](https://doi.org/10.1016/0370-2693(80)90909-0). (Cited on page 30.)
- [94] L.N. Lipatov, *Gauge invariant effective action for high-energy processes in QCD,* Nucl. Phys. B **452** (1995) 369 doi:[10.1016/0550-3213\(95\)00390-E](https://doi.org/10.1016/0550-3213(95)00390-E) [hep-ph/9502308]. (Cited on page 30.)
- [95] L.N. Lipatov, *Small x physics in perturbative QCD,* Phys. Rept. **286** (1997) 131 doi:[10.1016/S0370-1573\(96\)00045-2](https://doi.org/10.1016/S0370-1573(96)00045-2) [hep-ph/9610276]. (Cited on page 30.)
- [96] A.V. Kotikov, L.N. Lipatov, *NLO corrections to the BFKL equation in QCD and in supersymmetric gauge theories,* Nucl. Phys. B **582** (2000) 19 doi:[10.1016/S0550-3213\(00\)00329-1](https://doi.org/10.1016/S0550-3213(00)00329-1), [hep-ph/0004008]. (Cited on page 33.)
- [97] A.V. Kotikov, L.N. Lipatov, *DGLAP and BFKL equations in the $N = 4$ supersymmetric gauge theory,* Nucl. Phys. B **661** (2003) 19 [Erratum: Nucl. Phys. B **685** (2004) 405] doi:[10.1016/S0550-3213\(03\)00264-5](https://doi.org/10.1016/S0550-3213(03)00264-5), doi:[10.1016/j.nuclphysb.2004.02.032](https://doi.org/10.1016/j.nuclphysb.2004.02.032) [hep-ph/0208220]. (Cited on page 33.)
- [98] G.P. Salam, *A Resummation of large subleading corrections at small x ,* JHEP **9807** (1998) 019 doi:[10.1088/1126-6708/1998/07/019](https://doi.org/10.1088/1126-6708/1998/07/019) [hep-ph/9806482]. (Cited on page 37.)
- [99] M. Ciafaloni, D. Colferai, *The BFKL equation at next-to-leading level and beyond,* Phys. Lett. B **452** (1999) 372 doi:[10.1016/S0370-2693\(99\)00281-6](https://doi.org/10.1016/S0370-2693(99)00281-6) [hep-ph/9812366]. (Cited on page 37.)

- [100] M. Ciafaloni, D. Colferai, G. P. Salam, *renormalization group improved small x equation*, Phys. Rev. D **60** (1999) 114036 doi:[10.1103/PhysRevD.60.114036](https://doi.org/10.1103/PhysRevD.60.114036) [hep-ph/9905566]. (Cited on page 37.)
- [101] M. Ciafaloni, D. Colferai, G.P. Salam, *A collinear model for small x physics*, JHEP **9910** (1999) 017 doi:[10.1088/1126-6708/1999/10/017](https://doi.org/10.1088/1126-6708/1999/10/017) [hep-ph/9907409]. (Cited on page 37.)
- [102] M. Ciafaloni, D. Colferai, G.P. Salam, *On factorization at small x* , JHEP **0007** (2000) 054 doi:[10.1088/1126-6708/2000/07/054](https://doi.org/10.1088/1126-6708/2000/07/054) [hep-ph/0007240]. (Cited on page 37.)
- [103] M. Ciafaloni, D. Colferai, G.P. Salam, A.M. Stasto, *Tunneling transition to the pomeron regime*, Phys. Lett. B **541** (2002) 314 doi:[10.1016/S0370-2693\(02\)02271-2](https://doi.org/10.1016/S0370-2693(02)02271-2) [hep-ph/0204287]. (Cited on page 37.)
- [104] M. Ciafaloni, D. Colferai, G.P. Salam, A.M. Stasto, *Expanding running coupling effects in the hard pomeron*, Phys. Rev. D **66** (2002) 054014 doi:[10.1103/PhysRevD.66.054014](https://doi.org/10.1103/PhysRevD.66.054014) [hep-ph/0204282]. (Cited on page 37.)
- [105] M. Ciafaloni, D. Colferai, D. Colferai, G.P. Salam, A.M. Stasto, *Extending QCD perturbation theory to higher energies*, Phys. Lett. B **576** (2003) 143 doi:[10.1016/j.physletb.2003.09.078](https://doi.org/10.1016/j.physletb.2003.09.078) [hep-ph/0305254]. (Cited on page 37.)
- [106] M. Ciafaloni, D. Colferai, G.P. Salam, A.M. Stasto, *renormalization group improved small x Green's function*, Phys. Rev. D **68** (2003) 114003 doi:[10.1103/PhysRevD.68.114003](https://doi.org/10.1103/PhysRevD.68.114003) [hep-ph/0307188]. (Cited on page 37.)
- [107] M. Ciafaloni, D. Colferai, G.P. Salam, A.M. Stasto, Phys. Lett. B **587** (2004) 87 doi:[10.1016/j.physletb.2004.02.054](https://doi.org/10.1016/j.physletb.2004.02.054) [hep-ph/0311325]. (Cited on page 37.)

- [108] A. Sabio Vera, *An 'All-poles' approximation to collinear resummations in the Regge limit of perturbative QCD*, Nucl. Phys. B **722** (2005) 65 doi:[10.1016/j.nuclphysb.2005.06.003](https://doi.org/10.1016/j.nuclphysb.2005.06.003) [hep-ph/0505128]. (Cited on page 37.)
- [109] F. Caporale, A. Papa, A. Sabio Vera, *Collinear improvement of the BFKL kernel in the electroproduction of two light vector mesons*, Eur. Phys. J. C **53** (2008) 525 doi:[10.1140/epjc/s10052-007-0481-6](https://doi.org/10.1140/epjc/s10052-007-0481-6) [arXiv:0707.4100 [hep-ph]]. (Cited on page 37.)
- [110] J. Kwiecinski, L. Motyka, *Probing the QCD pomeron in doubly tagged e^+e^- collisions*, Phys. Lett. B **462** (1999) 203 doi:[10.1016/S0370-2693\(99\)00866-7](https://doi.org/10.1016/S0370-2693(99)00866-7) [hep-ph/9905567]. (Cited on page 37.)
- [111] C.R. Schmidt, *Rapidity separation dependence and the large next-to-leading corrections to the BFKL equation*, Phys. Rev. D **60** (1999) 074003 doi:[10.1103/PhysRevD.60.074003](https://doi.org/10.1103/PhysRevD.60.074003) [hep-ph/9901397]. (Cited on page 38.)
- [112] J.R. Forshaw, D.A. Ross, A. Sabio Vera, *Rapidity veto effects in the NLO BFKL equation*, Phys. Lett. B **455** (1999) 273 doi:[10.1016/S0370-2693\(99\)00451-7](https://doi.org/10.1016/S0370-2693(99)00451-7) [hep-ph/9903390]. (Cited on page 38.)
- [113] P.M. Stevenson, *Resolution of the renormalization Scheme Ambiguity in Perturbative QCD*, Phys. Lett. **100B** (1981) 61 doi:[10.1016/0370-2693\(81\)90287-2](https://doi.org/10.1016/0370-2693(81)90287-2). (Cited on page 38.)
- [114] P.M. Stevenson, *Optimized Perturbation Theory*, Phys. Rev. D **23** (1981) 2916 doi:[10.1103/PhysRevD.23.2916](https://doi.org/10.1103/PhysRevD.23.2916). (Cited on page 38.)

- [115] G. Grunberg, *Renormalization Group Improved Perturbative QCD*, Phys. Lett. **95B** (1980) 70 [Erratum: Phys. Lett. **110B** (1982) 501] doi:[10.1016/0370-2693\(80\)90402-5](https://doi.org/10.1016/0370-2693(80)90402-5). (Cited on page 38.)
- [116] G. Grunberg, *Renormalization Group Improved Predictions for Quarkonium Decay*, Phys. Lett. **114B** (1982) 271 doi:[10.1016/0370-2693\(82\)90494-4](https://doi.org/10.1016/0370-2693(82)90494-4). (Cited on page 38.)
- [117] G. Grunberg, *Renormalization Scheme Independent QCD and QED: The Method of Effective Charges*, Phys. Rev. D **29** (1984) 2315 doi:[10.1103/PhysRevD.29.2315](https://doi.org/10.1103/PhysRevD.29.2315). (Cited on page 38.)
- [118] *On the elimination of scale ambiguities in perturbative quantum chromodynamics*, S.J. Brodsky, G.P. Lepage, P.B. Mackenzie, Phys. Rev. D **28**, (1983) 228 doi:[10.1103/PhysRevD.28.228](https://doi.org/10.1103/PhysRevD.28.228) (Cited on pages 38 and 147.)
- [119] S.J. Brodsky, F. Hautmann, D.E. Soper, *Probing the QCD Pomeron in e^+e^- collisions*, Phys. Rev. Lett. **78**, (1997) 803 [Erratum: Phys. Rev. Lett. **79**, (1997) 3544] doi:[10.1103/PhysRevLett.78.803](https://doi.org/10.1103/PhysRevLett.78.803) [hep-ph/9610260]. (Cited on pages 38 and 147.)
- [120] S.J. Brodsky, F. Hautmann, D.E. Soper, *Virtual photon scattering at high-energies as a probe of the short distance Pomeron*, Phys. Rev. D **56**, (1997) 6957 doi:[10.1103/PhysRevD.56.6957](https://doi.org/10.1103/PhysRevD.56.6957). [hep-ph/9706427]. (Cited on pages 38 and 147.)
- [121] S.J. Brodsky, V.S. Fadin, V.T. Kim, L.N. Lipatov, G.B. Pivovarov, *The QCD Pomeron with optimal renormalization*, JETP Lett. **70**, (1999) 155 doi:[10.1134/1.568145](https://doi.org/10.1134/1.568145). (Cited on pages 38 and 147.)

- [122] S.J. Brodsky, V.S. Fadin, V.T. Kim, L.N. Lipatov, G.B. Pivovarov, *High-energy QCD asymptotic behavior of photon-photon collisions*, JETP Lett. **76**, (2002) 249 doi:[10.1134/1.1520615](https://doi.org/10.1134/1.1520615). (Cited on pages [38](#) and [147](#).)
- [123] V.S. Fadin, D.Yu. Ivanov, M.I. Kotsky, *Photon Reggeon interaction vertices in the NLA*, Phys. Atom. Nucl. **65** (2002) 1513 [Yad. Fiz. **65** (2002) 1551] doi:[10.1134/1.1501664](https://doi.org/10.1134/1.1501664) [hep-ph/0106099]. (Cited on page [39](#).)
- [124] E.C. Titchmarsh, *The Theory of the Riemann Zeta Function*, 2nd ed. New York: Oxford University Press, ISBN 10: 0198533691/ISBN 13: 978-0198533696, 1986. (Cited on page [46](#).)
- [125] P.M. Morse, H. Feshbach, *Methods of Theoretical Physics, Part I*, New York: McGraw-Hill, ISBN 10: 007043316X/ISBN 13: 978-0070433168, 1953 doi:[10.1063/1.3061460](https://doi.org/10.1063/1.3061460). (Cited on page [46](#).)
- [126] A.P. Prudnikov, Yu.A. Brychkov, O.I. Marichev, *Calculation of integrals and the Mellin transform*, Itogi Nauki i Tekhn. Ser. Mat. Anal. **27** (1989), 3-146 doi:[10.1007/BF01373648](https://doi.org/10.1007/BF01373648). (Cited on page [46](#).)
- [127] I.S. Gradshteyn, I.M. Ryzhik, *Table of Integrals, Series, and Products*, 6th ed. San Diego, CA: Academic Press, ISBN 10: 0122947576/ISBN 13: 978-0122947575, 2000 doi:[10.2307/2007757](https://doi.org/10.2307/2007757). (Cited on page [46](#).)
- [128] D. Zwillinger, *CRC Standard Mathematical Tables and formulas*, 32nd ed. Boca Raton, FL: CRC Press, ISBN 10: 1439835489/ISBN 13: 978-1439835487, 2012. (Cited on page [46](#).)

- [129] G. Arfken, H.J. Weber, F.E. Harris, *Mathematical Methods for Physicists*, 7th ed. Elsevier, ISBN 10: 0123846544/ISBN 13: 978-0123846549, 2013 doi:[10.1119/1.1973757](https://doi.org/10.1119/1.1973757). (Cited on page 46.)
- [130] F. Oberhettinger, *Tables of Mellin Transforms*, reprint edition New York: Springer-Verlag, ISBN 10: 3540069429/ISBN 13: 978-3540069423, 2013 doi:[10.1007/978-3-642-65975-1](https://doi.org/10.1007/978-3-642-65975-1). (Cited on page 46.)
- [131] F.G. Celiberto, D.Yu. Ivanov, B. Murdaca, A. Papa, *Mueller–Navelet Jets at the LHC: Discriminating BFKL from DGLAP by Asymmetric Cuts*, Acta Phys. Polon. Supp. **8** (2015) 935 doi:[10.5506/APhysPolBSupp.8.935](https://doi.org/10.5506/APhysPolBSupp.8.935) [arXiv:1510.01626 [hep-ph]]. (Cited on page 49.)
- [132] F.G. Celiberto, D.Yu. Ivanov, B. Murdaca, A. Papa, *BFKL effects and central rapidity dependence in Mueller–Navelet jet production at 13 TeV LHC*, PoS DIS **2016** (2016) 176 [arXiv:1606.08892 [hep-ph]]. (Cited on page 49.)
- [133] S.D. Ellis, Z. Kunszt, D.E. Soper, *The One Jet Inclusive Cross-Section at Order α_s^3 . 1. Gluons Only*, Phys. Rev. D **40** (1989) 2188 doi:[10.1103/PhysRevD.40.2188](https://doi.org/10.1103/PhysRevD.40.2188). (Cited on page 52.)
- [134] M. Furman, *Study of a Nonleading QCD Correction to Hadron Calorimeter Reactions*, Nucl. Phys. B **197** (1982) 413 doi:[10.1016/0550-3213\(82\)90452-7](https://doi.org/10.1016/0550-3213(82)90452-7). (Cited on page 53.)
- [135] F. Aversa, P. Chiappetta, M. Greco, J.P. Guillet, *QCD Corrections to Parton-Parton Scattering Processes*, Nucl. Phys. B **327** (1989) 105 doi:[10.1016/0550-3213\(89\)90288-5](https://doi.org/10.1016/0550-3213(89)90288-5). (Cited on page 53.)
- [136] J.R. Andersen, V. Del Duca, S. Frixione, C.R. Schmidt, W.J. Stirling, *Mueller–Navelet jets at hadron colliders*, JHEP **0102** (2001) 007

- doi:[10.1088/1126-6708/2001/02/007](https://doi.org/10.1088/1126-6708/2001/02/007) [hep-ph/0101180]. (Cited on page 64.)
- [137] M. Fontannaz, J.P. Guillet, G. Heinrich, *Is a large intrinsic $k(T)$ needed to describe photon + jet photoproduction at HERA?*, Eur. Phys. J. C **22** (2001) 303 doi:[10.1007/s100520100797](https://doi.org/10.1007/s100520100797) [hep-ph/0107262]. (Cited on page 64.)
- [138] J. Currie, A. Gehrmann-De Ridder, E.W.N. Glover, J. Pires, *NNLO QCD corrections to jet production at hadron colliders from gluon scattering*, JHEP **1401** (2014) 110 doi:[10.1007/JHEP01\(2014\)110](https://doi.org/10.1007/JHEP01(2014)110) [arXiv:1310.3993 [hep-ph]]. (Cited on page 70.)
- [139] J.C. Collins, R.K. Ellis, *Heavy quark production in very high-energy hadron collisions*, Nucl. Phys. B **360** (1991) 3 doi:[10.1016/0550-3213\(91\)90288-9](https://doi.org/10.1016/0550-3213(91)90288-9). (Cited on pages 71 and 74.)
- [140] L.V. Gribov, E.M. Levin, M.G. Ryskin, *Semihard Processes in QCD*, Phys. Rept. **100** (1983) 1 doi:[10.1016/0370-1573\(83\)90022-4](https://doi.org/10.1016/0370-1573(83)90022-4). (Cited on pages 71 and 74.)
- [141] E.M. Levin, M.G. Ryskin, Y.M. Shabelski, A.G. Shuvaev, *Heavy quark production in semihard nucleon interactions*, Sov. J. Nucl. Phys. **53** (1991) 657 [Yad. Fiz. **53** (1991) 1059]. (Cited on pages 71 and 74.)
- [142] J. Bartels, A. Sabio Vera, F. Schwennsen, *NLO inclusive jet production in k_T -factorization*, JHEP **0611** (2006) 051 doi:[10.1088/1126-6708/2006/11/051](https://doi.org/10.1088/1126-6708/2006/11/051) [hep-ph/0608154]. (Cited on pages 71, 133 and 167.)
- [143] S. Sapeta, *QCD and Jets at Hadron Colliders*, Prog. Part. Nucl. Phys. **89** (2016) 1 doi:[10.1016/j.pnnp.2016.02.002](https://doi.org/10.1016/j.pnnp.2016.02.002) [arXiv:1511.09336 [hep-ph]]. (Cited on page 71.)

- [144] A.D. Martin, W.J. Stirling, R.S. Thorne, G. Watt, *Parton distributions for the LHC*, Eur. Phys. J. C **63** (2009) 189 doi:[10.1140/epjc/s10052-009-1072-5](https://doi.org/10.1140/epjc/s10052-009-1072-5) [arXiv:0901.0002 [hep-ph]]. (Cited on pages [89](#), [105](#), [126](#), [156](#) and [193](#).)
- [145] L.A. Harland-Lang, A.D. Martin, P. Motylinski, R.S. Thorne, *Parton distributions in the LHC era: MMHT 2014 PDFs*, Eur. Phys. J. C **75** (2015) no.5, 204 doi:[10.1140/epjc/s10052-015-3397-6](https://doi.org/10.1140/epjc/s10052-015-3397-6) [arXiv:1412.3989 [hep-ph]]. (Cited on pages [89](#) and [126](#).)
- [146] CERNLIB Homepage: <http://cernlib.web.cern.ch/cernlib>. (Cited on pages [89](#), [90](#) and [126](#).)
- [147] R. Forrey, *Computing the Hypergeometric Function*, J. Comput. Phys. **137** (1997) 79 doi:[10.1006/jcph.1997.5794](https://doi.org/10.1006/jcph.1997.5794). (Cited on pages [89](#) and [126](#).)
- [148] W.J. Cody, A.J. Strecok, H.C. Thacher, *Chebyshev Approximations for the Psi Function*, Math. Comput. **27** (1973) 121. doi:[10.1090/S0025-5718-1973-0326986-3](https://doi.org/10.1090/S0025-5718-1973-0326986-3). (Cited on pages [89](#), [126](#), [156](#) and [193](#).)
- [149] G.A. Chirilli, B.W. Xiao, F. Yuan, *Inclusive Hadron Productions in pA Collisions*, Phys. Rev. D **86** (2012) 054005 doi:[10.1103/PhysRevD.86.054005](https://doi.org/10.1103/PhysRevD.86.054005) [arXiv:1203.6139 [hep-ph]]. (Cited on page [99](#).)
- [150] E. Iancu, A.H. Mueller, D.N. Triantafyllopoulos, *CGC factorization for forward particle production in proton-nucleus collisions at next-to-leading order*, JHEP **1612** (2016) 041 doi:[10.1007/JHEP12\(2016\)041](https://doi.org/10.1007/JHEP12(2016)041) [arXiv:1608.05293 [hep-ph]]. (Cited on page [99](#).)
- [151] F.G. Celiberto, D.Yu. Ivanov, B. Murdaca, A. Papa, *High energy resummation in dihadron production at the LHC*, Phys. Rev. D **94** (2016) no.3, 034013

- doi:[10.1103/PhysRevD.94.034013](https://doi.org/10.1103/PhysRevD.94.034013) [arXiv:1604.08013 [hep-ph]]. (Cited on pages 99, 113 and 196.)
- [152] F.G. Celiberto, D.Yu. Ivanov, B. Murdaca, A. Papa, *Dihadron production at the LHC: full next-to-leading BFKL calculation*, Eur. Phys. J. C **77** (2017) no.6, 382 doi:[10.1140/epjc/s10052-017-4949-8](https://doi.org/10.1140/epjc/s10052-017-4949-8) [arXiv:1701.05077 [hep-ph]]. (Cited on pages 99 and 197.)
- [153] F.G. Celiberto, *BFKL phenomenology: resummation of high-energy logs in semi-hard processes at LHC*, Frascati Phys. Ser. **63** (2016) 43, ISBN: 978-88-86409-82-7 [arXiv:1606.07327 [hep-ph]]. (Cited on pages 99, 134 and 168.)
- [154] F.G. Celiberto, D.Yu. Ivanov, B. Murdaca, A. Papa, *Dihadron Production at LHC: BFKL Predictions for Cross Sections and Azimuthal Correlations*, AIP Conf. Proc. **1819** (2017) no.1, 060005 doi:[10.1063/1.4977161](https://doi.org/10.1063/1.4977161) [arXiv:1611.04811 [hep-ph]]. (Cited on page 99.)
- [155] F.G. Celiberto, D.Yu. Ivanov, B. Murdaca, A. Papa, *Charged light di-hadron production at 7 and 13 TeV LHC in the full NLA BFKL approach*, in progress. (Cited on page 99.)
- [156] F.G. Celiberto, D.Yu. Ivanov, B. Murdaca, A. Papa, *Inclusive dihadron production at the LHC in the NLA BFKL*, in progress. (Cited on page 99.)
- [157] S. Albino, B.A. Kniehl, G. Kramer, *AKK Update: Improvements from New Theoretical Input and Experimental Data*, Nucl. Phys. B **803**, (2008) 42 doi:[10.1016/j.nuclphysb.2008.05.017](https://doi.org/10.1016/j.nuclphysb.2008.05.017) [arXiv:0803.2768 [hep-ph]]. (Cited on pages 105 and 126.)

- [158] M. Hirai, S. Kumano, T.-H. Nagai, K. Sudoh, *Determination of fragmentation functions and their uncertainties*, Phys. Rev. D **75**, (2007) 094009 doi:[10.1103/PhysRevD.75.094009](https://doi.org/10.1103/PhysRevD.75.094009) [hep-ph/0702250]. (Cited on pages 105 and 126.)
- [159] B. Jager, M. Stratmann, W. Vogelsang, *Single inclusive jet production in polarized pp collisions at $O(\alpha_s^3)$* , Phys. Rev. D **70** (2004) 034010 doi:[10.1103/PhysRevD.70.034010](https://doi.org/10.1103/PhysRevD.70.034010) [hep-ph/0404057]. (Cited on pages 114 and 199.)
- [160] N. Kidonakis, G. Oderda, G.F. Sterman, *Threshold resummation for dijet cross-sections*, Nucl. Phys. B **525** (1998) 299 doi:[10.1016/S0550-3213\(98\)00243-0](https://doi.org/10.1016/S0550-3213(98)00243-0) [hep-ph/9801268]. (Cited on pages 114 and 199.)
- [161] D. de Florian, W. Vogelsang, *Resummed cross-section for jet production at hadron colliders* Phys. Rev. D **76** (2007) 074031 doi:[10.1103/PhysRevD.76.074031](https://doi.org/10.1103/PhysRevD.76.074031) [arXiv:0704.1677 [hep-ph]]. (Cited on pages 114 and 199.)
- [162] S. Catani, M.L. Mangano, P. Nason, L. Trentadue, *The Resummation of soft gluons in hadronic collisions,* Nucl. Phys. B **478** (1996) 273 doi:[10.1016/0550-3213\(96\)00399-9](https://doi.org/10.1016/0550-3213(96)00399-9) [hep-ph/9604351]. (Cited on pages 114 and 199.)
- [163] S. Dulat et al. *New parton distribution functions from a global analysis of quantum chromodynamics*, Phys. Rev. D **93** (2016) no.3, 033006 doi:[10.1103/PhysRevD.93.033006](https://doi.org/10.1103/PhysRevD.93.033006) [arXiv:1506.07443 [hep-ph]]. (Cited on page 126.)
- [164] D. de Florian, R. Sassot, M. Stratmann, *Global analysis of fragmentation functions for pions and kaons and their uncertainties*, Phys. Rev. D

- 75 (2007) 114010 doi:[10.1103/PhysRevD.75.114010](https://doi.org/10.1103/PhysRevD.75.114010) [hep-ph/0703242 [hep-ph]]. (Cited on page 126.)
- [165] D. de Florian, R. Sassot, M. Stratmann, *Global analysis of fragmentation functions for protons and charged hadrons*, Phys. Rev. D **76** (2007) 074033 doi:[10.1103/PhysRevD.76.074033](https://doi.org/10.1103/PhysRevD.76.074033) [arXiv:0707.1506 [hep-ph]]. (Cited on page 126.)
- [166] D.J. Yang, F.J. Jiang, W.C. Chang, C.W. Kao, S.i. Nam, *Consistency check of charged hadron multiplicities and fragmentation functions in SIDIS*, Phys. Lett. B **755**, (2016) 393 doi:[10.1016/j.physletb.2016.02.046](https://doi.org/10.1016/j.physletb.2016.02.046) [arXiv:1511.08026 [hep-ph]]. (Cited on page 109.)
- [167] J.F. Owens, *A Next-to-leading order study of dihadron production*, Phys. Rev. D **65**, (2002) 034011 doi:[10.1103/PhysRevD.65.034011](https://doi.org/10.1103/PhysRevD.65.034011) [hep-ph/0110036]. (Cited on page 127.)
- [168] L.G. Almeida, G.F. Sterman, W. Vogelsang, *Threshold Resummation for Di-hadron Production in Hadronic Collisions*, Phys. Rev. D **80**, (2009) 074016 doi:[10.1103/PhysRevD.80.074016](https://doi.org/10.1103/PhysRevD.80.074016) [arXiv:0907.1234 [hep-ph]]. (Cited on page 127.)
- [169] F. Schwennsen, *Phenomenology of jet physics in the BFKL formalism at NLO*, hep-ph/0703198 [hep-ph]. (Cited on page 133.)
- [170] F. Caporale, G. Chachamis, B. Murdaca, A. Sabio Vera, *Balitsky-Fadin-Kuraev-Lipatov Predictions for Inclusive Three Jet Production at the LHC*, Phys. Rev. Lett. **116** (2016) no.1, 012001 doi:[10.1103/PhysRevLett.116.012001](https://doi.org/10.1103/PhysRevLett.116.012001) [arXiv:1508.07711 [hep-ph]]. (Cited on pages 134, 139, 142, 153 and 197.)

- [171] F. Caporale, F.G. Celiberto, G. Chachamis, D. Gordo Gomez, A. Sabio Vera, *BFKL Azimuthal Imprints in Inclusive Three-jet Production at 7 and 13 TeV*, Nucl. Phys. B **910** (2016) 374 doi:[10.1016/j.nuclphysb.2016.07.012](https://doi.org/10.1016/j.nuclphysb.2016.07.012) [arXiv:1603.07785 [hep-ph]]. (Cited on pages [134](#) and [197](#).)
- [172] F. Caporale, F.G. Celiberto, G. Chachamis, D. Gordo Gomez, A. Sabio Vera, *Stability of Azimuthal-angle Observables under Higher Order Corrections in Inclusive Three-jet Production*, Phys. Rev. D **95** (2017) no.7, 074007 doi:[10.1103/PhysRevD.95.074007](https://doi.org/10.1103/PhysRevD.95.074007) [arXiv:1612.05428 [hep-ph]]. (Cited on pages [134](#) and [197](#).)
- [173] F. Caporale, G. Chachamis, B. Murdaca, A. Sabio Vera, *Inclusive three jet production at the LHC as a new BFKL probe*, arXiv:1603.08292 [hep-ph]. (Cited on page [134](#).)
- [174] G. Chachamis, F. Caporale, F.G. Celiberto, D. Gordo Gomez, A. Sabio Vera, *Inclusive three jet production at the LHC at 7 and 13 TeV collision energies*, PoS DIS **2016** (2016) 178 arXiv:1610.01342 [hep-ph]. (Cited on page [134](#).)
- [175] F. Caporale, F.G. Celiberto, G. Chachamis, D. Gordo Gomez, B. Murdaca, A. Sabio Vera, *High energy effects in multi-jet production at LHC*, arXiv:1610.04765 [hep-ph]. (Cited on pages [134](#) and [168](#).)
- [176] F. Caporale, F.G. Celiberto, G. Chachamis, D. Gordo Gomez, A. Sabio Vera, *Inclusive three- and four-jet production in multi-Regge kinematics at the LHC*, AIP Conf. Proc. **1819** (2017) no.1, 060009 doi:[10.1063/1.4977165](https://doi.org/10.1063/1.4977165) [arXiv:1611.04813 [hep-ph]]. (Cited on pages [134](#) and [168](#).)
- [177] F. Caporale, F.G. Celiberto, G. Chachamis, D. Gordo Gomez, A. Sabio Vera, *Probing the BFKL dynamics in inclusive three jet production at the LHC*, arXiv:1612.02771 [hep-ph]. (Cited on page [134](#).)

- [178] G. Chachamis, F. Caporale, F.G. Celiberto, D. Gordo Gomez, A. Sabio Vera, *Azimuthal-angle Observables in Inclusive Three-jet Production*, to appear in PoS DIS 2017. (Cited on page [134](#).)
- [179] E.E. Salpeter, H.A. Bethe, *Relativistic equation for bound state problems*, Phys. Rev. **84** (1951) 1232 doi:[10.1103/PhysRev.84.1232](#). (Cited on page [154](#).)
- [180] G. Chachamis, M. Deak, A. Sabio Vera, P. Stephens, *A Comparative study of small x Monte Carlos with and without QCD coherence effects*, Nucl. Phys. B **849** (2011) 28 doi:[10.1016/j.nuclphysb.2011.03.011](#) [arXiv:1102.1890 [hep-ph]]. (Cited on pages [140](#) and [199](#).)
- [181] G.P. Lepage, *A New Algorithm for Adaptive Multidimensional Integration*, J. Comput. Phys. **27** (1978) 192 doi:[10.1016/0021-9991\(78\)90004-9](#). (Cited on pages [156](#) and [193](#).)
- [182] T. Hahn, *CUBA: A Library for multidimensional numerical integration*, Comput. Phys. Commun. **168** (2005) 78 doi:[10.1016/j.cpc.2005.01.010](#) [hep-ph/0404043]. (Cited on pages [156](#) and [193](#).)
- [183] T. Hahn, *Concurrent Cuba*, J. Phys. Conf. Ser. **608** (2015) 1 doi:[10.1088/1742-6596/608/1/012066](#) [arXiv:1408.6373 [physics.comp-ph]]. (Cited on pages [156](#) and [193](#).)
- [184] R. Piessens, E. De Doncker-Kapenga, C.W. Überhuber, *QUADPACK: a subroutine package for automatic integration*, Berlin, Heidelberg: Springer-Verlag, ISBN 10: 3540125531/ ISBN 13: 978-3540125532, 1983 doi:[10.1007/978-3-642-61786-7](#). (Cited on pages [156](#) and [193](#).)

- [185] F. Caporale, F.G. Celiberto, G. Chachamis, A. Sabio Vera, *Multi-Regge kinematics and azimuthal angle observables for inclusive four-jet production*, Eur. Phys. J. C **76** (2016) no.3, 165 doi:[10.1140/epjc/s10052-016-3963-6](https://doi.org/10.1140/epjc/s10052-016-3963-6) [arXiv:1512.03364 [hep-ph]]. (Cited on pages [168](#) and [197](#).)
- [186] F. Caporale, F.G. Celiberto, G. Chachamis, D. Gordo Gomez, A. Sabio Vera, *Inclusive Four-jet Production at 7 and 13 TeV: Azimuthal Profile in Multi-Regge Kinematics*, Eur. Phys. J. C **77** (2017) no.1, 5 doi:[10.1140/epjc/s10052-016-4557-z](https://doi.org/10.1140/epjc/s10052-016-4557-z) arXiv:1606.00574 [hep-ph]. (Cited on pages [168](#) and [197](#).)
- [187] F. Caporale, F.G. Celiberto, G. Chachamis, A. Sabio Vera, *Inclusive four-jet production: a study of Multi-Regge kinematics and BFKL observables*, PoS DIS **2016** (2016) 177 [arXiv:1610.01880 [hep-ph]]. (Cited on page [168](#).)
- [188] M. Diehl, D. Ostermeier, A. Schafer, *Elements of a theory for multiparton interactions in QCD*, JHEP **1203** (2012) 089 doi:[10.1007/JHEP03\(2012\)089](https://doi.org/10.1007/JHEP03(2012)089) [arXiv:1111.0910 [hep-ph]]. (Cited on page [199](#).)
- [189] H. Jung, M. Kraemer, A.V. Lipatov, N.P. Zotov, *Investigation of beauty production and parton shower effects at LHC*, Phys. Rev. D **85**, 034035 (2012) doi:[10.1103/PhysRevD.85.034035](https://doi.org/10.1103/PhysRevD.85.034035) [arXiv:1111.1942 [hep-ph]]. (Cited on page [199](#).)
- [190] S.P. Baranov, A.V. Lipatov, M.A. Malyshev, A.M. Snigirev, N.P. Zotov, *Associated $W^\pm D^{(*)}$ production at the LHC and prospects to observe double parton interactions*, Phys. Lett. B **746**, 100 (2015) doi:[10.1016/j.physletb.2015.04.059](https://doi.org/10.1016/j.physletb.2015.04.059) [arXiv:1503.06080 [hep-ph]]. (Cited on page [199](#).)
- [191] R. Maciula, A. Szczurek, *Double-parton scattering contribution to production of jet pairs with large rapidity separation at the LHC*, Phys. Rev. D **90**, (2014)

no. 1, 014022 doi:[10.1103/PhysRevD.90.014022](https://doi.org/10.1103/PhysRevD.90.014022) [arXiv:1403.2595 [hep-ph]].

(Cited on page 199.)

- [192] R. Maciula, A. Szczurek, *Searching for and exploring double-parton scattering effects in four-jet production at the LHC*, Phys. Lett. B **749**, 57 (2015) doi:[10.1016/j.physletb.2015.07.035](https://doi.org/10.1016/j.physletb.2015.07.035) [arXiv:1503.08022 [hep-ph]]. (Cited on page 199.)
- [193] K. Kutak, R. Maciula, M. Serino, A. Szczurek, A. van Hameren, *Four-jet production in single- and double-parton scattering within high-energy factorization*, JHEP **1604** (2016) 175 doi:[10.1007/JHEP04\(2016\)175](https://doi.org/10.1007/JHEP04(2016)175) [arXiv:1602.06814 [hep-ph]]. (Cited on page 199.)
- [194] K. Kutak, R. Maciula, M. Serino, A. Szczurek, A. van Hameren, *Search for optimal conditions for exploring double-parton scattering in four-jet production: k_t -factorization approach*, Phys. Rev. D **94** (2016) no.1, 014019 doi:[10.1103/PhysRevD.94.014019](https://doi.org/10.1103/PhysRevD.94.014019) [arXiv:1605.08240 [hep-ph]]. (Cited on page 199.)
- [195] F. Caporale, F.G. Celiberto, G. Chachamis, M. Deak, D. Gordo Gomez, A. Sabio Vera, *Full NLA BFKL Effects in Inclusive Multi-jet Production at the LHC*, in progress. (Cited on page 199.)
- [196] G. Chachamis, A. Sabio Vera, *The Colour Octet Representation of the Non-Forward BFKL Green Function*, Phys. Lett. B **709** (2012) 301 doi:[10.1016/j.physletb.2012.02.036](https://doi.org/10.1016/j.physletb.2012.02.036) [arXiv:1112.4162 [hep-th]]. (Cited on page 199.)
- [197] G. Chachamis, A. Sabio Vera, *The NLO $N = 4$ SUSY BFKL Green function in the adjoint representation*, Phys. Lett. B **717** (2012) 458

- doi:[10.1016/j.physletb.2012.09.051](https://doi.org/10.1016/j.physletb.2012.09.051) [arXiv:1206.3140 [hep-th]]. (Cited on page 199.)
- [198] G. Chachamis, A. Sabio Vera, C. Salas, *Bootstrap and momentum transfer dependence in small x evolution equations*, Phys. Rev. D **87** (2013) 1, 016007 doi:[10.1103/PhysRevD.87.016007](https://doi.org/10.1103/PhysRevD.87.016007) [arXiv:1211.6332 [hep-ph]]. (Cited on page 199.)
- [199] F. Caporale, G. Chachamis, J.D. Madrigal, B. Murdaca, A. Sabio Vera, *A study of the diffusion pattern in $N = 4$ SYM at high energies*, Phys. Lett. B **724** (2013) 127 doi:[10.1016/j.physletb.2013.05.058](https://doi.org/10.1016/j.physletb.2013.05.058) [arXiv:1305.1474 [hep-th]]. (Cited on page 199.)
- [200] G. Chachamis, A. Sabio Vera, *Monte Carlo study of double logarithms in the small x region*, Phys. Rev. D **93**, (2016) no. 7, 074004 doi:[10.1103/PhysRevD.93.074004](https://doi.org/10.1103/PhysRevD.93.074004) [arXiv:1511.03548 [hep-ph]]. (Cited on page 199.)
- [201] G. Chachamis, A. Sabio Vera, *The high-energy radiation pattern from BFKLex with double-log collinear contributions*, JHEP **1602** (2016) 064 doi:[10.1007/JHEP02\(2016\)064](https://doi.org/10.1007/JHEP02(2016)064) [arXiv:1512.03603 [hep-ph]]. (Cited on page 199.)
- [202] G. Chachamis, A. Sabio Vera, *Solution of the Bartels-Kwiecinski-Praszalowicz equation via Monte Carlo integration*, Phys. Rev. D **94**, (2016) no. 3, 034019 doi:[10.1103/PhysRevD.94.034019](https://doi.org/10.1103/PhysRevD.94.034019) [arXiv:1606.07349 [hep-ph]]. (Cited on page 199.)
- [203] S. Catani, M. Fontannaz, J.P. Guillet, E. Pilon, *Isolating Prompt Photons with Narrow Cones*, JHEP **1309** (2013) 007 doi:[10.1007/JHEP09\(2013\)007](https://doi.org/10.1007/JHEP09(2013)007) [arXiv:1306.6498 [hep-ph]]. (Cited on page 199.)

- [204] M. Dasgupta, F. Dreyer, G.P. Salam, G. Soyez, *Small-radius jets to all orders in QCD*, JHEP **1504** (2015) 039 doi:[10.1007/JHEP04\(2015\)039](https://doi.org/10.1007/JHEP04(2015)039) [arXiv:1411.5182 [hep-ph]]. (Cited on page [199](#).)